

Design of Elastin-like Protein and Poly(ethylene glycol) Hydrogels for Neural Tissue Engineering Applications

A Dissertation

Presented to

the faculty of the School of Engineering and Applied Science

University of Virginia

in partial fulfillment
of the requirements for the degree

Doctor of Philosophy

by

Edi Mecho

August 2020

APPROVAL SHEET

This Dissertation
is submitted in partial fulfillment of the requirements
for the degree of
Doctor of Philosophy

Author Signature: Edi Meco

This Dissertation has been read and approved by the examining committee:

Advisor: Kyle Lampe

Committee Member: Steven Caliari

Committee Member: Christopher Highley

Committee Member: Shayn Peirce-Cottler

Committee Member: Rachel Letteri

Committee Member: _____

Accepted for the School of Engineering and Applied Science:



Craig H. Benson, School of Engineering and Applied Science

August 2020

Abstract

Biomaterial scaffolds are promising tools in developing treatments for central nervous system (CNS) injury and disease. *In vitro* biomaterial systems can be designed to help elucidate the complex signaling interplay between cells and their extracellular matrix (ECM). Recombinant engineered proteins are ideal biomaterials to create *in vitro* models of native ECM because they are derived from native proteins, have a well-defined protein primary structure, bioactivity can be imbedded in the amino acid sequence, and amino acid residue side chains can be modified to adapt the cross-linking mechanism to form hydrogels suitable for a variety of applications. Recombinant engineered elastin-like proteins (ELPs) are derived from tropoelastin and are composed of repeating VPGxG penta-peptide sequences, where x is any amino acid guest residue except for proline. ELPs undergo a unique lower critical solution temperature (LCST) transition above which they aggregate into a protein-rich coacervate phase in aqueous solution. The ELP LCST transition was used to develop poly(ethylene glycol) (PEG) and ELP hydrogels with micro-architecture. Two distinct hydrogels with differing properties were formed by controlling the temperature at which the cross-linking reactions occurred. Bioactivity is incorporated into ELP hydrogels by imbedding small bioactive peptide sequences, such as cell-adhesive RGD, into the protein sequence. ELP sequences with differing bioactive peptides can be combined to form hydrogels with multiple bioactivities, and the small differences in the amino acid content result in hydrogels with almost identical physical properties. This allows for independent tuning of ELP hydrogel physical properties, which is controlled by adjusting protein concentration and crosslinking ratios, from bioactivity, which is controlled by adjusting the mixture of ELP sequences. Hydrogels that were either enzymatically degradable by urokinase plasminogen activator (uPA) or non-degradable had similar stiffness and stress relaxation properties to native brain tissue, making them suitable *in vitro* models of brain ECM. uPA degradable hydrogels promoted encapsulated oligodendrocyte

precursor cell (OPC) maturation when compared to non-degradable hydrogels. This work identifies the usefulness of ELPs in designing *in vitro* hydrogel models of the CNS ECM, and illustrates the types of interactions between cells and their ECM that can be analyzed through ELP hydrogel systems.

Acknowledgements

I would like to start by thanking my family for supporting me through the journey of graduate school. They have been there to listen and support me through my struggles, and I would not be here without them.

I want to thank my advisor Dr. Kyle Lampe for his patience throughout this process. It took a long time to get some of the hydrogel systems to work and my scientific writing did not start out great. Without his help I would not have made the progress that I did and be here right now.

I want to thank my committee for taking the time to provide research advice and resources: Dr. Stephen Caliari, Dr. Christopher Highley, Dr. Shayn Peirce-Cottler, and Dr. Rachel Letteri.

I want to thank my fellow graduate students of the Lampe lab that helped provide feedback on my experiments, presentations and writing. Dr. James Tang, Dr. Nick Murphy, Dr. Lauren Russell, Deniz Unal, Zhiqi Zhang and Rachel Mazur. I have spent so much time discussing projects, troubleshooting experiments, and having some fun outside the lab with them.

I would like to thank my wonderful undergraduate students that made significant contributions to this work: Meghan Hefferon, Anne Katherine Brooks, Sharon Zheng and Anahita Sharma. It was great to watch them grow as researchers. There were many memorable moments that I'll have with me forever. While I was helping them, they helped me grow as a mentor.

A special shout out to my good friend and colleague Preston Fuks. It feels like we've talked about everything together: Life, research, best pizza place in Charlottesville, etc. I'll never forget the trip Preston, James and myself made to Thailand. Now that I am at the end of the graduate school journey, the Thai saying "same same" seems resoundingly wise.

I would like to thank my first-year roommates Dr. Arch Creasy, Dr. Eric "Zen Master" Dybeck, and Dr. Ben Huang for showing me the graduate school lifestyle. Letting me pick their

brains about graduate school life and showing me that there is more to being a graduate student than running experiments in the lab.

Finally, I want to thank all of my fellow graduate student friends that I made here at UVA. There are too many to list so I will end by saying that they made my experience at UVA wonderful. This school and department have an amazing culture and it has been great to be part of the UVA CHE family.

Table of Contents

	Page
1 Introduction and Background	1
1.1 Need for CNS injury and disease treatments	1
1.2 The roles of biomaterial scaffolds in treatment development.....	1
1.3 Poly(ethylene glycol) hydrogels	3
1.4 Elastin-like proteins	5
1.5 Micro-architecture in hydrogel systems	6
1.6 OPC urokinase plasminogen activator (uPA) activity	7
1.7 Synopsis of research.....	9
1.8 References	11
2 Microscale architecture in biomaterial scaffolds for spatial control of neural cell behavior .	20
2.1 Abstract	20
2.2 Introduction	21
2.2.1 Tissue damage in the CNS	21
2.2.2 Reparative effects of endogenous neural cells	22
2.2.3 Bulk biomaterials for tissue repair	24
2.2.4 Microscale architecture in biomaterials	25
2.3 Lithography	27
2.3.1 Lithographic techniques	27
2.3.2 Grooves on scaffold surfaces	28
2.3.3 Immobilization of bioactive motifs	30
2.3.4 Microscale design in 3D space.....	33

2.4	Electrospinning	34
2.4.1	Electrospinning techniques.....	34
2.4.2	Neural cells on aligned fibers.....	35
2.4.3	Fiber material composition.....	36
2.4.4	Fiber diameter.....	38
2.4.5	Fibers in 3D scaffolds.....	38
2.4.6	Fiber scaffolds in vivo	40
2.5	3D bioprinting	41
2.5.1	Bioprinting techniques	41
2.5.2	Strategies for biomaterial printing.....	43
2.5.3	Bioprinting bioactive molecules.....	46
2.6	Future perspectives.....	46
2.7	Funding	51
2.8	References	51
3	Impact of Elastin-like Protein Temperature Transition on PEG-ELP Hybrid Hydrogel Properties	68
3.1	Abstract	68
3.2	Introduction	69
3.3	Materials and methods	73
3.3.1	Methacrylation of poly(ethylene glycol).....	73
3.3.2	Elastin-like protein expression	74
3.3.3	Optical density analysis.....	75
3.3.4	Analysis of ELP domains	76

3.3.5	Protein release	76
3.3.6	Rheological measurements.....	77
3.3.7	Lower critical solution temperature measurements.....	77
3.3.8	Statistical analysis	78
3.4	Results and discussion	78
3.4.1	PEG-ELP micro-architecture formation.....	78
3.4.2	ELP release kinetics	81
3.4.3	PEG-ELP mechanical properties.....	87
3.4.4	PEG-ELP optical properties	91
3.5	Conclusions	93
3.6	Funding	93
3.7	References	94
4	Guiding oligodendrocyte precursor cell maturation with urokinase plasminogen activator-degradable elastin-like protein hydrogels.....	105
4.1	Abstract	105
4.2	Introduction	106
4.3	Experimental Methods	109
4.3.1	Materials.....	109
4.3.2	ELP expression and purification	109
4.3.3	ELP azide functionalization and characterization	109
4.3.4	PEG-BCN synthesis and characterization	110
4.3.5	ELP LCST measurements	111
4.3.6	MADM OPC culture	111

4.3.7	Hydrogel formation	111
4.3.8	Rheological measurements.....	112
4.3.9	Zymography	112
4.3.10	MADM OPC degradation of ELP hydrogels	113
4.3.11	Viability analysis.....	113
4.3.12	ATP and DNA quantification.....	114
4.3.13	EdU and DAPI imaging	114
4.3.14	F-Actin and DAPI imaging	115
4.3.15	RNA quantification	115
4.3.16	Statistical analysis	116
4.4	Results and Discussion.....	116
4.4.1	Azide functionalization of ELPs	116
4.4.2	Independent tuning of hydrogel bioactivity from stiffness	119
4.4.3	MADM OPC uPA expression	121
4.4.4	Encapsulated MADM OPC metabolic activity	125
4.4.5	MADM OPC maturation in ELP hydrogels.....	128
4.4.6	Impact of the encapsulation process on MADM OPC gene expression	133
4.5	Conclusions	134
4.6	Funding	135
4.7	References	136
5	Micro-localization of adhesive RGD peptide sequence within PEG-ELP single-network hydrogels.....	145
5.1	THPC cytotoxicity of MADM OPCs.....	146

5.2	SPAAC cross-linking.....	148
5.3	Impact of ELP azide functionalization on protein properties	150
5.4	Conclusions and future perspectives.....	152
5.5	References	154
6	Creation of UV-light induced self-healing ELP hydrogels for 3D bioprinting.....	158
6.1	Introduction.....	158
6.2	ELP bioinks: Mixing with yield stress materials	158
6.3	ELP bioinks: UV-light induced self-healing.....	161
6.4	Conclusions and future perspectives.....	167
6.5	References	168
7	MADM OPCs in media with FBS.....	172
7.1	Introduction.....	172
7.2	MADM OPCs in media with serum.....	172
7.3	Conclusions and future perspectives.....	176
7.4	References	178
8	Appendix A: Chapter 3 Supplementary Information.....	180
9	Appendix B: Chapter 4 Supplementary Information.....	182
10	Appendix C: Procedures and Protocols	187
10.1	Zymography for uPA degradable ELP.....	187
10.2	ELP hydrogel RT-qPCR	190
10.3	OPC cryopreservation	193
10.4	ELP azide functionalization	194
10.5	ELP norbornene functionalization	195

10.6	PEG-BCN synthesis	196
10.7	HNMR quick guide (Flipper).....	197
10.8	Addition of Alexa Fluor 405 NHS Ester onto PEG-amine	199
10.9	Addition of Rhodamine onto ELP	200
10.10	PEG microwave-assisted methacrylation.....	201
10.11	Cell expansion (passage).....	202
10.12	Cell expansion (OPC)	204

Table of Figures

Figure 2-1: (A) Chitosan solution gelled by contacting with ammonia vapors and then fragmented mechanically into differing average microscale architecture. (B-D) Immunostaining of spinal cord lesion site 4 weeks post injury/injection for neurofilament (NF), astrocytes (GFAP), and cell nuclei (DAPI). (B) Lesion only, (C) lesion with chitosan-FPHS hydrogel implant with 150 μm average fragment size, and (D) lesion with chitosan-FPHS 20 μm average fragment size. Smaller fragments result in greater presence of neurofilament in the lesion site. (B, D) Scale bar = 240 μm and (C) Scale bar = 300 μm . Reproduced with permission of ref. 29, Copyright 2017, Elsevier.26

Figure 2-2: Schematic of 3D bioprinting, electrospinning, and lithography techniques. The type of 3D bioprinter is chosen based on biomaterial rheological properties. Electrospun fibers are patterned by changing the collector. Lithography patterning is done by adjusting light based techniques or using a mold.27

Figure 2-3: Radial glial cells seeded on (A) unpatterned PMMA surface and (B) PMMA surface with 2 μm wide channels. Cell nuclei stained with TO-PRO-S (blue) and neurons stained with beta tubulin III (red). (C) Particle tracks of neuronal trajectories over 3 hours in unpatterned PMMA (top) and PMMA with 2 μm wide channels (bottom). Scale bar = 200 μm . Reproduced with permission of ref. 40, Copyright 2012, Elsevier.30

Figure 2-4: Human astrocytoma cell line U373 cultured on (A) poly-L-lysine substrate for 4 days and (B) aligned PCL fibers for 7 days. Arrows indicate (A) process extensions and (B) fiber orientation. Reproduced with permission of Gerardo-Nava et al. (2009), Copyright 2009, Future Medicine LTD. Human umbilical cord mesenchymal stem cells cultured on (C) tissue culture plastic, (D) randomly oriented fibrin fibers, and (E) aligned fibrin fibers

for 1 day. Arrow indicates fiber orientation. Reproduced with permission of ref. 69, Copyright 2016, Royal Society of Chemistry. (A, B) Cell nuclei (blue), GFAP (green), vimentin (red) and scale bars = 100 μm . (C, D, E) Cell nuclei (blue) and F-actin (red)...37

Figure 2-5: (A) Lateral view of 3D printed alginate gel matching anatomical features of the cortex and cerebellum with microscale resolution. (B) Top view with black dye dripped on alginate gels. Scale bars = 1 cm. Reproduced with permission of ref. 116, Creative Commons Copyright (CC-BY).....43

Figure 3-1: Elastin-Like protein amino acid sequence and illustration of primary amines available for crosslinking with tetrakis(hydroxymethyl) phosphonium chloride (THPC).....73

Figure 3-2: Schematic of PEG and ELP hydrogel gelation at 25 and 37°C. Representative images of PEG-ELP hydrogels after gelation, showing TRITC labeled ELP (red). Scale bars = 100 μm74

Figure 3-3: ELP-rich domain formation in 6/1.5 PEG-ELP hydrogels gelled at 37°C. Rows showing gels with a 2:1 THPC crosslinker to ELP amines ratio (A-C) and without crosslinker (B-F). Columns showing ELP domains immediately after gelation (A, D), after 3 hours in a relative humidity-controlled chamber (B, E) and after swelling in PBS for 24 h (E, F). ELP labeled with TRITC (Red) and scale bars = 100 μm81

Figure 3-4: Temperature dependence of ELP release from 6/1.5 PEG-ELP hydrogels. Panels are of PEG-ELP hydrogels gelled at 37°C (A-F) and 25°C (G-L). Rows show gels with a 2:1 THPC crosslinker to ELP amines ratio (A-C and G-I) and without the THPC crosslinker (D-F and J-L). Columns showing ELP domains immediately after gelation (A, D, G, J), and after incubating in PBS for 1 h at 25°C (B, E, H, K) and 37°C (C, F, I, L). ELP labeled with TRITC (Red) and scale bars = 100 μm . Dashed lines indicate the hydrogel edge....83

Figure 3-5: Cumulative release of ELP from 6/1.5 PEG-ELP hydrogels gelled at 37°C (A) and 25°C (B) after swelling in PBS for 1, 3, 8, and 48 hours. Data also shown as a function of THPC crosslinker presence (With THPC (C) and without THPC (D)). Representative data fits of Fickian diffusion model shown in (A). Showing standard error. Stars indicate statistical significance in mean values of ELP release from hydrogels made with and without THPC (A, B), and hydrogels gelled at 37°C and 25°C (C, D) using 2 way anova with replication ($p < 0.05$).86

Figure 3-6: The effect of PEG and ELP concentration, THPC presence and gelation temperature on PEG-ELP hydrogel swollen shear storage modulus. Representative strain (A) and frequency (B) sweeps of swollen 8/1.5 PEG-ELP hydrogels. Swollen shear storage modulus of 8 wt/v% PEG gelled at 37°C (C), 10 wt/v% PEG gelled at 37°C (D), 8 wt/v% PEG gelled at 25°C (E), and 10 wt/v% PEG gelled at 25°C (F). The effect of gelation temperature on the swollen shear storage modulus of PEG-ELP hydrogels with 8 wt/v % PEG (G) and 10 wt/v% PEG (H). Showing standard error. Statistics show significance in mean values of using student T-test ($p < 0.05$).89

Figure 3-7: Optical density of 6/x wt/v% PEG-ELP hydrogels incubated at 37°C (A, B), 25°C (C, D) and 4°C (E,F). (B, D, F) hydrogel optical density after cycling through a round of incubations at 37, 25 and 4°C.92

Figure 4-1: Formation of urokinase plasminogen activator (uPA) degradable and non-degradable elastin-like protein (ELP) hydrogels using strain-promoted azide alkyne cycloaddition (SPAAC) chemistry. (A) Three ELP sequences with different bioactivities were used: ELP-RGD promotes integrin binding, ELP-RDG is a non-bioactive scramble, and ELP-u1 is uPA cleavable. Lysine residues on ELP were converted into azide groups. (B) ELPs were

cross-linked with 4 arm-PEG-BCN using SPAAC chemistry. (C) uPA degradable hydrogels consisted of a 50/50 % mix of ELP-RGD and ELP-u1, while non-degradable hydrogels consisted of a 50/50 % mix of ELP-RGD and ELP-RDG. Both hydrogels contain identical concentrations of integrin-binding RGD motifs.118

Figure 4-2: ELP LCST shift from azide reaction. (A) The LCST of all ELP sequences decreased when modified with azide groups. (B) The ELP LCST shift was dependent on the number of primary amines converted into azides119

Figure 4-3: Biomechanics of uPA degradable (Deg) and non-degradable (Non-Deg) ELP hydrogels. (A) Representative time sweeps indicate gelation occurs within 6 min and is complete after 20 min. (B) Representative strain sweeps show the linear viscoelastic range exists up to 300 % strain. (C) Representative frequency sweeps demonstrate hydrogel elastic and loss modulus are frequency dependent. (D) The average storage modulus was similar for both hydrogels while the average loss modulus differed. The storage modulus of both hydrogels was consistent with native neural tissue white matter tracts, where oligodendrocyte precursor cells (OPCs) and oligodendrocytes (OLs) reside. (E) uPA degradable and non-degradable hydrogels relax 43 and 60 % of initial stress over 3.5 min, respectively. Error bars represent standard error (SE) ($n \geq 4$). Asterisks indicate statistical significance using student T-test ($p < 0.05$) and n.s. indicates no statistical significance ($p > 0.05$).121

Figure 4-4: Zymograms of poly(acrylamide) gels dosed with immobilized (A, D) ELP-u1, (B) – RGD, (C) –RDG. (A, B, C) MADM OPCs express low molecular weight uPA to cleave ELP-u1, and do not express any enzymes capable of cleaving ELP-RGD and ELP-RDG sequences. Wells loaded with recombinant uPA (positive control), homogenized MADM

OPCs grown in monolayer, homogenized MADM OPCs encapsulated in degradable gel, homogenized MADM OPCs encapsulated in non-degradable gel, and base OPC culture media (negative control). (D) Wells of a gel dosed with immobilized ELP-u1 protein were loaded with OPC media (negative control), recombinant uPa (positive control), and conditioned media from OPCs in monolayers, conditioned media from OPCs encapsulated in uPa-degradable hydrogels, and conditioned media from OPCs encapsulated in non-degradable hydrogels. MADM OPCs do not release soluble uPA into the surrounding media environment; it remains cell membrane bound and only found in zymogram wells loaded with homogenized cells.....124

Figure 4-5: MADM OPC GFP+ signal (represented in green for day 1, blue for day 2, and gray for day 3) of representative ELP hydrogels with and without uPA cleavage sites over 3 days. Hydrogels with uPA cleavage sites have regions with visible degradation that increase in area over 3 days. Degradation is not observed in non-degradable hydrogels. Lines in merged degradable hydrogel image display area of degraded region over time; green, blue and white represent day 1, 2, and 3, respectively. Scale bars are 1,000 μm125

Figure 4-6: Encapsulated MADM OPC viability and metabolic activity. (A) Representative 3D-projection (252 μm z-stack) of MADM OPCs encapsulated and cultured in uPA degradable hydrogel for 3 days (green is GFP, red is dead cells). Scale bars are 100 μm . (B) The viability of MADM OPCs encapsulated in ELP hydrogels was not affected by the uPA-degradability of the hydrogel matrix. Error bars represent SE (n = 3). Encapsulated MADM OPC (C) ATP concentration, (D) DNA concentration, and (E) ATP/DNA ratio was similar in both uPA degradable and non-degradable ELP hydrogels over 5 days. Error bars

represent SE ($n \geq 12$). Asterisks indicate statistical significance using student T-test ($p < 0.05$) and n.s. indicates no statistical significance ($p > 0.05$).127

Figure 4-7: Encapsulated MADM OPC proliferation at day 3 of culture. (A) Representative z-projections of 20 μm stacks (blue is DAPI, red is EdU, green is GFP). Scale bars are 100 μm . (B) A similar fraction of encapsulated MADM OPCs were proliferative in uPA degradable and non-degradable hydrogels after 3 days. Error bars represent SE ($n = 3$). n.s. indicates no statistical significance using student T-test ($p > 0.05$).127

Figure 4-8: Encapsulated MADM OPC morphology. (A) Confocal depth projections display MADM OPC F-actin expression within uPA degradable and non-degradable hydrogels cultured for 4 days. The color indicates the depth from the hydrogel surface (with orange to yellow being deepest into the hydrogel). Encapsulated MADM OPCs appear to only develop significant processes near the surface of ELP hydrogels. (B) Max projection of the stacks shown in Figure 4-8A with blue staining for DAPI, green representing GFP, and red staining for phalloidin. Scale bars are 100 μm131

Figure 4-9: Encapsulated MADM OPC gene expression over 5 days. (A) As OPCs differentiate into oligodendrocytes and oligodendrocytes mature, NG2 and PDGFR α gene expression is reduced, while GalC and MBP gene expression increases. (B) Within our 3D hydrogel system, MADM OPC gene expression of NG2 and PDGFR α decreased over time in uPA degradable hydrogels relative to non-degradable hydrogels, indicating that uPA degradation promotes maturation of immature OPCs. (C) MADM OPC gene expression of GalC and MBP do not increase over time when encapsulated in uPA degradable hydrogels relative to non-degradable hydrogels. This indicated that uPA degradation does not induce the fate transition from OPC to OL. (D) uPA gene expression is initially upregulated for

MADM OPCs encapsulated in uPA degradable hydrogels before dropping to levels below that of MADM OPCs encapsulated in non-degradable hydrogels. Error bars represent SE (n = 3). Asterisks indicate statistical significance using student T-test ($p < 0.05$).132

Figure 4-10: Effect of encapsulation process on MADM OPC gene expression. MADM OPC gene expression of (A) NG2, (B) PDGFR α , (C) GalC, (D) MBP, and (E) uPA was affected by the encapsulation process. Displaying SE (n = 3). Asterisks indicate statistical significance using student T-test ($p < 0.05$).134

Figure 5-1: MADM OPCs encapsulated in PEG-ELP double-network hydrogels did not survive the gelation process. (A) Max z-projections of 225 μ m slice of MADM OPCs encapsulated in 6/1.5 wt/v % PEG-ELP (2:1 THPC hydroxyl group to amine ratio) hydrogels for 4 days. Scale bars = 100 μ m. Green represents MADM OPC GFP+ signal, red represents dead stain, and blue represents ELP tagged with AlexaFluor 405 dye. (B) OPC viability, (C) ATP concentration and (D) DNA concentration in 10/1.5 PEG-ELP hydrogels with and without THPC over 7 days as determined via alamarBlue, ATP and DNA assays, respectively. Gelation performed at temperatures above the ELP LCST. Error bars show standard deviation.147

Figure 5-2: (A) SPAAC cross-linking between azides and strained alkyne bonds. (B) HNMR of BCN functionalized PEG (PEG-BCN). BCN functionalization determined by comparing BCN hydrogen peaks (highlighted with red box) to the PEG backbone hydrogen peak (highlighted with blue box).....149

Figure 5-3: Creation of PEG- and ELP-azide (PEA) single-network hydrogels. ELP-azide (tagged with Alexa Fluor 405) distribution in 3/3 PEA (0.5:1) hydrogels cross-linked (A) on ice and (B) at RT. ELP distribution is homogeneous in hydrogels made at temperatures below

the ELP LCST (A) and ELP is clustered in hydrogels made at temperatures above the ELP LCST (B). Both (C) homogeneous and (D) clustered ELP distribution is preserved after swelling PEA hydrogels in PBS for 24 hours. (E) MADM OPCs encapsulated for 9 days in 3/3 PEA (0.5:1) hydrogels cross-linked on ice (ELP not shown) grew into large clusters. (F) ELP micro-architecture was preserved when MADM OPCs were encapsulated for 2 days in 3/3 PEA (0.5:1) hydrogels cross-linked at RT. Scale bars = 100 μm150

Figure 5-4: Problems with PEA hydrogel domain formation and retention. (A) 6/1.5 PEA (1:1) hydrogels cross-linked at temperatures above the ELP LCST did not form ELP aggregates with consistent size and shape. ELP is tagged with Alexa Fluor 405 (represented in blue) and 11/14 primary amines were functionalized into azides. (B) 6/1.5 PEA (1:1) hydrogels cross-linked at temperatures above the ELP LCST did form ELP aggregates with consistent size and shape when only 4/14 ELP amines were converted into azides. (C) 6/1.5 PEA (1:1) hydrogels with uniform ELP aggregates did not maintain ELP aggregate structure after swelling in PBS for 24 hours. Scale bars = 100 μm . (D) Encapsulation of MADM OPCs in 6/1.5 PEA (1:1) hydrogels interferes with ELP micro-architecture. Scale bar = 1,000 μm152

Figure 6-1: ELP/XG bioinks. (A) Schematic of the 3D bioprinting process. XG helps maintain printed filament structural integrity while ELP and THPC cross-linking reaction proceeds. (B) Thixotropic testing of ELP/XG bioink. Bioink does not flow when 0.1 % strain is applied ($G' > G''$), becomes fluid at 100 % strain ($G'' > G'$), and quickly regains non-flow behavior when returning to 1 % strain ($G' > G''$). Test performed with 25 mm cone plate at 1 Hz. (C) Time sweeps of ELP/XG bioink with THPC cross-linker, XG with THPC cross-linker and XG. Test performed with 25 mm cone plate at 1 % strain and 1 Hz. (D)

Viability of smooth muscle cells (SMC) 24 hours after 3D printing with ELP/XG bioink.
Scale bars = 100 μm161

Figure 6-2: UV light sensitive ELP hydrogels (A) Free radical reaction with trithiolcarbonate molecule produces two molecular fragments [Adapted from ref. 11]. (B) Trithiolcarbonates absorb UV light to produce free radicals [Adapted from ref. 19]. (C) Norbornene functionalization of ELP was determined by comparing norbornene double bond hydrogen peaks (6.3 ppm, highlighted with red bar) to the tyrosine hydrogen peak (6.6 ppm, highlighted with blue bar). (D) Cross-linking of 5 wt/v % ELP solution with 1:1 ratio of norbornene to thiol functional groups and 0.5 wt/v % LAP. Measurements taken with 25 mm cone plate at 4°C, 1 % strain, 1 Hz and 6 mW/cm² light power.....164

Figure 6-3: BsTC chemistry. (A) TTCA chemical structure. (B) BsTC chemical structure. (C) PEG-acrylate (1,000 kDa, 10 wt/v %) and BsTC (0.05 wt/v %) solutions gel after exposure to 320-390 nm UV light. (D) Absorbance spectrum of BsTC, LAP and PBS.165

Figure 6-4: BsTC norbornene reaction mixture HNMR. (A) HNMR prediction of norbornene functionalized BsTC has one multiplet peak near 6 ppm. (B) Only one dimerized aminolysis fragment was predicted to have multiple multiplets near 6 ppm. (C) The BsTC norbornene reaction mixture contains two multiplets near 6 ppm that indicate the aminolysis fragment from B is present.166

Figure 7-1: MADM OPCs cultured in media supplemented with FBS. Cells were seeded on polyornithine coated 24-well plates at a density of 1e4 cells/cm². All cells were cultured in base media on day 1. Media was changed on day 2, 4, 6, 7, 8, 9, and 10 for all conditions. MADM OPCs are green fluorescent protein positive (GFP+) and the signal was used to

image morphology over time. FBS inhibits MADM OPC proliferation and process extensions. Scale bars = 100 μm	173
Figure 7-2: MADM OPCs in base media on days 6-11. (A, B, C) In acidic media MADM OPCs cluster together. (D, E, F) When base media is replenished MADM OPCs spread across the surface and cell clusters dissipate. Scale bars = 100 μm	174
Figure 7-3: MADM OPCs in base media supplemented with 1 % FBS on days 6-11. MADM OPC proliferation is slowed down, but cells act in a similar manner to MADM OPCs in base media. Scale bars = 100 μm	175
Figure 7-4: MADM OPCs in base media supplemented with 20 % FBS on days 6-11. (A) Timeline of media changes during days 6-11. Media was changed to proliferation media after imaging cells on days 7 and returned to 20 % FBS media after imaging on day 9. (B, C) MADM OPCs remain senescent in 20 % FBS media. (D, E) MADM OPCs proliferate normally in base media. (F, G) The re-addition of FBS causes MADM OPCs to retract process extensions and return to a senescent state. The effects of FBS on MADM OPCs are reversible. Scale bars = 100 μm	176
Figure A-1: Optical density of ELP, TRITC modified ELP, and the mixture used for fluorescent microscopy (1:19 ELP:ELP-TRITC) as a function of temperature.	180
Figure A-2: PEGMA and ELP cross-reactions. (A) No rheological changes to 6 wt % PEGMA solution occur over 10 minutes when mixed with THPC (1 mg/ml). (B) No rheological changes to 3wt % ELP solution occur when mixed with LAP (0.05 wt/v %) and exposed to UV light for 10 minutes.	181
Figure B-1: FTIR of ELP pre- and post-azide functionalization. The appearance of a peak at 2100 cm^{-1} for (A) uPA degradable sequence ELP-u1, (B) integrin binding sequence ELP-RGD,	

and (C) non-bioactive sequence ELP-RDG indicated the presence of azide bonds within the protein structure. (D) The azide peak intensity increased with higher azide functionalization as indicated by FTIR of ELP-RGD sequence pre-modification and protein batches modified with an average of 3.78 and 12 azides. The average azide group addition was controlled by stoichiometrically limiting the number of azides present during the diazotransfer reaction.....182

Figure B-2: High resolution electrospray ionization-mass spectrometry (ESI-MS) of ELP pre- and post-azide functionalization. (A) Each lysine residue modification with azides increases protein mass by 26 Da. Pre-azide modification ELP sequence appears as one peak, indicating monodisperse protein molecular weight. Post-azide modification ELP appears as multiple peaks with 26 Da differences, indicating that the diazo transfer reaction created ELPs with a distribution of attached azides: (B) uPA degradable sequence ELP-u1 pre- and post-azide functionalization, (C) cell-adhesive sequence ELP-RGD pre- and post-azide functionalization, and (D) non-bioactive sequence ELP-RDG pre- and post-azide functionalization. The relative peak intensities were quantified to determine the molecular average of azides added to ELP-u1, -RGD and -RDG, which were 6.28, 3.78, and 3.74, respectively.183

Figure B-3: THPC used to immobilize ELP to poly(acrylamide) gel for zymography. (A) Poly(acrylamide) crosslinking chemistry creates a gel with primary amines in the structure. (B) THPC has four primary amine reactive sites that allow for ELP to be immobilized onto poly(acrylamide) gel network. (C) Poly(acrylamide) gel dosed with ELP without THPC causes ELP to migrate down the wells during electrophoresis. (D) Poly(acrylamide gel

dosed with immobilized ELP maintains uniform protein distribution after electrophoresis.
.....185

Figure B-4: OPC differentiation relevant pathways are impacted by the absence of Nf1 and p53.

Disruption of ERK 1 & 2 pathway results in delayed OPC differentiation in vivo. Solid arrows indicate pathway promotion, solid bars indicate pathway inhibition, dashed lines indicate pathways not occurring in MADM OPCs. Red bars indicate drugs used to assess changes to OPC differentiation in vivo from the disruption of the ErK 1 & 2 and mTORC1 pathways.186

Index of Tables

Table 4-1: The amino acid sequences of ELP-u1, -RGD, and -RDG. Each ELP amino acid sequence contains a T7 tag, His Tag, enterokinase cleavage sequence, elastin-like sequence and a bioactive sequence (in bold).....	109
Table 4-2: List of primers used for quantitative reverse transcription polymerase chain reaction (RT-qPCR).....	116

1. Introduction and Background

1.1. Need for CNS injury and disease treatments

Central nervous system (CNS) tissue damage does not substantially recover from injury and disease through endogenous healing mechanisms. Current treatments to CNS injury and disease focus on mitigating further tissue damage rather than promoting neurogenesis and functional recovery. For example, the autoimmune disease Multiple Sclerosis (MS) is clinically treated with immune system suppressants, such as Rebif (Merck) and Avonex (Biogen), to inhibit disease progression, and complimented with steroid supplements (e.g. Prednisone) to manage symptoms during attacks. The mechanisms of nerve cell death vary based on the specific disease or injury, but the requirements for effective treatments of CNS tissue are similar: The extracellular matrix (ECM) needs to be remodeled to remove inhibitory scar tissue, damaged cells should be replaced, and functionality restored. The complexity of the biological signaling cascades used by neural cells to interact with each other and their ECM make the development of treatments a difficult feat. Biomaterial scaffolds have garnered interest both as therapeutics for CNS injuries and diseases, and as ECM mimetics in the development of *in vitro* models to investigate CNS cellular signaling.

1.2. The roles of biomaterial scaffolds in treatment development

Applications of biomaterial scaffolds include *in vivo* implantation into CNS injury to improve endogenous cellular infiltration and functional recovery, and the creation of *in vitro* CNS ECM mimetic model systems. It's important to note that the CNS does have some reparative mechanisms, and there is evidence of endogenous cells attempting to repair tissue damage¹⁻⁴. For example, the number of nestin-positive cells in mice with an ipsilateral cerebral cortex infarction induced by the middle cerebral artery occlusion (MCAO) stroke model increased post-injury³.

When extracted, the nestin-positive cells displayed neural stem cell (NSC) proliferative and differentiation properties³. Cross-linking most biomaterials creates hydrogels that retain large amounts of water (> 30 v/v %) within the cross-linked polymer network and are amenable for mammalian cell culture^{5,6}. Hydrogels are administered to damaged CNS tissue, either through invasive surgeries or by injection of biomaterials with self-healing properties, for the purpose of bolstering endogenous repair mechanisms⁷⁻¹³. For example, a collagen and Puramatrix-based hydrogel mixture improved animal hind limb mobility as measured through Basso, Beattie, and Bresnahan (BBB) scores 4 months post-surgery over phosphate buffered saline (PBS) controls when administered to a 5 mm gap thoracic (T9-T11) rat spinal cord (SC) injury⁷. In addition, the collagen and Puramatrix hydrogel improved neuronal and astrocyte cell infiltration into the injury lesion⁷. Biomaterial scaffolds are also used to transplant NSCs into damaged CNS injury because they improve transplanted cell viability. Combinatorial treatments of NSCs with biomaterial scaffolds display improved functional recovery over the two stand-alone treatments^{14,15}. However, while these treatments promote CNS tissue recovery in animal models, regeneration is limited and functionality cannot be restored to the pre-injury state. The complex biological signaling used to choreograph cell and ECM interactions need to be further elucidated to improve on current treatment strategies.

The role and influence the CNS ECM has on cellular behavior is not fully understood. Biomaterial scaffolds have helped elucidate cell-matrix interactions because they can mimic specific aspects of the ECM in *in vitro* systems, which contain limited bioactivity. *In vitro* hydrogel models were successfully used to research the impact of both physical hydrogel properties (matrix stiffness, mesh size, degradation, stress relaxation) and bioactivity (integrin binding, chemo-suppressants) on cell behavior¹⁶⁻¹⁹. For example, neural progenitor cell (NPC) metabolic activity

was reduced in stiffer poly(ethylene glycol) (PEG) hydrogels after 7 days of encapsulation¹⁶. Since the hydrogel mesh size was reduced in stiffer PEG hydrogels, it is likely that cells were more constricted inside the stiffer hydrogels. This result was not replicated by NPCs seeded on top of PEG hydrogels, where metabolic activity remained unchanged across all hydrogel stiffness¹⁶. This study highlights two important factors in understanding cell-matrix interactions: cells cultured on 2-dimensional (2D) *in vitro* systems do not adequately capture cellular behavior in native tissue, which is 3-dimensional (3D), and small changes to the physical properties of biomaterial scaffolds have a profound impact on cellular behavior through mechanotransduction signaling. Bioactivity is often incorporated into hydrogel systems by immobilizing proteins and/or small peptide chains to the crosslinked hydrogel network. The protein semaphorin 6A, tethered to an agarose-based hydrogel, inhibited the process extensions of dorsal root ganglion (DRG) explants¹⁹. In addition, by selectively tethering semaphorin 6A to specific locations in an agarose hydrogel via photolithography techniques the direction in which DRG extended processes could be controlled¹⁹. *In vitro* hydrogel systems do not recapitulate all properties of the native CNS ECM but they help to elucidate specific cell-matrix interactions and inform *in vivo* treatment strategies.

1.3. Poly(ethylene glycol) hydrogels

Hydrogels can be made from both native and synthetic materials. Native materials display inherent bioactivity but do not have a clearly defined chemical composition. Synthetic materials are well defined but usually require chemical modification to incorporate bioactivity into the hydrogel matrix. PEG is a bioinert synthetic polymer that has been adapted to a wide range of cross-linking chemistries, allowing for the design of many *in vitro* hydrogel systems^{20–26}. PEG-based polymers can be cross-linked to form hydrogels through mixing-based chemical reactions (vinyl sulfone/thiol, copper-catalyzed azide-alkyne cycloaddition (CuAAC), strain-promoted

azide-alkyne cycloaddition (SPAAC)), photoinitiated reactions (acrylate, methacrylate, norbornene/thiol) or a combination of both²⁰⁻²⁶. Encapsulated cells have high viability in PEG hydrogels, and bioactivity is added by either modifying the PEG polymer or through the addition of bioactive materials in the crosslinking scheme^{16,17,20,21}. PEG-based hydrogels are made degradable either by adding lactide groups to the polymer before crosslinking to induce ester hydrolysis in aqueous solution, or by using matrix metalloproteinase (MMP) cleavable peptide sequences as crosslinkers to induce enzymatic degradation^{17,27}. Cells adhere to the PEG hydrogel matrix when integrin binding peptide sequences, such as arginine-glycine-aspartate (RGD) and isoleucine-lysine-valine-alanine-valine (IKVAV), are added during crosslinking^{21,22,27}.

The plethora and versatility of PEG crosslinking schemes allows for the design of sophisticated *in vitro* hydrogel models. For instance, PEG hydrogels were designed with control over how proteins in the supernatant diffuse into the hydrogel matrix²⁸. The scheme involved first forming a hydrogel by photo-crosslinking large molecular weight (Mw) PEG-diacrylate, and was followed by soaking the hydrogel in a solution containing small Mw PEG-diacrylate^{28,29}. Photolithography was then used to control the spatial location of a second photo-crosslinking reaction within the original hydrogel, which created regions with a densely packed PEG-network that inhibited bovine serum albumen (BSA) diffusion^{28,29}. In another crosslinking scheme, PEG hydrogel degradation was designed to follow programmable Boolean logic³⁰. Cross-linkers were designed to degrade through three different mechanisms (pH adjustment, ultraviolet (UV) light exposure, and MMP enzymatic activity) and PEG hydrogels with all combinations of YES/OR/AND degradation logic outputs were created³⁰. PEG is a desirable polymer to design *in vitro* biomaterial scaffold systems because it is bioinert and compatible with many cross-linking chemistries.

1.4. Elastin-like proteins

Recombinant engineered proteins bridge the divide between natural and synthetic materials because they are derived from native proteins and have a well-defined protein primary structure. Elastin-like proteins (ELPs) are developed using recombinant engineering technology and are derived from tropoelasin, which provides extensibility in connective tissue^{31,32}. ELPs are made from repeating units of the valine-proline-glycine-guest residue-glycine (VPGxG) penta-peptide sequence, where the guest residue can be any amino acid except for proline^{31,32}. The unique lower critical solution temperature (LCST) transition that ELPs undergo allows for purification of large quantities of protein^{31,33}. Below the LCST transition ELPs are soluble in aqueous solution and above the LCST they aggregate into a protein rich coacervate phase^{34,35}. ELPs can be used as drug delivery vehicles because the LCST transition of specific ELP sequences can induce self-assembly into micro- and nanoparticles^{36,37}.

Bioactive amino acid sequences that allow for cells to adhere to the ELP structure and/or enzymatically degrade it can be incorporated into the protein backbone³³. Crosslinking multiple ELPs with minor differences in the peptide sequence (created from differences in the bioactive sequence) allows for tuning of bioactivity within the hydrogel independently of physical properties because the overall protein concentration can be kept constant³³. This is important for developing *in vitro* models of the CNS ECM because both physical properties (through mechanotransduction signaling pathways) and bioactive cues affect cell-matrix interactions³⁸⁻⁴⁰. In most hydrogel systems adjusting the bioactivity of the crosslinked matrix alters the physical properties, making it difficult to isolate the impact of specific individual changes to the hydrogel matrix on cell cultures. The incorporation of bioactivity to ELP-based hydrogels is not limited to small peptide sequences in protein primary structure. Growth factors tethered to ELPs maintain some bioactivity

and can be purified using the LCST property^{36,41}. The advantages of having a known primary protein structure, containing bioactive cues in the amino acid backbone, easy purification of large protein quantities, and tuning physical properties independently from biochemical cues makes ELPs an ideal biomaterial for designing *in vitro* tissue engineering models.

1.5. Micro-architecture in hydrogel systems

Hydrogel micro-architecture impacts cellular behavior and examples of this phenomena appear both *in vivo* and *in vitro*. For example, chitosan-based hydrogels implanted into rat T8 – 9 spinal cord hemisection ablation injury induced cellular infiltration into the injured lesion 4 weeks post-surgery⁴². Furthermore, a procedure coined fragmented physical hydrogel suspension (FPHS) was used to create bulk hydrogels composed of either 150 μm or 20 μm size fragments⁴². Both neuronal and glial cellular infiltration into the spinal cord injury lesion was improved in chitosan hydrogels made from 20 μm fragments over hydrogels made from 150 μm fragments⁴². While the chitosan-based hydrogels were not designed to induce a specific cellular response, the results illustrate that hydrogels consisting of the same material(s) can be designed with micro-architecture to further impact cellular behavior.

In vitro hydrogel systems with micro-architecture have helped to elucidate the impact of specific designs on cell behavior. For example, the proliferative behavior of human umbilical vein endothelial cells (HUVECs) seeded on top of an electrospun ELP fiber mesh was dependent on the local, microscale level, RGD concentration^{43,44}. ELP fibers with microscale control over RGD concentration were created by mixing two ELPs with minor differences in peptide sequence: one containing the adhesive RGD sequence and the other containing the non-adhesive RDG scramble⁴³. A dual needle system was used to electrospin two solutions simultaneously to create the fiber mesh: one containing a mixture of ELP sequences with RGD and RDG, and the other

containing only ELP with RDG⁴³. Local, single fiber (1.8 μm width), RGD concentration was controlled by adjusting the ELP-RGD and -RDG mixture ratio while global, entire fiber mesh, RGD concentration was controlled by adjusting the relative flow rates of each solution during electrospinning^{43,44}. The fraction of HUVECs expressing Ki-67, a marker for proliferation, was dependent on both global and local RGD concentrations⁴³. This work demonstrated that hydrogel systems are capable of influencing cell behavior by spatially orienting integrin-mediated focal adhesion within the hydrogel network. Currently, few hydrogel systems can be designed with similar micro-architecture. The efficacy of biomaterials as CNS disease and injury therapeutics would be improved by developing techniques to imbed micro-architecture within hydrogel systems.

1.6. OPC urokinase plasminogen activator (uPA) activity

Oligodendrocyte precursor cells (OPCs) have the potential to repair demyelination injuries and diseases because they have the capability to both self-renew and differentiate into oligodendrocytes (OLs), the myelin producing cells of the CNS. Effective treatments for demyelinating injuries and diseases, such as MS, require hydrogel systems designed to both improve encapsulated OPC viability and influence OPC behavior. During MS demyelination the CNS ECM is remodeled to include OPC differentiation inhibitors fibronectin and chondroitin sulfate proteoglycans (CSPG)⁴⁵. The demyelinated ECM environment makes it impossible for encapsulated OPCs to replace damaged OLs and restore myelin without the hydrogel system promoting OPC maturation. *In vitro* hydrogel systems help elucidate cell interactions with ECM bioactivity. For example, the incorporation of integrin binding sites, such as the RGD peptide sequence, into hydrogel networks influences encapsulated cell migration, proliferation and viability⁴⁶. Urokinase plasminogen activator (uPA) is a serine protease that acts as an activator of

the plasminogen system. uPA enzymatic activity correlates with OPC maturation *in vivo*, and utilization of uPA enzymatic degradation sites within a hydrogel network may be an effective tool to promote OPC maturation.

uPA expression impacts cell process extensions and correlates with myelin production *in vivo*, both of which are identifiers of OPC differentiation. uPA expression is upregulated during myelin development in white matter regions of the rat brain. uPA was transiently expressed in rat cerebellum myelinated fiber tracts, appearing in 80-90 % of cells in postnatal day 14 (P14) rats, ~10 % of cells in P21-P28 rats, and completely disappearing in P56 rats⁴⁷. Similar results were found in the hippocampus fimbria and corpus callosum, where uPA was expressed by most cells in P14 rats, and that expression disappeared in P56 rats⁴⁷. This timeline correlates with the rapid increase in myelin production that occurs in the juvenile rat brain between P10 and P14⁴⁸. OPC differentiation into mature OLs is marked by an increase in the number of process extensions and branching⁴⁹. Although no study has tested the effects of uPA expression on OPC morphology, uPA impacts the processes of other cell types. For example, inhibition of Dorsal root ganglion (DRG) uPA expression reduced the average axon length⁵⁰. uPA is expressed by specific rat neurons, and the expression is not transient⁴⁷. Taken together these studies indicate that uPA may have a role in OPC maturation by promoting process outgrowth and branching.

uPA functions as an activator of the plasminogen system in addition to its protease activity. The plasminogen system is a cascade that initiates the activation of matrix metalloproteinases (MMPs). MMPs are linked to many biological functions^{51,52}, including OPC differentiation and OL myelin formation⁵³. In particular matrix metalloproteinase-9 (MMP-9) is linked to myelin production. MMP-9 is upregulated during developmental myelination in nerve tissue of both the corpus callosum and optic nerve regions^{54,55}. In addition, MMP-9 was upregulated at the onset of

remyelination after experimental autoimmune encephalomyelitis- (EAE) and lysolecithin-induced demyelination injuries^{54,56}. MMP-9 null mice had reduced remyelination one-week post lysolecithin-induced spinal cord injury (SCI) when compared to wild-type mice⁵⁴. MMPs are chemokines, but the difference in remyelination was found to occur from a decrease in the number of mature OLs in the SCI lesion of MMP-9 null mice, and not from differences in macrophage infiltration⁵⁴. uPA activates MMPs (including MMP-9), but it is unknown if it affects MMP expression. However, OPC differentiation and OL myelin production are linked to an increase in MMP-9 activation and not necessarily increased expression^{57,58}. OPCs seeded onto a fibronectin scaffold, an inhibitor of OPC differentiation, had reduced MMP-9 activity and similar MMP-9 expression to OPCs seeded onto laminin scaffolds, a promoter of OPC differentiation, after 7 days⁵⁷. In addition, MMP-9 is linked with protein kinase C (PKC), which promotes OL process outgrowth⁵⁸. Pharmacological activation and inhibition of PKC resulted in increased and decreased OL MMP-9 activity, respectively⁵⁸. It's important to note that administration of MMP-9 to demyelinated regions of the CNS is not therapeutic because abnormal increases in MMP-9 expression disrupt the blood-brain barrier and cause neuroinflammation^{51,52,56}. These results indicate that MMP-9 activation with limited increase in expression could be beneficial for OPC maturation. uPA may promote OPC maturation and OL process outgrowth indirectly through activation of the plasminogen system and MMP-9.

1.7. Synopsis of research

The objectives of this work were to design ELP- and PEG-based hydrogel systems that mimic specific aspects of native CNS tissue in order to help elucidate OPC interactions with their ECM. Native CNS tissue is heterogeneous making it difficult to recapitulate the ECM in its entirety. Hydrogel systems with micro-architecture capture the complexity of CNS tissue in part. Current

literature on the techniques used to design biomaterial scaffolds with micro-architecture was reviewed⁵⁹.

ELPs exhibit two unique properties: the LCST transition that allows for easy purification post expression, and the ability to cross-link similar ELP sequences together to form hydrogels with independent tuning of bioactivity from biomechanical properties. The ELP LCST transition was used to create PEG- and ELP-based (PEG-ELP) hydrogels with either homogeneous or heterogeneous ELP distribution by controlling gelation temperature⁶⁰. Because ELP contains bioactive small peptide chains in the sequence the PEG-ELP hydrogel system allowed for the localization of bioactivity with microscale resolution without changing the hydrogel contents. OPC maturation is impacted by both hydrogel biomechanical properties, such as stiffness, and bioactive cues, such as growth factors, and it is important to isolate the impact of each hydrogel property on OPCs *in vitro*. Two ELP hydrogels with similar biomechanical properties were created: one that was uPA degradable and another that was non-degradable [Meco et al., in review]. uPA enzymatic degradation promoted encapsulated OPC maturation when compared to OPCs in non-degradable hydrogels [Meco et al., in review]. OPC interactions with their ECM can be elucidated with the ELP- and PEG-based hydrogels developed in this work.

1.8. References

- (1) Cooke, M. J.; Vulic, K.; Shoichet, M. S. Design of Biomaterials to Enhance Stem Cell Survival When Transplanted into the Damaged Central Nervous System. *Soft Matter* 2010, 6, 4988. <https://doi.org/10.1039/c0sm00448k>.
- (2) ANDREAS ARVIDSSON, TOVE COLLIN, DENIZ KIRIK, Z. K. & O. L. Neuronal Replacement from Endogenous Precursors in the Adult Brain after Stroke. *Nat Med* 2002, 8 (9), 963–970. <https://doi.org/10.1038/nm>.
- (3) Nakagomi, T.; Taguchi, A.; Fujimori, Y.; Saino, O.; Nakano-Doi, A.; Kubo, S.; Gotoh, A.; Soma, T.; Yoshikawa, H.; Nishizaki, T.; Nakagomi, N.; Stern, D. M.; Matsuyama, T. Isolation and Characterization of Neural Stem/Progenitor Cells from Post-Stroke Cerebral Cortex in Mice. *Eur. J. Neurosci.* 2009, 29 (9), 1842–1852. <https://doi.org/10.1111/j.1460-9568.2009.06732.x>.
- (4) Barnabé-Heider, F.; Göritz, C.; Sabelström, H.; Takebayashi, H.; Pfrieger, F. W.; Meletis, K.; Frisén, J. Origin of New Glial Cells in Intact and Injured Adult Spinal Cord. *Cell Stem Cell* 2010, 7 (4), 470–482. <https://doi.org/10.1016/j.stem.2010.07.014>.
- (5) Li, Z.; Guan, J. Hydrogels for Cardiac Tissue Engineering. *Polymers (Basel)*. 2011, 3 (2), 740–761. <https://doi.org/10.3390/polym3020740>.
- (6) Nih, L. R.; Carmichael, S. T.; Segura, T. Hydrogels for Brain Repair after Stroke: An Emerging Treatment Option. *Curr. Opin. Biotechnol.* 2016, 40, 155–163. <https://doi.org/10.1016/j.copbio.2016.04.021>.
- (7) Kaneko, A.; Matsushita, A.; Sankai, Y. A 3D Nanofibrous Hydrogel and Collagen Sponge Scaffold Promotes Locomotor Functional Recovery, Spinal Repair, and Neuronal

- Regeneration after Complete Transection of the Spinal Cord in Adult Rats. *Biomed. Mater.* 2015, 10 (1), 015008. <https://doi.org/10.1088/1748-6041/10/1/015008>.
- (8) Truby, R. L.; Lewis, J. A. Printing Soft Matter in Three Dimensions. *Nature* 2016, 540 (7633), 371–378. <https://doi.org/10.1038/nature21003>.
- (9) Qin, G.; Glassman, M. J.; Lam, C. N.; Chang, D.; Schaible, E.; Hexemer, A.; Olsen, B. D. Topological Effects on Globular Protein-ELP Fusion Block Copolymer Self-Assembly. *Adv. Funct. Mater.* 2015, 25 (5), 729–738. <https://doi.org/10.1002/adfm.201403453>.
- (10) Huang, C. C.; Ravindran, S.; Yin, Z.; George, A. 3-D Self-Assembling Leucine Zipper Hydrogel with Tunable Properties for Tissue Engineering. *Biomaterials* 2014, 35 (20), 5316–5326. <https://doi.org/10.1016/j.biomaterials.2014.03.035>.
- (11) Lu, H. D.; Charati, M. B.; Kim, I. L.; Burdick, J. A. Injectable Shear-Thinning Hydrogels Engineered with a Self-Assembling Dock-and-Lock Mechanism. *Biomaterials* 2012, 33 (7), 2145–2153. <https://doi.org/10.1016/j.biomaterials.2011.11.076>.
- (12) King, V. R.; Henseler, M.; Brown, R. A.; Priestley, J. V. Mats Made from Fibronectin Support Oriented Growth of Axons in the Damaged Spinal Cord of the Adult Rat. *Exp. Neurol.* 2003, 182 (2), 383–398. [https://doi.org/10.1016/S0014-4886\(03\)00033-5](https://doi.org/10.1016/S0014-4886(03)00033-5).
- (13) King, V. R.; Phillips, J. B.; Hunt-Grubbe, H.; Brown, R.; Priestley, J. V. Characterization of Non-Neuronal Elements within Fibronectin Mats Implanted into the Damaged Adult Rat Spinal Cord. *Biomaterials* 2006, 27 (3), 485–496. <https://doi.org/10.1016/j.biomaterials.2005.06.033>.
- (14) Pritchard, C. D.; Slotkin, J. R.; Yu, D.; Dai, H.; Lawrence, M. S.; Bronson, R. T.; Reynolds, F. M.; Teng, Y. D.; Woodard, E. J.; Langer, R. S. Establishing a Model Spinal Cord Injury in the African Green Monkey for the Preclinical Evaluation of Biodegradable Polymer Scaffolds

- Seeded with Human Neural Stem Cells. *J. Neurosci. Methods* 2010, 188 (2), 258–269.
<https://doi.org/10.1016/j.jneumeth.2010.02.019>.
- (15) Lu, P.; Wang, Y.; Graham, L.; McHale, K.; Gao, M.; Wu, D.; Brock, J.; Blesch, A.; Rosenzweig, E. S.; Havton, L. A.; Zheng, B.; Conner, J. M.; Marsala, M.; Tuszynski, M. H. Long-Distance Growth and Connectivity of Neural Stem Cells after Severe Spinal Cord Injury. *Cell* 2012, 150 (6), 1264–1273. <https://doi.org/10.1016/j.cell.2012.08.020>.
- (16) Lampe, K. J.; Mooney, R. G.; Bjugstad, K. B.; Mahoney, M. J. Effect of Macromer Weight Percent on Neural Cell Growth in 2D and 3D Nondegradable PEG Hydrogel Culture. *J. Biomed. Mater. Res. - Part A* 2010, 94 (4), 1162–1171. <https://doi.org/10.1002/jbm.a.32787>.
- (17) Lampe, K. J.; Bjugstad, K. B.; Mahoney, M. J. Impact of Degradable Macromer Content in a Poly (Ethylene Glycol) Hydrogel on Neural Cell Metabolic Activity, Redox State, Proliferation, and Differentiation. *Tissue Engineering part A*. 2010, 16 (6), 1857–1866.
- (18) Chaudhuri, O.; Gu, L.; Klumpers, D.; Darnell, M.; Bencherif, S. A.; Weaver, J. C.; Huebsch, N.; Lee, H.-P.; Lippens, E.; Duda, G. N.; Mooney, D. J. Hydrogels with Tunable Stress Relaxation Regulate Stem Cell Fate and Activity. *Nat. Mater.* 2015, advance on (November). <https://doi.org/10.1038/nmat4489>.
- (19) Curley, J. L.; Catig, G. C.; Horn-Ranney, E. L.; Moore, M. J. Sensory Axon Guidance with Semaphorin 6A and Nerve Growth Factor in a Biomimetic Choice Point Model. *Biofabrication* 2014, 6 (3), 35026. <https://doi.org/10.1088/1758-5082/6/3/035026>.
- (20) McGann, C. L.; Levenson, E. A.; Kiick, K. L. Resilin-Based Hybrid Hydrogels for Cardiovascular Tissue Engineering. *Macromol. Chem. Phys.* 2013, 214 (2), 203–213. <https://doi.org/10.1002/macp.201200412>.

- (21) Zhu, J. Bioactive Modification of Poly(Ethylene Glycol) Hydrogels for Tissue Engineering. *Biomaterials* 2010, 31 (17), 4639–4656. <https://doi.org/10.1016/j.biomaterials.2010.02.044>.
- (22) Fairbanks, B. D.; Schwartz, M. P.; Halevi, A. E.; Nuttelman, C. R.; Bowman, C. N.; Anseth, K. S. A Versatile Synthetic Extracellular Matrix Mimic via Thiol-Norbornene Photopolymerization. *Adv. Mater.* 2009, 21 (48), 5005–5010. <https://doi.org/10.1002/adma.200901808>.
- (23) Fairbanks, B. D.; Singh, S. P.; Bowman, C. N.; Anseth, K. S. Photodegradable, Photoadaptable Hydrogels via Radical-Mediated Disulfide Fragmentation Reaction. *Macromolecules* 2011, 44, 2444–2450. <https://doi.org/10.1021/ma200202w>.
- (24) Deforest, C. A.; Tirrell, D. A. A Photoreversible Protein-Patterning Approach for Guiding Stem Cell Fate in Three-Dimensional Gels. *Nat. Mater.* 2015, 14 (5), 523–531. <https://doi.org/10.1038/nmat4219>.
- (25) Anseth, K. S.; Metters, a T.; Bryant, S. J.; Martens, P. J.; Elisseeff, J. H.; Bowman, C. N. In Situ Forming Degradable Networks and Their Applications in Tissue Engineering and Drug Delivery. *J. Cont. Rel.* 2002, 78 (1–3), 199–209.
- (26) McGann, C. L.; Dumm, R. E.; Jurusik, A. K.; Sidhu, I.; Kiick, K. L. Thiol-Ene Photocrosslinking of Cytocompatible Resilin-Like Polypeptide-PEG Hydrogels. *Macromol. Biosci.* 2016, 16, 129–138. <https://doi.org/10.1002/mabi.201500305>.
- (27) Lutolf, M. P.; Lauer-Fields, J. L.; Schmoekel, H. G.; Metters, a T.; Weber, F. E.; Fields, G. B.; Hubbell, J. a. Synthetic Matrix Metalloproteinase-Sensitive Hydrogels for the Conduction of Tissue Regeneration: Engineering Cell-Invasion Characteristics. *Proc. Natl. Acad. Sci. U. S. A.* 2003, 100 (9), 5413–5418. <https://doi.org/10.1073/pnas.0737381100>.

- (28) Hahn, M. S.; Taite, L. J.; Moon, J. J.; Rowland, M. C.; Ruffino, K. A.; West, J. L. Photolithographic Patterning of Polyethylene Glycol Hydrogels. *Biomaterials* 2006, 27 (12), 2519–2524. <https://doi.org/10.1016/j.biomaterials.2005.11.045>.
- (29) Hahn, M. S.; Miller, J. S.; West, J. L. Three-Dimensional Biochemical and Biomechanical Patterning of Hydrogels for Guiding Cell Behavior. *Adv. Mater.* 2006, No. 18, 2679–2684. <https://doi.org/10.1002/adma.200600647>.
- (30) Badeau, B. A.; Comerford, M. P.; Arakawa, C. K.; Shadish, J. A.; Deforest, C. A. Engineered Modular Biomaterial Logic Gates for Environmentally Triggered Therapeutic Delivery. *Nat. Chem.* 2018, 10 (3), 251–258. <https://doi.org/10.1038/nchem.2917>.
- (31) Wright, E. R.; McMillan, R. A.; Cooper, A.; Apkarian, R. P.; Conticello, V. P. Thermoplastic Elastomer Hydrogels via Self-Assembly of an Elastin-Mimetic Triblock Polypeptide. *Adv. Funct. Mater.* 2002, 12 (2), 149–154. [https://doi.org/10.1002/1616-3028\(20020201\)12:2<149::AID-ADFM149>3.0.CO;2-N](https://doi.org/10.1002/1616-3028(20020201)12:2<149::AID-ADFM149>3.0.CO;2-N).
- (32) Catherine, C.; Oh, S. J.; Lee, K.-H. H.; Min, S.-E. E.; Won, J.-I. I.; Yun, H.; Kim, D.-M. M. Engineering Thermal Properties of Elastin-like Polypeptides by Incorporation of Unnatural Amino Acids in a Cell-Free Protein Synthesis System. *Biotechnol. Bioprocess Eng.* 2015, 20 (3), 417–422. <https://doi.org/10.1007/s12257-015-0190-1>.
- (33) Straley, K. S.; Heilshorn, S. C. Independent Tuning of Multiple Biomaterial Properties Using Protein Engineering. *Soft Matter* 2009, 5 (1), 114. <https://doi.org/10.1039/b808504h>.
- (34) Biesheuvel, P. M.; Cohen Stuart, M. A. Electrostatic Free Energy of Weakly Charged Macromolecules in Solution and Intermacromolecular Complexes Consisting of Oppositely Charged Polymers. *Langmuir* 2004, 20 (7), 2785–2791. <https://doi.org/10.1021/la036204l>.

- (35) Bataille, L.; Dieryck, W.; Hocquellet, A.; Cabanne, C.; Bathany, K.; Lecommandoux, S.; Garbay, B.; Garanger, E. Recombinant Production and Purification of Short Hydrophobic Elastin-like Polypeptides with Low Transition Temperatures. *Protein Expr. Purif.* 2016, 121, 81–87. <https://doi.org/10.1016/j.pep.2016.01.010>.
- (36) Korla, P.; Yagi, H.; Kitagawa, Y.; Megeed, Z.; Nahmias, Y.; Sheridan, R.; Yarmush, M. L. Self-Assembling Elastin-like Peptides Growth Factor Chimeric Nanoparticles for the Treatment of Chronic Wounds. *Proc. Natl. Acad. Sci. U. S. A.* 2011, 108 (3), 1034–1039. <https://doi.org/10.1073/pnas.1009881108>.
- (37) Luo, T.; Kiick, K. L. Noncovalent Modulation of the Inverse Temperature Transition and Self-Assembly of Elastin-b-Collagen-like Peptide Bioconjugates. *J. Am. Chem. Soc.* 2015, 137, 15362–15365. <https://doi.org/10.1021/jacs.5b09941>.
- (38) Tysseling-Mattiace, V. M.; Sahni, V.; Niece, K. L.; Birch, D.; Czeisler, C.; Fehlings, M. G.; Stupp, S. I.; Kessler, J. A. Self-Assembling Nanofibers Inhibit Glial Scar Formation and Promote Axon Elongation after Spinal Cord Injury. *J. Neurosci.* 2008, 28 (14), 3814–3823. <https://doi.org/10.1523/JNEUROSCI.0143-08.2008>.
- (39) Leach, J. B.; Brown, X. Q.; Jacot, J. G.; Dimilla, P. A.; Wong, J. Y. Neurite Outgrowth and Branching of PC12 Cells on Very Soft Substrates Sharply Decreases below a Threshold of Substrate Rigidity. *J. Neural Eng.* 2007, 4 (2), 26–34. <https://doi.org/10.1088/1741-2560/4/2/003>.
- (40) Levental, I.; Georges, P. C.; Janmey, P. A. Soft Biological Materials and Their Impact on Cell Function. *Soft Matter* 2007, 3 (3), 299–306. <https://doi.org/10.1039/B610522J>.

- (41) Johnson, T.; Koria, P. Expression and Purification of Neurotrophin-Elastin-Like Peptide Fusion Proteins for Neural Regeneration. *BioDrugs* 2016, 30 (2), 117–127. <https://doi.org/10.1007/s40259-016-0159-4>.
- (42) Chedly, J.; Soares, S.; Montembault, A.; von Boxberg, Y.; Veron-Ravaille, M.; Mouffle, C.; Benassy, M. N.; Taxi, J.; David, L.; Nothias, F. Physical Chitosan Microhydrogels as Scaffolds for Spinal Cord Injury Restoration and Axon Regeneration. *Biomaterials* 2017, 138, 91–107. <https://doi.org/10.1016/j.biomaterials.2017.05.024>.
- (43) Benitez, P. L.; Mascharak, S.; Proctor, A. C.; Heilshorn, S. C. Use of Protein-Engineered Fabrics to Identify Design Rules for Integrin Ligand Clustering in Biomaterials. *Integr. Biol. (Camb)*. 2016, 8 (1), 50–61. <https://doi.org/10.1039/c5ib00258c>.
- (44) Benitez, P. L.; Sweet, J. A.; Fink, H.; Chennazhi, K. P.; Nair, S. V.; Enejder, A.; Heilshorn, S. C. Sequence-Specific Crosslinking of Electrospun, Elastin-Like Protein Preserves Bioactivity and Native-Like Mechanics. *Adv. Healthc. Mater.* 2013, 2 (1), 114–118. <https://doi.org/10.1002/adhm.201200115>.
- (45) Lau, L. W.; Cua, R.; Keough, M. B.; Haylock-Jacobs, S.; Yong, V. W. Pathophysiology of the Brain Extracellular Matrix: A New Target for Remyelination. *Nat. Rev. Neurosci.* 2013, 14 (10), 722–729. <https://doi.org/10.1038/nrn3550>.
- (46) Kapp, T. G.; Rechenmacher, F.; Neubauer, S.; Maltsev, O. V.; Cavalcanti-Adam, E. A.; Zarka, R.; Reuning, U.; Notni, J.; Wester, H. J.; Mas-Moruno, C.; Spatz, J.; Geiger, B.; Kessler, H. A Comprehensive Evaluation of the Activity and Selectivity Profile of Ligands for RGD-Binding Integrins. *Sci. Rep.* 2017, 7 (January), 1–13. <https://doi.org/10.1038/srep39805>.

- (47) Dent, M. A. R.; Sumi, Y.; Morris, R. J.; Seeley, P. J. Urokinase-Type Plasminogen Activator Expression by Neurons and Oligodendrocytes During Process Outgrowth in Developing Rat Brain. *Eur. J. Neurosci.* 1993, 5, 633–647.
- (48) Downes, N.; Mullins, P. The Development of Myelin in the Brain of the Juvenile Rat. *Toxicol. Pathol.* 2014, 42 (5), 913–922. <https://doi.org/10.1177/0192623313503518>.
- (49) Emery, B. Regulation of Oligodendrocyte Differentiation and Myelination. *Science* (80-.). 2010, 330 (6005), 779–782. <https://doi.org/10.1126/science.1190927>.
- (50) Semina, E.; Rubina, K.; Sysoeva, V.; Rysenkova, K.; Klimovich, P.; Plekhanova, O.; Tkachuk, V. Urokinase and Urokinase Receptor Participate in Regulation of Neuronal Migration, Axon Growth and Branching. *Eur. J. Cell Biol.* 2016, 95 (9), 295–310. <https://doi.org/10.1016/j.ejcb.2016.05.003>.
- (51) Sorokin, L. The Impact of the Extracellular Matrix on Inflammation. *Nat. Rev. Immunol.* 2010, 10 (10), 712–723. <https://doi.org/10.1038/nri2852>.
- (52) Cuzner, M. L.; Opdenakker, G. Plasminogen Activators and Matrix Metalloproteases, Mediators of Extracellular Proteolysis in Inflammatory Demyelination of the Central Nervous System. *J. Neuroimmunol.* 1999, 94 (1–2), 1–14. [https://doi.org/10.1016/S0165-5728\(98\)00241-0](https://doi.org/10.1016/S0165-5728(98)00241-0).
- (53) Mehra, A.; Ali, C.; Parcq, J.; Vivien, D.; Docagne, F. The Plasminogen Activation System in Neuroinflammation. *Biochim. Biophys. Acta* 2016, 1862, 395–402. <https://doi.org/10.1016/j.bbadis.2015.10.011>.
- (54) Larsen, P. H.; Wells, J. E.; Stallcup, W. B.; Opdenakker, G.; Yong, V. W. Matrix Metalloproteinase-9 Facilitates Remyelination in Part by Processing the Inhibitory NG2 Proteoglycan. *J. Neurosci.* 2003, 23 (35), 11127–11135. <https://doi.org/23/35/11127> [pii].

- (55) Uhm, J. H.; Dooley, N. P.; Oh, L. Y. S.; Yong, V. W. Oligodendrocytes Utilize a Matrix Metalloproteinase, MMP-9, to Extend Processes along an Astrocyte Extracellular Matrix. *Glia* 1998, 22 (1), 53–63. [https://doi.org/10.1002/\(SICI\)1098-1136\(199801\)22:1<53::AID-GLIA5>3.0.CO;2-9](https://doi.org/10.1002/(SICI)1098-1136(199801)22:1<53::AID-GLIA5>3.0.CO;2-9).
- (56) Yong, V. W.; Krekoski, C. a; Forsyth, P. a; Bell, R.; Edwards, D. R. Matrix Metalloproteinases and Diseases of the CNS. *Trends Neurosci.* 1998, 21 (2), 75–80. [https://doi.org/10.1016/S0166-2236\(97\)01169-7](https://doi.org/10.1016/S0166-2236(97)01169-7).
- (57) Šišková, Z.; Yong, V. W.; Nomden, A.; van Strien, M.; Hoekstra, D.; Baron, W. Fibronectin Attenuates Process Outgrowth in Oligodendrocytes by Mislocalizing MMP-9 Activity. *Mol. Cell. Neurosci.* 2009, 42 (3), 234–242. <https://doi.org/10.1016/j.mcn.2009.07.005>.
- (58) Uhm, J. H.; Dooley, N. P.; OH, L. Y. S.; Yong, V. W. Oligodendrocytes Utilize a Matrix Metalloproteinase , MMP-9 , to Extend Processes Along an Astrocyte Extracellular Matrix. *Glia* 1998, 22, 53–63.
- (59) Meco, E.; Lampe, K. J. Microscale Architecture in Biomaterial Scaffolds for Spatial Control of Neural Cell Behavior. *Front. Mater.* 2018, 5 (2). <https://doi.org/10.3389/fmats.2018.00002>.
- (60) Meco, E.; Lampe, K. J. Impact of Elastin-like Protein Temperature Transition on PEG-ELP Hybrid Hydrogel Properties. *Biomacromolecules* 2019, 20, [acs.biomac.9b00113](https://doi.org/10.1021/acs.biomac.9b00113). <https://doi.org/10.1021/acs.biomac.9b00113>.

2. Microscale architecture in biomaterial scaffolds for spatial control of neural cell behavior

Published as: E. Meco, KJ Lampe, “Microscale architecture in biomaterial scaffolds for spatial control of neural cell behavior,” *Frontiers in Materials*, 5: 2 (2018)

2.1. Abstract

Biomaterial scaffolds mimic aspects of the native central nervous system (CNS) extracellular matrix (ECM) and have been extensively utilized to influence neural cell (NC) behavior in *in vitro* and *in vivo* settings. These biomimetic scaffolds support NC cultures, can direct the differentiation of NCs, and have recapitulated some native NC behavior in an *in vitro* setting. However, NC transplant therapies and treatments used in animal models of CNS disease and injury have not fully restored functionality. The observed lack of functional recovery occurs despite improvements in transplanted NC viability when incorporating biomaterial scaffolds and the potential of NC to replace damaged native cells. The behavior of NCs within biomaterial scaffolds must be directed in order to improve the efficacy of transplant therapies and treatments. Biomaterial scaffold topography and imbedded bioactive cues, designed at the microscale level, can alter NC phenotype, direct migration, and differentiation. Microscale patterning in biomaterial scaffolds for spatial control of NC behavior has enhanced the capabilities of *in vitro* models to capture properties of the native CNS tissue ECM. Patterning techniques such as lithography, electrospinning and 3D bioprinting can be employed to design the microscale architecture of biomaterial scaffolds. Here, the progress and challenges of the prevalent biomaterial patterning techniques of lithography, electrospinning, and 3D bioprinting are reported. This review analyzes NC behavioral response to specific microscale topographical patterns and spatially organized bioactive cues.

2.2. Introduction

2.2.1. Tissue damage in the CNS

Tissue damage in the central nervous system (CNS) caused by injury and disease cannot be fully repaired through endogenous healing mechanisms. For therapeutic treatments of CNS injury and disease to be successful they need to address a variety of challenges that are specific to the individual injury or disease, but can be broadly defined as replacing dead neural cells (NCs), remodeling the extracellular matrix (ECM) to a healthy state, and restoring nervous system functionality. In the autoimmune disease multiple sclerosis (MS), for instance, immune cells infiltrate the CNS and cause demyelination of neuronal axons¹. In the aftermath of this demyelination the axons deteriorate and neuronal death occurs, leading to reactive astrogliosis¹. During reactive astrogliosis astrocytes form inhibitory glial scars around the demyelinated lesion and prevent both remyelination of damaged axons and axonal regeneration¹. The therapeutic needs for successful tissue regeneration of this particular disease are to replace dead neurons and oligodendrocytes, remodel the inhibitory scar tissue to allow for infiltration of endogenous cells, and prevent further immune cell infiltration into the CNS. A related sequence of events occurs in ischemic stroke, where the blood supply to the CNS is blocked, leading to hypoxia. Unlike MS, where preventative medicine is used to inhibit immune cell infiltration and mitigate tissue damage, tissue damage in ischemic stroke is difficult to prevent because it only takes approximately four minutes for the adenosine triphosphate (ATP) concentration to be fully depleted². Most of the cell death occurs during reperfusion, when blood flow returns to the CNS and the oxygen concentration suddenly elevates³. Re-established metabolism of oxygen causes the overproduction of reactive oxygen species (ROS), leading to lipid peroxidation of unsaturated fatty acids on the cell membranes, increasing their permeability and causing apoptosis^{3,4}. This is followed by reactive

astrogliosis and formation of a glial scar around the original oxygen deficient region⁵. Successful therapeutic treatment of damaged tissue after ischemic stroke would replace dead NCs and remodel the inhibitory scar tissue to allow for infiltration of endogenous cells. There is a significant difference in the types of cells that need to be replaced when comparing ischemic stroke, which indiscriminately leads to NC death within a region, to diseases like MS which targets specific cell types. Unlike MS and ischemic stroke, tissue damage in the form of cell necrosis, occurs immediately after a mechanical insult in spinal cord (SC) contusion injury⁶. Cell debris and ROS cause cytotoxicity in the microenvironment, and subsequently apoptosis of surrounding cells⁷. Over the course of several days to months after the initial injury, reactive astrocytes, in conjunction with infiltrating periphery cells in some instances, form glial scar tissue in the area of the mechanical insult^{3,7}. Treatment of CNS tissue damaged by SC contusion injury requires ECM remodeling to remove the cytotoxic cell debris and excess ROS before cells in the injury lesion can be replaced. The mechanisms of NC death are different in each case, but the requirements for effective treatments can be broadly defined as remodeling the ECM to remove cytotoxic and inhibitory aspects, replacing damaged cells, and recovering functionality.

2.2.2. Reparative effects of endogenous neural cells

Interest in developing NC transplant therapies to treat tissue damage caused by CNS injury and disease is derived from evidence that endogenous NCs have reparative effects on damaged tissue⁸. After ischemic stroke in the rat striatum via middle cerebral artery occlusion (MCAO), new neurons derived from proliferating neural precursor cells (NPCs) in the subventricular zone (SVZ) were observed⁹. Similar results occurred in mice with an ipsilateral cerebral cortex infarction induced by MCAO, where the number of Nestin-positive cells in the ischemic region increased¹⁰. When extracted and cultured, the nestin-positive cells from the ischemic region

displayed neural stem cell (NSC) properties *in vitro*¹⁰. NSC populations, derived from ependymal cells, were also discovered in mouse SC after a transverse dorsal funiculus incision¹¹. These findings have led researchers to transplant NCs as therapies to heal CNS tissue damage in both the brain and spinal cord. However, most of the NCs transplanted to the injury environment do not survive and cells that do survive do not display integrative behavior. Only 2-4.5% of mouse NPCs transplanted into rats after traumatic brain injury survived 24 hours after the transplant¹². In addition, the caspase activity of transplanted NPCs that survived was higher in injured rats than sham surgery controls, indicating that the population of cells that survived was apoptotic in the CNS injury environment¹². While transplanted cell viability is higher if the transplant is performed 1 week post injury^{13,14}, NCs alone do not restore functionality to pre-injury baselines.

It is important to highlight distinctions between NC populations used to research *in vitro* and *in vivo* models because there is a wide range of capabilities of each cell line. Mature NCs such as neurons do not contain the capacity to self-renew or further differentiate and are typically not used because *in vitro* cell cultures cannot be maintained. NSCs can self-renew indefinitely and exhibit multipotent differentiation, while NPCs and neural progenitor cells have a limited capacity to self-renew and have a restricted capacity to differentiate¹⁵. Typically NPCs display unipotent differentiation behavior while neural progenitor cells maintain multipotent differentiation, but these descriptions are not rigid rules so overlap between NPCs and neural progenitor cells does exist in literature. Neural precursor and progenitor cells are preferred over NSCs for transplant therapies because their differentiation is more controlled, resulting in less heterogeneous cell cultures. Many NC lines are derived from neuronal tumors because these cell lines are immortalized and are relatively easy to grow and maintain in *in vitro* cell cultures¹⁶. The capabilities and limitations of NC lines are discussed by other reviews¹⁵⁻¹⁹. Here, we will focus on

the microscale architecture design of biomaterial scaffolds and how NCs respond to that architecture.

2.2.3. Bulk biomaterials for tissue repair

Biomaterial scaffolds are designed to be biocompatible and influence cell behavior, making them promising tools for developing CNS tissue treatment therapies. Implantation of biomaterials into CNS injury lesions has helped improve cell infiltration and functional recovery²⁰. A collagen and PuraMatrix hydrogel transplanted into a 5 mm gap thoracic (T9-T11) rat SC transection increased animal Basso, Beattie, and Bresnahan (BBB) scores over phosphate buffered saline (PBS) controls 4 months post-surgery²¹. Neuronal and astrocyte infiltration into the injury lesion increased in animals with the collagen and PuraMatrix biomaterial scaffold. A similar endogenous cell response occurred when implanting a fibronectin based scaffold into 2 mm gap thoracic (T7-T9) rat SC transection^{22,23}. Axons infiltrated the fibronectin scaffold and were myelinated by Schwann cells 4 weeks post-injury²². Animals with the fibronectin scaffold also had early and aggressive macrophage infiltration into the lesion site, which was speculated to provide trophic support for axon infiltration²³. Biomaterial scaffolds have also been utilized to transplant NCs into damaged CNS tissue. NCs transplanted with biomaterial scaffolds have improved post-transplant viability and improve functional recovery over the standalone scaffold and NC transplantations. Improved functional recovery from a 10 mm gap thoracic (T9-T10) SC hemisection injury on African green monkeys was observed when implanting human NSCs seeded on a poly(lactide-co-glycolide) (PLGA) scaffold²⁴. Implanting the PLGA scaffold improved the left hindlimb neuromotor score 44 days post injury over no-treatment controls, and incorporating human NSCs into the PLGA scaffold led to further improvement. Similar results were found when human NSCs in a fibrin scaffold were transplanted into a complete 2 mm long thoracic (T3) rat SC transection,

where the inclusion of human NSCs with the fibrin scaffold improved hindlimb locomotion BBB scores 8 weeks post injury over untreated controls²⁵. While implanting NCs with biomaterial scaffolds has been shown to promote CNS tissue recovery in animal models, regeneration is still limited and functionality cannot be restored to the pre-injury state. Biomaterial scaffolds need to be designed with greater control over NC behavior to improve the efficacy of transplant therapies.

2.2.4. Microscale architecture in biomaterials

Current biomaterial design strategies are focused on controlling NC behavior at the microscale level (less than 1 mm in size). The goals for controlling microscale architecture within biomaterial scaffolds are to direct NC behavior towards clinical therapy needs and to investigate how NCs interact with the ECM. The microscale architecture within biomaterials has a significant impact on cell behavior and differentiation²⁶⁻²⁸. Chitosan based hydrogels were fragmented into varying microscale sizes (Figure 2-1A) and incorporated into thoracic (T8-T9) rat SC bilateral dorsal hemisection injury model²⁹. The hydrogel transplants improved endogenous cell infiltration into the injury lesion (Figure 2-1B-D) and the degree of cell infiltration depended largely on the chitosan fragment size. Hydrogels with 20 micron chitosan fragments (Figure 2-1D) lead to robust endogenous cell infiltration while hydrogels with 150 micron chitosan fragments (Figure 2-1C) had limited cell infiltration 4 weeks post injury. In addition, scaffolds with 150 micron fragments did not have infiltration of axons and few glial cells, while scaffolds with 20 micron fragments had robust infiltration of both. While the microstructure alterations were not designed to direct endogenous NC behavior in a specific way, these results illustrate the significance scaffold microstructure on NC behavior for clinical applications. For SC injury a clinical goal is to guide axons through the injury lesion, which was only achieved by the hydrogel with 20 micron fragments. These results provide motivation for exploring techniques that allow greater control

over material architecture and cell positioning to guide tissue growth. The prevailing techniques used to design microscale architecture in biomaterial scaffolds for influence over NC behavior are lithography, electrospinning and 3D bioprinting (Figure 2-2).

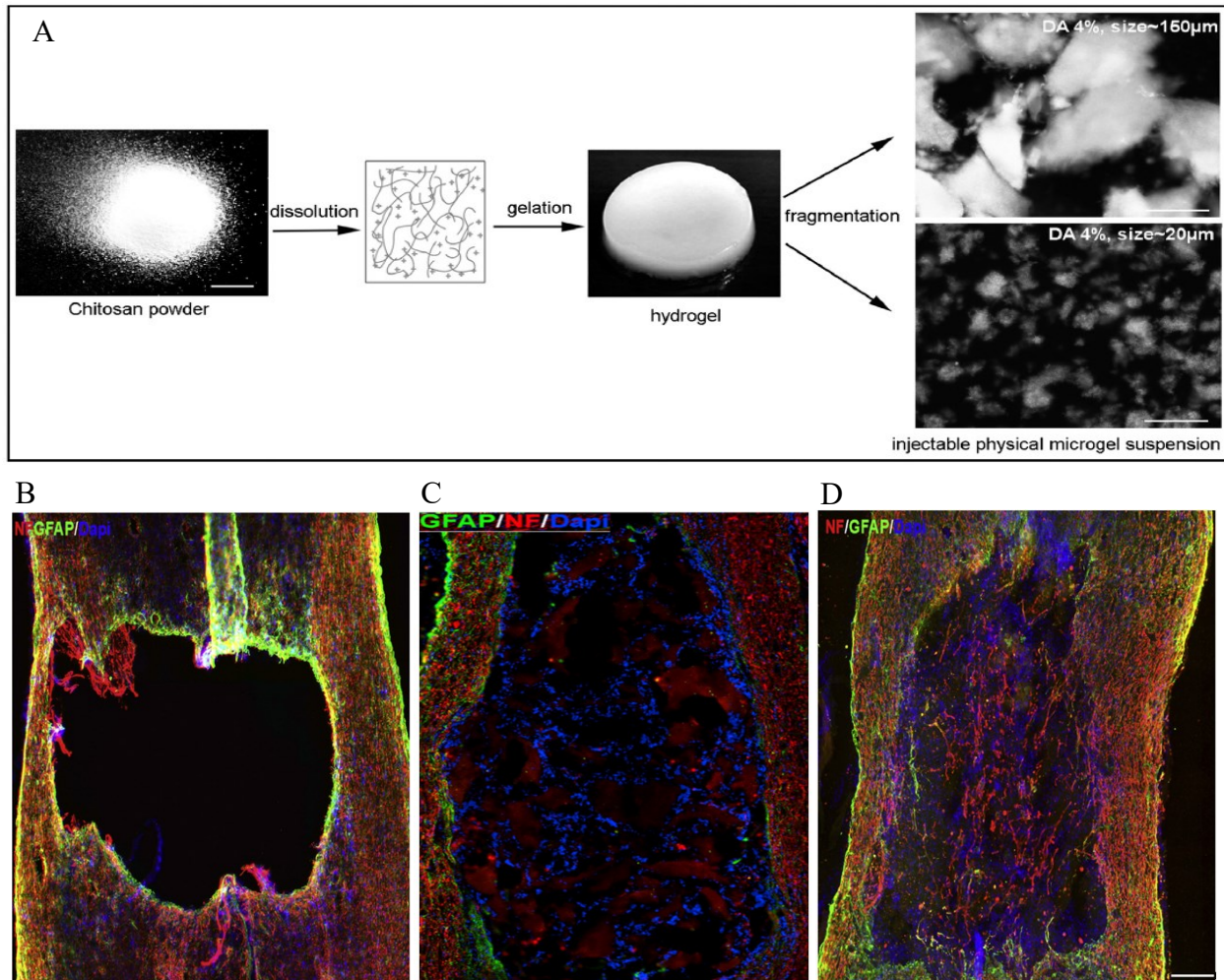


Figure 2-1: (A) Chitosan solution gelled by contacting with ammonia vapors and then fragmented mechanically into differing average microscale architecture. (B-D) Immunostaining of spinal cord lesion site 4 weeks post injury/injection for neurofilament (NF), astrocytes (GFAP), and cell nuclei (DAPI). (B) Lesion only, (C) lesion with chitosan-FPHS hydrogel implant with 150 μm average fragment size, and (D) lesion with chitosan-FPHS 20 μm average fragment size. Smaller fragments result in greater presence of neurofilament in the lesion site. (B, D) Scale bar = 240 μm and (C) Scale bar = 300 μm . Reproduced with permission of ref. 29, Copyright 2017, Elsevier.

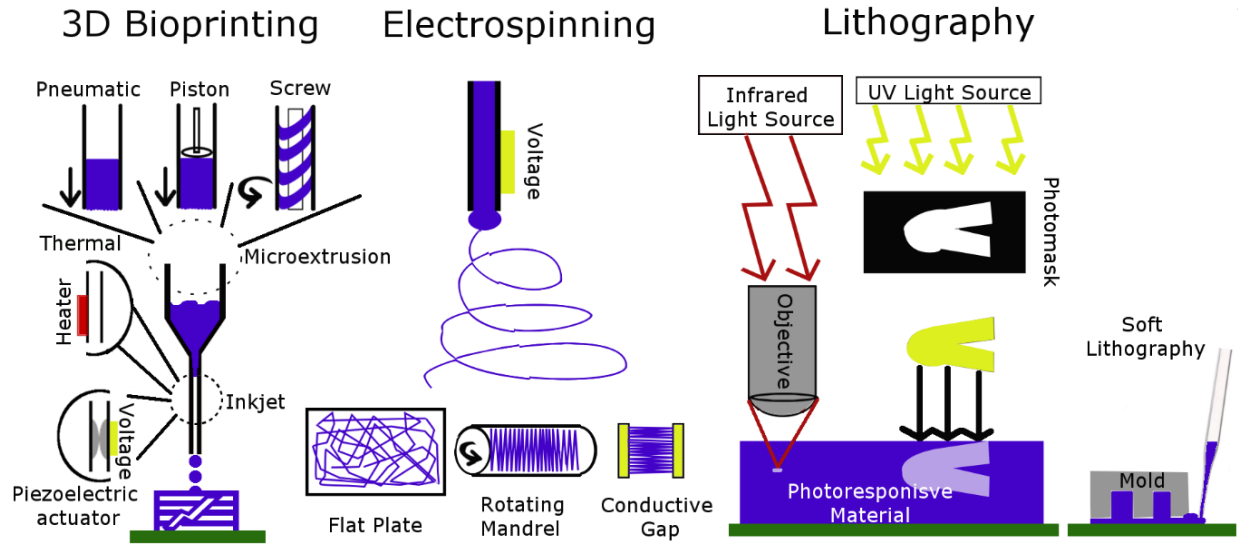


Figure 2-2: Schematic of 3D bioprinting, electrospinning, and lithography techniques. The type of 3D bioprinter is chosen based on biomaterial rheological properties. Electrospun fibers are patterned by changing the collector. Lithography patterning is done by adjusting light based techniques or using a mold.

2.3. Lithography

2.3.1. Lithographic techniques

Several lithographic techniques are used to pattern biomaterial scaffolds: photolithography, soft lithography, stereolithography and 2-photon lithography (sometimes referred to by the more general term multiphoton lithography in literature). Photolithography refers to techniques that pattern a photoresist onto a substrate using a photomask and a light source, usually in the ultraviolet (UV) wavelength range³⁰. The substrate is the biomaterial housing and the photoresist is a material that is chemically responsive to the presence of light within a specific wavelength range. A photomask is used to create a pattern by shielding parts of the photoresist material from the light source. The process can be repeated to create multiple layers with differing patterns. Since most of the processing is cytotoxic, for biological research the photoresist is patterned, washed and cells are seeded on top of the material afterwards. Stereolithography is similar to photolithography except the photoresist material is replaced with a photocurable polymer resin or solution³¹. The

polymer resin or solution is solidified in the presence of a light source. Patterns are made either by using a photomask or a mobile laser light source. Soft lithography is a technique used in conjunction with photolithography. First a patterned stamp or mold is made from materials such as polydimethylsiloxane (PDMS) using photolithography³². The patterned stamp is then placed on the substrate and the voids created by the stamp's pattern are filled with a biomaterial of interest, called ink. The benefits of patterning using soft lithography are that the ink solidification chemistry does not need to be light based and the processing can be biocompatible. 2-photon lithography is an extension of photolithography and stereolithography because it is used to pattern the same materials, either a photoresist or photocurable polymer, with a different light source. The UV light source is replaced with a femtosecond pulsed infrared (IR) laser, such as titanium:sapphire lasers, going through an objective lens to focus the beam. The laser wavelength is twice that of the maximum absorbance wavelength of UV light-based chemistry, therefore two of these lower energy photons are required to generate the same free radical³³. Since the process of absorbing two photons requires a high light intensity, absorbance only occurs at the objective lens focal point, allowing for patterning in the z-direction of a UV light responsive material. The advantage of 2-photon lithography is the increased resolution in the z-direction, which allows for patterning in three dimensions. In contrast, photo- and stereolithography techniques require repeating the processing to create multiple layers for design of three dimensional (3D) structures. Lithography based techniques have been successfully used to organize biomaterial topography and spatially immobilized ECM materials.

2.3.2. *Grooves on scaffold surfaces*

Lithographic patterning of grooves into biomaterial surfaces has been extensively shown to direct NC alignment, migration and differentiation^{34,35}. Astrocytes seeded onto a polystyrene mold

patterned with channels that were 10 μm wide and 3 μm deep using photolithography, and subsequently coated with laminin, had elongated process extensions that aligned with the grooves³⁶. In the non-patterned surface astrocytes had rounded cell bodies and process extensions were not oriented towards a particular direction. Adult hippocampal progenitor cells behaved in a similar manner by aligning processes with patterned channels on a laminin coated polystyrene scaffold³⁷. In addition, cells seeded onto the patterned scaffold had longer process extensions than those on the non-patterned surface. Differentiation down the neuronal, oligodendrocyte and astrocyte pathways was similar for cells seeded on both the patterned and non-patterned polystyrene surfaces, indicating that this effect was not caused by a difference in the cell differentiation. The dimensions of the grooves are important for being able to control both differentiation and alignment. Dorsal root ganglion cells (DRG) seeded onto the surface of a coumarin based biomaterial scaffold that was patterned into square pillars using a modified stereolithography technique did not show robust alignment with the grooves³⁸. This could be because the grooves were very shallow, with 20 nm being the largest depth tested. Other studies have investigated the effects of groove width on NC behavior. Adult human NSCs aligned better on smaller, 5 μm wide, channels than on larger, 60 μm wide, channels when seeded onto patterned PDMS channels coated with poly-L-lysine³⁹. However, more cells seeded on the PDMS scaffold with larger channels differentiated down the neuronal lineage, and had more neurites per cell. Similar results were found when radial glia cells were seeded on polymethylmethacrylate (PMMA) scaffolds patterned with 2 and 10 μm wide channels, where cells aligned with the grooves and migrated along the channels (Figure 2-3)⁴⁰. Patterning channels on the scaffold surface can also affect the behavior of NCs encapsulated within the biomaterial scaffold. Bone marrow-derived stem cells encapsulated in alginate gels with 500 μm wide surface microchannels had a 4-fold

decrease in the glial cell to neuron differentiation ratio when compared to non-patterned hydrogels⁴¹. Simulations of oxygen and water transport into the alginate hydrogels indicated that the surface microchannels improved oxygen and water diffusion into the scaffolds. The decrease in the glial cell to neuron differentiation ratio was attributed to better nutrient transport in hydrogels with the surface microchannels. Lithographic patterning can also be used to spatially orient bioactive motifs to direct NC behavior.

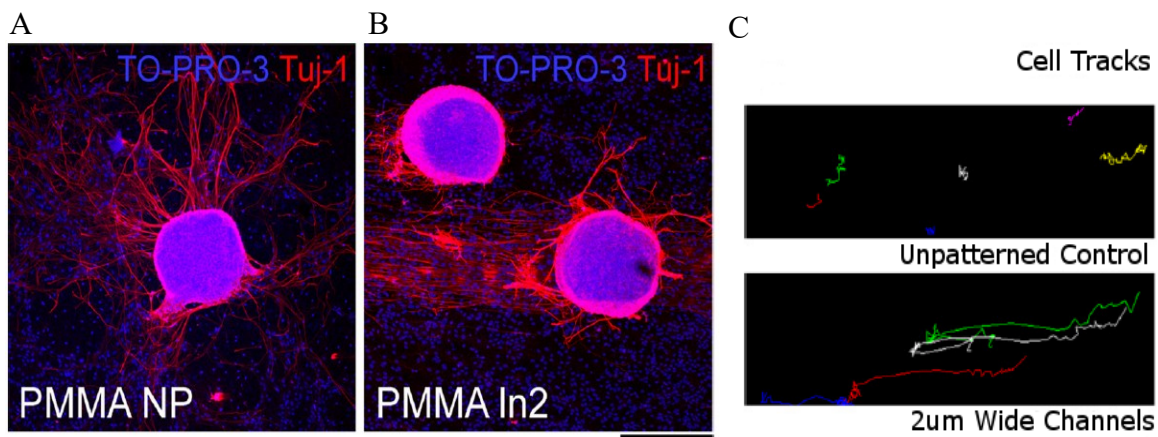


Figure 2-3: Radial glial cells seeded on (A) unpatterned PMMA surface and (B) PMMA surface with 2 μm wide channels. Cell nuclei stained with TO-PRO-S (blue) and neurons stained with beta tubulin III (red). (C) Particle tracks of neuronal trajectories over 3 hours in unpatterned PMMA (top) and PMMA with 2 μm wide channels (bottom). Scale bar = 200 μm . Reproduced with permission of ref. 40, Copyright 2012, Elsevier.

2.3.3. Immobilization of bioactive motifs

Lithographic techniques have been developed that can spatially immobilize proteins and ECM molecules onto the polymer network of biomaterial scaffolds. A prevalent theme in literature is the microscale attachment of adhesive ECM proteins and peptide sequences, such as arginine-glycine-aspartic acid (RGD), which can be used to direct cell migration and the extension of processes^{42,43}. DRG seeded on the surface of an agarose scaffold migrated and extended processes into the interior of the scaffold when RGD was immobilized within the agarose scaffold^{44,45}. The

RGD polypeptide was incorporated into the agarose hydrogel by first functionalizing agarose with 2-nitrobenzyl-protected cysteine. The nitrobenzyl group was cleaved to expose a free thiol group when UV light was shined onto the agarose scaffold. The free thiol group subsequently reacted with a maleimide-modified RGD polypeptide dissolved in the scaffold encompassing solution. RGD attachment onto the agarose scaffold was constrained to cylindrical sections down the z-axis by using a photomask with open circles. The versatility of this method was demonstrated by achieving the similar results on a hyaluronic acid (HA) based scaffold⁴⁶. Adhesive motifs can also be used to direct where NCs attach on biomaterial surfaces. LRM55 astrogloma and primary rat hippocampal neurons seeded onto an acrylamide-based substrate with immobilized fibronectin, laminin and the IKVAV polypeptide sequence (separately) only attached to the fibronectin, laminin or IKVAV portion of the scaffold^{47,48}. Soft lithography was used to immobilize the adhesive motifs into a crosshatch pattern. Primary rat hippocampal neurons extended processes preferentially along the grid pattern and were found to have functional synapses 10 days post seeding. Similar results were achieved when hybrid mouse neuroblastoma and rat glioma cell cultures were seeded onto a bovine serum albumen (BSA) modified collagen scaffold surface with immobilized matrigel⁴⁹. Matrigel was immobilized into a crosshatch pattern and cells migrated to the nodes of the matrigel pattern, extended processes along the matrigel grid 15 hours after seeding. Although, most research has focused patterning motifs that promote adhesion, the techniques described here are versatile and can be expanded to immobilize other proteins.

The biological activity of immobilized proteins depends on the immobilization process and the specific protein tolerances to the processing environment(s). Photolithography was used to test if the activity of two known axon inhibitor proteins, semaphorin 6A and ephrin-B3, was affected by immobilizing them onto an agarose-based hydrogel^{50,51}. The technique involved creating a mold

from poly(ethylene glycol) (PEG) designed in the shape of a well attached to a channel that splits into two separate channels. The mold was then filled with 2-nitrobenzyl-protected cysteine modified-agarose solution, similar to the chemistry described above. Semaphorin 6A or ephrin-B3 were immobilized onto one of the two channels by exposing the scaffold to UV light and using a photomask. The second channel did not contain immobilized protein and was used as a control. DRG explants from the lumbosacral, thoracic, and cervicothoracic regions were placed inside the well and the direction of their process extensions was used to determine if the immobilized proteins maintained biological activity. DRG explants from the lumbosacral region did not extend processes into the channel with immobilized semaphorin 6A, indicating that the immobilized protein was still biologically active. However, processes from thoracic and cervicothoracic DRG explants were not inhibited by semaphorin 6A. In addition, Ephrin-B3 did not inhibit the process extensions from any of the DRG explants. These results demonstrate one of the weaknesses of photolithography, where the process of immobilizing proteins can denature them. However, it is unclear what part of the immobilization process (exposure to UV light or the chemical reaction) had deleterious effects. Another chemical reaction scheme available to immobilize proteins onto biomaterial scaffolds uses UV light to cleave a nitrobenzyl ester bond and expose an alkoxyamine that can react with aldehyde groups on proteins in the encompassing solution⁵²⁻⁵⁴. This scheme was used to immobilize collagenase to a PEG based scaffold and the immobilized collagenase activity was quantified to be 24% of the soluble enzyme. In addition, immobilized mouse anti-6xHis monoclonal antibody attached to the PEG scaffold retained sufficient bioactivity to recognize a secondary antibody. Finally, vitronectin was immobilized in the PEG scaffolds and encapsulated human mesenchymal stem cells only differentiated in regions where the protein was

attached. These studies demonstrate that proteins can be spatially immobilized onto biomaterial scaffolds, but the process does affect biological activity.

2.3.4. Microscale design in 3D Space

While most lithographic processes are used for surface-based patterning and protein immobilization on biomaterial scaffolds, there have been several advances that have allowed for patterning in three dimensions. The design of biocompatible materials that are sensitive to UV light has allowed for encapsulating NCs inside biomaterial scaffolds using stereolithography. PC12 cells encapsulated in methacrylate-modified gelatin hydrogels patterned as a crosshatch survived the gelation process and could differentiate 14 days post encapsulation⁵⁵. A similar process was used to encapsulate PC12 cells in an acrylate-modified PEG (PEGDA) hydrogel, where cells could differentiate 3 days post encapsulation⁵⁶. Combining cytocompatible materials with 2-photon lithography has allowed for the design of biomaterials with sophisticated 3D architecture⁵⁷. Channels with a denser concentration of PEG were created by first crosslinking a large molecular weight PEGDA to form a bulk hydrogel, then leaching in a small molecular weight PEGDA into the scaffold, and finally exposing specific regions in the bulk hydrogel to a 2-photon laser for a second round of crosslinking⁵⁸. Fluorescent BSA was then leached into the PEG scaffold to demonstrate that regions exposed to the 2-photon laser did not allow for BSA diffusion because of the denser network created by crosslinking the small molecular weight PEGDA. The same technique was used to add adhesive domains to the scaffold in various 3D spatial patterns by attaching the RGD polypeptide to the small molecular weight PEGDA before leaching it into the scaffold⁵⁸. 2-photon lithography was also used to create a PEG-based scaffold patterned with tunnels inside the scaffold⁵⁹. Encapsulated DRG preferentially migrated through the tunnels over 4 days. 2-photon lithography has been combined with other chemical processes to spatially orient

bioactive motifs. BSA was immobilized into a HA based hydrogel in the shape of a spiral using 2-photon lithography⁶⁰. The adhesive IKVAV polypeptide was then linked to the immobilized BSA using an avidin-biotin complex. DRG encapsulated in the scaffold and near the immobilized IKVAV polypeptide extended processes towards the IKVAV protein and followed designed spiral pattern. Proteins have been immobilized onto biomaterial scaffolds with a 3D resolution of a couple of microns, which allows for influencing single cell behavior. BSA was immobilized to a PEG-based scaffold with a resolution of 1 x 1 μm in the xy-plane and 3-5 μm down the z-axis⁵². A similar resolution of 0.5 μm radially and 1-2 μm down the z-axis was achieved for the immobilization of the IKVAV polypeptide⁶⁰. Biomaterial scaffold architecture can be designed at the microscale level by utilizing a combination of lithographic techniques with cytocompatible materials.

2.4. Electrospinning

2.4.1. Electrospinning techniques

The electrospinning process involves pumping a polymer solution through a charged needle^{61,62}. Enough voltage is applied to the needle tip to cause droplets of the polymer solution to overcome the surface tension and emerge from the needle tip in the form of a liquid jet. The liquid jet then undergoes bending instability and rapidly whips into multiple expanding loops. During this whipping process the polymer solution stretches and thins into micrometer and nanometer fibers, and solvents evaporate. The jet is ultimately collected on a grounded or oppositely charged plate that is a variable distance away from the needle tip. The distance of the collector from the needle tip is selected to allow enough time for solvents to evaporate fully and to control the diameter of the fibers. There are several parameters that require careful tuning in order to

electrospin a polymer solution into fibers: polymer solution viscosity, conductivity, and flow rate, applied voltage to the needle, and the temperature and humidity of the environment.

Electrospun fibers are patterned by changing the collector used to gather the polymer (Figure 2-2). A flat plate collector produces fibers with a random orientation. A rotating mandrel is used to align fibers in a singular direction⁶³. Increasing the speed of the mandrel improves fiber alignment but also affects the mechanical properties of the bulk scaffold formed. Another way to align fibers is to collect them using two conducting electrodes separated by an insulating gap⁶⁴. The gap causes the electrostatic forces to become directional and the fibers align in-between the two electrodes. This method of fiber alignment is limited to thin fiber scaffolds because the fibers carry a charge. As more fiber layers are added the collector starts to behave like a flat plate and subsequent fiber layers become randomly oriented. There are workarounds to this limitation that involve gathering the fibers layer-by-layer and combining them into a single scaffold post electrospinning⁶⁵. Electrospun fibers can also be aligned by using two parallel magnets as a collector⁶⁶. This method is not limited to thin layered scaffolds but does require magnetizing the polymer solution. More sophisticated patterns can be created by adjusting the topography of the collector. Researchers have gathered polyurethane-based fibers on a PDMS collector with a square grid pattern etched onto the surface⁶⁷. The resulting scaffold had aligned fibers along the grid lines and random fibers in the square sections.

2.4.2. Neural cells on aligned fibers

The alignment of electrospun fibers has a robust effect on NC behavior. Researchers seeded human neural progenitor-derived astrocytes (hNP-AC), human astrocytoma cell line U373, and human neuroblastoma cell line SH-SY5Y on aligned polycaprolactone (PCL) and PCL/collagen blended fibers⁶⁸. All three cell types had elongated cell bodies in alignment with fiber direction,

extended processes in that direction, and migrated preferentially in parallel with the aligned fibers (Figure 2-4A, B). These findings were consistent on both PCL and PCL/collagen blended fiber scaffolds. Human umbilical mesenchymal stem cells (hUMSC) displayed similar behavior when seeded onto aligned fibrin fibers by orienting actin filaments with the fiber orientation (Figure 2-4E)⁶⁹. When hUMSC were seeded on randomly aligned fibrin fibers they expressed actin filaments in a random orientation, but their morphology did differ from cells cultured on tissue culture plastic controls (Figure 2-4C, D)⁶⁹. Alignment of electrospun fibers influences both the direction of NC process extensions and promotes longer processes. DRG seeded on randomly oriented polypyrrole tube fibers extended neurites radially⁷⁰. By comparison, DRG seeded on aligned polypyrrole tube fibers extended neurites in the directions of the fibers, and displayed a longer maximum neurite length. The effects of aligned fibers are robust and can be repeated across many NC lines.

2.4.3. *Fiber material composition*

Most biocompatible materials are difficult to electrospin into fibrous scaffolds and some cell lines do not adhere to commonly electrospun polymers like PCL. As a result, many electrospun fiber scaffolds used to seed NCs are either blended with native ECM proteins and polymers or coated with a bioactive material. The effects of material composition on NC behavior are cell line dependent. The adhesion and migration rate of hNP-AC was improved on the PCL/collagen blended fibers when compared to the PCL fibers⁶⁸. In contrast, U373 cells did not display a difference in migration rate or adhesion behavior when seeded on PCL/collagen blended and PCL fiber scaffolds. SH-SY5Y neuroblastoma cells had an increased metabolic activity when seeded on PCL/hyaluronan blended fibers over PCL fibers⁷¹. Electrospun fibers made from PCL blended with gelatin increased C17.2 NSC neurite length over PCL fiber scaffold controls⁷². Fibers made from conductive biomaterials, such as polypyrrole, have gained interest because electrical

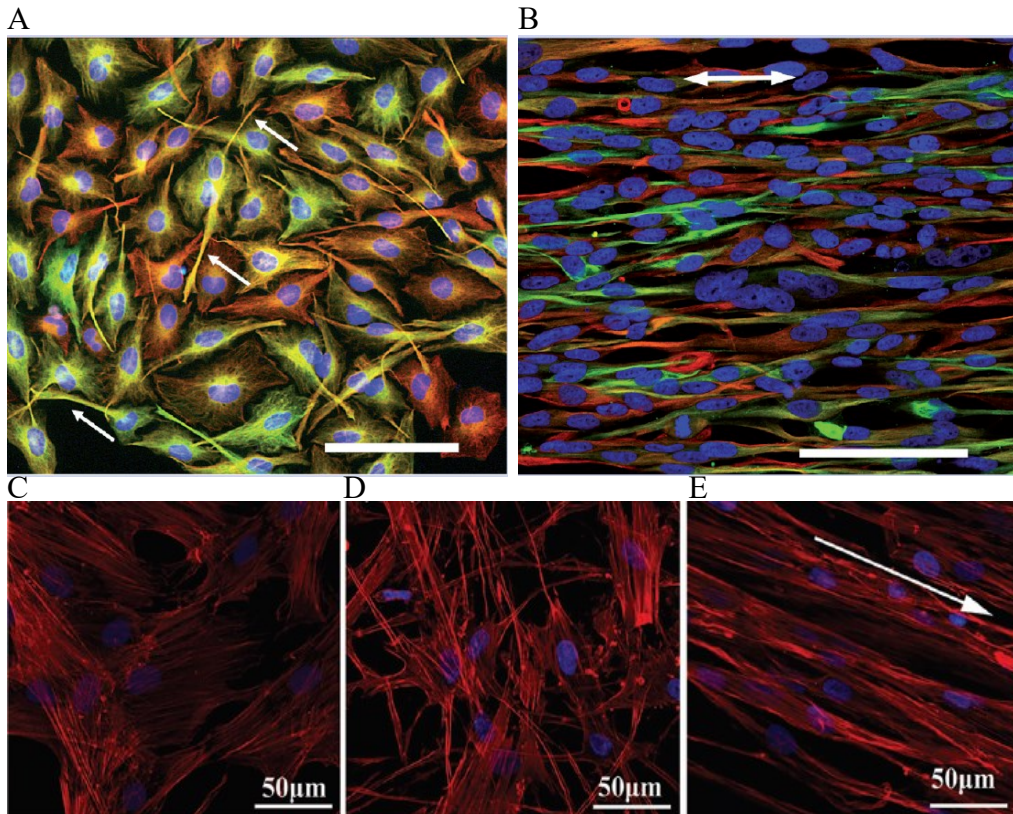


Figure 2-4: Human astrocytoma cell line U373 cultured on (A) poly-L-lysine substrate for 4 days and (B) aligned PCL fibers for 7 days. Arrows indicate (A) process extensions and (B) fiber orientation. Reproduced with permission of Gerardo-Nava et al. (2009), Copyright 2009, Future Medicine LTD. Human umbilical cord mesenchymal stem cells cultured on (C) tissue culture plastic, (D) randomly oriented fibrin fibers, and (E) aligned fibrin fibers for 1 day. Arrow indicates fiber orientation. Reproduced with permission of ref. 69, Copyright 2016, Royal Society of Chemistry. (A, B) Cell nuclei (blue), GFAP (green), vimentin (red) and scale bars = 100 μm . (C, D, E) Cell nuclei (blue) and F-actin (red).

stimulation also promotes process extensions. Applying an electrical stimulation to randomly oriented and aligned polypyrrole nanotubes increased the DRG maximum neurite length over unstimulated controls⁷⁰. Electrical stimulation can also increase the number of processes NSCs extend. The percentage of PC12 cells seeded on silk fibroin fibers coated with reduced graphene oxide that extended neurites increased after applying electrical stimulation⁷³. The increase was comparable to the increase in number of cells with neurites observed when adding soluble nerve growth factor to the media. In addition, multiple rounds of electrical stimulation did not further

promote more PC12 cells to extend neurites. NC behavior can also be directed by controlling the electrospun fiber diameter.

2.4.4. Fiber diameter

The distance between the charged needle tip and the fiber collector can be adjusted to control fiber diameter. Several 2D studies have investigated the impact of fiber diameter on NC behavior. Hippocampus-derived adult rat NSCs were seeded on laminin coated poly(ethersulfone) fibers with 0.283, 0.749 and 1.452 μm diameters⁷⁴. In proliferation media conditions, an increase in fiber diameter led to reduced NSC migration, spreading and proliferation. Under differentiation media conditions, NSCs on 0.283 μm diameter fibers preferentially differentiated into oligodendrocytes, while NSCs on 0.749 and 1.452 μm diameter fibers preferentially differentiated down a neuronal lineage. Differences in electrospun fiber diameter have also been utilized to elucidate oligodendrocyte myelination behavior. Researchers seeded oligodendrocyte precursor cells on poly(L-lysine) coated polystyrene fibers with diameter ranges of 0.2 - 0.4 and 2 - 4 μm ⁷⁵. In part, fibers served as artificial axons, and a higher percentage of the cells cultured on the larger diameter fibers wrapped myelin around the fibers than cells cultured on the smaller diameter fibers. This suggests that axon diameter is an influencing factor in determining which axons are myelinated by oligodendrocytes and which axons are not in the CNS. While electrospinning has been successfully utilized to direct NC behavior on biomaterial scaffolds in 2D culture systems, it has been difficult to translate those results to three dimensions.

2.4.5. Fibers in 3D scaffolds

The effects of electrospun fibers have also been investigated in 3D biomaterial scaffolds. Fibers produced by the electrospinning process do not fully mimic the 3D nature of native tissue. Electrospun fibers are too densely packed to allow for cell infiltration into the biomaterial scaffold.

The effects of fiber topography, material composition, and orientation on NCs are limited to surface effects. However, researchers have developed several techniques to incorporate electrospun fibers in 3D biomaterial scaffolds. A simple way to do this is to gel a hydrogel scaffold on top of the fibers. Researchers gelled a Puramatrix based hydrogel on top of aligned PCL fibers and investigated if human pluripotent stem cell-derived neuron (hPSC) could sense the presence of the fibers⁷⁶. hPSCs seeded on top of a 15 μm thick Puramatrix hydrogel could not sense the aligned PCL fibers at the bottom and extended processes with random orientation. hPSCs encapsulated inside the Puramatrix hydrogel and within 10 μm of the fibers did align processes along the PCL fiber axis. Cells further away from the PCL fibers, yet still inside the gel, extended processes with a random orientation. A similar study was conducted using stereolithography to gel a square grid patterned PEGDA hydrogel on top of aligned PCL and PCL/gelatin fibers⁷⁷. Primary cortical neurons and NSCs seeded on top the PEGDA hydrogel did orient process extensions with PCL/gelatin fiber alignment. Although there was no mention of how thick the PEGDA hydrogel was, it suggests that NCs do not need to be in direct contact with aligned fibers to direct behavior. Similar results were obtained by placing PCL, PCL/gelatin, and laminin coated PCL aligned fibers in the center of HA based hydrogels using soft lithography⁷⁸. Encapsulated SH-5Y5Y neuronal cells grew into large spherical clusters away from the fiber layer and had an elongated phenotype at the fiber layer. NCs at the fiber layer extended processes in the direction of the fiber orientation. The average neurite length was quantified and shown to be highest in HA hydrogels with laminin coated PCL fibers, indicating that cell adhesion to fibers plays a critical role in their behavior. In order get a more uniform cell response across the z-axis of 3D biomaterial scaffolds, researchers have stacked multiple fiber layers in-between hydrogel layers. A single scaffold layer consisted of aligned poly-L,D-lactic acid fibers placed on top of a thin collagen gel with cells seeded on top of

the fibers⁷⁹. Astrocytes, oligodendrocytes and oligodendrocyte precursor cells had elongated cell bodies in alignment with fiber direction and extended processes in that direction. It is unclear if this stacking method truly represents a 3D culture system because cells cannot migrate through the individual fiber layers. The effects of electrospun fibers on directing NSC behavior have been consistent across the *in vitro* literature, and researchers have begun incorporating them into animal studies.

2.4.6. *Fiber scaffolds in vivo*

The implementation of electrospun fiber based biomaterial scaffolds into animal models has not yielded similar results to *in vitro* experiments. Poly(ϵ -caprolactone-co-ethyl ethylene phosphate) aligned fibers were incorporated into a collagen hydrogel and implanted into a C5 rat SC incision injury⁸⁰. Endogenous cell response to a collagen scaffold without fibers, a collagen scaffold with fibers in parallel with the SC longitudinal axis, and a collagen scaffold with fibers at an angle to the SC longitudinal axis was analyzed. Collagen scaffolds with fibers had more neurite infiltration and longer neurites 12 weeks post implantation when compared to the collagen scaffold without fibers. However, aligning the fibers in parallel to the SC longitudinal axis did not further improve endogenous cell response. Similar results were found with the implantation of aligned and randomly oriented fibrin fibers into a 4 mm gap thoracic (T9-T10) SC hemisection injury⁶⁹. Endogenous cell infiltration into the aligned fibers did follow the fiber orientation 4 weeks post implant, but total cell infiltration was similar into both randomly oriented and aligned fibrin scaffolds. From these animal studies it is unclear as to whether or not fiber alignment is important *in vivo*. Researchers have also investigated the effects of fiber surface charge on endogenous cell infiltration. Polyurethane fibers were plasma coated with films of positive, negative and neutral relative surface charge and implanted into rat dorsum for 5 weeks⁸¹. Cell infiltration into the

implants were similar for all conditions, and the study did not investigate infiltrating cell morphology. NCs have also been incorporated with electrospun fiber based scaffolds *in vivo*. Dopaminergic neurons encapsulated in a xyloglucan hydrogel with short poly(L-lactic acid) fibers were injected into the ventral midbrain of Parkinsonian mice⁸². There was no difference in transplanted cell viability between xyloglucan scaffolds with and without fibers. Taken together, these findings indicate that the incorporation of scaffolds made from electrospun fibers into animal models have not confirmed *in vitro* findings and more investigation is necessary.

2.5. 3D bioprinting

2.5.1. Bioprinting techniques

3D bioprinting is defined as the layer-by-layer positioning of biomaterials, biochemicals and cells with spatial control to build a bulk 3D structure. Computer-aided design software is used to control the placement of materials in a syringe, or print head, onto a substrate in the x, y and z directions. 3D bioprinting techniques have the potential to mimic the complex micro-architecture of tissue because the biomaterial scaffolds are built using an additive approach and multiple print heads with different biomaterials can be combined to create a single construct (Figure 2-5). The vast majority of printed biomaterial scaffolds are patterned using the inkjet and microextrusion printing techniques⁸³⁻⁸⁵. Inkjet bioprinting is used to print controlled volumes and works best when printing low viscosity materials or cells. There are two types of inkjet 3D printing heads, thermal and piezoelectric actuated, that provide similar benefits. Thermal inkjet printing is done by electrically heating the print head to produce a pulse of pressure. Although the localized heat generates temperatures in the range of 200-300°C, the short time frame of heating (~2 μs) only results in a material temperature increase of 4-10°C⁸⁶. While cells can survive the thermal stress, the technique may be incompatible with biomaterials, such as agarose, that undergo a thermal

transition to gel or solidify. Piezoelectric actuator inkjet printing is done by applying a voltage to change the actuator shape and produce a droplet of controlled volume. This printing technique does not alter the printed material properties but the mechanical stress produced by the actuator change in shape can induce some cell membrane damage⁸⁷. Microextrusion 3D printing is used for higher viscosity biomaterials or high cell density applications because inkjet printers are prone to clogging under those conditions. Instead of printing controlled volumes, microextrusion 3D printing applies a force to break the material up into beads in the print head. The force is applied either pneumatically, or mechanically with a piston or screw assembly. While there are advantages and disadvantages to each print head set up, they are not limiting for printing biomaterial scaffolds. Microextrusion printers do not have the resolution of inkjet printers and cell viability is lower in some cases^{88,89}, but the technique is usable with a larger variety of biomaterials. Ultimately, the print head is selected based on the biomaterial physical properties because scaffold resolution is currently limited by how well biomaterials maintain the printed structure and not the print head capabilities.

For biomaterial applications, the 3D printing process works best with materials that exhibit yield stress and shear thinning rheological properties⁹⁰. Materials going through the printing process undergo three stress profiles: low stress while the material is inside the syringe, high stress when the material flows through the print head, and low stress when the printed material is on the stage. Yield stress materials exhibit two types of responses to stress: When a small stress is applied they deform elastically, maintaining their structure, and when a high stress is applied they deform plastically, causing the material to flow. The transition between the two responses, called the yield point, is material dependent. Any viscous material can be pushed through a print head, but only materials with yield stress rheological properties will maintain the printed structure on the

stage^{91,92}. Most yield stress materials also exhibit shear thinning behavior, which helps shield cells from the high shear forces caused by traveling through the print head⁹³.

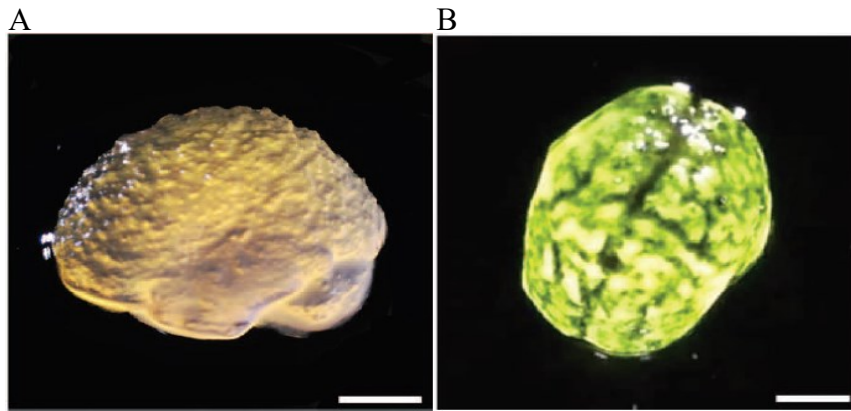


Figure 2-5: (A) Lateral view of 3D printed alginate gel matching anatomical features of the cortex and cerebellum with microscale resolution. (B) Top view with black dye dripped on alginate gels. Scale bars = 1 cm. Reproduced with permission of ref. 116, Creative Commons Copyright (CC-BY).

2.5.2. *Strategies for biomaterial printing*

Bioinks are materials that can be 3D printed, maintain their structure and are cytocompatible. Most biomaterials do not exhibit favorable rheological properties for 3D printing so bioinks are developed by simple mixing of existing materials that individually exhibit desired properties, or through chemical modification of existing biomaterials⁹⁴⁻⁹⁶. Cortical human NSCs were encapsulated in 3D printed blend of alginate, carboxymethyl-chitosan and agarose⁹⁷. The bioink maintained the printed crosshatch structure initially through the cooling of agarose and was subsequently soaked in a calcium chloride solution to crosslink the alginate component. Encapsulated NSCs had an initial cell viability of ~75% and were able to differentiate into neurons and glial cells. Similar results were found with a bioink of sodium alginate, fibrinogen and gelatin⁹⁸. The bioink was soaked in calcium chloride and thrombin solutions after printing to crosslink the sodium alginate and fibrinogen components, respectively. Glioma stem cells

encapsulated in the bioink had an initial cell viability of ~85% and could differentiate into glial and neural cells. Cells encapsulated in the printed bioink had a higher resistance to the cancer drug temozolomide than two dimensional controls, highlighting that cells in native 3D tissue do not behave similar to cell cultures on surfaces. This study also demonstrated the potential of 3D printing to form hierarchical structures because the crosshatch structure at the microscale level was used to form a bulk scaffold in the shape of a tube. Materials can also be mixed during the printing process. Alginate, matrigel and human NSCs were printed through a coaxial syringe with 3 chambers⁹⁹. Human NSCs and matrigel were surrounded by alginate to form capsules and were printed into a calcium chloride bath for crosslinking. Cells extended neurites within the capsules indicating that they were still functional. Ideally, this system would not require alginate to hold the capsule structure of the NSCs in matrigel, but matrigel does not have favorable physical properties for 3D printing. In addition, the chemical structure of matrigel is not well-defined so it would be difficult to chemically modify the structure reliably for 3D printing applications. Biomaterials with well-defined chemical structures do not have this limitation and have been chemically modified to alter their rheological properties for 3D printing.

Most biomaterials do not exhibit favorable rheological properties for 3D printing so researchers have transformed the rheological properties of biomaterials by functionalizing them with moieties that form physical crosslinks¹⁰⁰⁻¹⁰². An example of this, involves supramolecular bonding of adamantane and β -cyclodextrin moieties, which assemble into a complex at low stress and disassemble when exposed to high stress¹⁰¹. HA scaffolds were formed using supramolecular bonds by modifying the HA macromer with adamantane and β -cyclodextrin separately, and mixing of the two modified HA solutions together to form the scaffold¹⁰¹. Modified HA was successfully printed into a crosshatch pattern, but the scaffold could only maintain the crosshatch structure

when few layers were printed. In order to prevent the scaffold from collapsing from the stress caused by overlaying layers and maintain the crosshatch pattern at higher printing heights, HA was further modified with methacrylate groups. HA hydrogels crosslinked with both the supramolecular assembly and chemical methacrylate bonds, after being exposed to UV light, maintained their printed structure for up to one month with as many as 16 printed layers. This study also highlights the importance of gelation kinetics for maintaining printed structure integrity. Only the scaffolds that were exposed to additional UV light in the presence of a photoinitiator after the printing process was complete maintained their structure for 1 month. This indicated that UV exposure during the printing process did not fully crosslink methacrylate groups. Crosslinking kinetics are important considerations for 3D printing biomaterials.

Researchers have investigated inducing fast gelation kinetics in biomaterials to avoid requiring yield stress rheological properties to maintain the printed structure. Gellan gum was printed using a coaxial syringe needle set up, with the gellan gum solution in the inner syringe ring and a crosslinking solution on the outer ring¹⁰³. The material was not printed into a pattern, instead layers with and without encapsulated primary cortical neurons were alternately printed on top of each other. Encapsulated primary cortical neurons had a viability of 70-80%, differentiated into neurons and glia, and extended processes into up to 100 μm into layers without cells 5 days after printing. Waterborne polyurethane, which undergoes gelation through a temperature transition at 37°C, was successfully 3D printed by mixing with soy protein isolate to reduce the gelation time and printing onto a heated stage^{104,105}. Up to 8 layers were printed into a crosshatch pattern, and encapsulated murine NSCs had high viability three days after printing. However, cell metabolic activity was lower than tissue culture polystyrene controls, indicating that the printing process had a negative impact on the murine NSCs.

2.5.3. *Bioprinting bioactive molecules*

The 3D bioprinting technique is not limited to printing bioinks with cells, proteins and other bioactive molecules can also be incorporated. Growth factors incorporated with bioinks maintain protein bioactivity after being printed. Fibroblast growth factor-2 (FGF2) and ciliary neurotrophic factor (CNTF) were printed onto polyacrylamide hydrogels, and primary fetal NSCs were subsequently seeded onto the hydrogels to demonstrate that the growth factors remained biologically active after printing⁹⁸. Soluble FGF2 promotes proliferation and NSCs seeded on portions of the gel with FGF2 did not differentiate into glial cells. Soluble CNTF promotes differentiation and NSCs did differentiate into glial cells when seeded on portions of the hydrogel with CNTF. The amount of NSC differentiation into glial cells could be spatially controlled by printing a concentration gradient of CNTF across the polyacrylamide scaffold. 3D bioprinting has the potential to be utilized as a local drug delivery mechanism because the printed pattern affects cumulative drug release. The chemotherapeutic drug 5-fluorouracil was printed with a bioink composed of PLGA and PCL¹⁰⁶. The cumulative release of the drug from the printed scaffold depended on both the printed pore structure and the number of printed layers in the z-direction. Combinations of bioinks with growth factors have directed NSC behavior. A fibrin hydrogel was printed with vascular endothelial growth factor (VEGF) and placed next to a collagen gel with murine NSCs encapsulated¹⁰⁷. The NSCs migrated and proliferated towards the fibrin hydrogel when VEGF was incorporated and did not do so when fibrin was printed without VEGF.

2.6. Future perspectives

Advances in microscale patterning of biomaterial scaffolds have allowed researchers to investigate NC behavior in response to both physical and biochemical environmental cues. Topographical cues such as grooves and aligned fibers can direct NSC differentiation and neural process extensions. Similar effects can also be biochemically induced by spatially patterning

adhesive motifs. Microscale patterning of biomaterial scaffolds has been performed predominantly by the use of lithography, electrospinning and 3D bioprinting techniques. The final goal remains to develop microarchitecture to direct NC behavior for *in vivo* therapeutic treatments and tissue regeneration, and the immediate challenges for further developing each technique vary significantly.

Lithography has been successfully implemented to pattern grooves on surfaces, channels within biomaterial scaffolds, and spatially immobilize proteins to scaffolds. It has proved to be a powerful tool for developing *in vitro* models to mimic some aspects of native tissue at the microscale level. However, it will be challenging to translate the techniques developed for *in vitro* models to *in vivo* applications. The use of light as a source for patterning at the microscale level is inherently limited to thin or transparent scaffolds. Optically transparent materials, such as PEG, can be patterned well using light but scaffolds made from proteins, such as collagen, are optically dense and cannot be patterned deep within the scaffold. This limitation will be significant when attempting to translate these scaffolds to large animal studies and clinical trials because the biomaterial scaffolds will need to be scaled to appropriate sizes. In addition, current protein immobilization techniques require incubating the biomaterial scaffold in the protein of interest and then using a light source to initiate the immobilization reaction. This has limited application *in vivo* because it takes hours for large proteins, such as growth factors, to diffuse into the scaffold and the process requires several rinse steps. For this technique to be used in a transplant *in vivo* the scaffold must be designed *in vitro* and then transplanted. While applicable for acellular “device” implants, this method has several drawbacks when incorporating NC into the scaffolds. For example, encapsulated NCs may uptake the protein during the incubation step and not allow for the protein to be dispersed throughout the scaffold as desired for immobilization. These issues

do not limit investigating the effects of microscale architecture on NC behavior in *in vitro* models but do hamper translation into *in vivo* studies.

Electrospinning of fibers into an aligned orientation affects a wide range of cell lines in a similar fashion in a 2D setting. NCs elongate cell bodies, extend processes, and migrate preferentially in alignment with fiber scaffold orientation. However, electrospun fibers have not yet been translated into homogeneous 3D biomaterial scaffolds, and differences in NC behavior have been observed when moving from 2D culture systems to 3D culture systems^{108–111}. Current attempts at creating 3D biomaterial scaffolds from electrospun fiber are limited to layering a fiber mesh sandwiched between gels or in-between another biomaterial and NCs. While the bulk material is 3D, this method does not allow for cells to readily embed past a single layer in the z-direction because electrospun fiber meshes are generally too dense for deep cell infiltration. Cell infiltration into the fiber mesh can be improved by electrospinning sacrificial fibers alongside the main fiber material¹¹². The sacrificial fibers are dissolved in solution after electrospinning, leaving behind a more porous fiber mesh. Attempts at incorporating electrospun fibers into animal studies have not induced similar NC behavior as observed *in vitro*^{69,80–82}. The challenge for the field is to recapitulate the desired NC behavior observed on 2D fiber meshes into 3D biomaterial scaffolds. Collector topography has been used to pattern fiber scaffolds into more sophisticated patterns than simply aligning fibers^{67,113}, and may become a useful tool in creating a porous 3D fiber mesh. The alignment of fibers has the potential to direct NC process extensions *in vivo*, which has many applications like aligning neural synapses along a damaged SC. However, this potential using electrospun materials has yet to be realized in a 3D culture system. The problem can be tackled by either improving the porosity of the electrospun fibers, incorporating cells in the electrospinning process^{114,115}, or by combining electrospinning with another technique such as 3D bioprinting.

3D bioprinting has the most potential for developing tissue-like biomaterial scaffolds because it is an additive process. However, 3D bioprinting of scaffolds is currently limited by the available biomaterials. The printing process requires cytocompatible materials that exhibit yield stress and shear thinning rheological properties. Research has focused on blending biomaterials with materials that exhibit the desired rheological properties, or modifying biomaterials chemically. However, simple blending of materials and chemical modifications have many limitations. For example, the blend ratios have a drastic impact on the rheological properties of bioinks created by simply mixing materials. Adding a new protein or bioactive cue to the mixture may alter the rheological properties of the bioink enough to where it is no longer printable⁹⁵. Chemical modifications are limited to materials that have a well-defined chemical structure and materials such as collagen are challenging to modify reliably and repeatably. The current challenge is developing biomaterials with favorable properties for 3D printing. A universal way to tackle these issues is to use a sacrificial material to act as a mold to contain the biomaterial scaffold until it is solidified through crosslinking¹¹⁶. Using sacrificial materials allows for 3D printing a plethora of biomaterials with differing crosslinking kinetics but also slows down the printing process since the sacrificial material needs to be printed in conjunction to the desired biomaterial. The development of suitable biomaterials for 3D bioprinting will remain a challenge in the field for the foreseeable future.

A major challenge in tissue engineering is to develop microscale architectures that will lead to therapeutic treatments of CNS injury and disease. Microscale architecture can be used to spatially direct NC differentiation, process extensions, and migration. However, the field is uncertain as to how NC behavior should be directed and which NC line should be used for therapeutic treatments. For example, for repair of SC contusion injury it is important to replace

damaged neurons, but that is not the only cell type required to restore functionality. When designing a biomaterial scaffold, should NSC be directed solely towards a neuronal pathway or are other cell types, such as oligodendrocytes and/or astrocytes, also required? In addition, are NSC the best cell type to transplant or would a scaffold with several encapsulated NPC lines be more effective? Encapsulating NCs in biomaterial scaffolds with microscale architecture in an *in vitro* setting may help answer some of these questions. For example, in order to determine how NSC differentiation should be directed for transplant therapies it is important to investigate how each cell line remodels the ECM. However, the CNS ECM is complex, difficult to isolate intact and challenging to characterize. By immobilizing individual proteins onto a scaffold NC behavior can be investigated on an individual protein basis. Spatial control of NCs and proteins within biomaterial scaffolds will help create reductionist *in vitro* models of *in vivo* features such as the glial scar which may help elucidate the importance of specific interactions. A common challenge shared by research using all three techniques discussed here is the development of relevant microscale patterns. For example, can astrocytes, neurons and proteins be organized at the microscale level to mimic glial scar behavior *in vitro*? Currently there are few patterns that accomplish this because most research has focused on developing the capability to control microscale architecture and refining the resolution. Finding a clear link between microscale patterning techniques and physiological relevance remains a challenge for the neural tissue engineering field to meet. As the technical challenges of patterning biomaterial scaffolds at the microscale level are now being overcome, meaningful designs and patterns must be achieved that replicate the complicated architecture of native tissue in order to improve NC treatment therapies.

2.7. Funding

This work was supported by the University of Virginia, and the School of Engineering and Applied Science Research Innovation Award

2.8. References

- (1) Correale, J.; Farez, M. F. The Role of Astrocytes in Multiple Sclerosis. *Front. Neurol.* 2015, 6 (180), 1–12. <https://doi.org/10.3389/fneur.2015.00180>.
- (2) Krause, G. S.; White, B. C.; Aust, S. D.; Nayini, N. R.; Kumar, K. Brain Cell Death Following Ischemia and Reperfusion: A Proposed Biochemical Sequence. *Crit. Care Med.* 1988, 16 (7), 714–726.
- (3) White, B. C.; Sullivan, J. M.; DeGracia, D. J.; O’Neil, B. J.; Neumar, R. W.; Grossman, L. I.; Rafols, J. A.; Krause, G. S. Brain Ischemia and Reperfusion: Molecular Mechanisms of Neuronal Injury; 2000; Vol. 179. [https://doi.org/10.1016/S0022-510X\(00\)00386-5](https://doi.org/10.1016/S0022-510X(00)00386-5).
- (4) Lipinski, B. Hydroxyl Radical and Its Scavengers in Health and Disease. *Oxid. Med. Cell. Longev.* 2011, 2011. <https://doi.org/10.1155/2011/809696>.
- (5) Huang, L.; Wu, Z.; Zhuge, Q.; Zheng, W.; Shao, B.; Wang, B.; Sun, F. Glial Scar Formation Occurs in the Human Brain after Ischemic Stroke. *Int. J. Med. Sci.* 2014, 11, 344–348. <https://doi.org/10.7150/ijms.8140>.
- (6) Yuan, Y.-M.; He, C. The Glial Scar in Spinal Cord Injury and Repair. *Neurosci. Bull.* 2013, 29 (4), 421–435. <https://doi.org/10.1007/s12264-013-1358-3>.
- (7) Macaya, D.; Spector, M. Injectable Hydrogel Materials for Spinal Cord Regeneration: A Review. *Biomed. Mater.* 2012, 7 (1), 012001. <https://doi.org/10.1088/1748-6041/7/1/012001>.

- (8) Cooke, M. J.; Vulic, K.; Shoichet, M. S. Design of Biomaterials to Enhance Stem Cell Survival When Transplanted into the Damaged Central Nervous System. *Soft Matter* 2010, 6, 4988. <https://doi.org/10.1039/c0sm00448k>.
- (9) ARVIDSSON, A.; COLLIN, T.; KIRIK, D.; KOKAIA, Z.; LINDVALL, O. Neuronal Replacement from Endogenous Precursors in the Adult Brain after Stroke. *Nat Med* 2002, 8 (9), 963–970. <https://doi.org/10.1038/nm>.
- (10) Nakagomi, T.; Taguchi, A.; Fujimori, Y.; Saino, O.; Nakano-Doi, A.; Kubo, S.; Gotoh, A.; Soma, T.; Yoshikawa, H.; Nishizaki, T.; Nakagomi, N.; Stern, D. M.; Matsuyama, T. Isolation and Characterization of Neural Stem/Progenitor Cells from Post-Stroke Cerebral Cortex in Mice. *Eur. J. Neurosci.* 2009, 29 (9), 1842–1852. <https://doi.org/10.1111/j.1460-9568.2009.06732.x>.
- (11) Barnabé-Heider, F.; Göritz, C.; Sabelström, H.; Takebayashi, H.; Pfrieder, F. W.; Meletis, K.; Frisén, J. Origin of New Glial Cells in Intact and Injured Adult Spinal Cord. *Cell Stem Cell* 2010, 7 (4), 470–482. <https://doi.org/10.1016/j.stem.2010.07.014>.
- (12) Bakshi, A.; Keck, C. A.; Koshkin, V. S.; Lebold, D. G.; Siman, R.; Snyder, E. Y.; McIntosh, T. K. Caspase-Mediated Cell Death Predominates Following Engraftment of Neural Progenitor Cells into Traumatically Injured Rat Brain. *Brain Res.* 2005, 1065 (1–2), 8–19. <https://doi.org/10.1016/j.brainres.2005.09.059>.
- (13) Hill, C. E.; Moon, L. D. F.; Wood, P. M.; Bunge, M. B. Labeled Schwann Cell Transplantation: Cell Loss, Host Schwann Cell Replacement, and Strategies to Enhance Survival. *Glia* 2006, 53 (3), 338–343. <https://doi.org/10.1002/glia.20287>.
- (14) Walker, C. L.; Wang, X.; Bullis, C.; Liu, N.-K.; Lu, Q.; Fry, C.; Deng, L.; Xu, X.-M. Biphasic Bisperoxovanadium Administration and Schwann Cell Transplantation for Repair after Cervical

- Contusive Spinal Cord Injury. *Exp. Neurol.* 2015, 264, 163–172.
<https://doi.org/10.1016/j.expneurol.2014.12.002>.
- (15) Seaberg, R. M.; Van Der Kooy, D. Stem and Progenitor Cells: The Premature Desertion of Rigorous Definitions. *Trends Neurosci.* 2003, 26 (3), 125–131. [https://doi.org/10.1016/S0166-2236\(03\)00031-6](https://doi.org/10.1016/S0166-2236(03)00031-6).
- (16) Gordon, J.; Amini, S.; White, M. K. General Overview of Neuronal Cell Culture. *Methods Mol. Biol.* 2013, 1078, 1–6. <https://doi.org/10.1007/978-1-62703-640-5>.
- (17) Murry, C. E.; Keller, G. Differentiation of Embryonic Stem Cells to Clinically Relevant Populations: Lessons from Embryonic Development. *Cell* 2008, 132 (4), 661–680. <https://doi.org/10.1016/j.cell.2008.02.008>.
- (18) Politis, M.; Lindvall, O. Clinical Application of Stem Cell Therapy in Parkinson’s Disease. *BMC Med.* 2012, 10 (1), 1. <https://doi.org/10.1186/1741-7015-10-1>.
- (19) Dell’Albani, P. Stem Cell Markers in Gliomas. *Neurochem. Res.* 2008, 33 (12), 2407–2415. <https://doi.org/10.1007/s11064-008-9723-8>.
- (20) Shrestha, B.; Coykendall, K.; Li, Y.; Moon, A.; Priyadarshani, P.; Yao, L. Repair of Injured Spinal Cord Using Biomaterial Scaffolds and Stem Cells. *Stem Cell Res. Ther.* 2014, 1–11. <https://doi.org/10.1186/scrt480>.
- (21) Kaneko, A.; Matsushita, A.; Sankai, Y. A 3D Nanofibrous Hydrogel and Collagen Sponge Scaffold Promotes Locomotor Functional Recovery, Spinal Repair, and Neuronal Regeneration after Complete Transection of the Spinal Cord in Adult Rats. *Biomed. Mater.* 2015, 10 (1), 015008. <https://doi.org/10.1088/1748-6041/10/1/015008>.

- (22) King, V. R.; Henseler, M.; Brown, R. A.; Priestley, J. V. Mats Made from Fibronectin Support Oriented Growth of Axons in the Damaged Spinal Cord of the Adult Rat. *Exp. Neurol.* 2003, 182 (2), 383–398. [https://doi.org/10.1016/S0014-4886\(03\)00033-5](https://doi.org/10.1016/S0014-4886(03)00033-5).
- (23) King, V. R.; Phillips, J. B.; Hunt-Grubbe, H.; Brown, R.; Priestley, J. V. Characterization of Non-Neuronal Elements within Fibronectin Mats Implanted into the Damaged Adult Rat Spinal Cord. *Biomaterials* 2006, 27 (3), 485–496. <https://doi.org/10.1016/j.biomaterials.2005.06.033>.
- (24) Pritchard, C. D.; Slotkin, J. R.; Yu, D.; Dai, H.; Lawrence, M. S.; Bronson, R. T.; Reynolds, F. M.; Teng, Y. D.; Woodard, E. J.; Langer, R. S. Establishing a Model Spinal Cord Injury in the African Green Monkey for the Preclinical Evaluation of Biodegradable Polymer Scaffolds Seeded with Human Neural Stem Cells. *J. Neurosci. Methods* 2010, 188 (2), 258–269. <https://doi.org/10.1016/j.jneumeth.2010.02.019>.
- (25) Lu, P.; Wang, Y.; Graham, L.; McHale, K.; Gao, M.; Wu, D.; Brock, J.; Blesch, A.; Rosenzweig, E. S.; Havton, L. A.; Zheng, B.; Conner, J. M.; Marsala, M.; Tuszynski, M. H. Long-Distance Growth and Connectivity of Neural Stem Cells after Severe Spinal Cord Injury. *Cell* 2012, 150 (6), 1264–1273. <https://doi.org/10.1016/j.cell.2012.08.020>.
- (26) Dye, B. R.; Dedhia, P. H.; Miller, A. J.; Nagy, M. S.; White, E. S.; Shea, L. D.; Spence, J. R. A Bioengineered Niche Promotes in Vivo Engraftment and Maturation of Pluripotent Stem Cell Derived Human Lung Organoids. *Elife* 2016, 5 (September2016), 1–18. <https://doi.org/10.7554/eLife.19732>.
- (27) Lynam, D. A.; Shahriari, D.; Wolf, K. J.; Angart, P. A.; Koffler, J.; Tuszynski, M. H.; Chan, C.; Walton, P.; Sakamoto, J. Brain Derived Neurotrophic Factor Release from Layer-by-Layer Coated Agarose Nerve Guidance Scaffolds. *Acta Biomater.* 2015, 18, 128–131. <https://doi.org/10.1016/j.actbio.2015.02.014>.

- (28) Gunther, M. I.; Weidner, N.; Muller, R.; Blesch, A. Cell-Seeded Alginate Hydrogel Scaffolds Promote Directed Linear Axonal Regeneration in the Injured Rat Spinal Cord. *Acta Biomater.* 2015, 27, 140–150. <https://doi.org/10.1016/j.actbio.2015.09.001>.
- (29) Chedly, J.; Soares, S.; Montebault, A.; von Boxberg, Y.; Veron-Ravaille, M.; Mouffle, C.; Benassy, M. N.; Taxi, J.; David, L.; Nothias, F. Physical Chitosan Microhydrogels as Scaffolds for Spinal Cord Injury Restoration and Axon Regeneration. *Biomaterials* 2017, 138, 91–107. <https://doi.org/10.1016/j.biomaterials.2017.05.024>.
- (30) Jang, J.; Song, Y.; Yoo, D.; Ober, C. K.; Lee, J.; Lee, T. The Development of Fluorous Photolithographic Materials and Their Applications to Achieve Flexible Organic Electronic Devices. *Flex. Print. Electron.* 2016, 1 (2), 1–16. <https://doi.org/10.1088/2058-8585/1/2/023001>.
- (31) Wang, X.; Jiang, M.; Zhou, Z.; Gou, J.; Hui, D. 3D Printing of Polymer Matrix Composites: A Review and Prospective. *Compos. Part B Eng.* 2017, 110, 442–458. <https://doi.org/10.1016/j.compositesb.2016.11.034>.
- (32) Turunen, S.; Haaparanta, A.; Äänismaa, R.; Kellomäki, M. Chemical and Topographical Patterning of Hydrogels for Neural Cell Guidance in Vitro. *J. Tissue Eng. Regen. Med.* 2013, 7 (December 2011), 253–270. <https://doi.org/10.1002/term>.
- (33) Ciuciu, A. I.; Cywiński, P. J. Two-Photon Polymerization of Hydrogels-Versatile Solutions to Fabricate Well-Defined 3D Structures. *RSC Adv.* 2014, 4 (85), 45504–45516. <https://doi.org/10.1039/c4ra06892k>.
- (34) Dos Reis, G.; Fenili, F.; Gianfelice, A.; Bongiorno, G.; Marchesi, D.; Scopelliti, P. E.; Borgonovo, A.; Podestà, A.; Indrieri, M.; Ranucci, E.; Ferruti, P.; Lenardi, C.; Milani, P. Direct Microfabrication of Topographical and Chemical Cues for the Guided Growth of Neural Cell

- Networks on Polyamidoamine Hydrogels. *Macromol. Biosci.* 2010, 10 (8), 842–852. <https://doi.org/10.1002/mabi.200900410>.
- (35) Haring, A. P.; Sontheimer, H.; Johnson, B. N. Microphysiological Human Brain and Neural Systems-on-a-Chip: Potential Alternatives to Small Animal Models and Emerging Platforms for Drug Discovery and Personalized Medicine. *Stem Cell Rev. Reports* 2017, 13 (3), 381–406. <https://doi.org/10.1007/s12015-017-9738-0>.
- (36) Recknor, J. B.; Recknor, J. C.; Sakaguchi, D. S.; Mallapragada, S. K. Oriented Astroglial Cell Growth on Micropatterned Polystyrene Substrates. *Biomaterials* 2004, 25, 2753–2767. <https://doi.org/10.1016/j.biomaterials.2003.11.045>.
- (37) Oh, J.; Recknor, J. B.; Recknor, J. C.; Mallapragada, S. K.; Sakaguchi, D. S. Soluble Factors from Neocortical Astrocytes Enhance Neuronal Differentiation of Neural Progenitor Cells from Adult Rat Hippocampus on Micropatterned Polymer Substrates. *J. Biomed. Mater. Res.* 2008, 10–14. <https://doi.org/10.1002/jbm.a.32242>.
- (38) McCormick, A. M.; Maddipatla, M. V. S. N.; Shi, S.; Chamsaz, E. A.; Yokoyama, H.; Joy, A.; Leipzig, N. D. Micropatterned Coumarin Polyester Thin Films Direct Neurite Orientation. *ACS Appl. Mater. Interfaces* 2014, 6 (22), 19655–19667. <https://doi.org/10.1021/am5044328>.
- (39) Loubinoux, I.; Vaysse, L. Engineering of Adult Human Neural Stem Cells Differentiation through Surface Micropatterning. *Biomaterials* 2012, 33 (2), 504–514. <https://doi.org/10.1016/j.biomaterials.2011.09.073>.
- (40) Mattotti, M.; Alvarez, Z.; Ortega, J. A.; Planell, J. A.; Engel, E.; Alcántara, S. Inducing Functional Radial Glia-like Progenitors from Cortical Astrocyte Cultures Using Micropatterned PMMA. *Biomaterials* 2012, 33 (6), 1759–1770. <https://doi.org/10.1016/j.biomaterials.2011.10.086>.

- (41) Lee, M. K.; Rich, M. H.; Baek, K.; Lee, J.; Kong, H. Bioinspired Tuning of Hydrogel Permeability-Rigidity Dependency for 3D Cell Culture. *Sci. Rep.* 2015, 5, 8948. <https://doi.org/10.1038/srep08948>.
- (42) Hahn, M. S.; Taite, L. J.; Moon, J. J.; Rowland, M. C.; Ruffino, K. A.; West, J. L. Photolithographic Patterning of Polyethylene Glycol Hydrogels. *Biomaterials* 2006, 27 (12), 2519–2524. <https://doi.org/10.1016/j.biomaterials.2005.11.045>.
- (43) Huval, R. M.; Miller, O. H.; Curley, J. L.; Fan, Y.; Hall, B. J.; Moore, M. J. Microengineered Peripheral Nerve-on-a-Chip for Preclinical Physiological Testing. *Lab Chip* 2015, 15 (10), 2221–2232. <https://doi.org/10.1039/C4LC01513D>.
- (44) Luo, Y.; Shoichet, M. S. A Photolabile Hydrogel for Guided Three-Dimensional Cell Growth and Migration. *Nat. Mater.* 2004, 3 (4), 249–253. <https://doi.org/10.1038/nmat1092>.
- (45) Luo, Y.; Shoichet, M. S. Light-Activated Immobilization of Biomolecules to Agarose Hydrogels for Controlled Cellular Response. *Biomacromolecules* 2004, 5 (6), 2315–2323. <https://doi.org/10.1021/bm0495811>.
- (46) Musoke-Zawedde, P.; Shoichet, M. S. Anisotropic Three-Dimensional Peptide Channels Guide Neurite Outgrowth within a Biodegradable Hydrogel Matrix. *Biomed. Mater.* 2006, 1 (3), 162–169. <https://doi.org/10.1088/1748-6041/1/3/011>.
- (47) Hynd, M. R.; Frampton, J. P.; Burnham, M.-R.; Martin, D. L.; Dowell-mesfin, N.; Turner, J. N.; Shain, W. Functionalized Hydrogel Surfaces for the Patterning of Multiple Biomolecules. *J. Biomed. Mater. Res.* 2006, 347–354. <https://doi.org/10.1002/jbm.a>.
- (48) Hynd, M. R.; Frampton, J. P.; Dowell-mesfin, N.; Turner, J. N.; Shain, W. Directed Cell Growth on Protein Functionalized Hydrogel Surfaces. *J. Neurosci. Methods* 2009, 162, 255–263. <https://doi.org/10.1016/j.jneumeth.2007.01.024>. Directed.

- (49) Nagamine, K.; Hirata, T.; Okamoto, K.; Abe, Y.; Kaji, H.; Nishizawa, M. Portable Micropatterns of Neuronal Cells Supported by Thin Hydrogel Films. *ACS Biomater. Sci. Eng.* 2015, 1 (5), 329–334. <https://doi.org/10.1021/acsbiomaterials.5b00020>.
- (50) Curley, J. L.; Catig, G. C.; Horn-Ranney, E. L.; Moore, M. J. Sensory Axon Guidance with Semaphorin 6A and Nerve Growth Factor in a Biomimetic Choice Point Model. *Biofabrication* 2014, 6 (3), 35026. <https://doi.org/10.1088/1758-5082/6/3/035026>.
- (51) Horn-ranney, E. L.; Curley, J. L.; Catig, G. C.; Huval, R. M.; Michael, J. Structural and Molecular Micropatterning of Dual Hydrogel Constructs for Neural Growth Models Using Photochemical Strategies. *Biomed Microdevices* 2014, 15 (1), 49–61. <https://doi.org/10.1007/s10544-012-9687-y>.Structural.
- (52) DeForest, C. A.; Tirrell, D. A. A Photoreversible Protein-Patterning Approach for Guiding Stem Cell Fate in Three-Dimensional Gels. *Nat. Mater.* 2015, 14 (5), 523–531. <https://doi.org/10.1038/nmat4219>.
- (53) DeForest, C. A.; Anseth, K. S. Photoreversible Patterning of Biomolecules within Click-Based Hydrogels. *Angew. Chemie - Int. Ed.* 2012, 51 (8), 1816–1819. <https://doi.org/10.1002/anie.201106463>.
- (54) DeForest, C. A.; Anseth, K. S. Cytocompatible Click-Based Hydrogels with Dynamically Tunable Properties through Orthogonal Photoconjugation and Photocleavage Reactions. *Nat. Chem.* 2011, 3 (12), 925–931. <https://doi.org/10.1038/nchem.1174>.
- (55) Zhu, W.; Harris, B. T.; Zhang, L. G. Gelatin Methacrylamide Hydrogel with Graphene Nanoplatelets for Neural Cell - Laden 3D Bioprinting. *Eng. Med. Biol. Soc.* 2016, 4185–4188.

- (56) Jhaveri, S. J.; Senaratne, W.; Hynd, M. R.; Turner, J. N.; Sengupta, P.; Shain, W.; Ober, C. K. Defining the Biology-Materials Interface Using Both 2D and 3D Lithography. *J. Photopolym. Sci. Technol.* 2006, 19, 435–440.
- (57) Maruo, S.; Nakamura, O.; Kawata, S. Three-Dimensional Microfabrication with Two-Photon-Absorbed Photopolymerization. *Opt. Lett.* 1997, 22 (2), 132–134. <https://doi.org/10.1364/OL.22.000132>.
- (58) Hahn, M. S.; Miller, J. S.; West, J. L. Three-Dimensional Biochemical and Biomechanical Patterning of Hydrogels for Guiding Cell Behavior. *Adv. Mater.* 2006, No. 18, 2679–2684. <https://doi.org/10.1002/adma.200600647>.
- (59) Livnat, N.; Sarig-Nadir, O.; Zajdman, R.; Seliktar, D.; Shoham, S. A Hydrogel-Based Nerve Regeneration Conduit with Sub-Micrometer Feature Control. In *Proceedings of the 3rd International IEEE EMBS Conference on Neural Engineering*; Kohala Coast, HI, 2007; pp 101–103. <https://doi.org/10.1109/CNE.2007.369622>.
- (60) Seidlits, S. K.; Schmidt, C. E.; Shear, J. B. High-Resolution Patterning of Hydrogels in Three Dimensions Using Direct-Write Photofabrication for Cell Guidance. *Adv. Funct. Mater.* 2009, 19 (22), 3543–3551. <https://doi.org/10.1002/adfm.200901115>.
- (61) Kishan, A. P.; Cosgriff-Hernandez, E. M. Recent Advancements in Electrospinning Design for Tissue Engineering Applications: A Review. *J. Biomed. Mater. Res. - Part A* 2017, 105 (10), 2892–2905. <https://doi.org/10.1002/jbm.a.36124>.
- (62) Pham, Q. P.; Sharma, U.; Mikos, A. G. Electrospinning of Polymeric Nanofibers for Tissue Engineering Applications: A Review. *Tissue Eng.* 2006, 12 (5), 1197–1211. <https://doi.org/10.1089/ten.2006.12.1197>.

- (63) Matthews, J. A.; Wnek, G. E.; Simpson, D. G.; Bowlin, G. L. Electrospinning of Collagen Nanofibers. *Biomacromolecules* 2002, 3 (2), 232–238. <https://doi.org/10.1021/bm015533u>.
- (64) Li, D.; Wang, Y.; Xia, Y. Electrospinning Nanofibers as Uniaxially Aligned Arrays and Layer-by-Layer Stacked Films. *Adv. Mater.* 2004, 16 (4), 361–366. <https://doi.org/10.1002/adma.200306226>.
- (65) Orr, S. B.; Chainani, A.; Hippensteel, K. J.; Kishan, A.; Gilchrist, C.; Garrigues, N. W.; Ruch, D. S.; Guilak, F.; Little, D. Aligned Multilayered Electrospun Scaffolds for Rotator Cuff Tendon Tissue Engineering. *Acta Biomater.* 2015, 24, 117–126. <https://doi.org/10.1016/j.actbio.2015.06.010>.
- (66) Yang, D.; Lu, B.; Zhao, Y.; Jiang, X. Fabrication of Aligned Fibrous Arrays by Magnetic Electrospinning. *Adv. Mater.* 2007, 19 (21), 3702–3706. <https://doi.org/10.1002/adma.200700171>.
- (67) Dempsey, D. K.; Schwartz, C. J.; Ward, R. S.; Iyer, A. V.; Parakka, J. P.; Cosgriff-Hernandez, E. M. Micropatterning of Electrospun Polyurethane Fibers through Control of Surface Topography. *Macromol. Mater. Eng.* 2010, 295 (11), 990–994. <https://doi.org/10.1002/mame.201000152>.
- (68) Gerardo-Nava, J.; Führmann, T.; Klinkhammer, K.; Seiler, N.; Mey, J.; Klee, D.; Möller, M.; Dalton, P. D.; Brook, G. a. Human Neural Cell Interactions with Orientated Electrospun Nanofibers in Vitro. *Nanomedicine (Lond)*. 2009, 4 (1), 11–30. <https://doi.org/10.2217/17435889.4.1.11>.
- (69) Yao, S.; Liu, X.; Yu, S.; Wang, X.; Zhang, S.; Wu, Q.; Sun, X.; Mao, H. Co-Effects of Matrix Low Elasticity and Aligned Topography on Stem Cell Neurogenic Differentiation and Rapid Neurite Outgrowth. *Nanoscale* 2016, 8 (19), 10252–10265. <https://doi.org/10.1039/C6NR01169A>.

- (70) Xie, J.; MacEwan, M. R.; Willerth, S. M.; Li, X.; Moran, D. W.; Sakiyama-Elbert, S. E.; Xia, Y. Conductive Core-Sheath Nanofibers and Their Potential Application in Neural Tissue Engineering. *Adv. Funct. Mater.* 2009, 19 (14), 2312–2318. <https://doi.org/10.1002/adfm.200801904>.
- (71) Entekhabi, E.; Haghbin Nazarpak, M.; Moztarzadeh, F.; Sadeghi, A. Design and Manufacture of Neural Tissue Engineering Scaffolds Using Hyaluronic Acid and Polycaprolactone Nanofibers with Controlled Porosity. *Mater. Sci. Eng. C* 2016, 69, 380–387. <https://doi.org/10.1016/j.msec.2016.06.078>.
- (72) Ghasemi-Mobarakeh, L.; Prabhakaran, M. P.; Morshed, M.; Nasr-Esfahani, M. H.; Ramakrishna, S. Electrospun Poly(ϵ -Caprolactone)/Gelatin Nanofibrous Scaffolds for Nerve Tissue Engineering. *Biomaterials* 2008, 29 (34), 4532–4539. <https://doi.org/10.1016/j.biomaterials.2008.08.007>.
- (73) Aznar-Cervantes, S.; Pagán, A.; Martínez, J. G.; Bernabeu-Esclapez, A.; Otero, T. F.; Meseguer-Olmo, L.; Paredes, J. I.; Cenis, J. L. Electrospun Silk Fibroin Scaffolds Coated with Reduced Graphene Promote Neurite Outgrowth of PC-12 Cells under Electrical Stimulation. *Mater. Sci. Eng. C* 2017, 79, 315–325. <https://doi.org/10.1016/j.msec.2017.05.055>.
- (74) Christopherson, G. T.; Song, H.; Mao, H. Q. The Influence of Fiber Diameter of Electrospun Substrates on Neural Stem Cell Differentiation and Proliferation. *Biomaterials* 2009, 30 (4), 556–564. <https://doi.org/10.1016/j.biomaterials.2008.10.004>.
- (75) Lee, S.; Leach, M. K.; Redmond, S. A.; Chong, S. Y. C.; Mellon, S. H.; Tuck, S. J.; Feng, Z.-Q.; Corey, J. M.; Chan, J. R. A Culture System to Study Oligodendrocyte Myelination Processes Using Engineered Nanofibers. *Nat. Methods* 2012, 9 (9), 917–922. <https://doi.org/10.1038/nmeth.2105>.

- (76) Hyysalo, A.; Ristola, M.; Joki, T.; Honkanen, M.; Vippola, M.; Narkilahti, S. Aligned Poly(ϵ -Caprolactone) Nanofibers Guide the Orientation and Migration of Human Pluripotent Stem Cell-Derived Neurons, Astrocytes, and Oligodendrocyte Precursor Cells In Vitro. *Macromol. Biosci.* 2017, 17 (7), 1–8. <https://doi.org/10.1002/mabi.201600517>.
- (77) Lee, S.; Nowicki, M.; Harris, B.; Zhang, L. G. Fabrication of a Highly Aligned Neural Scaffold via a Table Top Stereolithography 3D Printing and Electrospinning. *Tissue Eng. Part A* 2017, 23 (11–12), 491–502. <https://doi.org/10.1089/ten.tea.2016.0353>.
- (78) McMurtrey, R. J. Patterned and Functionalized Nanofiber Scaffolds in Three-Dimensional Hydrogel Constructs Enhance Neurite Outgrowth and Directional Control. *J. Neural Eng.* 2014, 11 (6), 066009. <https://doi.org/10.1088/1741-2560/11/6/066009>.
- (79) Weightman, A.; Jenkins, S.; Pickard, M.; Chari, D.; Yang, Y. Alignment of Multiple Glial Cell Populations in 3D Nanofiber Scaffolds: Toward the Development of Multicellular Implantable Scaffolds for Repair of Neural Injury. *Nanomedicine Nanotechnology, Biol. Med.* 2014, 10 (2), 291–295. <https://doi.org/10.1016/j.nano.2013.09.001>.
- (80) Milbreta, U.; Nguyen, L. H.; Diao, H.; Lin, J.; Wu, W.; Sun, C. Y.; Wang, J.; Chew, S. Y. Three-Dimensional Nanofiber Hybrid Scaffold Directs and Enhances Axonal Regeneration after Spinal Cord Injury. *ACS Biomater. Sci. Eng.* 2016, 2 (8), 1319–1329. <https://doi.org/10.1021/acsbiomaterials.6b00248>.
- (81) Sanders, J. E.; Lamont, S. E.; Karchin, A.; Golledge, S. L.; Ratner, B. D. Fibro-Porous Meshes Made from Polyurethane Micro-Fibers: Effects of Surface Charge on Tissue Response. *Biomaterials* 2005, 26 (7), 813–818. <https://doi.org/10.1016/j.biomaterials.2004.03.030>.
- (82) Wang, T. Y.; Bruggeman, K. F.; Kauhausen, J. A.; Rodriguez, A. L.; Nisbet, D. R.; Parish, C. L. Functionalized Composite Scaffolds Improve the Engraftment of Transplanted Dopaminergic

- Progenitors in a Mouse Model of Parkinson's Disease. *Biomaterials* 2016, 74, 89–98.
<https://doi.org/10.1016/j.biomaterials.2015.09.039>.
- (83) Murphy, S. V; Atala, A. 3D Bioprinting of Tissues and Organs. *Nat. Biotechnol.* 2014, 32 (8), 773–785. <https://doi.org/10.1038/nbt.2958>.
- (84) Ratheesh, G.; Venugopal, J. R.; Chinappan, A.; Ezhilarasu, H.; Sadiq, A.; Ramakrishna, S. 3D Fabrication of Polymeric Scaffolds for Regenerative Therapy. *ACS Biomaterials Science and Engineering*. 2017, pp 1175–1194. <https://doi.org/10.1021/acsbmaterials.6b00370>.
- (85) Johnson, B. N.; Lancaster, K. Z.; Hogue, I. B.; Meng, F.; Kong, Y. L.; Enquist, L. W.; Mcalpine, M. C. 3D Printed Nervous System on a Chip. *Lab Chip* 2016, 16 (3), 1393–1400. <https://doi.org/10.1039/C5LC01270H>.
- (86) Cui, X.; Dean, D.; Ruggeri, Z. M.; Boland, T. Cell Damage Evaluation of Thermal Inkjet Printed Chinese Hamster Ovary Cells. *Biotechnol. Bioeng.* 2010, 106 (6), 963–969. <https://doi.org/10.1002/bit.22762>.
- (87) Chang, R.; Nam, J.; Sun, W. Effects of Dispensing Pressure and Nozzle Diameter on Cell Survival from Solid Freeform Fabrication–Based Direct Cell Writing. *Tissue Eng. Part A* 2008, 14 (1), 41–48. <https://doi.org/10.1089/ten.a.2007.0004>.
- (88) Cui, X.; Boland, T.; D'Lima, D. D.; Lotz, M. K. Thermal Inkjet Printing in Tissue Engineering and Regenerative Medicine. *Recent Pat Drug Deliv Formul* 2012, 6 (2), 149–155. <https://doi.org/10.1086/498510.Parasitic>.
- (89) Smith, C. M.; Stone, A. L.; Parkhill, R. L.; Stewart, R. L.; Simpkins, M. W.; Kachurin, A. M.; Warren, W. L.; Williams, S. K. Three-Dimensional BioAssembly Tool for Generating Viable Tissue-Engineered Constructs. *Tissue Eng.* 2004, 10 (9–10), 1566–1576. <https://doi.org/10.1089/ten.2004.10.1566>.

- (90) Truby, R. L.; Lewis, J. A. Printing Soft Matter in Three Dimensions. *Nature* 2016, 540 (7633), 371–378. <https://doi.org/10.1038/nature21003>.
- (91) Malek, S.; Raney, J. R.; Lewis, J. A.; Gibson, L. J. Lightweight 3D Cellular Composites Inspired by Balsa. *Bioinspir. Biomim.* 2017, 12 (2), 026014. <https://doi.org/10.1088/1748-3190/aa6028>.
- (92) Siqueira, G.; Kokkinis, D.; Libanori, R.; Hausmann, M. K.; Gladman, A. S.; Neels, A.; Tingaut, P.; Zimmermann, T.; Lewis, J. A.; Studart, A. R. Cellulose Nanocrystal Inks for 3D Printing of Textured Cellular Architectures. *Adv. Funct. Mater.* 2017, 27 (12). <https://doi.org/10.1002/adfm.201604619>.
- (93) Thakur, A.; Jaiswal, M. K.; Peak, C. W.; Carrow, J. K.; Gentry, J.; Dolatshahi-Pirouz, A.; Gaharwar, A. K. Injectable Shear-Thinning Nanoengineered Hydrogels for Stem Cell Delivery. *Nanoscale* 2016, 8 (24), 12362–12372. <https://doi.org/10.1039/C6NR02299E>.
- (94) Diamantides, N.; Wang, L.; Pruiksma, T.; Siemiatkoski, J.; Dugopolski, C.; Shortkroff, S.; Kennedy, S.; Bonassar, L. J. Correlating Rheological Properties and Printability of Collagen Bioinks: The Effects of Riboflavin Photocrosslinking and PH. *Biofabrication* 2017, 9 (3), 034102. <https://doi.org/10.1088/1758-5090/aa780f>.
- (95) Kim, J. Y.; Park, E. K.; Kim, S.; Shim, J.; Kim, J. Y.; Park, M.; Park, J.; Cho, D. Development of a Hybrid Scaffold with Synthetic Biomaterials and Hydrogel Using Solid Freeform Fabrication Technology. *Biofabrication* 2011, 3. <https://doi.org/10.1088/1758-5082/3/3/034102>.
- (96) Lee, W.; Pinckney, J.; Lee, V.; Lee, J.; Fischer, K.; Polio, S.; Park, J.; Yoo, S. Three-Dimensional Bioprinting of Rat Embryonic Neural Cells. *Neuroreport* 2009, 20 (8), 798–803. <https://doi.org/10.1097/WNR.0b013e32832b8be4>.
- (97) Gu, Q.; Tomaskovic-Crook, E.; Lozano, R.; Chen, Y.; Kapsa, R. M.; Zhou, Q.; Wallace, G. G.; Crook, J. M. Functional 3D Neural Mini-Tissues from Printed Gel-Based Bioink and Human

- Neural Stem Cells. *Adv. Healthc. Mater.* 2016, 5 (12), 1429–1438.
<https://doi.org/10.1002/adhm.201600095>.
- (98) Dai, X.; Ma, C.; Lan, Q.; Xu, T. 3D Bioprinted Glioma Stem Cells for Brain Tumor Model and Applications of Drug Susceptibility. *Biofabrication* 2016, 8 (4), 045005.
<https://doi.org/10.1088/1758-5090/8/4/045005>.
- (99) Alessandri, K.; Feyeux, M.; Gurchenkov, B.; Delgado, C.; Trushko, A.; Krause, K.-H.; Vignjević, D.; Nassoy, P.; Roux, A. A 3D Printed Microfluidic Device for Production of Functionalized Hydrogel Microcapsules for Culture and Differentiation of Human Neuronal Stem Cells (HNSC). *Lab Chip* 2016, 16 (9), 1593–1604. <https://doi.org/10.1039/C6LC00133E>.
- (100) Lu, H. D.; Charati, M. B.; Kim, I. L.; Burdick, J. A. Injectable Shear-Thinning Hydrogels Engineered with a Self-Assembling Dock-and-Lock Mechanism. *Biomaterials* 2012, 33 (7), 2145–2153. <https://doi.org/10.1016/j.biomaterials.2011.11.076>.
- (101) Ouyang, L.; Highley, C. B.; Rodell, C. B.; Sun, W.; Burdick, J. A. 3D Printing of Shear-Thinning Hyaluronic Acid Hydrogels with Secondary Cross-Linking. *ACS Biomater. Sci. Eng.* 2016, 2 (10), 1743–1751. <https://doi.org/10.1021/acsbomaterials.6b00158>.
- (102) Shepherd, J. N. H.; Parker, S. T.; Shepherd, R. F.; Gillette, M. U.; Lewis, J. A.; Nuzzo, R. G. 3D Microperiodic Hydrogel Scaffolds for Robust Neuronal Cultures. *Adv. Funct. Mater.* 2012, 61 (1), 47–54. <https://doi.org/10.1002/adfm.201001746.3D>.
- (103) Lozano, R.; Stevens, L.; Thompson, B. C.; Gilmore, K. J.; Gorkin, R.; Stewart, E. M.; in het Panhuis, M.; Romero-Ortega, M.; Wallace, G. G. 3D Printing of Layered Brain-like Structures Using Peptide Modified Gellan Gum Substrates. *Biomaterials* 2015, 67 (August), 264–273.
<https://doi.org/10.1016/j.biomaterials.2015.07.022>.

- (104) Lin, H.; Hsieh, F.; Tseng, C.; Hsu, S. Preparation and Characterization of a Biodegradable Polyurethane Hydrogel and the Hybrid Gel with Soy Protein for 3D Cell-Laden Bioprinting. *J. Mater. Chem. B* 2016, 4 (41), 6694–6705. <https://doi.org/10.1039/C6TB01501H>.
- (105) Hsieh, F. Y.; Lin, H. H.; Hsu, S. hui. 3D Bioprinting of Neural Stem Cell-Laden Thermoresponsive Biodegradable Polyurethane Hydrogel and Potential in Central Nervous System Repair. *Biomaterials* 2015, 71, 48–57. <https://doi.org/10.1016/j.biomaterials.2015.08.028>.
- (106) Yi, H.; Choi, Y.; Kang, K. S.; Hong, J. M.; Pati, R. G.; Park, M. N.; Shim, I. K.; Lee, C. M.; Kim, S. C.; Cho, D. A 3D-Printed Local Drug Delivery Patch for Pancreatic Cancer Growth Suppression. *J. Control. Release* 2016, 238, 231–241. <https://doi.org/10.1016/j.jconrel.2016.06.015>.
- (107) Lee, Y. B.; Polio, S.; Lee, W.; Dai, G.; Menon, L.; Carroll, R. S.; Yoo, S. S. Bio-Printing of Collagen and VEGF-Releasing Fibrin Gel Scaffolds for Neural Stem Cell Culture. *Exp. Neurol.* 2010, 223 (2), 645–652. <https://doi.org/10.1016/j.expneurol.2010.02.014>.
- (108) Shin, Y.; Yang, K.; Han, S.; Park, H. J.; Heo, Y. S.; Cho, S. W.; Chung, S. Reconstituting Vascular Microenvironment of Neural Stem Cell Niche in Three-Dimensional Extracellular Matrix. *Adv. Healthc. Mater.* 2014, 3 (9), 1457–1464. <https://doi.org/10.1002/adhm.201300569>.
- (109) Park, J. W.; Kang, Y. D.; Kim, J. S.; Lee, J. H.; Kim, H. W. 3D Microenvironment of Collagen Hydrogel Enhances the Release of Neurotrophic Factors from Human Umbilical Cord Blood Cells and Stimulates the Neurite Outgrowth of Human Neural Precursor Cells. *Biochem. Biophys. Res. Commun.* 2014, 447 (3), 400–406. <https://doi.org/10.1016/j.bbrc.2014.03.145>.
- (110) Lampe, K. J.; Bjugstad, K. B.; Mahoney, M. J. Impact of Degradable Macromer Content in a Poly (Ethylene Glycol) Hydrogel on Neural Cell Metabolic Activity, Redox State, Proliferation, and Differentiation. *Tissue Engineering part A.* 2010, 16 (6), 1857–1866.

- (111) Bozza, A.; Coates, E. E.; Incitti, T.; Ferlin, K. M.; Messina, A.; Menna, E.; Bozzi, Y.; Fisher, J. P.; Casarosa, S. Neural Differentiation of Pluripotent Cells in 3D Alginate-Based Cultures. *Biomaterials* 2014, 35 (16), 4636–4645. <https://doi.org/10.1016/j.biomaterials.2014.02.039>.
- (112) Baker, B. M.; Gee, A. O.; Metter, R. B.; Nathan, A. S.; Marklein, R. A.; Burdick, J. A.; Mauck, R. L. The Potential to Improve Cell Infiltration in Composite Fiber-Aligned Electrospun Scaffolds by the Selective Removal of Sacrificial Fibers. *Biomaterials* 2008, 29 (15), 2348–2358. <https://doi.org/10.1016/j.biomaterials.2008.01.032>.
- (113) Kishan, A. P.; Robbins, A. B.; Mohiuddin, S. F.; Jiang, M.; Moreno, M. R.; Cosgriff-Hernandez, E. M. Fabrication of Macromolecular Gradients in Aligned Fiber Scaffolds Using a Combination of In-Line Blending and Air-Gap Electrospinning. *Acta Biomater.* 2017, 56, 118–128. <https://doi.org/10.1016/j.actbio.2016.12.041>.
- (114) Zanatta, G.; Steffens, D.; Braghirolli, D. I.; Fernandes, R. A.; Netto, C. A.; Pranke, P. Viability of Mesenchymal Stem Cells during Electrospinning. *Brazilian J. Med. Biol. Res.* 2012, 45 (2), 125–130. <https://doi.org/10.1590/S0100-879X2011007500163>.
- (115) Stankus, J. J.; Guan, J.; Fujimoto, K.; Wagner, W. R. Microintegrating Smooth Muscle Cells into a Biodegradable Elastomeric Fiber Matrix. *Biomaterials* 2006, 27 (5), 735–744. <https://doi.org/10.1002/nbm.3066>. Non-invasive.
- (116) Hinton, T. J.; Jallerat, Q.; Palchesko, R. N.; Park, J. H.; Grodzicki, M. S.; Shue, H.-J.; Ramadan, M. H.; Hudson, A. R.; Feinberg, A. W. Three-Dimensional Printing of Complex Biological Structures by Freeform Reversible Embedding of Suspended Hydrogels. *Sci. Adv.* 2015, 1 (9), e1500758–e1500758. <https://doi.org/10.1126/sciadv.1500758>.

3. Impact of Elastin-like Protein Temperature Transition on PEG-ELP Hybrid Hydrogel Properties

Published as: E. Meco, KJ Lampe, “Impact of Elastin-like Protein Temperature Transition on PEG-ELP Hybrid Hydrogel Properties,” *Biomacromolecules*, 50, 5:1914-1925 (2019)

3.1. Abstract

Biomaterial hydrogels are made by crosslinking either natural materials, which exhibit inherent bioactivity but suffer from batch-to-batch variations, or synthetic materials, which have a well-defined chemical structure but usually require chemical modification to exhibit bioactivity. Recombinant engineered proteins bridge the divide between natural and synthetic materials because proteins incorporate bioactive domains within the biopolymer backbone and have a well-defined amino acid structure and sequence. Recombinant engineered elastin-like proteins (ELPs) are modeled from the native tropoelastin sequence. ELPs are composed of repeating VPGxG penta-peptide sequences, where x is any guest residue except proline. ELPs undergo a lower critical solution temperature (LCST) transition above which they aggregate into a coacervate phase in aqueous solution. Here we show that the LCST transition impacts hydrogel micro-architecture which may serve as a useful design feature in engineering ELP-based hydrogels. We investigate how the ELP LCST transition contributes to the properties of hybrid poly(ethylene glycol) (PEG) and ELP (PEG-ELP) hydrogels. PEG-ELP hydrogels gelled below the LCST have a homogeneous distribution of ELP, while gelling above the LCST results in the formation of spherical ELP-rich regions within the bulk hydrogel. The ELP-rich micro-architecture is maintained when an amine-reactive crosslinker is incorporated during the gelation process. The formation of ELP-rich regions reduces PEG-ELP hydrogel bulk stiffness and increases optical density. Our characterizations of

hydrogels created by using the LCST transition provide design criteria for incorporating microscale features. This may be a useful technique in understanding the role of localized bioactivity at the microscale level within hydrogel systems.

3.2. Introduction

Developing three-dimensional (3D) biomaterial scaffolds for tissue engineering applications is of significant interest. Biomaterial scaffolds implanted into spinal cord injury and myocardial infarction have improved endogenous cell infiltration and functional recovery¹⁻⁹. Biomaterial scaffolds can be made by crosslinking either natural materials, such as collagen and fibrin, or synthetic polymers, such as poly(ethylene glycol) (PEG) and polyacrylamide. Natural materials display inherent bioactivity, but suffer from batch-to-batch variations stemming from different sources and animal species¹⁰⁻¹². Synthetic materials have a well-defined chemical structure but display limited bioactivity, and require chemical modification to incorporate bioactive cues into the polymer backbone^{13,14}. Recombinant engineered proteins bridge the divide between natural and synthetic materials because they are derived from native proteins, but have a well-defined amino acid structure¹⁵⁻¹⁷. The tightly controlled transcription and translation process creates a monodisperse protein primary structure. Bioactive cues engineered into the amino acid backbone eliminate the need for post-expression modifications, such as the addition of integrin-binding peptide sequences, to induce cell-matrix interactions^{10,18}.

Recombinant engineered elastin-like proteins (ELPs) have applications in many tissue types: cartilage, liver, ocular, spinal cord and heart^{10,19,20}. The ELP amino acid sequence is derived from tropoelastin, which provides extensibility in connective tissue, and consist of repeating units of the penta-peptide sequence valine-proline-glycine-guest residue-glycine (VPGxG), where the guest residue can be any amino acid except for proline^{21,22}. ELPs are soluble in aqueous solution,

but exhibit a lower critical solution temperature (LCST) transition when heated^{18,22-24}. Upon heating above their transition temperature (T_t) ELPs aggregate into a protein rich coacervate phase^{18,22-26}. The LCST transition allows for purification of large ELP quantities without the need for chromatographic techniques, and has been successfully used to purify growth factors conjugated with ELPs, while maintaining some growth factor bioactivity^{27,28}. Temperature-induced self-assembling nanoparticles for drug delivery applications can be created by utilizing the ELP LCST transition²⁸⁻³⁰. Incorporating bioactive amino acid sequences into the ELP primary structure allows cells to adhere to the ELP matrix and/or enzymatically degrade it¹⁸. Both physical properties and bioactive cues of the biomaterial scaffold affect cell-matrix interactions, making it difficult to isolate the effects of individual properties³¹⁻³⁴. Crosslinking ELPs using different bioactive sequences in the amino acid structure while retaining the majority of the protein primary structure allows for tuning the concentration of bioactive cues independently from the hydrogel physical properties¹⁸. The advantages of having 1) a known primary protein structure, 2) bioactive cues in the amino acid backbone, 3) easy purification of large protein quantities, and 4) independent tuning of physical properties and biochemical cues, makes ELPs an ideal material for *in vitro* tissue engineering models.

Recombinant protein-based biomaterial scaffold properties can be further tuned by incorporating PEG macromers. PEG macromers resist protein adsorption and are adaptable to a wide variety of crosslinking chemistries^{20,35-40}. The structural properties and degradation of protein-based biomaterial scaffolds can be tuned by incorporating PEG either through PEGylation or during crosslinking⁴¹⁻⁴³. ELP-based biomaterial scaffolds are optically dense, making it difficult to image cellular behavior deeper than ~ 100 μm past the surface using light microscopy techniques⁴⁴. The combination of PEG with ELP for hydrogel formation improves the optical

properties of ELP-based hydrogels, allowing for imaging of cellular behavior deeper into the biomaterial scaffolds⁴⁴. In addition, PEG and ELP (PEG-ELP) hybrid hydrogels are highly extensible, reaching strains as high as 1500 %, and very resilient, with elastic recovery of 80-95 %⁴⁴. Incorporating PEG into recombinant engineered resilin-like protein (RLP) hydrogels increased the shear storage and Young's moduli, and altered hydrogel micro-architecture^{35,45,46}. Crosslinking RLP with PEG resulted in the formation of RLP-rich microstructures with 10-100 μm diameters when the molecular weight of the PEG macromer used was at least ~ 10 kDa⁴⁶.

The incorporation of micro-architecture into hydrogel systems impacts cellular behavior in *in vitro* and *in vivo* settings. Cellular infiltration into a thoracic (T8-T9) rat spinal cord bilateral dorsal hemisection injury filled with fragmented chitosan hydrogels was largely dependent on the average fragment micron size⁴⁷. Current methods to control local, micro- and nanoscale level, bioactivity within hydrogel systems utilize techniques such as electrospinning, photolithography, or 3D bioprinting⁴⁸⁻⁵⁰. Electrospinning ELP solutions allowed for the design of a fiber mesh with controllable arginine-glycine-aspartate (RGD) adhesive sequence clustering within micron sized fibers while maintaining a constant RGD concentration in the fiber mesh^{50,51}. Cellular proliferation was enhanced on the electrospun ELP fiber mesh when RGD was more densely clustered together^{50,51}. However, the processing steps of these techniques require stringent material properties, and are not ideal for controlling the micro-architecture of many biomaterial scaffold systems. Other methods to control micro-architecture of biomaterial scaffold systems would offer new design tools to guide material properties and perhaps, cellular interactions.

Designing biomaterial scaffolds with multiple chemically distinct hydrogel networks results in unique physical properties. Most improvements of protein-based hydrogel properties are achieved by incorporating PEG into a single crosslinking scheme. However, biomaterial scaffolds

can also be made by combining multiple chemically distinct hydrogel networks. Double-network biomaterial scaffolds made through the entanglement of two distinct networks have high extensibility, undergo viscoelastic deformation, and exhibit self-healing structural properties⁵¹⁻⁵³. Single-network scaffolds undergo elastic deformation, and have drastic losses in strength and extensibility due to defects that occur during the gelation process⁵⁴. For tissue engineering applications the structural properties of single-network hydrogels are altered when cells, proteins, and nanoparticles are incorporated into the pre-crosslinked solution. In addition, native tissue is viscoelastic and undergoes stress relaxation when under strain, so the elastic deformation behavior observed in single-network hydrogels do not adequately capture the properties of native tissue⁵⁵. ELP behavior in double-network hydrogel systems has not been investigated, but the inherent extensibility of ELPs and the unique temperature dependent behavior make it an interesting material for tissue engineering applications.

Here we describe the formation of PEG and ELP (PEG-ELP) double-network hydrogels by crosslinking PEG-dimethacrylate (PEGMA) using ultraviolet light (UV) photoinitiation, and crosslinking ELP using Mannich-type condensation with tetrakis(hydroxymethyl) phosphonium chloride (THPC) crosslinker. The ELP sequence used in this study has a T_t between room temperature and 37°C, and contains lysine residues for the crosslinking reaction with THPC (Figure 3-1)^{18,56}. We investigate how the ELP LCST phase transition affects PEG-ELP double-network hydrogel physical properties when gelation occurs below and above the ELP LCST transition (Figure 3-2). The formation and retention of PEG-ELP double-network hydrogel micro-architecture was compared to hybrid PEG-ELP hydrogels, where ELP was not crosslinked with THPC. ELP leaching from PEG-ELP hydrogels was assessed with the Bradford protein assay and fit to a Fickian diffusion model. PEG-ELP hydrogel stiffness was analyzed using small angle

oscillatory shear rheology and optical density properties were assessed through absorbance measurements. We demonstrate that the physical properties of ELP-based hydrogels are affected by the formation of micro-architecture caused by inducing gelation above the ELP T_t . The unique ELP LCST transition property may be a useful design feature in engineering ELP-based. This work documents how two physically distinct hydrogel systems can be created using the same starting materials by performing gelation at temperatures above and below the ELP LCST transition.

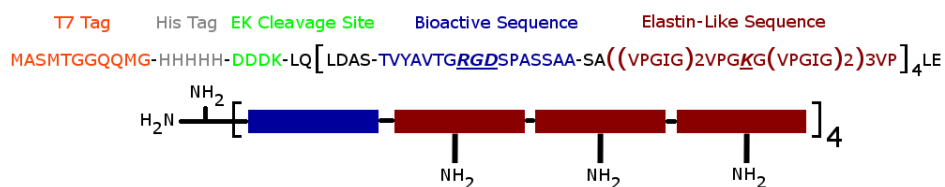


Figure 3-1: Elastin-Like protein amino acid sequence and illustration of primary amines available for crosslinking with tetrakis(hydroxymethyl) phosphonium chloride (THPC).

3.3. Materials and Methods

3.3.1. Methacrylation of poly(ethylene glycol)

Poly(ethylene glycol) (PEG, 6,000 Molecular weight (Mn), Sigma Aldrich) was methacrylated with 73 % modification efficiency using the microwave-assisted method described previously⁵⁷. Purification of PEGMA was performed with few modifications. Briefly, PEGMA was dissolved in dichloromethane, precipitated in ice-cold ethyl ether (10:1 v/v ratio), filtered using a Buchner funnel and flask, and dried using a vacuum pump with a solvent trap. Afterwards, PEGMA was dissolved in deionized (DI) water (5 wt%), dialyzed with cellulose ester (CE) tubing (500 – 1,000 Da MWCO, Biotech), frozen at -80°C overnight and lyophilized. Methacrylate

functionalization was quantified using proton nuclear magnetic resonance (HNMR), as previously described, with a 500 MHz spectrometer⁵⁷.

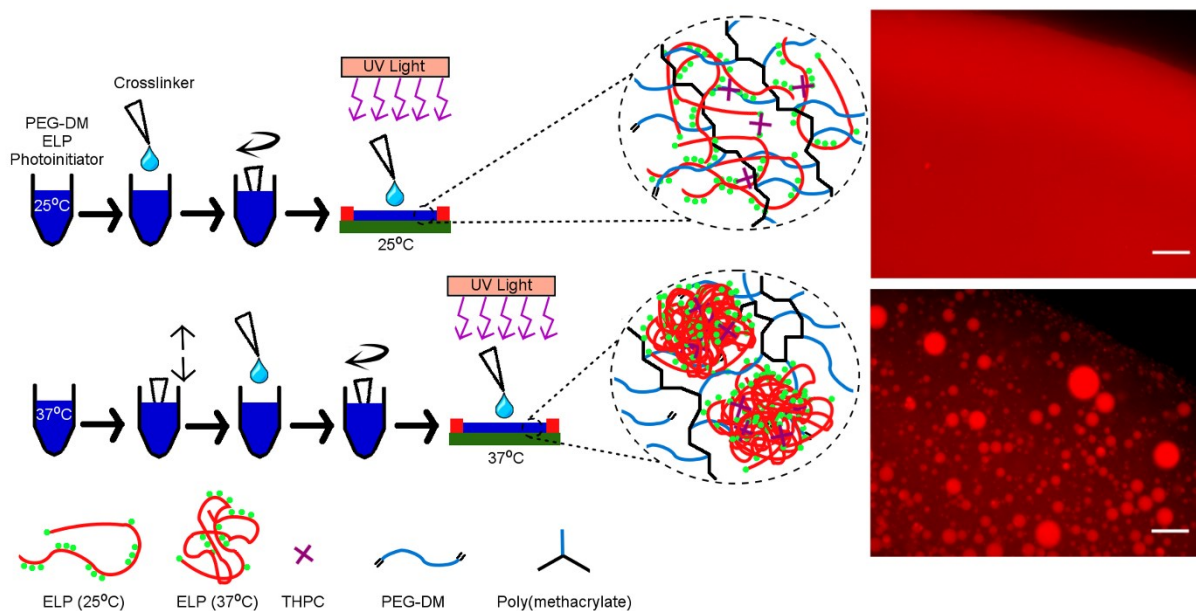


Figure 3-2: Schematic of PEG and ELP hydrogel gelation at 25 and 37°C. Representative images of PEG-ELP hydrogels after gelation, showing TRITC labeled ELP (red). Scale bars = 100 μm.

3.3.2. Elastin-like protein expression

ELP expression was induced in *Escherichia coli* using β -isopropyl thiogalactoside (IPTG) as previously described with a few modifications¹⁸. *Escherichia coli* cultures were allowed to express for 6-8 hours post IPTG induction. Cell cultures were spun down for 10 minutes at 7,000 rpm and 4°C. The cell pellet was suspended in TEN buffer (25 g/ml) and frozen at -80°C overnight. The cell solution was thawed, and a small amount of deoxyribonuclease 1 (DNase, Sigma Aldrich) and phenylmethylsulfonyl fluoride (PMSF) to a final concentration of 1 mM were added. Freeze-thaw cycles were repeated two more times without further addition of DNase or PMSF. The cell lysate pH was adjusted to 9 using NaOH and agitated at 4°C for at least 1 hour. Afterwards it was

centrifuged at 4°C and 10,000 rpm for 1 hour. The supernatant was collected, NaCl was added to a final concentration of 1 M, and the solution was agitated at 37°C and 250 rpm for at least 3 hours. Afterwards it was centrifuged at 37°C and 10,000 rpm for 1 hour. The pellet was collected, dissolved in sterile DI water (0.1 g/ml), and agitated overnight at 4°C. Hot and cold centrifugation cycles were repeated 2 more times. The protein solution was centrifuged at 4°C and 10,000 rpm for 1 hour. The supernatant was collected and dialyzed using CE tubing (3.5 – 5 kDa MWCO, Biotech). Dialyzed solutions were frozen at -80°C overnight and lyophilized. ELP purity was determined using SDS-PAGE. Protein yields of 50 – 80 mg/L were achieved.

3.3.3. *Optical density analysis*

Stock solutions of PEGMA, ELP and lithium phenyl-2,4,6-trimethylbenzoylphosphinate (LAP) were mixed to a final concentration of 6 wt/v% PEGMA, varying ELP concentrations and 0.05 wt/v% LAP⁵⁸. When the ELP crosslinker THPC was included, it was at a 2:1 ratio of primary amines on ELP to hydroxymethyl groups on THPC. 80 µl solutions were pipetted into a 96-well plate and gelled for 10 minutes under UV-light (365nm, 15W). 40 µl phosphate buffered saline (PBS) was pipetted on top of each hydrogel to prevent dehydration and 120 µl PBS was used as a control. Absorbance was measured at 500 nm. After the initial reading, samples were incubated for 1 hour at the next designated temperature before the next measurement.

Gelation at 37°C was performed by incubating stock solutions at 37°C for at least 30 minutes. The ELP solution phase separated and was triturated before mixing into the gel precursor solution. Gelation was induced by exposing the gel solution to 10 minutes of UV-light at 37°C.

3.3.4. Analysis of ELP domains

ELP was labeled with tetramethylrhodamine isothiocyanate (Thermo Fisher) as previously described⁴⁶. Fluorescently tagged ELP was mixed with unlabeled ELP at a 1:19 weight ratio (labeled:unlabeled) to form the stock ELP solution. Gelation of PEG and ELP hydrogels was performed as described above.

Images were taken on a Zeiss Axio Observer fluorescent microscope using dsRed filter set 43. Analysis of ELP domains was performed on ImageJ. Huang thresholding was used to convert raw images to binary and watershed used to segment overlaying ELP domains. Analysis was performed with constraints of particle size greater than 4 μm , particle circularity between 0.5 – 1, and ELP-rich regions on the picture edges were excluded. ELP domains that were not split accurately using watershed were manually removed from the calculations. Area, perimeter, Feret diameter, and minimum Feret diameter were quantified for 6 hydrogels with 3 images from each hydrogel sample.

3.3.5. Protein release

80 μl hydrogels with final concentrations of 6 wt/v% PEGMA and 1.5 wt/v% ELP were gelled as described previously. They were immersed in a bath of 700 μl PBS and incubated at varying temperatures. Supernatants were collected and replaced at 1, 3, 8 and 48 hours. ELP concentration in the supernatants was analyzed using the Bradford assay (Thermo Scientific) according to manufacturer protocol.

ELP cumulative release data was fit to a three-dimensional Fickian model of a disk-shaped hydrogel with a uniform concentration and equal surface concentration^{59,60}.

$$\frac{M_t}{M_\infty} = 4 \left(\frac{Dt}{\pi a^2} \right)^{\frac{1}{2}} - \pi \left(\frac{Dt}{\pi a^2} \right) - \frac{\pi}{3} \left(\frac{Dt}{\pi a^2} \right)^{\frac{3}{2}} + 4 \left(\frac{Dt}{\pi l^2} \right)^{\frac{1}{2}} - \frac{2a}{l} \left(8 \left(\frac{Dt}{\pi a^2} \right) - 2\pi \left(\frac{Dt}{\pi a^2} \right)^{\frac{3}{2}} - \frac{2\pi}{3} \left(\frac{Dt}{\pi a^2} \right)^{\frac{3}{2}} \right)$$

Hydrogel diameter (a) and thickness (l) were obtained from the dimensions of the mold used to gel the precursor solutions. Total releasable load (M_∞) was estimated from long time point data of ELP cumulative release plots. Diffusion coefficients were empirically estimated by regression analysis of the model to short time ELP release (M_t) data using mold dimensions of 8 mm diameter and 1 mm height.

3.3.6. Rheological measurements

Rheological measurements were conducted using Anton Paar MCR 301 and 302 Rheometers. 80 μ l PEG-ELP hydrogels were swelled in PBS for 24 hours prior to testing. Samples were tested using an 8 mm parallel plate, 25°C stage setting and the gap height was determined using 0.2 N normal force control. Strain sweeps were conducted from 0.01 – 100 % strain at a frequency of 1 Hz. Frequency sweeps were conducted from 0.01 – 5 Hz with a constant 1 % strain. Storage and loss moduli were measured by averaging values within the linear viscoelastic range of strain sweeps (< 10 % strain).

PEGMA and THPC interaction was measured with a time sweep using a 25 mm cone plate, 1 % strain and 1 Hz. ELP and LAP/UV-light interaction was measured with a time sweep using a 25 mm cone plate, 1 % strain, 1 Hz, and 7.5 mW/cm² light.

3.3.7. Lower critical solution temperature measurements

Lyophilized ELP, TRITC labeled ELP, and the experimental mixture of 1:19 weight ratio of TRITC labeled ELP to ELP were dissolved in PBS at a concentration of 10 mg/ml. 300 μ l of each solution and a PBS blank were pipetted into 96-well plate. Absorbance readings were taken

at 300 nm as a function of temperature using a CLARIOstar monochromatic microplate reader (BMG LABTECH). The temperature was increased from 25°C to 40°C at 0.5°C intervals with a 7.5 min wait time at each temperature interval. Before each measurement samples underwent double orbital shaking at 300 rpm.

3.3.8. *Statistical analysis*

Data is presented as average \pm standard error ($n \geq 3$). Statistical significance for ELP cumulative release curves was determined using 2 way anova with replication and multiple linear regression analysis. Student T-testing was performed to analyze statistical significance of D_{eff} differences. Statistical significance for hydrogel storage modulus was determined using student T-test and multiple linear regression analysis. For all tests $p < 0.05$ were considered statistically significant.

3.4. Results & Discussion

3.4.1. *PEG-ELP micro-architecture formation*

PEG-ELP hydrogel systems with distinct micro-architecture were created by controlling the temperature at which the gelation reactions occurred (Figure 3-2). Controlling the gelation temperature of the precursor solution to 37°C (above the ELP T_t) created PEG-ELP double-network hydrogels with LCST-driven hydrogel micro-architecture (Figure 3-2). Crosslinking PEG-ELP precursor solutions at 25°C (below the LCST transition) created a hydrogel with a homogeneous distribution of ELP (Figure 3-2). ELP was made fluorescent by covalently tethering a small quantity of rhodamine dye prior to mixing it into the hydrogel precursor solution, a modification that did not impact the T_t of the protein (Figure A-1). The T_t at which the ELP LCST transition occurs in aqueous solution can be tuned by controlling the ELP concentration, salt

concentration and the guest residue used in the amino acid sequence⁶¹⁻⁶³, so the observed behavior is not limited to the temperatures used in this study. We aimed to take advantage of this temperature-dependent phase transition to create hydrogel micro-architecture.

The ELP-rich regions were formed regardless of whether the THPC crosslinker was included during gelation, which indicates that the observed behavior is caused by the LCST transition not by interactions with the THPC crosslinker (Figure 3-3A, D). These ELP-rich regions remained intact several hours after gelation when the PEG-ELP hydrogels were not immersed in PBS (Figure 3-3B, E). This indicates that the ELP concentration gradient between ELP-rich regions and PEG-rich surroundings is not enough to disassociate the ELP to ELP interactions alone on this time scale. However, after swelling in PBS the ELP microstructures only remained intact when crosslinked with THPC (Figure 3-3C, F). In the presence of THPC, it is expected that the ELP molecules are covalently tethered together by the Mannich-type condensation crosslinking reaction and are too large to dissipate through the PEGMA hydrogel network. We quantified Feret diameters, which are caliper measurements, a common tool in the analysis of particle sizes that do not form perfect circles. The average Feret and minimum Feret diameters of the ELP microstructures after gelation were 23.0 ± 0.8 and 20.2 ± 0.6 μm , respectively. Since PEG-acrylate and -methacrylate hydrogels have a mesh size on the order of several nanometers^{63,64}, it is expected that the ELP microstructures were trapped within the surrounding PEGMA network when THPC was used during the gelation process. When ELP is not crosslinked with THPC, ELP microstructures dissociated after the hydrogels were immersed in room temperature PBS (Figure 3-3F). A skeletal structure of the ELP-rich regions did remain after the swelling process in hydrogels without the THPC crosslinker (Figure 3-3F), which may be a result of ELP molecules being covalently linked to the PEGMA hydrogel network at the interface between the PEG-rich

and ELP-rich regions. Although ELP is not expected to participate in the free radical chain growth crosslinking reaction of the PEGMA network, the ELP sequence contains several amino acid residues that contain phenyl groups, which have some reactivity with free radicals^{45,65,66}. The reaction of ELP via free radical chemistry is likely minimal since ELP solutions do not crosslink when exposed to UV-light in the presence of the LAP photoinitiator, as determined by a lack of change in solution behavior – no increase in storage and loss modulus, or gelation point crossover was observed (Figure 2).

The ELP LCST transition can be used to create either a homogenous and heterogeneous PEG-ELP hydrogels, which may be a useful biomaterial design feature. Since bioactive motifs are incorporated into the ELP amino acid sequence, PEG-ELP hybrid hydrogels may be a simple way to localize bioactivity within hydrogel systems for tissue engineering applications. The ELP sequence used in this study contains the RGD adhesive sequence (Figure 3-1) and controlling the gelation temperature provides a way to localize that bioactivity. Hydrogels with similar heterogeneous micro-architecture were created by crosslinking PEG with RLP⁴⁶. In the PEG-ELP hydrogel system gelation temperature is used to induce heterogeneity, whereas in PEG and RLP-based hydrogels the PEG macromer molecular weight was the driving factor for forming hydrogels with heterogeneous micro-architecture or homogeneous RLP distribution. However, changing the PEG macromer molecular weight will also change other hydrogel properties such as mesh size⁶⁷. The PEG-ELP hydrogel system allows for micro-architecture formation without changing the precursor solution macromer properties. However, simply maintaining the same hydrogel precursor solution content does not necessarily indicate that the homogeneous and heterogeneous hydrogels (Figure 3-2) would behave in a similar manner so both ELP retention/release and bulk hydrogel properties were further investigated.

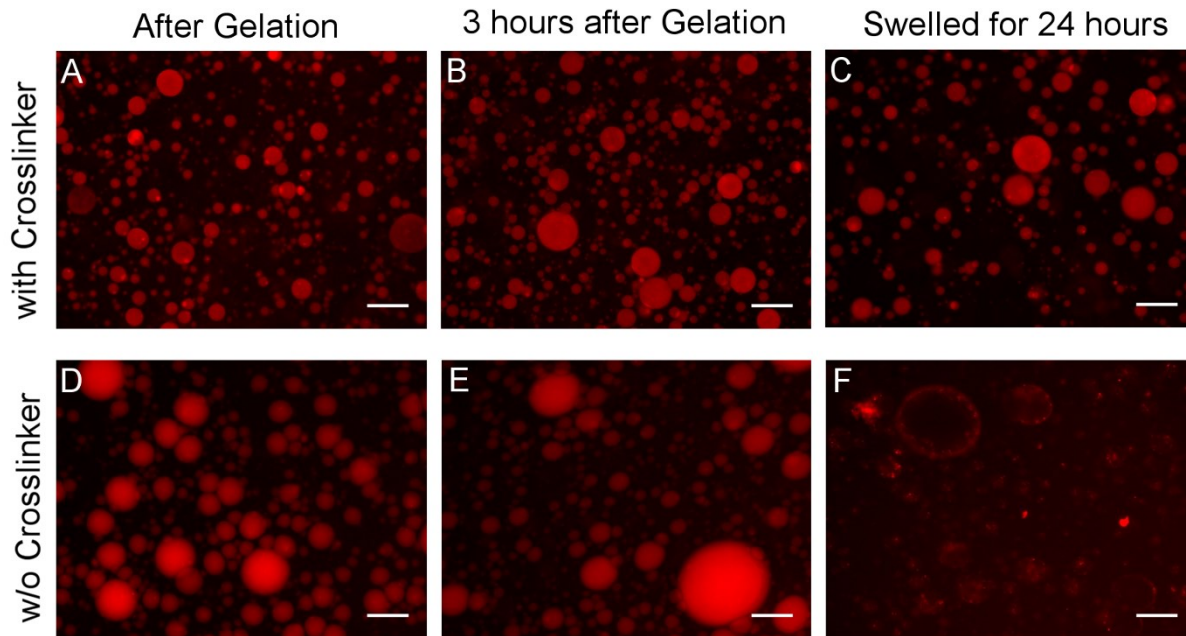


Figure 3-3: ELP-rich domain formation in 6/1.5 PEG-ELP hydrogels gelled at 37°C. Rows showing gels with a 2:1 THPC crosslinker to ELP amines ratio (A-C) and without crosslinker (B-F). Columns showing ELP domains immediately after gelation (A, D), after 3 hours in a relative humidity-controlled chamber (B, E) and after swelling in PBS for 24 h (E, F). ELP labeled with TRITC (Red) and scale bars = 100 μ m.

3.4.2. ELP release kinetics

The dissociation of ELP-rich regions in PEG-ELP hydrogels without the THPC crosslinker when swelled in PBS (Figure 3-3F) was a stark contrast to the observed behavior in hydrogels that were not swelled (Figure 3-3E). The LCST transition of soluble ELP is reversible in aqueous solution so we hypothesized that PEG-ELP hydrogel incubation temperature could be used as a mechanism to control the ELP release and preserve the ELP microstructure without the use of the THPC crosslinker⁵⁷. The kinetics of ELP-rich domain dissociation was further analyzed by imaging PEG-ELP hydrogels swelled over time (Figure 3-4). In PEG-ELP hydrogels without THPC, ELP-rich domains dissociated within an hour of being immersed in PBS regardless of incubation temperature (Figure 3-4D-F). This indicates that the driving force for ELP release is the concentration gradient between the hydrogel and the surrounding aqueous solution with

temperature having minimal impact. This effect is not expected to differ at incubation temperatures well above the ELP T_t because phase diagrams of ELP in solutions with high water content demonstrate that the two phase ELP coacervate reverts back into a single phase at temperatures well past the T_t ²⁶. This phenomenon is speculated to occur from high temperatures “denaturing” or removing secondary structure characteristics of ELP that form during the LCST transition²⁶. In addition, no structural change was observed in the ELP-rich regions of PEG-ELP hydrogels crosslinked with THPC (Figure 3-4A-C). Hydrogels gelled at room temperature did not exhibit any distinct visible structural changes after incubating in PBS (Figure 3-4G-L). The faded or layered coloring of the hydrogel is an imaging artifact that comes from taking a single xy-plane image of a swollen 3D hydrogel using a traditional “2D” epifluorescent microscope. The center is dimmer because it is a little out of focus.

The fluorescence intensity values from Figure 3-4 images do not provide accurate quantitative ELP concentrations within PEG-ELP hydrogels because of differences in camera exposure times, out of focus light, and photobleaching between samples⁶⁸. To quantify the ELP release kinetics from PEG-ELP hydrogels, we measured the protein concentration of the supernatant over time. ELP cumulative release from PEG-ELP hydrogels was affected by both the presence of THPC crosslinker and gelation temperature (Figure 3-5). The presence of THPC reduced the amount of ELP that was released, but did not completely trap all ELP within the hydrogel (Figure 3-5A, B). Since THPC tethers ELP molecules together, released ELP will also include ELP molecules that are tethered together, but not trapped within the PEGMA matrix, and reduce the observed protein transport. Gelation temperature had a lasting impact on ELP release behavior (Figure 3-5C, D). PEG-ELP hydrogels gelled at 37°C (above the ELP T_t) had a reduction in ELP release when compared to hydrogels made at 25°C (below the ELP T_t) across all incubation

temperatures (Figure 3-5C, D). This effect was consistent in both cases with and without the presence of THPC. The LCST transition of soluble ELP is reversible so the gelation temperature was not expected to have a lasting effect on the released ELP molecules. The gelation temperature likely affects the porosity of PEG-ELP hydrogels because of the micro-architecture formed when gelling above the ELP LCST transition. In cases without the THPC crosslinker, the observed ELP release behavior may be a result of the even distribution of ELP creating more defects within the PEGMA hydrogel network than when ELP is aggregated together (Figure 3-5D).

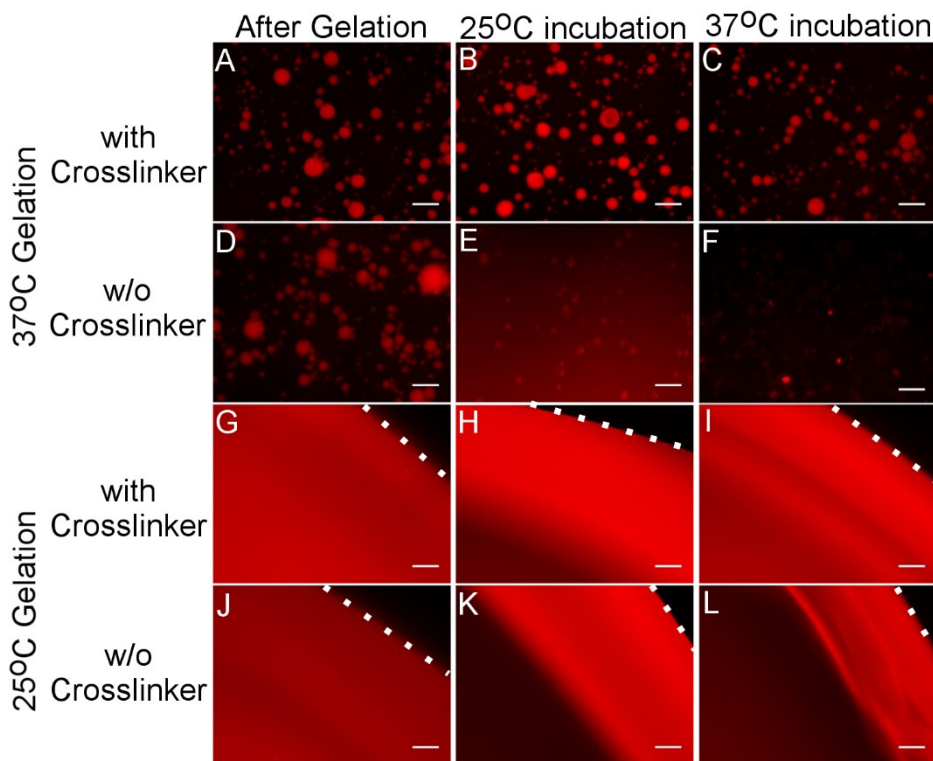


Figure 3-4: Temperature dependence of ELP release from 6/1.5 PEG-ELP hydrogels. Panels are of PEG-ELP hydrogels gelled at 37°C (A-F) and 25°C (G-L). Rows show gels with a 2:1 THPC crosslinker to ELP amines ratio (A-C and G-I) and without the THPC crosslinker (D-F and J-L). Columns showing ELP domains immediately after gelation (A, D, G, J), and after incubating in PBS for 1 h at 25°C (B, E, H, K) and 37°C (C, F, I, L). ELP labeled with TRITC (Red) and scale bars = 100 μm . Dashed lines indicate the hydrogel edge.

Comparison of ELP release data in PEG-ELP hydrogels with THPC (4°C) to the fluorescent images (Figure 3-4A-C, G-I) indicates that although there was no observable change in ELP distribution, ELP was still removed from the hydrogel over time. The same can be said for PEG-ELP hydrogels gelled at 25°C without the presence of THPC (Figures 3-4J-L, 5D). Images of PEG-ELP hydrogels created above the LCST transition without THPC demonstrate that the ELP-rich regions dissociate within 1 hour of swelling (Figure 3-4D-F). However, ELP release data demonstrates that while the ELP-rich regions are not maintained after 1 hour, ELP is still present within the hydrogel (Figure 3-5D).

The LCST transition of soluble ELP is reversible in aqueous solution, but crosslinked ELP experiences some hysteresis when cycled above and below the T_t ⁵¹ so the effects of incubation temperature on ELP release was analyzed. Multiple linear regression analysis ($p > 0.05$) showed that post-gelation incubation temperature did not significantly affect the amount of ELP that was released in hydrogels made at 37°C (Figure 3-5A). This was unexpected in PEG-ELP hydrogels made without THPC because the ELP is not crosslinked in these hydrogels and should still undergo a conformational change and aggregate above the T_t . This data contradicts our hypothesis that both the change in ELP-ELP interactions and the changes in protein conformation would impact transport through the hydrogel network. When gelation was performed at 25°C, incubation temperature did impact the ELP release, and a statistically significant interaction between incubation temperature and THPC was observed (Figure 3-5B). In cases without THPC, ELP incubated above the T_t (37°C) diffused out of PEG-ELP hydrogels slower when compared to hydrogels incubated below the T_t (4 and 25°C). This is in agreement with the hypothesis that ELP aggregates form above the T_t , which would reduce the observed transport properties due to an increase in size. When THPC is incorporated in PEG-ELP hydrogels gelled at 25°C, 2-way

ANOVA analysis determined that a statistically significant interaction between incubation temperature and THPC occurs (Figure 3-5B). The physical meaning from this statistical result is not easily identifiable. In these hydrogels the fastest ELP release occurred at the lowest incubation temperature (4°C). This effect doesn't appear to be a result of the ELP LCST transition property because protein release in these hydrogels was higher at 4°C incubation than both 25°C and 37°C incubations, and 25°C is below the T_t of this ELP sequence. The Mannich-type condensation reaction of ELPs with THPC is likely affected by temperature, which may explain the effects gelation temperature had on ELP release kinetics. This data indicates that PEG-ELP hydrogel gelation temperature has a lasting impact on ELP behavior in PEG-ELP hydrogels.

ELP release data was empirically fit to a diffusion model for release out of a disk at short time periods^{59,60}. The model assumes a uniform initial ELP concentration within the hydrogel, and a hydrogel surface concentration that is equal to the internal concentration. Comparing the diffusion of soluble ovalbumin, which has a comparable size to ELP (43 kDa, $1.07 \times 10^{-6} \text{ cm}^2/\text{s}$ ⁶⁹), to ELP release data indicated that ELP experiences resistance to diffusion from the crosslinked PEG-ELP hydrogel network because the predicted release profile for ovalbumin is much faster than ELP release measurements (Figure 3-5A). Data at short time periods (up to 8 h) were fit to the analytical diffusion model to determine an effective ELP diffusion coefficient (D_{eff}). For PEG-ELP hydrogels gelled at 37°C, ELP D_{eff} was $4.43 \pm 0.25 \times 10^{-8} \text{ cm}^2/\text{s}$ ($R^2 = 0.95-0.99$), and the incorporation of THPC during gelation drops the D_{eff} down to $4.12 \pm 0.38 \times 10^{-8} \text{ cm}^2/\text{s}$ ($R^2 = 0.90-0.99$). For PEG-ELP hydrogels gelled at 25°C, ELP D_{eff} was $3.91 \pm 0.28 \times 10^{-8} \text{ cm}^2/\text{s}$ ($R^2 = 0.95-0.99$) and the incorporation of THPC during gelation reduced D_{eff} to $3.57 \pm 0.65 \times 10^{-8} \text{ cm}^2/\text{s}$ ($R^2 = 0.95-0.99$). The addition of THPC resulted in 7.0 % and 8.8 % reductions to the diffusion coefficient in hydrogels made at 37°C and 25°C, respectively. In addition, ELP diffusion coefficients were 13.4 % and 11.6 % lower

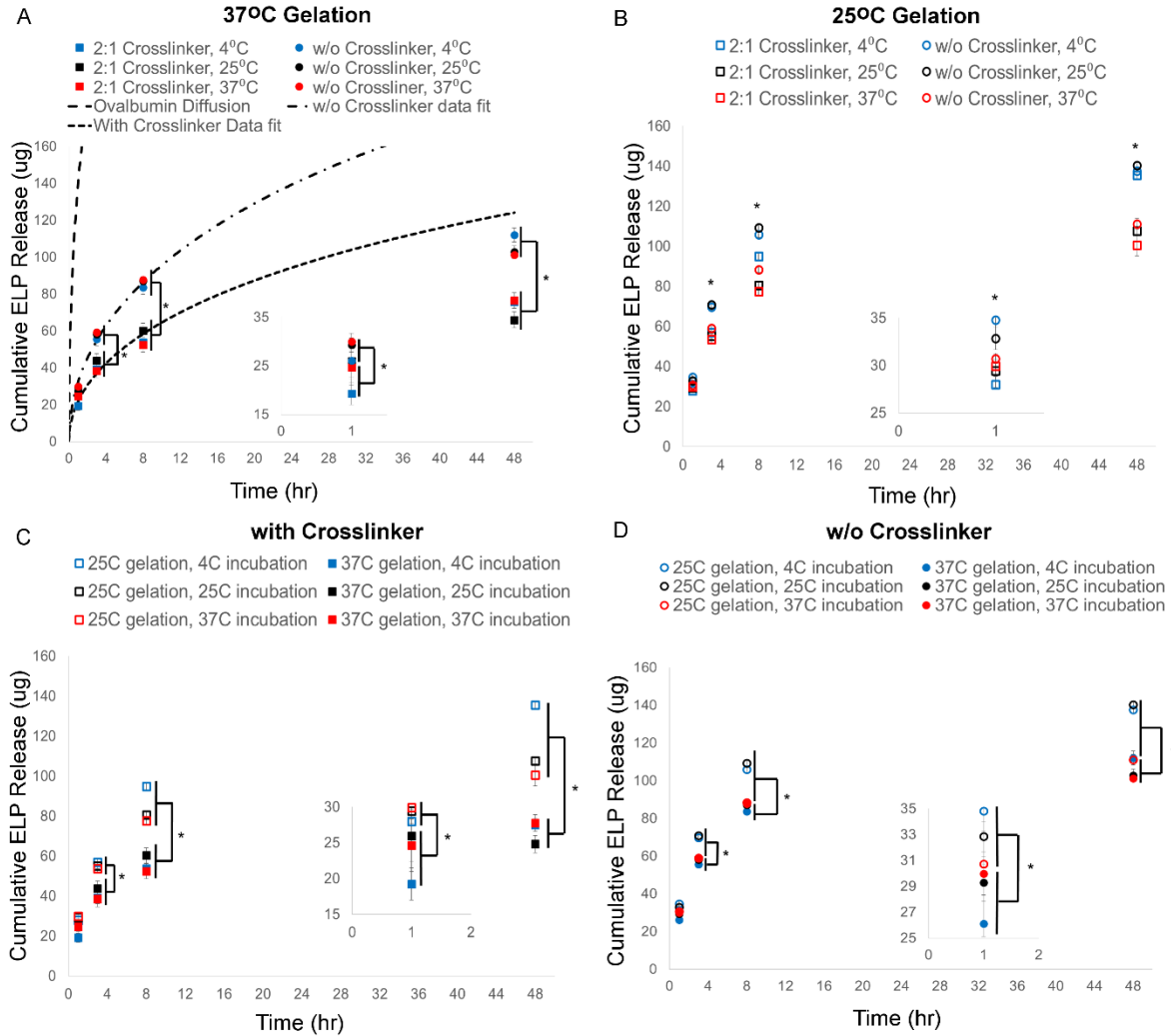


Figure 3-5: Cumulative release of ELP from 6/1.5 PEG-ELP hydrogels gelled at 37°C (A) and 25°C (B) after swelling in PBS for 1, 3, 8, and 48 hours. Data also shown as a function of THPC crosslinker presence (With THPC (C) and without THPC (D)). Representative data fits of Fickian diffusion model shown in (A). Showing standard error. Stars indicate statistical significance in mean values of ELP release from hydrogels made with and without THPC (A, B), and hydrogels gelled at 37°C and 25°C (C, D) using 2 way anova with replication ($p < 0.05$).

when gelation was performed at 25°C in hydrogels with and without THPC, respectively. All diffusion coefficient differences were found to be statistically insignificant ($p > 0.05$). Since the ELP release data was statistically significant (Figure 3-5) this may indicate that THPC and gelation temperature only impact the amount of ELP trapped within the hydrogel and not the transport properties of the protein itself. However, it could also indicate that the error from the regression

fit ($R^2 < 1$) is too high to discern any small differences to ELP diffusion coefficients caused by gelation temperature and THPC. Overall, this data correlates well with previous data of bovine serum albumin (BSA) diffusion through PEG-based hydrogels, which were calculated to be on the order of $1e^{-8} \text{ cm}^2/\text{s}$ ^{60,70,71}. While previous literature of protein diffusion through PEG-based hydrogels is not a direct analogy to ELP release in double-network hydrogels, it is analogous in cases where THPC was not used. This model indicates that the formation of micro-architecture in PEG-ELP hydrogels and the use of THPC crosslinker to preserve that micro-architecture in aqueous solution does not significantly affect ELP D_{eff} .

3.4.3. PEG-ELP mechanical properties

We investigated bulk PEG-ELP hydrogel stiffness because biomaterial scaffold physical properties impact cellular behavior through mechanotransduction pathways, and should be considered when designing biomaterial scaffolds^{13,67}. PEG-ELP hydrogels had similar linear viscoelastic ranges (< 10 % strain) to each other and display frequency independent behavior in all conditions (Figure 3-6A, B). The swelled storage modulus for all hydrogels ranged from 0.3 – 2.2 kPa, which is within the range of what previous literature on ELP- and PEG-based hydrogels have reported (Figure 3-6C-H)^{14,47,64,72–77}. PEG-ELP hydrogel stiffness can be tuned by adjusting many factors, and we focused on PEGMA and ELP concentration, THPC addition, and gelation temperature. The swollen shear storage modulus of PEG-ELP hydrogels, which is a measure of hydrogel stiffness, was affected by all factors that were analyzed as determined by multiple linear regression analysis ($p < 0.05$). Increasing the PEGMA and ELP concentrations in the hydrogel precursor solution increased the overall hydrogel stiffness (Figure 3-6C-F), which is similar to findings previously reported for ELP- and PEG-based hydrogels^{62,67,72,75}. The presence of the

THPC crosslinker also increased PEG-ELP hydrogel stiffness (Figure 3-6C-F). While increasing crosslinker concentration does not always lead to an increase in hydrogel stiffness^{14,51,55}, here only the presence and absence of THPC were tested, and the formation of a second hydrogel network was expected to increase the storage modulus over hydrogels without the THPC crosslinker. Not all samples displayed a statistically significant increase in swollen storage modulus with increasing PEG and ELP concentration, and incorporation of THPC (Figure 3-6C-F). This was likely a result of the small range of concentrations tested. However, PEG-ELP hydrogels with the highest macromer content and the presence of THPC formed the stiffest hydrogels with statistical significance from all other samples tested (Figure 3-6C-F).

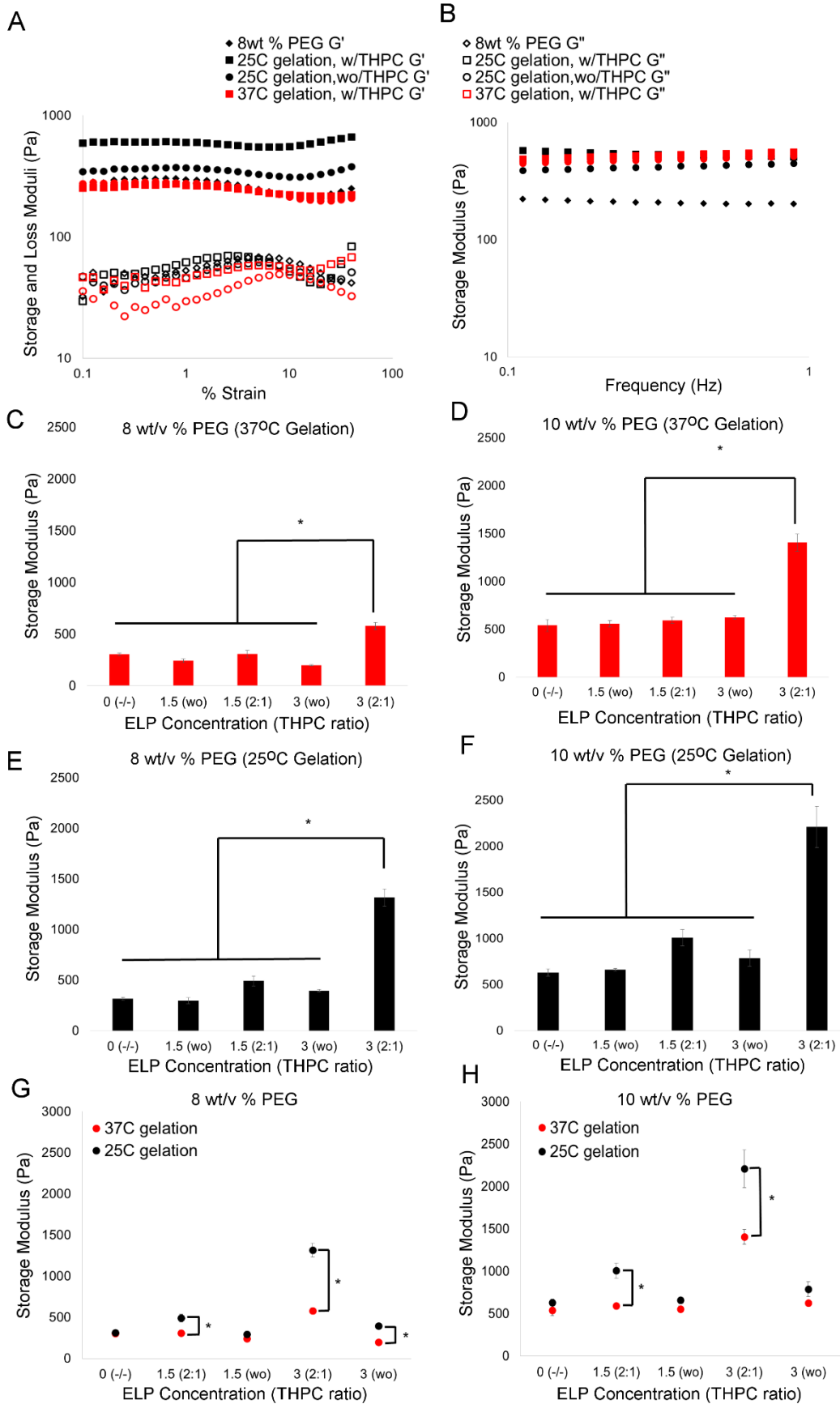


Figure 3-6: The effect of PEG and ELP concentration, THPC presence and gelation temperature on PEG-ELP hydrogel swollen shear storage modulus. Representative strain (A) and frequency (B) sweeps of swollen 8/1.5 PEG-ELP hydrogels. Swollen shear storage modulus of 8 wt/v% PEG gelled at 37°C (C), 10 wt/v% PEG gelled at 37°C (D), 8 wt/v% PEG gelled at 25°C (E), and 10 wt/v% PEG gelled at 25°C (F). The effect of gelation temperature on the swollen shear storage modulus of PEG-ELP hydrogels with 8 wt/v % PEG (G) and 10 wt/v% PEG (H). Showing standard error. Statistics show significance in mean values of using student T-test ($p < 0.05$).

The formation of micro-architecture in PEG-ELP hydrogels reduced the swollen storage modulus when compared to hydrogels with homogeneous ELP distribution (Figure 3-6G, H). Previous research on ELP-based hydrogels reported that going above the T_t increases hydrogel storage modulus, which is in contrast our findings⁷². However, those experiments were conducted on single-network hydrogel system and gelation was performed below the ELP LCST transition. Previously crosslinked ELP does not aggregate to form micro-architecture when the temperature is increased above the T_t , so the previously tested hydrogels are not a direct comparison to these hydrogels (Figure 3-4I). We hypothesize that PEG-ELP hydrogel stiffness was reduced when gelation occurred above the T_t because of defects formed in the PEGMA-network by voids created from the ELP aggregates. The ELP-rich regions in PEG-ELP hydrogels are large, on the order of 20 microns in diameter (Figure 3-2), when compared to the expected PEG-network mesh size on the order of several nanometers^{63,64}. There is evidence that local heterogeneities in PEG-based hydrogel networks reduce the hydrogel storage modulus, and the reduction in storage modulus is proportional to the size of the defects or voids in the PEG-network⁶⁶. Control of gelation temperature around the ELP T_t can be used to alter PEG-ELP hydrogel stiffness and may impact other hydrogel properties.

3.4.4. PEG-ELP optical properties

Biomaterial scaffold optical density is an important design feature to take into consideration because encapsulated cellular behavior is often inspected using light microscopy techniques. ELP-based hydrogels are typically optically dense, but previous literature demonstrated that incorporating PEG into a matrix with ELPs helps improve the optical density of ELP-based hydrogels⁴⁴. The optical properties of PEG-ELP hydrogels gelled below and above the ELP T_t were investigated at incubation temperatures of 4°C, 25°C and 37°C. The optical density of PEG-ELP hydrogels increased with increasing ELP concentration when hydrogels were incubated above the ELP T_t regardless of gelation temperature and THPC concentration (Figure 3-7A). At higher ELP concentrations a subset of the data reached the detection limits of the instrument (Supplemental information). Similar trends occurred for hydrogels incubated below the T_t when THPC was present during gelation (Figure 3-7C, E). PEG-ELP hydrogels without THPC did not exhibit an increase in optical density with increasing ELP concentration when incubated below the T_t (Figure 3-7C, E). Gelling above the T_t increased hydrogel optical density when compared to hydrogels made below the T_t (Figure 3-7C, E). However, this trend disappears when hydrogels are incubated above the T_t , where the data clusters together (Figure 3-7A). This indicates that the formation of micro-architecture creates more optically dense hydrogels, but only when incubating below the T_t . For hydrogels gelled below the T_t , the absorbance increased when the incubation temperature was raised to 37°C, which indicates that the LCST transition of crosslinked ELP still occurs between 25°C and 37°C (Figure 3-7A, C, E (filled circles)). Finally, the reversibility of PEG-ELP hydrogel optical density behavior was assessed by cycling the hydrogels through 4°C, 25°C, and 37°C incubation temperatures a second time (Figures 3-7B, D, F). The overall trends observed from the first incubation cycle remained, indicating that PEG-ELP

hydrogel optical density behavior is reversible. This also indicates that gels formed above the T_t without THPC could be cycled to other, lower temperatures to improve imaging ability. The optical density of PEGMA only hydrogels (Figure 3-7, 0 on x-axis) remained constant for all incubation temperatures so the observed temperature dependent results occurred because of ELP behavior. Taken together this data indicates that PEG-ELP hydrogel optical density is predicated by ELP concentration and temperature behavior, with the PEGMA hydrogel-network having little impact.

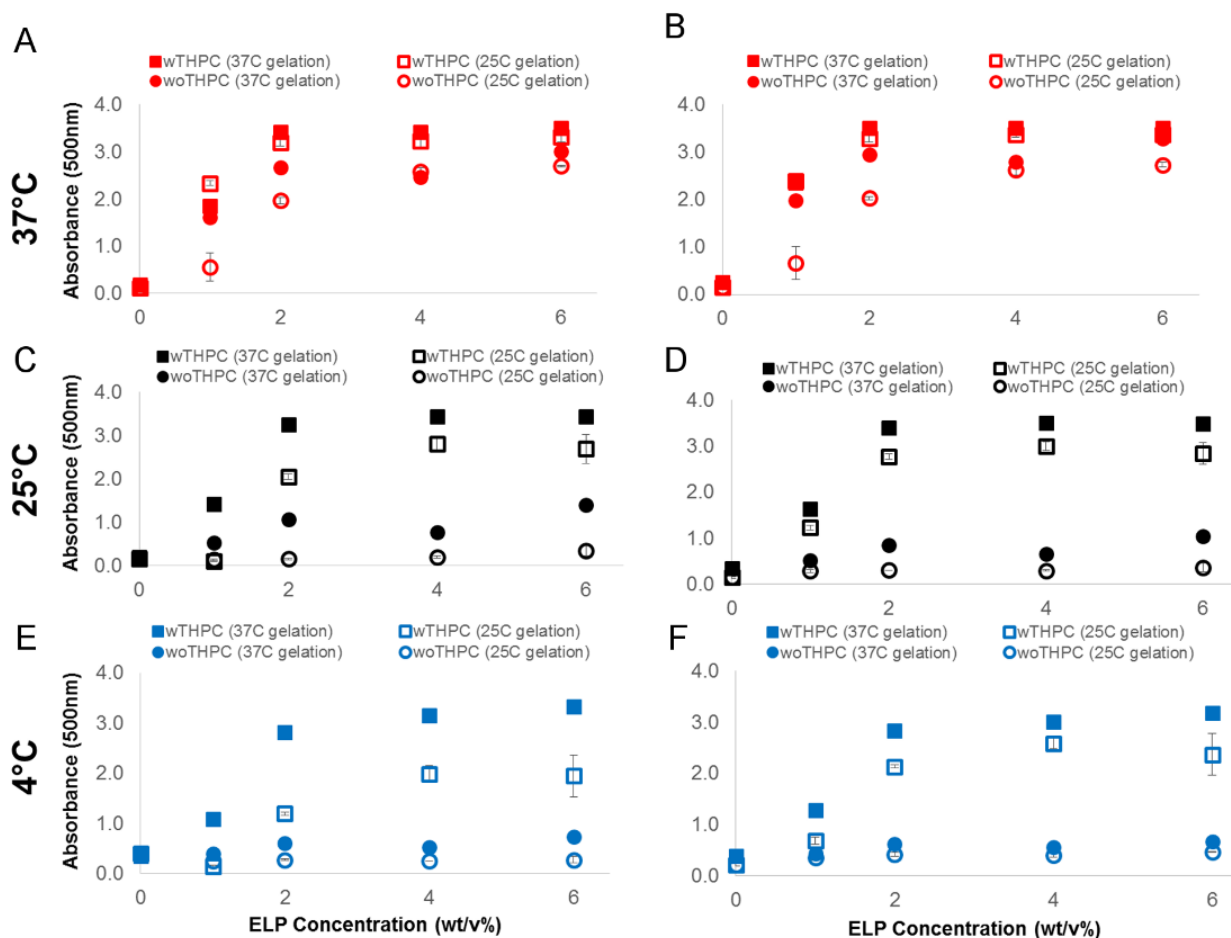


Figure 3-7: Optical density of 6/x wt/v% PEG-ELP hydrogels incubated at 37°C (A, B), 25°C (C, D) and 4°C (E,F). (B, D, F) hydrogel optical density after cycling through a round of incubations at 37, 25 and 4°C.

3.5. Conclusions

PEG-ELP hybrid hydrogels have homogeneous ELP distribution when gelation occurs below the T_t and develop microstructured ELP-rich regions when gelation occurs above the T_t . ELP-rich regions form because of the LCST transition, but can only be maintained by covalently crosslinking ELP molecules together when the hydrogel is immersed in aqueous solution. The formation of micro-architecture in PEG-ELP hydrogels impacted ELP cumulative release behavior, hydrogel storage modulus, and optical density. PEG-ELP hydrogels gelled above the T_t (those with heterogeneous microstructure) had lower cumulative ELP release. The observed D_{eff} of ELP in PEG-ELP hydrogels agrees with previous research into protein diffusion through a PEG hydrogel, indicating that ELP release is largely dependent on the PEG hydrogel-network characteristics. PEG-ELP hydrogels made above the T_t had a lower equilibrium storage modulus when compared to hydrogels made below the T_t because of defects created in the PEGMA hydrogel-network by ELP aggregates. The optical density of PEG-ELP hydrogels was mainly affected by ELP temperature behavior. Incubation temperature cycling around the LCST transition demonstrated that PEG-ELP hydrogel optical properties are reversible. Utilization of the ELP LCST transition during the gelation process may be a useful hydrogel design feature for localizing bioactivity or protein content within hydrogel systems.

3.6. Funding

This work was supported by the University of Virginia, the Translational Health Research Institute of Virginia (THRIV), and the School of Engineering and Applied Science Research Innovation Award.

3.7. References

- (1) Betre, H.; Ong, S. R.; Guilak, F.; Chilkoti, A.; Fermor, B.; Setton, L. A. Chondrocytic Differentiation of Human Adipose-Derived Adult Stem Cells in Elastin-like Polypeptide. *Biomaterials* 2006, 27 (1), 91–99. <https://doi.org/10.1016/j.biomaterials.2005.05.071>.
- (2) Kaneko, A.; Matsushita, A.; Sankai, Y. A 3D Nanofibrous Hydrogel and Collagen Sponge Scaffold Promotes Locomotor Functional Recovery, Spinal Repair, and Neuronal Regeneration after Complete Transection of the Spinal Cord in Adult Rats. *Biomed. Mater.* 2015, 10 (1), 015008. <https://doi.org/10.1088/1748-6041/10/1/015008>.
- (3) King, V. R.; Henseler, M.; Brown, R. A.; Priestley, J. V. Mats Made from Fibronectin Support Oriented Growth of Axons in the Damaged Spinal Cord of the Adult Rat. *Exp. Neurol.* 2003, 182 (2), 383–398. [https://doi.org/10.1016/S0014-4886\(03\)00033-5](https://doi.org/10.1016/S0014-4886(03)00033-5).
- (4) King, V. R.; Phillips, J. B.; Hunt-Grubbe, H.; Brown, R.; Priestley, J. V. Characterization of Non-Neuronal Elements within Fibronectin Mats Implanted into the Damaged Adult Rat Spinal Cord. *Biomaterials* 2006, 27 (3), 485–496. <https://doi.org/10.1016/j.biomaterials.2005.06.033>.
- (5) Shrestha, B.; Coykendall, K.; Li, Y.; Moon, A.; Priyadarshani, P.; Yao, L. Repair of Injured Spinal Cord Using Biomaterial Scaffolds and Stem Cells. *Stem Cell Res. Ther.* 2014, 1–11. <https://doi.org/10.1186/scrt480>.
- (6) Clifford, D. M. D. D. M.; Fisher, S. A. S.; Brunskill, S. J.; Doree, C.; Mathur, A.; Watt, S.; Martin-Rendon, E. Stem Cell Treatment for Acute Myocardial Infarction. *Cochrane database Syst. Rev.* 2012, 2 (2), CD006536. <https://doi.org/10.1002/14651858.CD006536.pub3>.
- (7) Li, Z.; Guan, J. Hydrogels for Cardiac Tissue Engineering. *Polymers (Basel)*. 2011, 3 (2), 740–761. <https://doi.org/10.3390/polym3020740>.
- (8) Assmus, B.; Schächinger, V.; Teupe, C.; Britten, M.; Lehmann, R.; Döbert, N.; Grünwald, F.; Aicher, A.; Urbich, C.; Martin, H.; Hoelzer, D.; Dimmeler, S.; Zeiher, A. M. Transplantation of

- Progenitor Cells and Regeneration Enhancement in Acute Myocardial Infarction (TOPCARE-AMI). *Circulation* 2002, 106 (24), 3009–3017. <https://doi.org/10.1161/01.CIR.0000043246.74879.CD>.
- (9) Rane, A. A.; Chuang, J. S.; Shah, A.; Hu, D. P.; Dalton, N. D.; Gu, Y.; Peterson, K. L.; Omens, J. H.; Christman, K. L. Increased Infarct Wall Thickness by a Bio-Inert Material Is Insufficient to Prevent Negative Left Ventricular Remodeling after Myocardial Infarction. *PLoS One* 2011, 6 (6). <https://doi.org/10.1371/journal.pone.0021571>.
- (10) Lampe, K. J.; Antaris, A. L.; Heilshorn, S. C. Design of Three-Dimensional Engineered Protein Hydrogels for Tailored Control of Neurite Growth. *Acta Biomater.* 2013, 9 (3), 5590–5599. <https://doi.org/10.1016/j.actbio.2012.10.033>.
- (11) Ju, Y. El; Janmey, P. A.; McCormick, M. E.; Sawyer, E. S.; Flanagan, L. A. Enhanced Neurite Growth from Mammalian Neurons in Three-Dimensional Salmon Fibrin Gels. *Biomaterials* 2007, 28 (12), 2097–2108. <https://doi.org/10.1016/j.biomaterials.2007.01.008>.
- (12) Wang, L. Z.; Gorlin, J.; Michaud, S. E.; Janmey, P. A.; Goddeau, R. P.; Kuuse, R.; Uibo, R.; Adams, D.; Sawyer, E. S. Purification of Salmon Clotting Factors and Their Use as Tissue Sealants. *Thromb. Res.* 2000, 100 (6), 537–548. [https://doi.org/10.1016/S0049-3848\(00\)00362-5](https://doi.org/10.1016/S0049-3848(00)00362-5).
- (13) Zustiak, S. P.; Pubill, S.; Ribeiro, A.; Leach, J. B. Hydrolytically Degradable Poly(Ethylene Glycol) Hydrogel Scaffolds as a Cell Delivery Vehicle: Characterization of PC12 Cell Response. *Biotechnol. Prog.* 2013, 29 (5), 1255–1264. <https://doi.org/10.1002/btpr.1761>.
- (14) Zustiak, S. P.; Leach, J. B. Hydrolytically Degradable Poly(Ethylene Glycol) Hydrogel Scaffolds with Tunable Degradation and Mechanical Properties. *Biomacromolecules* 2010, 11 (5), 1348–1357. <https://doi.org/10.1021/bm100137q>.

- (15) Park, W. M.; Yee, C. M.; Champion, J. A. Self-Assembled Hybrid Supraparticles That Proteolytically Degrade Tumor Necrosis Factor- α . *J. Mater. Chem. B* 2016, 4 (9), 1633–1639. <https://doi.org/10.1039/c5tb01647a>.
- (16) Jang, Y.; Champion, J. A. Self-Assembled Materials Made from Functional Recombinant Proteins. *Acc. Chem. Res.* 2016, 49 (10), 2188–2198. <https://doi.org/10.1021/acs.accounts.6b00337>.
- (17) Tang, J. D.; Lampe, K. J. From de Novo Peptides to Native Proteins: Advancements in Biomaterial Scaffolds for Acute Ischemic Stroke Repair. *Biomed. Mater.* 2018, 13 (3), 034103.
- (18) Straley, K. S.; Heilshorn, S. C. Independent Tuning of Multiple Biomaterial Properties Using Protein Engineering. *Soft Matter* 2009, 5 (1), 114. <https://doi.org/10.1039/b808504h>.
- (19) Nettles, D. L.; Chilkoti, A.; Setton, L. A. Applications of Elastin-like Polypeptides in Tissue Engineering. *Adv. Drug Deliv. Rev.* 2010, 62 (15), 1479–1485. <https://doi.org/10.1016/j.addr.2010.04.002>.
- (20) Daamen, W. F.; Veerkamp, J. H.; van Hest, J. C. M.; van Kuppevelt, T. H. Elastin as a Biomaterial for Tissue Engineering. *Biomaterials* 2007, 28 (30), 4378–4398. <https://doi.org/10.1016/j.biomaterials.2007.06.025>.
- (21) Wright, E. R.; McMillan, R. A.; Cooper, A.; Apkarian, R. P.; Conticello, V. P. Thermoplastic Elastomer Hydrogels via Self-Assembly of an Elastin-Mimetic Triblock Polypeptide. *Adv. Funct. Mater.* 2002, 12 (2), 149–154. [https://doi.org/10.1002/1616-3028\(20020201\)12:2<149::AID-ADFM149>3.0.CO;2-N](https://doi.org/10.1002/1616-3028(20020201)12:2<149::AID-ADFM149>3.0.CO;2-N).
- (22) Catherine, C.; Oh, S. J.; Lee, K.-H. H.; Min, S.-E. E.; Won, J.-I. I.; Yun, H.; Kim, D.-M. M. Engineering Thermal Properties of Elastin-like Polypeptides by Incorporation of Unnatural Amino

- Acids in a Cell-Free Protein Synthesis System. *Biotechnol. Bioprocess Eng.* 2015, 20 (3), 417–422. <https://doi.org/10.1007/s12257-015-0190-1>.
- (23) Biesheuvel, P. M.; Cohen Stuart, M. A. Electrostatic Free Energy of Weakly Charged Macromolecules in Solution and Intermacromolecular Complexes Consisting of Oppositely Charged Polymers. *Langmuir* 2004, 20 (7), 2785–2791. <https://doi.org/10.1021/la036204l>.
- (24) Bataille, L.; Dieryck, W.; Hocquellet, A.; Cabanne, C.; Bathany, K.; Lecommandoux, S.; Garbay, B.; Garanger, E. Recombinant Production and Purification of Short Hydrophobic Elastin-like Polypeptides with Low Transition Temperatures. *Protein Expr. Purif.* 2016, 121, 81–87. <https://doi.org/10.1016/j.pep.2016.01.010>.
- (25) Urry, D. W.; Gowda, D. C.; Parker, T. M.; Luan, C. H.; Reid, M. C.; Harris, C. M.; Pattanaik, a; Harris, R. D. Hydrophobicity Scale for Proteins Based on Inverse Temperature Transitions. *Biopolymers* 1992, 32 (9), 1243–1250. <https://doi.org/10.1002/bip.360320913>.
- (26) Urry, D. W.; Trapano, T. L.; Prasad, K. U. Phase-Structure Transitions of the Elastin Polypentapeptide-Water System within the Framework of Composition-Temperature Studies. *Biopolymers* 1985, 24 (12), 2345–2356. <https://doi.org/10.1002/bip.360241212>.
- (27) Johnson, T.; Koria, P. Expression and Purification of Neurotrophin-Elastin-Like Peptide Fusion Proteins for Neural Regeneration. *BioDrugs* 2016, 30 (2), 117–127. <https://doi.org/10.1007/s40259-016-0159-4>.
- (28) Koria, P.; Yagi, H.; Kitagawa, Y.; Megeed, Z.; Nahmias, Y.; Sheridan, R.; Yarmush, M. L. Self-Assembling Elastin-like Peptides Growth Factor Chimeric Nanoparticles for the Treatment of Chronic Wounds. *Proc. Natl. Acad. Sci. U. S. A.* 2011, 108 (3), 1034–1039. <https://doi.org/10.1073/pnas.1009881108>.

- (29) Luo, T.; Kiick, K. L. Noncovalent Modulation of the Inverse Temperature Transition and Self-Assembly of Elastin-b-Collagen-like Peptide Bioconjugates. *J. Am. Chem. Soc.* 2015, 137, 15362–15365. <https://doi.org/10.1021/jacs.5b09941>.
- (30) Kracke, B.; Cole, J. T.; Kaiser, C. J. O.; Hellenkamp, B.; Krysiak, S.; Ghoorchian, A.; Braun, G. B.; Holland, N. B.; Hugel, T. Thermoswitchable Nanoparticles Based on Elastin-like Polypeptides. *Macromolecules* 2015, 48, 5868–5877. <https://doi.org/10.1021/acs.macromol.5b00932>.
- (31) Tysseling-Mattiace, V. M.; Sahni, V.; Niece, K. L.; Birch, D.; Czeisler, C.; Fehlings, M. G.; Stupp, S. I.; Kessler, J. A. Self-Assembling Nanofibers Inhibit Glial Scar Formation and Promote Axon Elongation after Spinal Cord Injury. *J. Neurosci.* 2008, 28 (14), 3814–3823. <https://doi.org/10.1523/JNEUROSCI.0143-08.2008>.
- (32) Leach, J. B.; Brown, X. Q.; Jacot, J. G.; Dimilla, P. A.; Wong, J. Y. Neurite Outgrowth and Branching of PC12 Cells on Very Soft Substrates Sharply Decreases below a Threshold of Substrate Rigidity. *J. Neural Eng.* 2007, 4 (2), 26–34. <https://doi.org/10.1088/1741-2560/4/2/003>.
- (33) Levental, I.; Georges, P. C.; Janmey, P. A. Soft Biological Materials and Their Impact on Cell Function. *Soft Matter* 2007, 3 (3), 299–306. <https://doi.org/10.1039/B610522J>.
- (34) Yu, L. M. Y.; Kazazian, K.; Shoichet, M. S. Peptide Surface Modification of Methacrylamide Chitosan for Neural Tissue Engineering Applications. *J. Biomed. Mater. Res. Part A* 2007, 82A, 243–255. <https://doi.org/10.1002/jbm.a.31069>.
- (35) McGann, C. L.; Levenson, E. A.; Kiick, K. L. Resilin-Based Hybrid Hydrogels for Cardiovascular Tissue Engineering. *Macromol. Chem. Phys.* 2013, 214 (2), 203–213. <https://doi.org/10.1002/macp.201200412>.
- (36) Zhu, J. Bioactive Modification of Poly(Ethylene Glycol) Hydrogels for Tissue Engineering. *Biomaterials* 2010, 31 (17), 4639–4656. <https://doi.org/10.1016/j.biomaterials.2010.02.044>.

- (37) Fairbanks, B. D.; Schwartz, M. P.; Halevi, A. E.; Nuttelman, C. R.; Bowman, C. N.; Anseth, K. S. A Versatile Synthetic Extracellular Matrix Mimic via Thiol-Norbornene Photopolymerization. *Adv. Mater.* 2009, 21 (48), 5005–5010. <https://doi.org/10.1002/adma.200901808>.
- (38) Fairbanks, B. D.; Singh, S. P.; Bowman, C. N.; Anseth, K. S. Photodegradable, Photoadaptable Hydrogels via Radical-Mediated Disulfide Fragmentation Reaction. *Macromolecules* 2011, 44, 2444–2450. <https://doi.org/10.1021/ma200202w>.
- (39) Deforest, C. A.; Tirrell, D. A. A Photoreversible Protein-Patterning Approach for Guiding Stem Cell Fate in Three-Dimensional Gels. *Nat. Mater.* 2015, 14 (5), 523–531. <https://doi.org/10.1038/nmat4219>.
- (40) Anseth, K. S.; Metters, a T.; Bryant, S. J.; Martens, P. J.; Elisseeff, J. H.; Bowman, C. N. In Situ Forming Degradable Networks and Their Applications in Tissue Engineering and Drug Delivery. *J. Cont. Rel.* 2002, 78 (1–3), 199–209.
- (41) Rizzi, S. C.; Hubbell, J. A. Recombinant Protein- Co -PEG Networks as Cell-Adhesive and Proteolytically Degradable Hydrogel Matrixes. Part I: Development and Physicochemical Characteristics. *Biomacromolecules* 2005, 6 (3), 1226–1238. <https://doi.org/10.1021/bm049614c>.
- (42) Rizzi, S. C.; Ehrbar, M.; Halstenberg, S.; Raeber, G. P.; Schmoekel, H. G.; Hagenmüller, H.; Müller, R.; Weber, F. E.; Hubbell, J. A.; Hubbell, J. A. Recombinant Protein-Co-PEG Networks as Cell-Adhesive and Proteolytically Degradable Hydrogel Matrixes. Part II: Biofunctional Characteristics. *Biomacromolecules* 2006, 7 (11), 3019–3029. <https://doi.org/10.1021/bm060504a>.
- (43) Gonen-Wadmany, M.; Oss-Ronen, L.; Seliktar, D. Protein-Polymer Conjugates for Forming Photopolymerizable Biomimetic Hydrogels for Tissue Engineering. *Biomaterials* 2007, 28 (26), 3876–3886. <https://doi.org/10.1016/j.biomaterials.2007.05.005>.

- (44) Wang, H.; Cai, L.; Paul, A.; Enejder, A.; Heilshorn, S. C. Hybrid Elastin-like Polypeptide-Polyethylene Glycol (ELP-PEG) Hydrogels with Improved Transparency and Independent Control of Matrix Mechanics and Cell Ligand Density. *Biomacromolecules* 2014, 15 (9), 3421–3428. <https://doi.org/10.1021/bm500969d>.
- (45) McGann, C. L.; Dumm, R. E.; Jurusik, A. K.; Sidhu, I.; Kiick, K. L. Thiol-Ene Photocrosslinking of Cytocompatible Resilin-Like Polypeptide-PEG Hydrogels. *Macromol. Biosci.* 2016, 16, 129–138. <https://doi.org/10.1002/mabi.201500305>.
- (46) McGann, C. L.; Akins, R. E.; Kiick, K. L. Resilin-PEG Hybrid Hydrogels Yield Degradable Elastomeric Scaffolds with Heterogeneous Microstructure. *Biomacromolecules* 2016, 17 (1), 128–140. <https://doi.org/10.1021/acs.biomac.5b01255>.
- (47) Chedly, J.; Soares, S.; Montembault, A.; von Boxberg, Y.; Veron-Ravaille, M.; Mouffle, C.; Benassy, M. N.; Taxi, J.; David, L.; Nothias, F. Physical Chitosan Microhydrogels as Scaffolds for Spinal Cord Injury Restoration and Axon Regeneration. *Biomaterials* 2017, 138, 91–107. <https://doi.org/10.1016/j.biomaterials.2017.05.024>.
- (48) Schneider, M. C.; Chu, S.; Sridhar, S. L.; de Roucy, G.; Vernerey, F. J.; Bryant, S. J. Local Heterogeneities Improve Matrix Connectivity in Degradable and Photoclickable Poly(Ethylene Glycol) Hydrogels for Applications in Tissue Engineering. *ACS Biomater. Sci. Eng.* 2017, 3, 2480–2492. <https://doi.org/10.1021/acsbiomaterials.7b00348>.
- (49) Meco, E.; Lampe, K. J. Microscale Architecture in Biomaterial Scaffolds for Spatial Control of Neural Cell Behavior. *Front. Mater.* 2018, 5 (2). <https://doi.org/10.3389/fmats.2018.00002>.
- (50) Benitez, P. L.; Sweet, J. A.; Fink, H.; Chennazhi, K. P.; Nair, S. V.; Enejder, A.; Heilshorn, S. C. Sequence-Specific Crosslinking of Electrospun, Elastin-Like Protein Preserves Bioactivity and

- Native-Like Mechanics. *Adv. Healthc. Mater.* 2013, 2 (1), 114–118.
<https://doi.org/10.1002/adhm.201200115>.
- (51) Benitez, P. L.; Mascharak, S.; Proctor, A. C.; Heilshorn, S. C. Use of Protein-Engineered Fabrics to Identify Design Rules for Integrin Ligand Clustering in Biomaterials. *Integr. Biol. (Camb)*. 2016, 8 (1), 50–61. <https://doi.org/10.1039/c5ib00258c>.
- (52) Desai, M. S.; Wang, E.; Joyner, K.; Chung, T. W.; Jin, H. E.; Lee, S. W. Elastin-Based Rubber-Like Hydrogels. *Biomacromolecules* 2016, 17 (7), 2409–2416.
<https://doi.org/10.1021/acs.biomac.6b00515>.
- (53) Gong, J. P.; Katsuyama, Y.; Kurokawa, T.; Osada, Y. Double-Network Hydrogels with Extremely High Mechanical Strength. *Adv. Mater.* 2003, 15 (14), 1155–1158.
<https://doi.org/10.1002/adma.200304907>.
- (54) Ouyang, L.; Highley, C. B.; Rodell, C. B.; Sun, W.; Burdick, J. A. 3D Printing of Shear-Thinning Hyaluronic Acid Hydrogels with Secondary Cross-Linking. *ACS Biomater. Sci. Eng.* 2016, 2 (10), 1743–1751. <https://doi.org/10.1021/acsbio.6b00158>.
- (55) Chaudhuri, O.; Gu, L.; Klumpers, D.; Darnell, M.; Bencherif, S. A.; Weaver, J. C.; Huebsch, N.; Lee, H.; Lippens, E.; Duda, G. N.; Mooney, D. J. Hydrogels with Tunable Stress Relaxation Regulate Stem Cell Fate and Activity. *Nat. Mater.* 2015, No. November.
<https://doi.org/10.1038/nmat4489>.
- (56) Chung, C.; Lampe, K. J.; Heilshorn, S. C. Tetrakis(Hydroxymethyl) Phosphonium Chloride as a Covalent Cross-Linking Agent for Cell Encapsulation within Protein-Based Hydrogels. *Biomacromolecules* 2012, 13 (12), 3912–3916. <https://doi.org/10.1021/bm3015279>.

- (57) Van Hove, A. H.; Wilson, B. D.; Benoit, D. S. W. Microwave-Assisted Functionalization of Poly(Ethylene Glycol) and On-Resin Peptides for Use in Chain Polymerizations and Hydrogel Formation. *J. Vis. Exp.* 2013, No. 80, e50890. <https://doi.org/10.3791/50890>.
- (58) Fairbanks, B. D.; Schwartz, M. P.; Bowman, C. N.; Anseth, K. S. Photoinitiated Polymerization of PEG-Diacrylate with Lithium Phenyl-2,4,6-Trimethylbenzoylphosphinate: Polymerization Rate and Cytocompatibility. *Biomaterials* 2009, 30 (35), 6702–6707. <https://doi.org/10.1016/j.biomaterials.2009.08.055>.
- (59) Ritger, P. L.; Peppas, N. A. A Simple Equation for Description of Solute Release I. Fickian and Non-Fickian Release from Non-Swellable Devices in the Form of Slabs, Spheres, Cylinders or Discs. *J. Control. Release* 1987, 5 (1), 23–36. [https://doi.org/10.1016/0168-3659\(87\)90034-4](https://doi.org/10.1016/0168-3659(87)90034-4).
- (60) Lee, S.; Tong, X.; Yang, F. The Effects of Varying Poly(Ethylene Glycol) Hydrogel Crosslinking Density and the Crosslinking Mechanism on Protein Accumulation in Three-Dimensional Hydrogels. *Acta Biomater.* 2014, 10 (10), 4167–4174. <https://doi.org/10.1016/j.actbio.2014.05.023>.
- (61) Lim, D. W.; Nettles, D. L.; Setton, L. A.; Chilkoti, A. Rapid Cross-Linking of Elastin-like Polypeptides with (Hydroxymethyl)Phosphines in Aqueous Solution. *Biomacromolecules* 2007, 8 (5), 1463–1470. <https://doi.org/10.1021/bm061059m>.
- (62) Trabbic-Carlson, K.; Setton, L. A.; Chilkoti, A. Swelling and Mechanical Behaviors of Chemically Cross-Linked Hydrogels of Elastin-like Polypeptides. *Biomacromolecules* 2003, 4 (3), 572–580. <https://doi.org/10.1021/bm025671z>.
- (63) Sun, J. Y.; Zhao, X.; Illeperuma, W. R. K.; Chaudhuri, O.; Oh, K. H.; Mooney, D. J.; Vlassak, J. J.; Suo, Z. Highly Stretchable and Tough Hydrogels. *Nature* 2012, 489 (7414), 133–136. <https://doi.org/10.1038/nature11409>.

- (64) Browning, M. B.; Wilems, T.; Hahn, M.; Cosgriff-Hernandez, E. Compositional Control of Poly(Ethylene Glycol) Hydrogel Modulus Independent of Mesh Size. *J. Biomed. Mater. Res. - Part A* 2011, 98 A (2), 268–273. <https://doi.org/10.1002/jbm.a.33109>.
- (65) Bryant, S. J.; Anseth, K. S. Hydrogel Properties Influence ECM Production by Chondrocytes Photoencapsulated in Poly(Ethylene Glycol) Hydrogels. *J. Biomed. Mater. Res.* 2002, 59 (1), 63–72. <https://doi.org/10.1002/jbm.1217>.
- (66) Aisenbrey, E. A.; Tomaschke, A.; Kleinjan, E.; Muralidharan, A.; Pascual-Garrido, C.; McLeod, R. R.; Ferguson, V. L.; Bryant, S. J. A Stereolithography-Based 3D Printed Hybrid Scaffold for In Situ Cartilage Defect Repair. *Macromol. Biosci.* 2018, 18 (2). <https://doi.org/10.1002/mabi.201700267>.
- (67) Lampe, K. J.; Mooney, R. G.; Bjugstad, K. B.; Mahoney, M. J. Effect of Macromer Weight Percent on Neural Cell Growth in 2D and 3D Nondegradable PEG Hydrogel Culture. *J. Biomed. Mater. Res. - Part A* 2010, 94 (4), 1162–1171. <https://doi.org/10.1002/jbm.a.32787>.
- (68) Waters, J. C. Accuracy and Precision in Quantitative Fluorescence Microscopy. *J. Cell Biol.* 2009, 185 (7), 1135–1148. <https://doi.org/10.1083/jcb.200903097>.
- (69) Weber, L. M.; Lopez, C. G.; Anseth, K. S. Effects of PEG Hydrogel Crosslinking Density on Protein Diffusion and Encapsulated Islet Survival and Function. *J. Biomed. Mater. Res. A* 2009, 90 (3), 720–729. <https://doi.org/10.1002/jbm.a.32134>.
- (70) Gaigalas, A. K.; Hubbard, J. B.; McCurley, M.; Woo, S. Diffusion of Bovine Serum Albumin in Aqueous Solutions. *J. Phys. Chem.* 1992, 96 (5), 2355–2359. <https://doi.org/10.1021/j100184a063>.

- (71) Zustiak, S. P.; Boukari, H.; Leach, J. B. Solute Diffusion and Interactions in Cross-Linked Poly(Ethylene Glycol) Hydrogels Studied by Fluorescence Correlation Spectroscopy. *Soft Matter* 2010, 6 (15), 3609. <https://doi.org/10.1039/c0sm00111b>.
- (72) Wang, H.; Zhu, D.; Paul, A.; Cai, L.; Enejder, A.; Yang, F.; Heilshorn, S. C. Covalently Adaptable Elastin-Like Protein–Hyaluronic Acid (ELP–HA) Hybrid Hydrogels with Secondary Thermoresponsive Crosslinking for Injectable Stem Cell Delivery. *Adv. Funct. Mater.* 2017, 27 (28), 1–11. <https://doi.org/10.1002/adfm.201605609>.
- (73) Sallach, R. E.; Cui, W.; Balderrama, F.; Martinez, A. W.; Wen, J.; Haller, C. A.; Taylor, J. V.; Wright, E. R.; Long, R. C.; Chaikof, E. L. Long-Term Biostability of Self-Assembling Protein Polymers in the Absence of Covalent Crosslinking. *Biomaterials* 2010, No. 31, 5371–5379. <https://doi.org/10.1016/j.biomaterials.2011.04.009>.
- (74) Madl, C. M.; Heilshorn, S. C. Tyrosine-Selective Functionalization for Bio-Orthogonal Cross-Linking of Engineered Protein Hydrogels. *Bioconjug. Chem.* 2017, 28 (3), 724–730. <https://doi.org/10.1021/acs.bioconjchem.6b00720>.
- (75) Madl, C. M.; Katz, L. M.; Heilshorn, S. C. Bio-Orthogonally Crosslinked, Engineered Protein Hydrogels with Tunable Mechanics and Biochemistry for Cell Encapsulation. *Adv. Funct. Mater.* 2016, 26 (21), 3612–3620. <https://doi.org/10.1002/adfm.201505329>.
- (76) Truong, V. X.; Zhou, K.; Simon, G. P.; Forsythe, J. S. Nitrile Oxide-Norbornene Cycloaddition as a Bioorthogonal Crosslinking Reaction for the Preparation of Hydrogels. *Macromolecular Rapid Commun.* 2015, 36, 1729–1734. <https://doi.org/10.1002/marc.201500314>.
- (77) Roberts, J. J.; Bryant, S. J. Comparison of Photopolymerizable Thiol-Ene PEG and Acrylate-Based PEG Hydrogels for Cartilage Development. *Biomaterials* 2013, 34 (38), 9969–9979. <https://doi.org/10.1016/j.biomaterials.2013.09.020>.

4. Guiding oligodendrocyte precursor cell maturation with urokinase plasminogen activator-degradable elastin-like protein hydrogels

Submitted for review as: E. Meco, WS Sharon, AH Sharma and KJ Lampe,” Guiding oligodendrocyte precursor cell maturation with urokinase plasminogen activator-degradable elastin-like protein hydrogels,” in Biomacromolecules

4.1. Abstract

Demyelinating injuries and diseases, like multiple sclerosis, affect millions of people worldwide. Oligodendrocyte precursor cells (OPCs) have the potential to repair demyelinated tissue because they can both self-renew and differentiate into oligodendrocytes (OLs), the myelin producing cells of the central nervous system (CNS). Cell-matrix interactions impact OPC differentiation into OLs, but the process is not fully understood. Biomaterial hydrogel systems help to elucidate cell-matrix interactions because they can mimic specific properties of native CNS tissue in an *in vitro* setting. We investigated whether OPC maturation into OLs is influenced by interacting with a urokinase plasminogen activator (uPA) degradable extracellular matrix (ECM). uPA is a proteolytic enzyme that is transiently upregulated in the developing rat brain, with peak uPA expression correlating with an increase in myelin production *in vivo*. OPC-like cells isolated through the Mosaic Analysis with Double Marker technique (MADM OPCs) produced low molecular weight uPA in culture. MADM OPCs were encapsulated into two otherwise similar elastin-like protein (ELP) hydrogel systems: one that was uPA degradable and one that was non-degradable. Encapsulated MADM OPCs had similar viability, proliferation, and metabolic activity in uPA degradable and non-degradable ELP hydrogels. Expression of OPC maturation-associated

genes, however, indicated that uPA degradable ELP hydrogels promoted MADM OPC maturation although not sufficiently for these cells to differentiate into OLs.

4.2. Introduction

Biomaterial hydrogel systems are effective cell carriers that support high transplanted cell viability in the context of cytotoxic extracellular environments^{1,2}. In order to improve the disease treatment potential of hydrogel systems, current research efforts focus on designing biomaterial systems that interact with encapsulated cells to induce desired behavior³. Demyelinating injuries and diseases, like multiple sclerosis (MS), affect millions of people worldwide⁴. The progression of demyelinating injuries and diseases damages central nervous system (CNS) oligodendrocytes, which extend processes to wrap an insulating myelin sheath around neuronal axons. This myelin supports nerves in the CNS by helping to propagate synaptic signals and provide trophic support to ensheathed axons^{5,6}. Oligodendrocyte precursor cells (OPCs) have the potential to repair damaged tissue because they can both self-renew and differentiate into OLs. However, endogenous OPCs are minimally able to repair demyelinated tissue because, in part, the extracellular matrix (ECM) within these lesions is not conducive for OPCs to migrate, differentiate, and replace damaged OLs^{7,8}. A key factor in the development of treatments for demyelinated tissue is to design hydrogel systems that promote OPC maturation into OLs.

OPC maturation into OLs is affected by many extrinsic factors, such as ECM stiffness and the presence of fibronectin⁸⁻¹⁰. In this study we investigated the influence of urokinase plasminogen activator (uPA) enzymatic activity and 3D uPA-responsive hydrogels on OPC maturation. uPA is a serine protease enzyme involved in ECM remodeling, and acts as an activator of the plasminogen system¹¹. uPA expression *in vivo* indicates that it plays a key role in the OPC maturation process. During rat development, uPA is transiently expressed in myelinating regions

(corpus collosum and fimbria) of the brain¹². Peak uPA expression in these regions occurs around postnatal day 14 (P14), and it is lost by adulthood (P56)¹². Peak myelin development (P10-17) in many myelinated regions of the rat brain coincides with peak uPA expression¹³. Further evidence that indicates uPA may play a role in OPC maturation comes from the impact it has on cell morphology. OPC maturation into OLs is marked by a morphological increase in the number of processes extended and branching of those processes¹⁴. Although no study has tested the effects of uPA expression changes on OPC morphology, its expression affects cellular process extension. Pharmacological inhibition of uPA in dorsal root ganglia explants encapsulated within a Matrigel matrix reduced the average axon length by 66 %¹⁵.

uPA may also impact OPC maturation indirectly through its role as an activator of the plasminogen system, which upregulates the expression of many matrix metalloproteinases (MMPs)¹¹. In particular, MMP-9 may promote OPC maturation because it is upregulated in the corpus collosum and optic nerve regions during developmental myelination in mice^{16,17}. MMP-9 also plays a significant role in the subsequent remyelination of demyelinated lesions post injury. MMP-9 null mice were found to have reduced remyelination 1-week post lysolecithin-induced demyelination spinal cord injury when compared to wild type mice¹⁶. The reduction in remyelination correlated with less mature OLs present within the injury lesion of MMP-9 null mice compared to wild type mice¹⁶. Taken together, previous findings indicate that uPA may affect OPC maturation either directly through ECM remodeling and/or indirectly through the plasminogen activation of MMP-9. Hydrogel systems that promote uPA expression could therefore also stimulate OPC maturation.

Hydrogels made from cross-linked elastin-like proteins (ELPs) are suitable for cell encapsulation¹⁸⁻²². Engineered ELPs are designed based on native tropoelastin, and consist of

repeating the penta-peptide sequence valine-proline-glycine-x-glycine (VPGxG), where x is any amino acid guest residue except for proline. ELPs exhibit a unique lower critical solution temperature (LCST) transition²³⁻²⁵. Above a sequence dependent transition temperature (T_i) the protein separates into a protein-rich coacervate phase. Bioactivity, adjunct to the elastin component of the penta-peptide sequence, is incorporated into ELPs by including other peptide sequences in the protein^{19,22,26}. In this study, we use three protein sequences composed of the same elastin-like penta-peptide repeating sequence and differing bioactive peptide sequences: ELP-u1 contains a uPA enzymatically cleavable sequence, ELP-RGD contains a sequence for integrin binding and ELP-RDG contains a sequence that is a scramble of RGD with no integrin-binding activity (Figure 4-1)²⁶. The similarity in the amino acid content (> 98 %) between these three ELPs allows for the creation of hydrogels with adjustable bioactivity (for instance, integrin binding and degradation) independent from the resulting hydrogel mechanical properties^{26,27}. Hydrogel bioactivity can be tuned by adjusting the ratios of each ELP sequence used, and mechanical properties can be tuned by adjusting the total protein concentration and cross-linking ratio. OPC maturation is impacted by both the macromolecular bioactivity and the mechanical properties of the surrounding ECM^{8-10,28,29}. Independent control of ELP hydrogel bioactivity and mechanical properties makes it a suitable *in vitro* model to investigate the impact of extrinsic factors on OPC behavior.

The goal of this study was to determine if OPC maturation could be influenced by incorporating uPA enzymatic degradability into the ELP hydrogel network. Immortalized OPC-like cells isolated from mice using the mosaic analysis with double markers method (MADM OPC) were encapsulated in both uPA degradable and non-degradable ELP hydrogels^{30,31}. MADM OPCs are NF1 and p53 gene knockouts that have delayed maturation *in vivo*. No current *in vitro* method to differentiate them into mature OLs exists^{30,31}. We aimed to test whether or not MADM OPCs

expressed uPA, to determine if encapsulating MADM OPCs in uPA degradable hydrogels would impact MADM OPC uPA expression, and to determine if uPA degradable hydrogels influenced MADM OPC maturation state.

4.3. Experimental Methods

4.3.1. Materials

All materials and reagents were purchased from Fisher Scientific, VWR, or Sigma-Aldrich and used without further modification unless otherwise noted.

4.3.2. ELP expression and purification

Three previously established ELP sequences were used (Table 1)²⁶: ELP expression in *Escherichia coli* strain BL21(DE3) was induced with β -isopropyl thiogalactoside and purified as previously described without modification³². Protein yields were 50-130 mg/L.

ELP-u1	MASMTGGQQMG-HHHHH-DDDDK-LQ[LDAS- YAVTGGTARSAPASSA -SA((VPGIG) ₂ VPGKG(VPGIG) ₂) ₃ VP] ₄ LE
ELP-RGD	MASMTGGQQMG-HHHHH-DDDDK-LQ[LDAS- TVYAVTGRGDSPASSAA -SA((VPGIG) ₂ VPGKG(VPGIG) ₂) ₃ VP] ₄ LE
ELP-RDG	MASMTGGQQMG-HHHHH-DDDDK-LQ[LDAS- TVYAVTGRDGSPASSAA -SA((VPGIG) ₂ VPGKG(VPGIG) ₂) ₃ VP] ₄ LE

Table 4-1: The amino acid sequences of ELP-u1, -RGD, and -RDG. Each ELP amino acid sequence contains a T7 tag, His Tag, enterokinase cleavage sequence, elastin-like sequence and a bioactive sequence (in bold).

4.3.3. ELP azide functionalization and characterization

Azide functionalization of primary amines on ELP was performed as previously described with minor modifications^{33,34}. ELP (25 mg/ml) was dissolved in reaction buffer (potassium carbonate (10 mg/ml) in deionized (DI) water). The ELP solution was mixed with 100 μ l copper (II) chloride solution (1 mg/ml in reaction buffer) in an argon purged round bottom flask (RBF).

1H-imidazole-1-sulfonyl azide HCl (25 mg/ml in reaction buffer, Enamine) was added to achieve a lysine residue amine to azide stoichiometric ratio of 14:4. The reaction was incubated for 24 hrs at 25°C with agitation. Azide-functionalized ELP was purified via dialysis using cellulose ester (CE) tubing (3.5-5 kDa molecular weight cut-off (MWCO)). Dialyzed ELP solution was frozen (-80 °C) and lyophilized to yield the final product, a white caked protein with slight red tint. Azide functionalization was confirmed with Fourier-transform infrared spectroscopy (FTIR, Figure B-1, F Perkin Elmer Frontier MIR/NIR spectrometer) and quantified with electrospray ionization-mass spectrometry (ESI-MS, Figure B-2, Thermo Scientific Q Exactive HF-X).

4.3.4. PEG-BCN synthesis and characterization

4-arm poly(ethylene glycol) amine (PEG-amine) was functionalized with strained alkyne rings (BCN) as previously described with minor modifications³⁵. PEG-amine (10 kDa, Laysan Bio) was dissolved in dimethylformamide (DMF) at a concentration of 200 mg/ml. In an argon purged RBF, PEG-amine was mixed with (1R, 8S, 9s)-Bicyclo[6.1.0]non-4-yn-9-ylmethyl N-succinimidyl carbonate (BCN-NHS) at a stoichiometric ratio of 1.5:1 BCN-NHS to amine groups. N,N-Diisopropylethylamine (DIEA) was added to the reaction mixture to achieve a 4:1 molar ratio DIEA to amine groups. The reaction mixture was stirred for 24 hrs at 25°C. The reaction mixture was diluted with DI water (20/80 v/v % reaction mixture/DI water), and the reacted product (PEG-BCN) was purified via dialysis using CE tubing (500-1,000 Da MWCO). Dialyzed PEG-BCN solution was frozen (-80 °C) and lyophilized to yield a white powder. PEG-BCN was dissolved in phosphate buffered saline (PBS, 200 mg/ml) and stored frozen (-80°C). PEG-BCN strained alkyne functionalization was quantified via proton nuclear magnetic resonance (HNMR, Varian INOVA 500 MHz Spectrometer) by comparing the PEG backbone peak (3.63 ppm) integral value to those of the attached BCN (0.92, 1.34, 1.57, and 2.24 ppm).

4.3.5. *ELP LCST measurements*

ELP and ELP azide were dissolved in PBS (50 mg/ml). 300 μ l of each ELP solution and a PBS blank were pipetted into a 96-well plate. Absorbance was measured at 300 nm (BMG LABTECH CLARIOstar monochromatic microplate reader) for temperatures from 23 – 40 °C at 0.5 °C increments with a 0.5 °C/min temperature ramp. Samples were shaken at 300 rpm before each measurement. The T_t was calculated as the center point of the temperature range where the absorbance rapidly increased.

4.3.6. *MADM OPC culture*

MADM OPCs were cultured on T-75 plates, coated with polyornithine, using base media, which consisted of DMEM, high glucose (4.5 g/L), pyruvate supplemented with Penicillin-Streptomycin (1x), B27 supplement (1x), and N2 supplement (1x). At 90 % confluency MADM OPCs were extracted using trypsin (0.5x), counted using a Bright-Line Hemocytometer, and suspended in PBS. For monolayer cell cultures MADM OPCs were seeded at a density of 1×10^4 cells/cm², and hydrogel encapsulations were performed at a concentration of 5×10^5 cells/ml. Media was changed every two days.

4.3.7. *Hydrogel formation*

Azide-functionalized ELP and PEG-BCN were dissolved in PBS and kept on ice prior to mixing. Gelation was performed by mixing the appropriate ELP and PEG-BCN solutions to form 10 wt % ELP hydrogels with a 0.5:1 BCN to azide stoichiometric cross-linking ratio; uPA degradable hydrogels consisted of a 50/50 % mixture of ELP-RGD and ELP-u1 sequences, and non-degradable gels consisted of a 50/50 % mixture of ELP-RGD and ELP-RDG sequences.

For MADM OPC encapsulations ELP was sterilized with ultraviolet light (UV) irradiation prior to dissolving in PBS. PEG-BCN solutions were sterilized by passing through a syringe filter

(0.2 μm). Hydrogels were formed by mixing ELP, MADM OPC and PEG-BCN solutions together and pipetting 25 μl into 5 mm diameter molds (final concentrations as previously stated). Gelation proceeded by incubating solutions at room temperature for 30 min, followed by 30 min at 37 $^{\circ}\text{C}$. Hydrogels were immersed in 700 μl base media.

4.3.8. *Rheological measurements*

Rheological measurements were conducted on an Anton Paar MCR 302 rheometer using a 25 mm cone and plate measuring probe with the stage set to 22 $^{\circ}\text{C}$. Azide-functionalized ELP and PEG-BCN solutions were kept on ice. Gelation was performed on the rheometer stage with the final concentrations as previously stated. 60 μl of the gel mixture was pipetted onto the stage for measurements. Time sweeps were conducted for 20 min with constant 1% strain and 1 Hz frequency. Strain sweeps were conducted with a logarithmic ramp from 0.01-1,000 % at a constant 1 Hz frequency. Frequency sweeps were conducted with a logarithmic ramp from 0.01-10 Hz at a constant 5 % strain. Stress relaxation was measured by holding the ELP hydrogels at 10 % strain for 15 min.

4.3.9. *Zymography*

The poly(acrylamide) gels were formed by immobilizing ELP onto the separating gel of a sodium dodecyl sulfate-polyacrylamide gel electrophoresis (SDS-PAGE) system. ELP was mixed with enough tetrakis(hydroxymethyl) phosphonium chloride (THPC) to achieve a 1:10 stoichiometric ratio of THPC hydroxyl groups to ELP primary amines, and added to the separating gel solution (2 mg/ml final ELP concentration). The stacking and separating gels were 3.9 and 7.5 % acrylamide, respectively.

Samples were collected as follows prior to use. Commercial uPA was diluted in PBS after purchase. MADM OPC base media was concentrated 30x using a protein concentrator PES

(10,000 MWCO). Cultured MADM OPC media, collected from both monolayers and hydrogels, was centrifuged at 1,000 rpm for 5 min, decanted to remove any pelleted cell debris, and concentrated 30x. MADM OPC monolayer was collected by immersing a cell pellet in lysis buffer at a concentration of 1.1×10^8 cells/ml. Encapsulated MADM OPCs were grown in ELP hydrogels for 4 days and collected by immersing in 700 μ l lysis buffer. Hydrogels were homogenized with a pestle before use. 3 μ l of each sample was mixed with 12 μ l 5x non-reducing buffer (4 % SDS, 20 % glycerol, 0.01 % bromophenol blue, 125 mM TrisHCl (pH 6.8)). 15 μ l of each sample were loaded into the acrylamide stacking gel wells, and electrophoresis was performed at 140 volts for 40 min.

Gels were washed twice for 30 min in washing buffer (2.5 % Triton X-100 in DI water)³⁶. This was followed by a 10 min rinse at 37°C in incubation buffer (0.1 M Glycine pH 8.3 in DI water) with agitation. Gels were then incubated in incubation buffer for 24 hrs at 37°C. Gels were stained with Coomassie blue solution (30/10/60 % methanol/acetic acid/water, Coomassie blue concentration of 5 mg/ml) for 1 hr and destained (30/10/60 % methanol/acetic acid/water) prior to imaging.

4.3.10. MADM OPC degradation of ELP hydrogels

MADM OPCs were encapsulated in uPA degradable and non-degradable hydrogels as previously described. Hydrogels were imaged on days 1, 2 and 3 (Zeiss Axio Observer fluorescent microscope) using green channel to visualize the green fluorescent protein positive (GFP+) OPCs. Tile images were stitched together and oriented in ImageJ software.

4.3.11. Viability analysis

MADM OPCs were encapsulated in uPA degradable and non-degradable hydrogels as previously described and cultured for 3 days. Media was removed and hydrogels underwent three

5 min washes with PBS. Hydrogels were incubated in 700 μ l Dead stain (2 μ M ethidium homodimer solution in PBSG) for 30 min at 37°C. This was followed by three 5 min washes in PBS. For imaging, hydrogels were sealed between two coverslips to prevent dehydration. Z-stacks of each hydrogel sample were taken at 3 xy-locations (Leica SP8 X confocal microscope). Max intensity projections were made of 15 μ m sections along the z-axis, with 15 μ m gaps between sections. Viability was quantified by counting the number of GFP+ cells against Dead stained cells in each max projection.

4.3.12. ATP and DNA quantification

MADM OPCs were encapsulated in ELP hydrogels as previously described and cultured for up to 5 days. Hydrogels were collected in 700 μ l lysis buffer and homogenized with a pestle. ATP was measured using CellTiter-Glo luminescent assay (Promega) using manufacturer's protocol. Homogenized solutions were sonicated for 10 seconds and DNA was measured using Quant-iT PicoGreen assay (Invitrogen) using manufacturer's protocol.

4.3.13. EdU and DAPI imaging

MADM OPCs were encapsulated in ELP hydrogels as previously described and cultured for 3 days. Hydrogels were stained for EdU using the Click-iT EdU Imaging kit (Life Technologies) with minor modification. Briefly, hydrogels were incubated in EdU solution for 1 hr at 37°C. They were then fixed in 3.7 % paraformaldehyde solution for 1 hr at 37°C. Two 5 min washes with 3 % bovine serum albumin (BSA) in PBS were conducted after fixation and in-between the following steps: Hydrogels were permeabilized in 0.5 % Triton X-100 for 20 min, incubated in Click-iT reaction buffer for 30 min, and incubated in 300 nM DAPI solution for 30 min. Hydrogels were stored in PBS at 4°C prior to imaging.

For imaging, hydrogels were sealed between two coverslips to prevent dehydration. Z-stacks of each hydrogel sample were taken at 5 xy-locations (Zeiss 780 confocal microscope). Max intensity projections were made of 20 μm sections along the z-axis, with 20 μm gaps between sections. Proliferation was quantified by counting the number of EdU+ cells against DAPI and GFP+ cells in each max projection.

4.3.14. *F-Actin and DAPI imaging*

MADM OPCs were encapsulated in ELP hydrogels as previously described and cultured for 4 days. Hydrogels were fixed in 3.7 % paraformaldehyde solution for 1 hr at 37°C. They were then permeabilized in 0.1 % Triton X-100 solution for 30 min. Hydrogels were stained for F-actin with Alexa Fluor 568 phalloidin (Invitrogen) by incubating for 30 min in a phalloidin solution (2 U/ml in PBS with 1 % BSA). Hydrogels were subsequently incubated in 300 nM DAPI solution for 30 min. Three 5 min washes with PBS were performed in-between each step. Images were taken on a Leica SP8 X confocal microscope and processed with ImageJ software.

4.3.15. *RNA quantification*

MADM OPCs were encapsulated in ELP hydrogels as previously described and cultured for up to 5 days. Hydrogels were collected in 700 μl TRIzol Reagent (Invitrogen), homogenized using a pestle, and sonicated for 10 seconds. RNA was isolated using manufacture's protocol without modification. 2 μl GlycoBlue was used to facilitate RNA precipitation. RNA purity was confirmed with 260/280 nm absorbance ratio > 1.7 and 260/230 nm absorbance ratio > 1 (BMG LABTECH CLARIOstar monochromatic microplate reader), and the concentration was normalized to 30 $\mu\text{g}/\text{ml}$. Complimentary DNA (cDNA) was made using an iScript cDNA synthesis kit (Bio-Rad, Bio-Rad CFX connect real-time polymerase chain (RT-PCR) machine). PCR was performed using the SsoAdvanced universal SYBR green supermix kit (Bio-Rad, Bio-Rad CFX

connect RT-PCR machine). Custom primers were used for gene amplification (Table 2, Bio-Rad)^{37,38}.

Gene	Forward Sequence	Reverse sequence
GAPDH	5'-TGTGTCCGTCGTGGATCTGA-3'	5'-TTGCTGTTGAAGTCGCAGGAG-3'
NG2	5'-AGCAAGGAAGTGCAGAGGAG-3'	5'-CATCGAAAGACACCATCACG-3'
PDGFRa	5'-GACGAGACCATCGAGGACAT-3'	5'-GCCTCGGGAACCTTCTCTCT-3'
GalC (O1)	5'-CACAGCTGACCTGGGTGGAT-3'	5'-AGGATCGTGCCGTTCAACAT-3'
MBP	5'-CTCAGAGTCCGACGAGCCTC-3'	5'-GACACGGGCATCCTTGAC-3'
uPA	5'-CCATCCAGTCCTTGCGTGTC-3'	5'-AGTACACTGCCACCTTCAGAGT-3'

Table 4-2: List of primers used for quantitative reverse transcription polymerase chain reaction (RT-qPCR).

4.3.16. Statistical analysis

Data is presented as average \pm standard error (SE). Statistical analysis was performed with the student T-test, and significance was determined by $p < 0.05$.

4.4. Results and Discussion

4.4.1. Azide functionalization of ELPs

Primary amines on each ELP sequence were modified with azides using the diazo transfer reaction (Figure 4-1)^{33,34}. Azide modification was confirmed by the appearance of a peak at 2100 cm^{-1} on the FTIR spectrum, and the intensity of the peak increased with the addition of more azide groups (Figure B-1). The number of azides attached to each ELP molecule were quantified with high resolution ESI-MS (Figure B-2). The conversion of each primary amine into an azide group resulted in a 26 Da increase in the protein molecular weight (Mw, Figure B-2A). One peak appeared

in the mass spectra of the pre-modified ELP sequences, confirming that the expression and purification process produced a monodisperse protein (Figure B-2 B-D)²⁷. Post diazo transfer reaction, the ELP mass spectra had multiple peaks, confirming that the reaction resulted in a distribution of azide addition (Figure B-2 B-D)³⁴. The mass increase of each of these peaks, relative to the unmodified ELP peak, was used to determine the number of azides attached, and the relative peak intensities were used to quantify the azide functionalization distribution. On average 6.28, 3.78, and 3.74 azide groups were added to ELP-u1, ELP-RGD, and ELP-RDG sequences used for MADM OPC encapsulations, respectively. We extended the findings of previous literature here by demonstrating that the average number of azide groups added to a protein can be controlled by stoichiometrically limiting the amount of azide available during the diazo transfer reaction.

The addition of azide groups to ELPs decreased their T_t (Figure 4-2A). This occurred because the conversion of amines into azide functional groups increases the hydrophobicity of ELPs³⁹. Similar work demonstrated that the opposite effect occurs when ELP methionine residue side chains were modified to become more hydrophilic⁴⁰. In addition, analogous work demonstrated that the ELP T_t decreases when the guest residue in the penta-peptide repeating sequence is swapped for a more hydrophobic amino acid⁴¹. If we consider the azide modification of lysine residues on these ELPs similar to replacing the lysine guest residue with a more hydrophobic amino acid, then a reduction in the T_t is the expected result. The T_t shift was dependent on the degree of azide functionalization, with the addition of more azide groups resulting in a lower T_t (Figure 4-2B). This is consistent with previous findings that the T_t of ELP sequences decreased as the guest amino acid residues are gradually swapped from alanines to more hydrophobic valines⁴¹. Azide functionalization of ELP-u1, ELP-RGD, and ELP RDG used for MADM OPC

encapsulations shifted the T_i from 35.6, 35, and 34.3°C to 26.6, 25.5 and 24.3°C, respectively (Figure 4-2A).

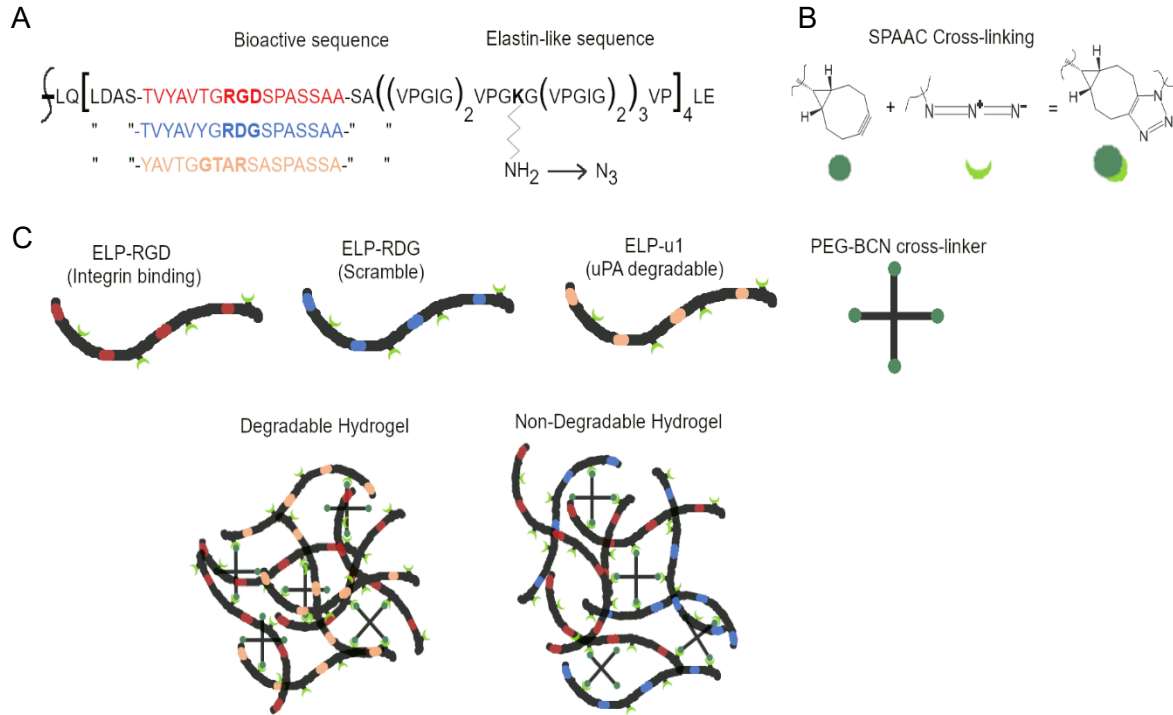


Figure 4-1: Formation of urokinase plasminogen activator (uPA) degradable and non-degradable elastin-like protein (ELP) hydrogels using strain-promoted azide alkyne cycloaddition (SPAAC) chemistry. (A) Three ELP sequences with different bioactivities were used: ELP-RGD promotes integrin binding, ELP-RDG is a non-bioactive scramble, and ELP-u1 is uPA cleavable. Lysine residues on ELP were converted into azide groups. (B) ELPs were cross-linked with 4 arm-PEG-BCN using SPAAC chemistry. (C) uPA degradable hydrogels consisted of a 50/50 % mix of ELP-RGD and ELP-u1, while non-degradable hydrogels consisted of a 50/50 % mix of ELP-RGD and ELP-RDG. Both hydrogels contain identical concentrations of integrin-binding RGD motifs.

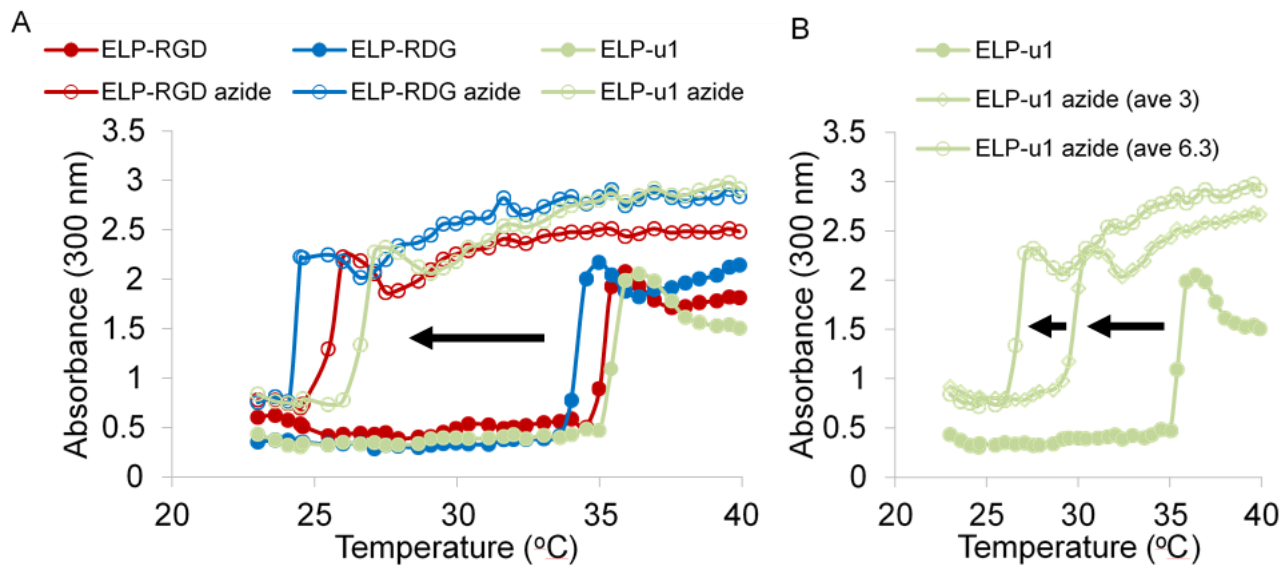


Figure 4-2: ELP LCST shift from azide reaction. (A) The LCST of all ELP sequences decreased when modified with azide groups. (B) The ELP LCST shift was dependent on the number of primary amines converted into azides.

4.4.2. Independent tuning of hydrogel bioactivity from stiffness

Hydrogels were formed by mixing azide-modified ELPs with a PEG-BCN cross-linker using strain-promoted azide alkyne cycloaddition (SPAAC) chemistry (Figure 4-1). uPA degradable hydrogels were formed by mixing ELP-RGD and ELP-u1 in a 1:1 ratio, and non-degradable hydrogels were formed by mixing ELP-RGD and ELP-RDG in a 1:1 ratio (Figure 4-1). Rheological time sweeps confirmed previous studies that indicate SPAAC cross-linking occurs on the order of several minutes (Figure 4-3A)^{33,42}. The crossover where the storage modulus (G') exceeded the loss modulus (G'') indicated that the solution-to-gel transition occurred between 5-6 min for both degradable and non-degradable hydrogels (Figure 4-3A). The cross-linking reaction was completed within 20 min as indicated by the plateauing of G' (Figure 4-3A). These ELP hydrogels have suitable cross-linking rates for cell encapsulation.

The similarity between the ELP sequences should create uPA degradable and non-degradable hydrogels with similar biomechanics^{26,43}. The linear viscoelastic range (LVER) of both hydrogels was 0 - 300 % strain, after which the hydrogel network was irreversibly altered (Figure 4-3B). Most protein-based hydrogels have a much lower LVER, but dosing PEG into hydrogel network results in a LVER resembling that of PEG-based hydrogels^{32,44}. The PEG-BCN crosslinker is large (10 kDa) and the LVER indicated that it impacted the hydrogel biomechanics. The G' and G'' were frequency dependent, which is consistent with previous work (Figure 4-3C)³³. The G' of uPA degradable and non-degradable hydrogels were 1.2 ± 0.14 and 1.42 ± 0.10 kPa (Figure 4-3D), respectively. These G' values were not statistically different, confirming that similar hydrogel stiffness was maintained despite the differences in ELP sequences used (Figure 4-3D). In addition, the G' of both hydrogels was similar to that of native brain tissue white matter tracts (1.895 ± 0.592), where most native OPCs and OLs reside^{45,46}. These ELP hydrogels have biomechanical properties suitable to be *in vitro* mimetics of native brain tissue.

The G'' of non-degradable hydrogels was higher than that of uPA degradable hydrogels (Figure 4-3D). This indicated that non-degradable hydrogels experienced higher viscous losses when strained and translated to a higher degree of stress relaxation (Figure 4-3E). uPA degradable and non-degradable hydrogels dissipated 43 ± 0.013 % and 60 ± 0.013 % of the initial stress within 3.5 min, respectively, before a plateau was reached (Figure 4-3E). Stress relaxation rate differences are known to impact encapsulated mesenchymal stem cell spreading, proliferation and differentiation fate^{47,48}. The stress relaxation rates of uPA degradable and non-degradable hydrogels, as indicated by the slopes of the curves, were similar to each other (Figure 4-3E). In addition, the stress relaxation curves for both hydrogels emulate that of brain, liver and adipose tissue⁴⁷. It is unclear how the difference in the magnitude of stress relaxation impacts encapsulated

cell behavior. Taken together our results indicated that uPA degradable and non-degradable hydrogels had similar, but not identical, biomechanics that mimic native brain tissue.

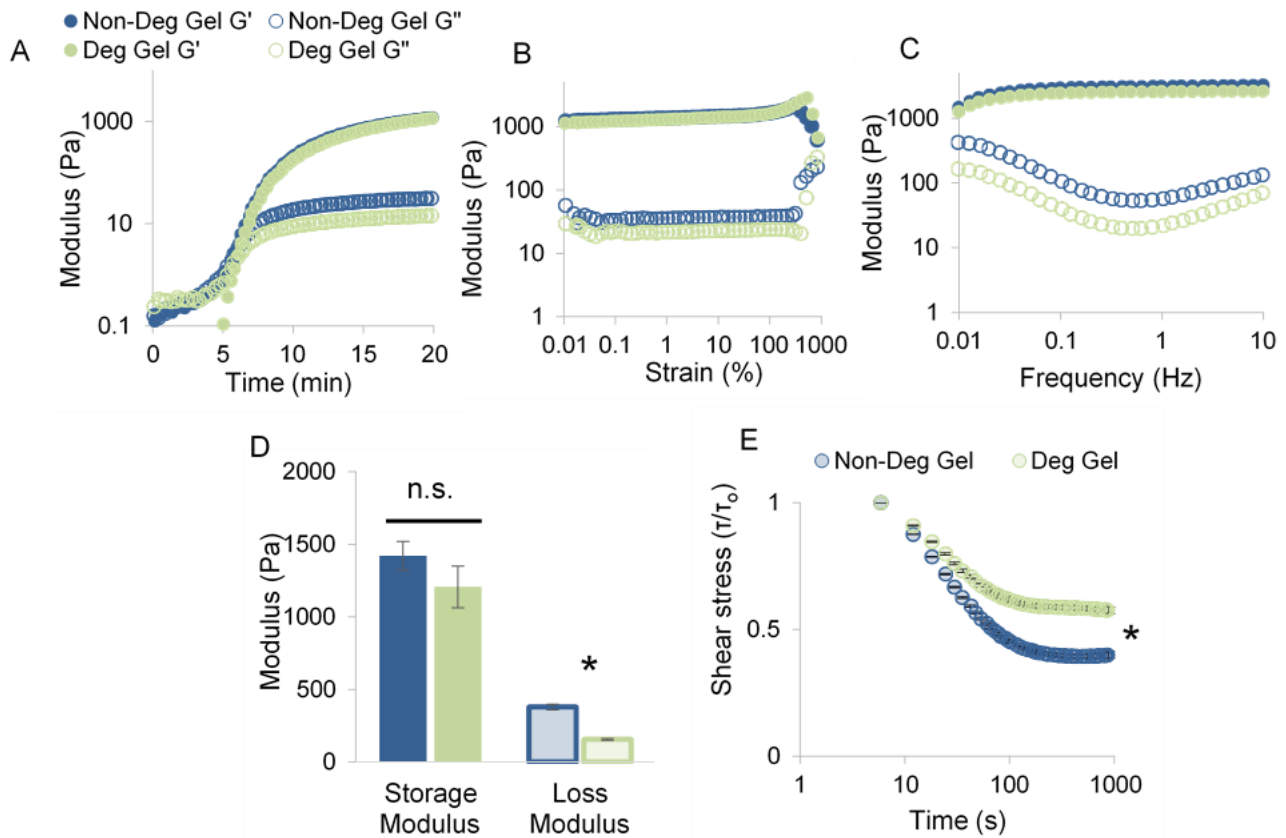


Figure 4-3: Biomechanics of uPA degradable (Deg) and non-degradable (Non-Deg) ELP hydrogels. (A) Representative time sweeps indicate gelation occurs within 6 min and is complete after 20 min. (B) Representative strain sweeps show the linear viscoelastic range exists up to 300 % strain. (C) Representative frequency sweeps demonstrate hydrogel elastic and loss modulus are frequency dependent. (D) The average storage modulus was similar for both hydrogels while the average loss modulus differed. The storage modulus of both hydrogels was consistent with native neural tissue white matter tracts, where oligodendrocyte precursor cells (OPCs) and oligodendrocytes (OLs) reside. (E) uPA degradable and non-degradable hydrogels relax 43 and 60 % of initial stress over 3.5 min, respectively. Error bars represent standard error (SE) ($n \geq 4$). Asterisks indicate statistical significance using student T-test ($p < 0.05$) and n.s. indicates no statistical significance ($p > 0.05$).

4.4.3. MADM OPC uPA expression

We were unsure as to whether or not MADM OPCs expressed uPA because OPC uPA expression *in vivo* is transient, and the p53 and Nf1 gene knockouts may have altered the uPA

expression profile of the MADM OPC line^{12,30,31}. uPA enzymatic activity of MADM OPCs was determined using a modified zymography technique. Traditionally zymography involves co-cross-linking an enzymatically degradable gel (called the substrate), such as gelatin, alongside a poly(acrylamide) gel^{17,21,49,50}. Instead of co-cross-linking ELP alongside poly(acrylamide) we immobilized ELP onto the primary amines readily available on the poly(acrylamide) gel network using THPC, an amine reactive molecule (Figure B-3 A, B). ELP dosed into the poly (acrylamide) gel traveled downwards during electrophoresis, but immobilized ELP remained evenly distributed (Figure B-3 C, D). Given the prevalence of amines in proteins and small peptides, use of this modified zymography technique to determine proteolytic enzymatic activity has extensive utility in the biomaterials field because it expands the number of digestible substrates that can be used. This, in turn, also expands the zymography technique to include exploring the activity of proteolytic enzymes that do not cleave traditionally used substrates like gelatin.

Wells loaded with recombinant uPA and run on a poly(acrylamide) gel dosed with immobilized ELP-u1 confirmed that ELP-u1 was cleavable by both high and low Mw uPA (Figure 4-4A)²⁶. MADM OPCs from a monolayer culture expressed only low Mw uPA, as indicated by a single band that appears adjacent to the low Mw positive control band (Figure 4-4A). The uPA enzyme exists in two Mw's, 51.6 and 34.5 kDa, that have similar peptide cleavage enzymatic activity, but high Mw uPA has a higher affinity for activating the plasminogen system⁵¹. No bands appeared from homogenized MADM OPCs encapsulated in ELP hydrogels (Figure 4-4A). This could mean that MADM OPCs lose their expression of uPA after being encapsulated in ELP hydrogels. However, it is more likely that this zymography technique was not sensitive enough to detect the low quantities of uPA present; the number of cells in the MADM OPC monolayer were ~100x that of MADM OPCs encapsulated within the ELP hydrogels, and we were unable to

homogenize and concentrate 100 gels into a small enough volume. No band appeared from concentrated cell media, indicating that low Mw uPA was expressed by MADM OPCs and not coming from an external source (Figure 4-4A).

Zymograms of poly(acrylamide) gels dosed with immobilized ELP-RGD and ELP-RDG confirmed that these sequences are not cleavable by uPA (Figure 4-4B, C)²⁶. The MADM OPC monolayer also did not produce any band on these zymograms (Figure 4-4B, C). This demonstrated that MADM OPCs did not produce any enzymes capable of cleaving ELP-RGD and ELP-RDG. Although these two sequences were not designed to be enzymatically degradable, cells have the machinery to modify peptides and recent work has shown that ELP-RGD is enzymatically cleavable by a disintegrin and metalloprotease 9 (ADAM9)⁵². No bands appeared on zymograms loaded with conditioned media from MADM OPCs (Figure 4-4D). This confirms that uPA remains bound to the cell membrane in complex with its receptor (uPAR) and is not released into the surrounding environment¹¹.

Fluorescent images of the GFP signal expressed by MADM OPCs demonstrated that they degrade uPA degradable hydrogels (Figure 4-5). Over 3 days, regions with large clusters of cells appeared within the uPA degradable hydrogels. Both the size of the cell clusters and the area of the degraded regions increased over time. We hypothesize that these large cell clusters were a result of cells collapsing onto other cells (along the z-direction) to form multi-layers as the hydrogel matrix was cleaved. In non-degradable hydrogels, MADM OPCs remained homogeneously distributed in small, isolated clusters over the 3 days (Figure 4-5). This type of growth was similar to growth patterns previously observed when MADM OPCs were encapsulated in non-degradable PEG hydrogels⁵³. Taken together, this data demonstrated that MADM OPCs

were able to degrade uPA degradable hydrogels because of their expression of low Mw uPA, and they were unable to remodel the non-degradable ELP hydrogel matrix.

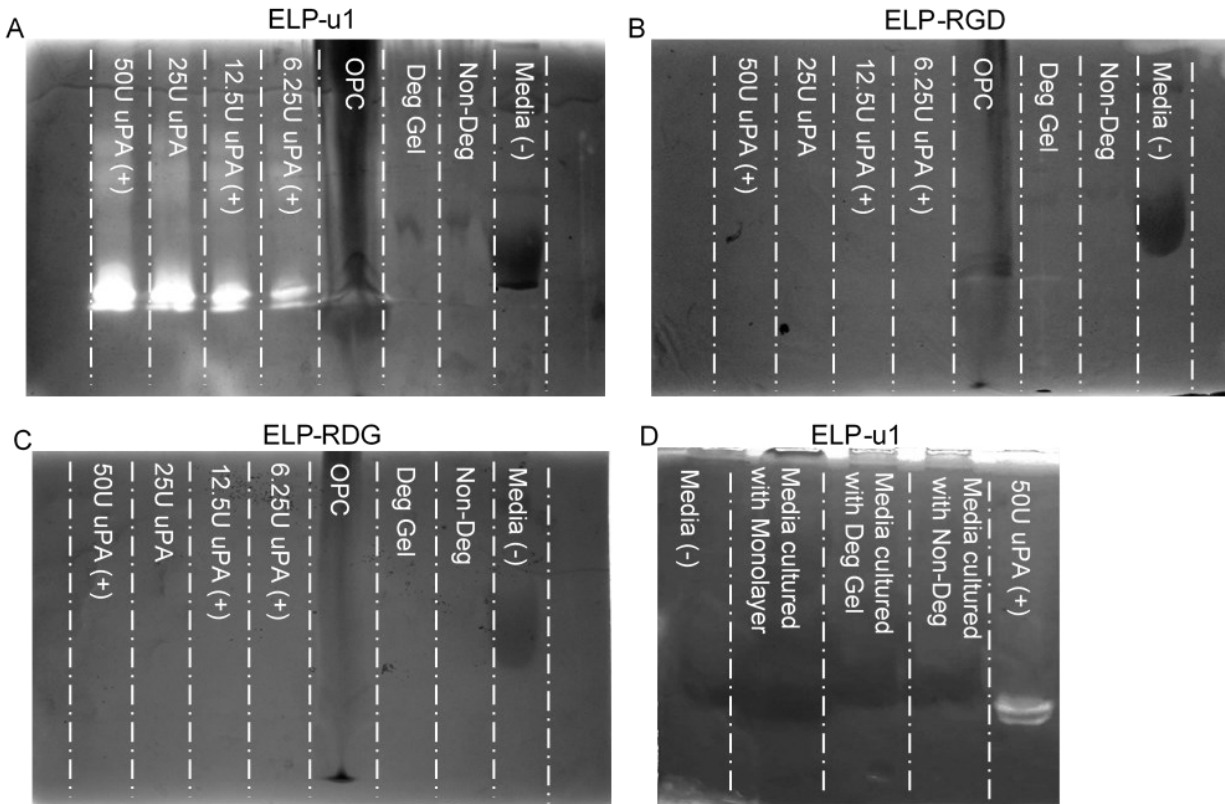


Figure 4-4: Zymograms of poly(acrylamide) gels dosed with immobilized (A, D) ELP-u1, (B) – RGD, (C) –RDG. (A, B, C) MADM OPCs express low molecular weight uPA to cleave ELP-u1, and do not express any enzymes capable of cleaving ELP-RGD and ELP-RDG sequences. Wells loaded with recombinant uPA (positive control), homogenized MADM OPCs grown in monolayer, homogenized MADM OPCs encapsulated in degradable gel, homogenized MADM OPCs encapsulated in non-degradable gel, and base OPC culture media (negative control). (D) Wells of a gel dosed with immobilized ELP-u1 protein were loaded with OPC media (negative control), recombinant uPa (positive control), and conditioned media from OPCs in monolayers, conditioned media from OPCs encapsulated in uPa-degradable hydrogels, and conditioned media from OPCs encapsulated in non-degradable hydrogels. MADM OPCs do not release soluble uPA into the surrounding media environment; it remains cell membrane bound and only found in zymogram wells loaded with homogenized cells.

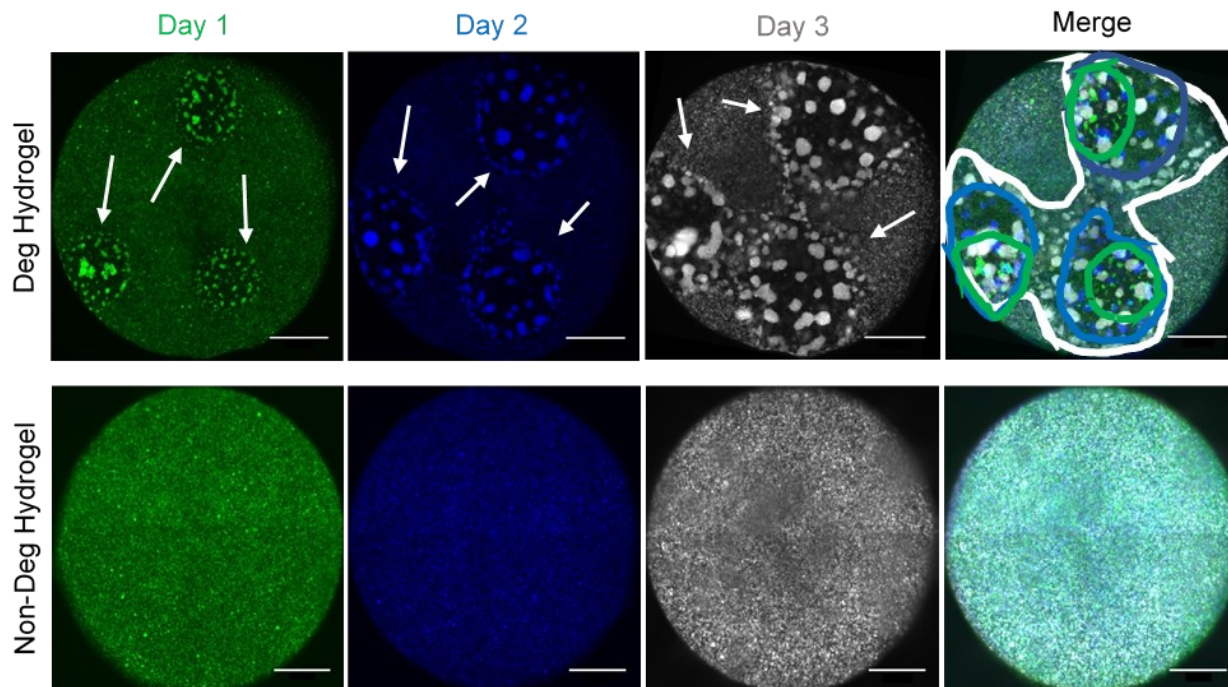


Figure 4-5: MADM OPC GFP+ signal (represented in green for day 1, blue for day 2, and gray for day 3) of representative ELP hydrogels with and without uPA cleavage sites over 3 days. Hydrogels with uPA cleavage sites have regions with visible degradation that increase in area over 3 days. Degradation is not observed in non-degradable hydrogels. Lines in merged degradable hydrogel image display area of degraded region over time; green, blue and white represent day 1, 2, and 3, respectively. Scale bars are 1,000 μm .

4.4.4. Encapsulated MADM OPC metabolic activity

Encapsulated MADM OPCs had similar viability in degradable and non-degradable hydrogels, with 77 ± 3.6 and 80 ± 2.3 % of cells remaining viable after 3 days, respectively (Figure 4-6A, B). The viability of MADM OPCs was on the lower end of what is typically observed for cells encapsulated within ELP hydrogels^{27,33,54}. We attribute the lower viability to the high sensitivity of MADM OPCs towards cross-linking chemistry. MADM OPCs encapsulated in ELPs cross-linked with amine reactive THPC, which is cytocompatible with several cell types^{27,54}, were not viable after gelation (data not shown). SPAAC chemistry is considered bio-orthogonal, meaning it does not cross-react with cellular machinery, however, there could be some reactivity

of the strained alkyne bond with cellular machinery⁵⁵. The increase in ATP and DNA content of MADM OPCs encapsulated over time confirmed that MADM OPCs are viable and proliferative in ELP hydrogels cross-linked using SPAAC chemistry (Figure 4-6C, D).

MADM OPC metabolic activity was similar in both hydrogel systems over 5 days (Figure 4-6C, D, E). While the total ATP and DNA content per hydrogel increased, on a per cells basis (ATP/DNA) there was no statistically significant shift in the metabolic activity over time (Figure 4-6C, D, E). In addition, no statistically significant differences in metabolic activity developed between MADM OPCs encapsulated in uPA degradable hydrogels versus those encapsulated in non-degradable hydrogels (Figure 4-6C, E). The differentiation of OPCs to OLs is marked by a decrease in cellular metabolic activity because OLs are not proliferative while OPCs are⁵⁶. ATP and DNA data did not indicate that uPA degradable hydrogels impacted MADM OPC maturation. MADM OPC proliferation was also similar in both uPA degradable and non-degradable hydrogels (Figure 4-7). While slightly less MADM OPCs were proliferative in uPA degradable hydrogels (33.2 ± 2.8 %) versus non-degradable hydrogels (36.6 ± 3.5 %) on day 3, the difference was not statistically significant (Figure 4-7B). Taken together, the data suggests that MADM OPC viability and metabolic activity was not influenced by the presence of uPA degradability in ELP hydrogels.

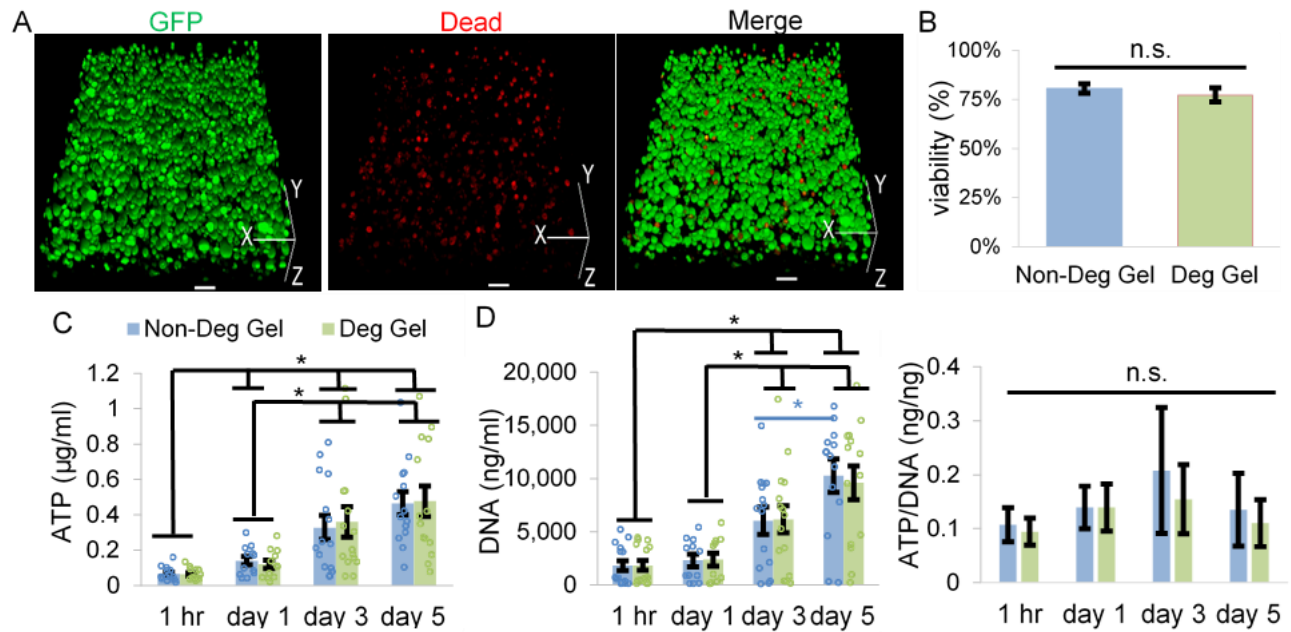


Figure 4-6: Encapsulated MADM OPC viability and metabolic activity. (A) Representative 3D-projection (252 μm z-stack) of MADM OPCs encapsulated and cultured in uPA degradable hydrogel for 3 days (green is GFP, red is dead cells). Scale bars are 100 μm . (B) The viability of MADM OPCs encapsulated in ELP hydrogels was not affected by the uPA-degradability of the hydrogel matrix. Error bars represent SE ($n = 3$). Encapsulated MADM OPC (C) ATP concentration, (D) DNA concentration, and (E) ATP/DNA ratio was similar in both uPA degradable and non-degradable ELP hydrogels over 5 days. Error bars represent SE ($n \geq 12$). Asterisks indicate statistical significance using student T-test ($p < 0.05$) and n.s. indicates no statistical significance ($p > 0.05$).

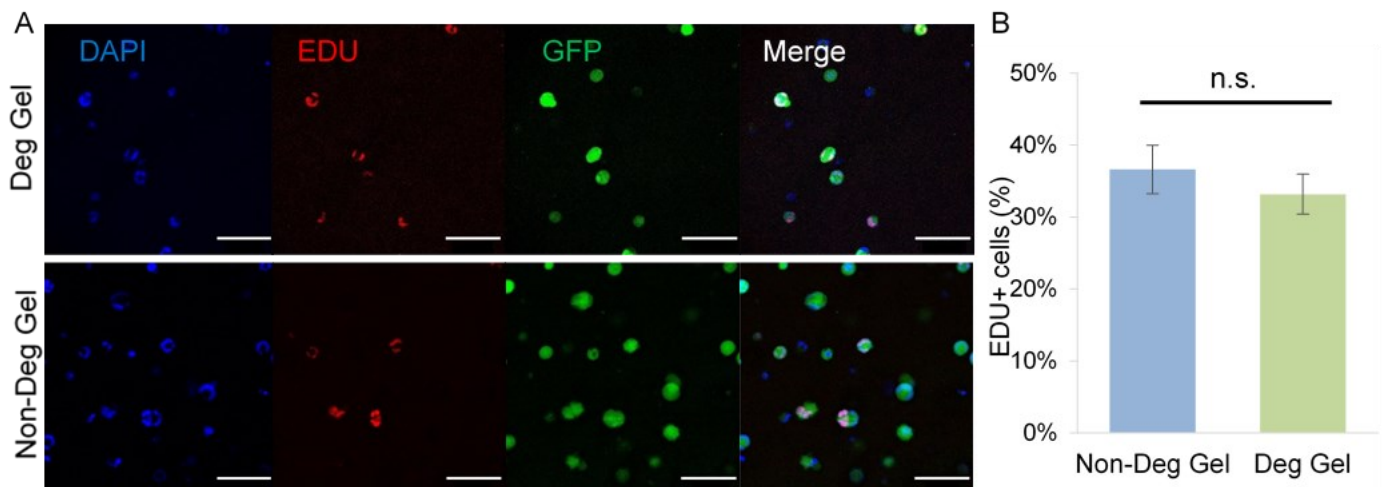


Figure 4-7: Encapsulated MADM OPC proliferation at day 3 of culture. (A) Representative z-projections of 20 μm stacks (blue is DAPI, red is EdU, green is GFP). Scale bars are 100 μm . (B) A similar fraction of encapsulated MADM OPCs were proliferative in uPA degradable and non-degradable hydrogels after 3 days. Error bars represent SE ($n = 3$). n.s. indicates no statistical significance using student T-test ($p > 0.05$).

4.4.5. MADM OPC maturation in ELP hydrogels

OPC maturation to OLs is measured through a morphological increase in process extensions and branching¹⁴. Encapsulated MADM OPC morphology was assessed by labeling f-actin (Figure 4-8). Some encapsulated MADM OPCs extended processes within both uPA degradable and non-degradable hydrogels, but this was limited to cells near the surface of the hydrogels (Figure 4-8A). The vast majority of MADM OPCs, especially ones located deeper into the hydrogel matrix, grew in circular clusters, which is similar to previous work (Figure 4-8A)⁵³. Encapsulated MADM OPC morphology was not indicative of maturation in either hydrogel.

Several gene and protein expression changes occur during OPC maturation⁵⁷⁻⁶¹. We examined encapsulated MADM OPC expression of four genes relevant to the maturation process (Figure 4-9A)^{60,61}. Neural antigen 2 (NG2) and platelet derived growth factor receptor alpha (PDGFR α) are genes expressed by OPCs and their expression decreases as they mature into OLs. The gene expression of these early OPC markers decreased over 5 days in MADM OPCs encapsulated in degradable hydrogels relative to non-degradable hydrogels (Figure 4-9B). NG2 gene expression was higher in uPA degradable hydrogels at day 1, but then decreased from day 1 to day 3. PDGFR α was lower on day 1 in uPA degradable hydrogels and continued to decrease over 5 days. The gene expression of PDGFR α was lower than that of NG2 on day 5, which agrees with previous work that NG2 is expressed up until the immature OL stage, while PDGFR α is exclusively expressed only by OPCs^{60,61}. This data indicated that encapsulated MADM OPCs were moving towards a more mature OPC state in uPA degradable hydrogels.

Expression of the galactosylceramidase (GalC) protein is an identifier for when an OPC has transitioned into an OL, and GalC gene expression precedes this in a similar manner (Figure 4-9A). Increased expression of myelin basic protein (MBP) gene identifies the transition from an

immature OL to a myelinating one (Figure 4-9A). Gene expression of GalC and MBP was higher in MADM OPCs encapsulated in non-degradable hydrogels than those encapsulated in uPA degradable hydrogels (Figure 4-9C). The gene expression of GalC decreased in uPA degradable hydrogels relative to non-degradable hydrogels from day 1 to day 3. MBP gene expression remained static over the 5 days. If MADM OPCs were maturing into OLs, the gene expression of these two markers should have increased over time. Instead MBP is constant and GalC decreases over time. In addition, this data disagrees with previous research that indicates OPCs do not express GalC and MBP⁶⁰. Taken together this data indicates that uPA degradable hydrogels promote MADM OPC maturation, but do not induce the transition from OPC to OL.

Based on all data (morphology, metabolic activity, and OPC gene expression) MADM OPCs encapsulated in uPA degradable hydrogels were not transitioning from OPCs to OLs. The lack of MADM OPC maturation into myelinating OLs could be due to the cell line itself. MADM OPC differentiation *in vivo* is delayed relative to normal development³¹. This is likely caused by disruptions to the Erk 1/2 and mTORC1 pathways that result from the Nf1 and p53 gene knockouts (Figure B-4). In particular, p53 inhibits Akt, which digests Mek 1/2, and activates PTEN, which inhibits PI3K (Figure B-4). The knockout of the p53 gene does not allow for Erk 1/2 to activate and prevents the inhibition of the mTORC1 pathway (Figure B-4). Pharmacological disruptions to the Erk 1/2 and mTORC1 pathways inhibited OPC maturation to OLs *in vitro* and delayed it *in vivo*^{59,62,63}. It is not known what trophic support OPCs receive *in vivo* to overcome disruptions to the Erk 1/2 and mTORC1 pathways. Previous literature indicates that MADM OPC maturation within ELP hydrogels could be affected by disruptions to the Erk 1/2 and mTORC1 pathways.

The zymography technique did not have the sensitivity necessary to quantify uPA enzymatic activity changes from the encapsulation process with densitometry (Figure 4-4). To

determine if encapsulating MADM OPCs in uPA degradable hydrogels affected their expression of uPA, uPA RNA content was measured over 5 days (Figure 4-9D). Encapsulated MADM OPC uPA gene expression was higher in uPA degradable hydrogels relative to non-degradable hydrogels on day 1 (Figure 4-9D). Then the uPA gene expression of MADM OPCs encapsulated in degradable hydrogels dropped below that of MADM OPCs in non-degradable hydrogels on days 3 and 5 (Figure 4-9D). The rapid initial increase in uPA gene expression that was followed by inhibition could be a result of MADM OPCs becoming saturated with uPA after an initial upregulation of transcription. These data demonstrated that MADM OPCs do upregulate uPA gene expression when exposed to uPA degradable hydrogels.

This work demonstrates that the incorporation of enzymatic degradability into hydrogel networks can be used to do more than degrade the material, it can be used to influence cell behavior and fate. Previous literature found that neural progenitor cell (NPC) stemness was maintained within enzymatically degradable hydrogels, and that degradation primed cells for differentiation⁵². uPA degradable hydrogels may have impacted MADM OPCs in a similar manner. MADM OPCs were primed for differentiation by transitioning to a more mature OPC, but maintained their stemness because they never transitioned from OPCs to OLs (Figure 4-9). However, we argue that the specific enzyme(s) used to degrade the hydrogel matrix matters, with different enzymes leading to different cellular outcomes. uPA degradable hydrogels promoted MADM OPC maturation and disruptions to the Erk 1/2 and mTORC1 pathways prevented further differentiation of this cell line (Figure 4-9, Figure B-4). Hydrogel degradation can be utilized to allow encapsulated cells to do more than remodel the matrix; it can be used to curate encapsulated cell behavior.

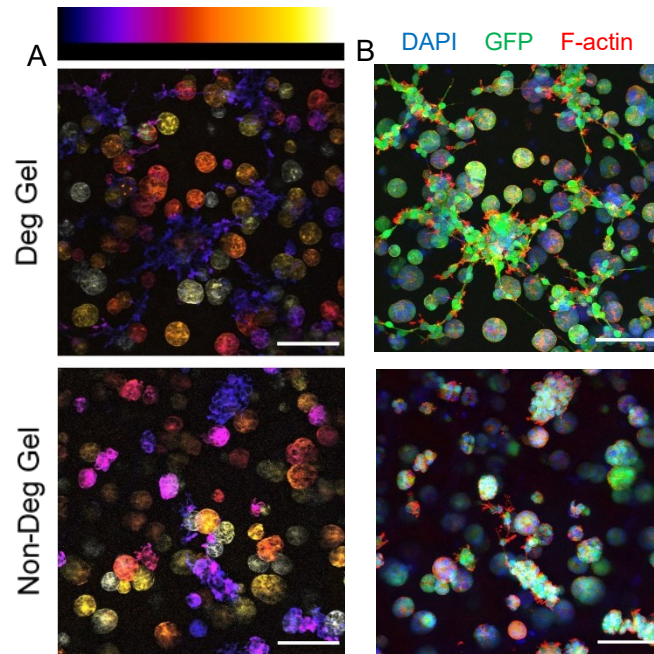


Figure 4-8: Encapsulated MADM OPC morphology. (A) Confocal depth projections display MADM OPC F-actin expression within uPA degradable and non-degradable hydrogels cultured for 4 days. The color indicates the depth from the hydrogel surface (with orange to yellow being deepest into the hydrogel). Encapsulated MADM OPCs appear to only develop significant processes near the surface of ELP hydrogels. (B) Max projection of the stacks shown in Figure 4-8A with blue staining for DAPI, green representing GFP, and red staining for phalloidin. Scale bars are 100 μm .

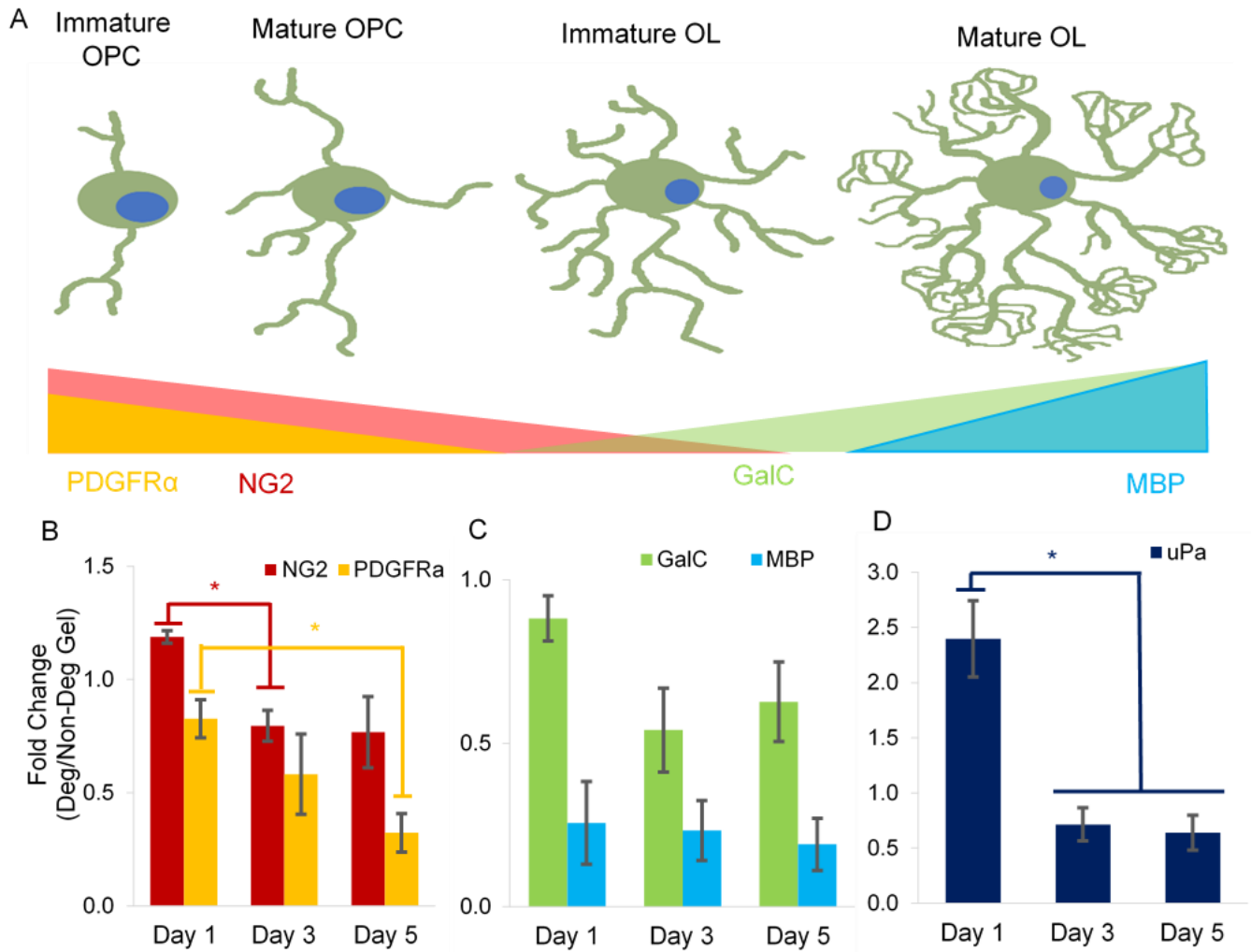


Figure 4-9: Encapsulated MADM OPC gene expression over 5 days. (A) As OPCs differentiate into oligodendrocytes and oligodendrocytes mature, NG2 and PDGFR α gene expression is reduced, while GalC and MBP gene expression increases. (B) Within our 3D hydrogel system, MADM OPC gene expression of NG2 and PDGFR α decreased over time in uPA degradable hydrogels relative to non-degradable hydrogels, indicating that uPA degradation promotes maturation of immature OPCs. (C) MADM OPC gene expression of GalC and MBP do not increase over time when encapsulated in uPA degradable hydrogels relative to non-degradable hydrogels. This indicated that uPA degradation does not induce the fate transition from OPC to OL. (D) uPA gene expression is initially upregulated for MADM OPCs encapsulated in uPA degradable hydrogels before dropping to levels below that of MADM OPCs encapsulated in non-degradable hydrogels. Error bars represent SE (n = 3). Asterisks indicate statistical significance using student T-test ($p < 0.05$).

4.4.6. *Impact of the encapsulation process on MADM OPC gene expression*

We investigated the impact of the encapsulation process on MADM OPC gene expression because the general effects of the encapsulation process on cell behavior are not well studied (Figure 4-10). Encapsulation of MADM OPCs in both hydrogels greatly increased NG2 gene expression relative to MADM OPCs in monolayer cultures on day 1, and while encapsulated MADM OPC NG2 gene expression decreased over time, it never returned to levels observed in MADM OPCs cultured in a monolayer (Figure 4-10A). Gene expression of PDGFR α and GalC followed a similar trend, except the initial gene expression increase was mild, and by day 5 expression fell below levels of MADM OPCs cultured in a monolayer (Figure 4-10B, C). MBP gene expression was found to be different in MADM OPCs encapsulated in degradable and non-degradable hydrogels (Figure 4-10D). In degradable hydrogels MADM OPC MBP gene expression started out higher than MADM OPCs in monolayer cultures and proceeded to decrease to sub-monolayer culture levels overtime (Figure 4-10D). In non-degradable hydrogels, MADM OPC MBP gene expression increased substantially relative to MADM OPCs in monolayer culture on day 1, dropped below monolayer levels on day 3, and then increased again on day 5 (Figure 4-10D). MADM OPC uPA expression was also different in the two hydrogel systems. In uPA degradable hydrogels MADM OPC uPA gene expression was upregulated relative to monolayer cultures initially and then dropped to sub monolayer levels by day 5 (Figure 4-10E). In non-degradable hydrogels MADM OPC uPA gene expression was unaffected initially, then increased briefly on day 3 before returning to monolayer levels on day 5 (Figure 4-10E).

The encapsulation process results in large changes to the MADM OPC extracellular environment, and it is difficult to assess why the observed gene expression changes occurred. The results could be from biomechanical changes like stiffness differences between the ELP hydrogels

and the tissue culture polystyrene (TCPS) on which monolayers are grown, or the introduction of a 3-dimensional mesh to the MADM OPC environment^{9,22}. These gene expression changes could also be induced by bioactivity differences, relative to the plate-based culture system, such as the RGD integrin binding that was incorporated into both uPA degradable and non-degradable ELP hydrogels. We archived the results here to help elucidate the effects of the encapsulation process on gene expression and to inform future studies.

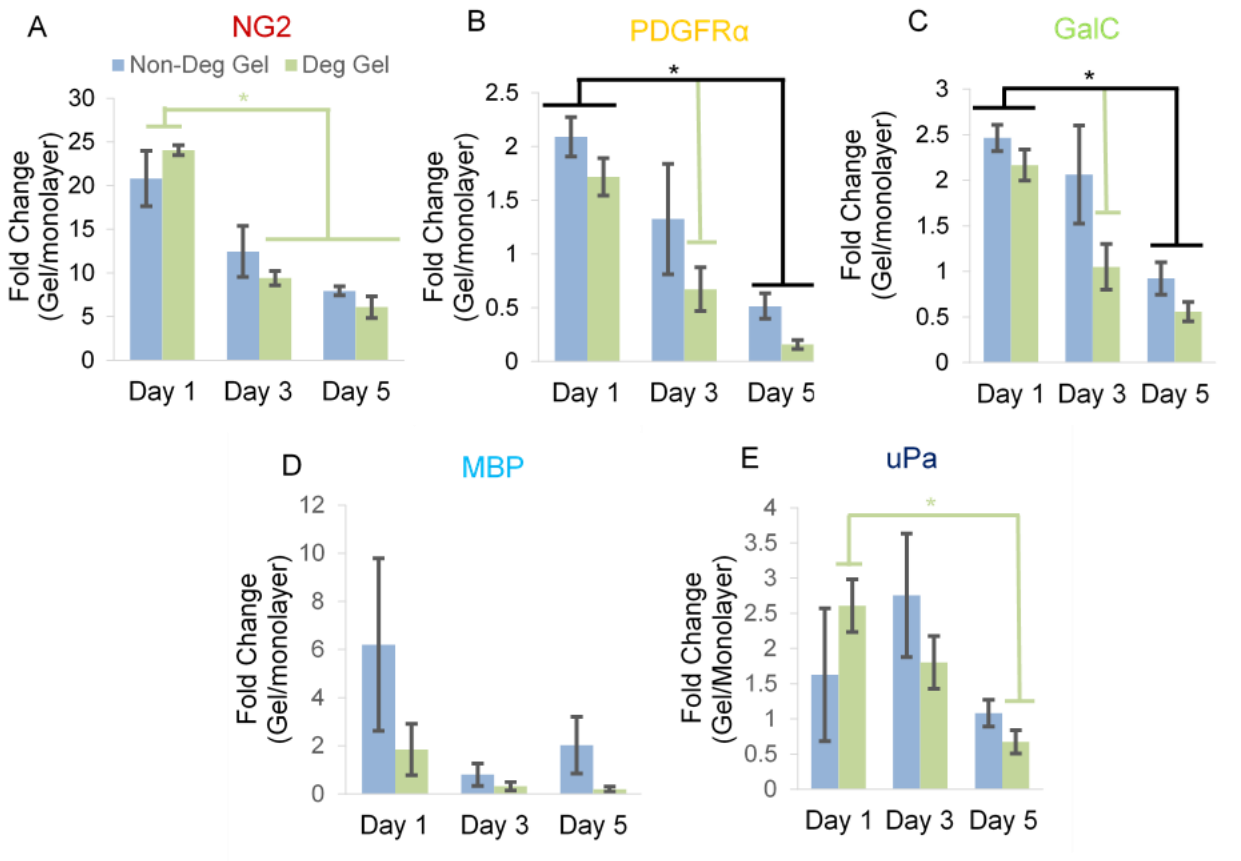


Figure 4-10: Effect of encapsulation process on MADM OPC gene expression. MADM OPC gene expression of (A) NG2, (B) PDGFR α , (C) GalC, (D) MBP, and (E) uPA was affected by the encapsulation process. Displaying SE (n = 3). Asterisks indicate statistical significance using student T-test (p < 0.05).

4.5. Conclusions

3D ELP hydrogels can be designed with similar biomechanical properties, to mimic native CNS ECM, and varying bioactivity (i.e., uPA enzymatic degradability) to influence encapsulated

cell behavior. Azide functionalization of ELP made the protein more hydrophobic and reduced the T_t . The average number of azides added to ELP could be controlled by limiting the azide present during the diazotransfer reaction. Three similar ELP sequences were mixed to form hydrogels with independent control over hydrogel stiffness and uPA enzymatic degradation. However, the small differences in the ELP amino acid sequences created hydrogels with different stress relaxation properties. A modified zymography technique was used to prove that MADM OPCs express low Mw uPA and were capable of cleaving the uPA degradable ELP sequence. This modified zymography technique expands the number of digestible substrates that can be used in gel electrophoresis to include any protein or small peptide sequence. MADM OPC viability, metabolic activity and proliferation was not altered by the presence of uPA enzymatic degradation in the ELP hydrogel network. MADM OPCs located near the surface of ELP hydrogels extended processes, but most cells grew in circular clusters deeper in the hydrogels. Gene expression changes in encapsulated MADM OPCs indicated that uPA degradable hydrogels promoted the transition from immature to mature OPCs, but did not promote the transition fully into OLs, likely inhibited by the genetic nature of the MADM OPCs. We demonstrated that enzymatic degradation in hydrogel systems can be used to influence cell behavior post encapsulation in addition to breaking down the hydrogel network.

4.6. Funding

We gratefully acknowledge financial support from NSF grant 1904198 and the Translational Health Research Institute of Virginia for a career development award to Kyle J. Lampe. We also acknowledge financial support from the University of Virginia's Harrison Undergraduate Research Awards given to W. Sharon Zheng and Anahita H. Sharma.

4.7. References

- (1) Macaya, D.; Spector, M. Injectable Hydrogel Materials for Spinal Cord Regeneration: A Review. *Biomed. Mater.* 2012, 7 (1), 012001. <https://doi.org/10.1088/1748-6041/7/1/012001>.
- (2) Nih, L. R.; Carmichael, S. T.; Segura, T. Hydrogels for Brain Repair after Stroke: An Emerging Treatment Option. *Curr. Opin. Biotechnol.* 2016, 40, 155–163. <https://doi.org/10.1016/j.copbio.2016.04.021>.
- (3) Straley, K. S.; Foo, C. W. P.; Heilshorn, S. C. Biomaterial Design Strategies for the Treatment of Spinal Cord Injuries. *J. Neurotrauma* 2010, 27 (1), 1–19. <https://doi.org/10.1089/neu.2009.0948>.
- (4) Luzzio, C.; Dangond, F. What is the worldwide prevalence of multiple sclerosis (MS), and what is the role of ethnicity in MS? <https://www.medscape.com/answers/1146199-5725/what-is-the-worldwide-prevalence-of-multiple-sclerosis-ms-and-what-is-the-role-of-ethnicity-in-ms> (accessed Apr 13, 2020).
- (5) Lau, L. W.; Cua, R.; Keough, M. B.; Haylock-Jacobs, S.; Yong, V. W.; Johnson, K. M.; Milner, R.; Crocker, S. J.; van Horssen, J.; Bö, L.; Dijkstra, C. D.; de Vries, H. E.; Reinhard, S. M.; Razak, K.; Ethell, I. M.; Silver, J.; Miller, J. H. Pathophysiology of the Brain Extracellular Matrix: A New Target for Remyelination. *Nat. Rev. Neurosci.* 2015, 14 (10), 722–729. <https://doi.org/10.1038/nrn3550>.
- (6) Willis, C. M.; Crocker, S. J. The Mosaic of Extracellular Matrix in the Central Nervous System as a Determinant of Glial Heterogeneity. In *Composition and Function of the Extracellular Matrix in the Human Body*; 2016. <https://doi.org/10.5772/62706>.
- (7) Huang, J. K.; Fancy, S. P. J.; Zhao, C.; Rowitch, D. H.; French-Constant, C.; Franklin, R. J. M. Myelin Regeneration in Multiple Sclerosis: Targeting Endogenous Stem Cells. *Neurotherapeutics* 2011, 8 (4), 650–658. <https://doi.org/10.1007/s13311-011-0065-x>.

- (8) Wheeler, N. A.; Fuss, B. Extracellular Cues Influencing Oligodendrocyte Differentiation and (Re)Myelination. *Exp. Neurol.* 2016, 283, 512–530. <https://doi.org/10.1016/j.expneurol.2016.03.019>.
- (9) Jagielska, A.; Lowe, A. L.; Makhija, E.; Wroblewska, L.; Guck, J.; Franklin, R. J. M.; Shivashankar, G. V.; Van Vliet, K. J. Mechanical Strain Promotes Oligodendrocyte Differentiation by Global Changes of Gene Expression. *Front. Cell. Neurosci.* 2017, 11 (April), 1–16. <https://doi.org/10.3389/fncel.2017.00093>.
- (10) Emery, B. Regulation of Oligodendrocyte Differentiation and Myelination. *Science* (80-.). 2010, 330 (6005), 779–782. <https://doi.org/10.1126/science.1190927>.
- (11) Mahmood, N.; Mihalcioiu, C.; Rabbani, S. A. Multifaceted Role of the Urokinase-Type Plasminogen Activator (UPA) and Its Receptor (UPAR): Diagnostic, Prognostic, and Therapeutic Applications. *Front. Oncol.* 2018, 8 (FEB). <https://doi.org/10.3389/fonc.2018.00024>.
- (12) Dent, M. A. R.; Sumi, Y.; Morris, R. J.; Seeley, P. J. Urokinase-Type Plasminogen Activator Expression by Neurons and Oligodendrocytes During Process Outgrowth in Developing Rat Brain. *Eur. J. Neurosci.* 1993, 5, 633–647.
- (13) Downes, N.; Mullins, P. The Development of Myelin in the Brain of the Juvenile Rat. *Toxicol. Pathol.* 2014, 42 (5), 913–922. <https://doi.org/10.1177/0192623313503518>.
- (14) Behar, T. N. Analysis of Fractal Dimension of O2A Glial Cells Differentiating in Vitro. *Methods* 2001, 24, 331–339. <https://doi.org/10.1016/j.expneurol.2016.03.019>.
- (15) Semina, E.; Rubina, K.; Sysoeva, V.; Rysenkova, K.; Klimovich, P.; Plekhanova, O.; Tkachuk, V. Urokinase and Urokinase Receptor Participate in Regulation of Neuronal Migration , Axon Growth and Branching. *Eur. J. Cell Biol.* 2016, 95 (9), 295–310. <https://doi.org/10.1016/j.ejcb.2016.05.003>.

- (16) Larsen, P. H.; Wells, J. E.; Stallcup, W. B.; Opdenakker, G.; Yong, V. W. Matrix Metalloproteinase-9 Facilitates Remyelination in Part by Processing the Inhibitory NG2 Proteoglycan. *J. Neurosci.* 2003, 23 (35), 11127–11135. <https://doi.org/23/35/11127> [pii].
- (17) Uhm, J. H.; Dooley, N. P.; Oh, L. Y. S.; Yong, V. W. Oligodendrocytes Utilize a Matrix Metalloproteinase, MMP-9, to Extend Processes along an Astrocyte Extracellular Matrix. *Glia* 1998, 22 (1), 53–63. [https://doi.org/10.1002/\(SICI\)1098-1136\(199801\)22:1<53::AID-GLIA5>3.0.CO;2-9](https://doi.org/10.1002/(SICI)1098-1136(199801)22:1<53::AID-GLIA5>3.0.CO;2-9).
- (18) Adnan, N.; Mie, M.; Haque, A.; Hossain, S.; Mashimo, Y.; Akaike, T.; Kobatake, E. Construction of a Defined Biomimetic Matrix for Long-Term Maintenance of Mouse Induced Pluripotent Stem Cells. *Bioconjug. Chem.* 2016, 27 (7), 1599–1605. <https://doi.org/10.1021/acs.bioconjchem.6b00141>.
- (19) Benitez, P. L.; Mascharak, S.; Proctor, A. C.; Heilshorn, S. C. Use of Protein-Engineered Fabrics to Identify Design Rules for Integrin Ligand Clustering in Biomaterials. *Integr. Biol. (Camb)*. 2016, 8 (1), 50–61. <https://doi.org/10.1039/c5ib00258c>.
- (20) Betre, H.; Ong, S. R.; Guilak, F.; Chilkoti, A.; Fermor, B.; Setton, L. A. Chondrocytic Differentiation of Human Adipose-Derived Adult Stem Cells in Elastin-like Polypeptide. *Biomaterials* 2006, 27 (1), 91–99. <https://doi.org/10.1016/j.biomaterials.2005.05.071>.
- (21) Chung, C.; Anderson, E.; Pera, R. R.; Pruitt, B. L.; Heilshorn, S. C. Hydrogel Crosslinking Density Regulates Temporal Contractility of Human Embryonic Stem Cell-Derived Cardiomyocytes in 3D Cultures. *Soft Matter* 2012, 8 (39), 10141–10148. <https://doi.org/10.1039/c2sm26082d>.
- (22) Leipzig, N. D.; Shoichet, M. S. The Effect of Substrate Stiffness on Adult Neural Stem Cell Behavior. *Biomaterials* 2009, 30 (36), 6867–6878. <https://doi.org/10.1016/j.biomaterials.2009.09.002>.

- (23) Asai, D.; Xu, D.; Liu, W.; Garcia Quiroz, F.; Callahan, D. J.; Zalutsky, M. R.; Craig, S. L.; Chilkoti, A. Protein Polymer Hydrogels by in Situ, Rapid and Reversible Self-Gelation. *Biomaterials* 2012, 33 (21), 5451–5458. <https://doi.org/10.1016/j.biomaterials.2012.03.083>.
- (24) Desai, M. S.; Wang, E.; Joyner, K.; Chung, T. W.; Jin, H. E.; Lee, S. W. Elastin-Based Rubber-Like Hydrogels. *Biomacromolecules* 2016, 17 (7), 2409–2416. <https://doi.org/10.1021/acs.biomac.6b00515>.
- (25) Li, N. K.; Garcia Quiroz, F.; Hall, C. K.; Chilkoti, A.; Yingling, Y. G. Molecular Description of the LCST Behavior of an Elastin-like Polypeptide. *Biomacromolecules* 2014. <https://doi.org/10.1021/bm500658w>.
- (26) Straley, K. S.; Heilshorn, S. C. Independent Tuning of Multiple Biomaterial Properties Using Protein Engineering. *Soft Matter* 2009, 5 (1), 114. <https://doi.org/10.1039/b808504h>.
- (27) Lampe, K. J.; Antaris, A. L.; Heilshorn, S. C. Design of Three-Dimensional Engineered Protein Hydrogels for Tailored Control of Neurite Growth. *Acta Biomater.* 2013, 9 (3), 5590–5599. <https://doi.org/10.1016/j.actbio.2012.10.033>.
- (28) Šišková, Z.; Yong, V. W.; Nomden, A.; van Strien, M.; Hoekstra, D.; Baron, W. Fibronectin Attenuates Process Outgrowth in Oligodendrocytes by Mislocalizing MMP-9 Activity. *Mol. Cell. Neurosci.* 2009, 42 (3), 234–242. <https://doi.org/10.1016/j.mcn.2009.07.005>.
- (29) Lourenço, T.; Faria, J. P. De; Bippes, C. A.; Maia, J.; Lopes-da-Silva, José, A.; Relvas, J. B.; Grãos, M. Modulation of Oligodendrocyte Differentiation and Maturation by Combined Biochemical and Mechanical Cues. *Sci. Rep.* 2016, No. February, 1–17. <https://doi.org/10.1038/srep21563>.
- (30) Zong, H.; Espinosa, J. S.; Su, H. H.; Muzumdar, M. D.; Luo, L. Mosaic Analysis with Double Markers in Mice. *Cell* 2005, 121 (3), 479–492. <https://doi.org/10.1016/j.cell.2005.02.012>.

- (31) Liu, C.; Sage, J. C.; Miller, M. R.; Verhaak, R. G. W.; Hippenmeyer, S.; Vogel, H.; Foreman, O.; Bronson, R. T.; Nishiyama, A.; Luo, L.; Zong, H. Mosaic Analysis with Double Markers Reveals Tumor Cell of Origin in Glioma. *Cell* 2011, 146 (2), 209–221. <https://doi.org/10.1016/j.cell.2011.06.014>.
- (32) Meco, E.; Lampe, K. J. Impact of Elastin-like Protein Temperature Transition on PEG-ELP Hybrid Hydrogel Properties. *Biomacromolecules* 2019, 20, acs.biomac.9b00113. <https://doi.org/10.1021/acs.biomac.9b00113>.
- (33) Madl, C. M.; Katz, L. M.; Heilshorn, S. C. Bio-Orthogonally Crosslinked, Engineered Protein Hydrogels with Tunable Mechanics and Biochemistry for Cell Encapsulation. *Adv. Funct. Mater.* 2016, 26 (21), 3612–3620. <https://doi.org/10.1002/adfm.201505329>.
- (34) Van Dongen, S. F. M.; Teeuwen, R. L. M.; Nallani, M.; Van Berkel, S. S.; Cornelissen, J. J. L. M.; Nolte, R. J. M.; Van Hest, J. C. M. Single-Step Azide Introduction in Proteins via an Aqueous Diazo Transfer. *Bioconjug. Chem.* 2009, 20 (1), 20–23. <https://doi.org/10.1021/bc8004304>.
- (35) DeForest, C. A.; Tirrell, D. A. A Photoreversible Protein-Patterning Approach for Guiding Stem Cell Fate in Three-Dimensional Gels. *Nat. Mater.* 2015, 14 (5), 523–531. <https://doi.org/10.1038/nmat4219>.
- (36) Heussen, C.; Dowdle, E. B. Electrophoretic Analysis of Plasminogen Activators in Polyacrylamide Gels Containing Sodium Dodecyl Sulfate and Copolymerized Substrates. *Anal. Biochem.* 1980, 102 (1), 196–202.
- (37) Kato, S.; Aoyama, M.; Kakita, H.; Hida, H.; Kato, I.; Ito, T.; Goto, T.; Hussein, M. H.; Sawamoto, K.; Togari, H.; Asai, K. Endogenous Erythropoietin from Astrocyte Protects the Oligodendrocyte Precursor Cell against Hypoxic and Reoxygenation Injury. *J. Neurosci. Res.* 2011, 89 (10), 1566–1574. <https://doi.org/10.1002/jnr.22702>.

- (38) Pinezich, M. R.; Russell, L. N.; Murphy, N. P.; Lampe, K. J. Encapsulated Oligodendrocyte Precursor Cell Fate Is Dependent on PDGF-AA Release Kinetics in a 3D Microparticle-Hydrogel Drug Delivery System. *J. Biomed. Mater. Res. - Part A* 2018, 106 (9), 2402–2411. <https://doi.org/10.1002/jbm.a.36432>.
- (39) Muiznieks, L. D.; Reichheld, S. E.; Sitarz, E. E.; Miao, M.; Keeley, F. W. Proline-Poor Hydrophobic Domains Modulate the Assembly and Material Properties of Polymeric Elastin. *Biopolymers* 2015, 103 (10), 563–573. <https://doi.org/10.1002/bip.22663>.
- (40) Kramer, J. R.; Petitdemange, R.; Bataille, L.; Bathany, K.; Wirotius, A. L.; Garbay, B.; Deming, T. J.; Garanger, E.; Lecommandoux, S. Quantitative Side-Chain Modifications of Methionine-Containing Elastin-Like Polypeptides as a Versatile Tool to Tune Their Properties. *ACS Macro Lett.* 2015, 4 (11), 1283–1286. <https://doi.org/10.1021/acsmacrolett.5b00651>.
- (41) McDaniel, J. R.; Radford, D. C.; Chilkoti, A. A Unified Model for de Novo Design of Elastin-like Polypeptides with Tunable Inverse Transition Temperatures. *Biomacromolecules* 2013, 14 (8), 2866–2872. <https://doi.org/10.1021/bm4007166>.
- (42) Zhan, H.; De Jong, H.; Löwik, D. W. P. M. Comparison of Bioorthogonally Cross-Linked Hydrogels for in Situ Cell Encapsulation. *ACS Appl. Bio Mater.* 2019, 2 (7), 2862–2871. <https://doi.org/10.1021/acsabm.9b00253>.
- (43) Sengupta, D.; Straley, K.; Heilshorn, S. C. Adaptive Protein-Based Scaffolds for Neural Engineering. *Polym. Prepr.* 2010, 51 (1), 40–41. [https://doi.org/10.1089/neu.2009.0948.\(7\)](https://doi.org/10.1089/neu.2009.0948.(7)).
- (44) Chen, M. H.; Wang, L. L.; Chung, J. J.; Kim, Y. H.; Atluri, P.; Burdick, J. A. Methods to Assess Shear-Thinning Hydrogels for Application As Injectable Biomaterials. *ACS Biomater. Sci. Eng.* 2017, 3 (12), 3146–3160. <https://doi.org/10.1021/acsbiomaterials.7b00734>.

- (45) Budday, S.; Nay, R.; de Rooij, R.; Steinmann, P.; Wyrobek, T.; Ovaert, T. C.; Kuhl, E. Mechanical Properties of Gray and White Matter Brain Tissue by Indentation. *J. Mech. Behav. Biomed. Mater.* 2015, 46, 318–330. <https://doi.org/10.1016/j.jmbbm.2015.02.024>.
- (46) Moeendarbary, E.; Weber, I. P.; Sheridan, G. K.; Koser, D. E.; Soleman, S.; Haenzi, B.; Bradbury, E. J.; Fawcett, J.; Franze, K. The Soft Mechanical Signature of Glial Scars in the Central Nervous System. *Nat. Commun.* 2017, 8, 14787. <https://doi.org/10.1038/ncomms14787>.
- (47) Chaudhuri, O.; Gu, L.; Klumpers, D.; Darnell, M.; Bencherif, S. A.; Weaver, J. C.; Huebsch, N.; Lee, H.-P.; Lippens, E.; Duda, G. N.; Mooney, D. J. Hydrogels with Tunable Stress Relaxation Regulate Stem Cell Fate and Activity. *Nat. Mater.* 2015, advance on (November). <https://doi.org/10.1038/nmat4489>.
- (48) Brown, T. E.; Carberry, B. J.; Worrell, B. T.; Dudaryeva, O. Y.; McBride, M. K.; Bowman, C. N.; Anseth, K. S. Photopolymerized Dynamic Hydrogels with Tunable Viscoelastic Properties through Thioester Exchange. *Biomaterials* 2018, 178, 496–503. <https://doi.org/10.1016/j.biomaterials.2018.03.060>.
- (49) Teesalu, T.; Hinkkanen, A. E.; Vaheri, A. Coordinated Induction of Extracellular Proteolysis Systems during Experimental Autoimmune Encephalomyelitis in Mice. *Am. J. Pathol.* 2001, 159 (6), 2227–2237. [https://doi.org/10.1016/S0002-9440\(10\)63073-8](https://doi.org/10.1016/S0002-9440(10)63073-8).
- (50) Hadler-Olsen, E.; Kanapathipillai, P.; Berg, E.; Svineng, G.; Winberg, J. O.; Uhlin-Hansen, L. Gelatin in Situ Zymography on Fixed, Paraffin-Embedded Tissue: Zinc and Ethanol Fixation Preserve Enzyme Activity. *J. Histochem. Cytochem.* 2010, 58 (1), 29–39. <https://doi.org/10.1369/jhc.2009.954354>.
- (51) Nobuhara, M.; Sakamaki, M.; Ohnishi, H.; Suzuki, Y. A Comparative Study of High Molecular Weight Urokinase and Low Molecular Weight Urokinase. *J. Biochem.* 1981, 90 (1), 225–232.

- (52) Madl, C. M.; LeSavage, B. L.; Dewi, R. E.; Lampe, K. J.; Heilshorn, S. C. Matrix Remodeling Enhances the Differentiation Capacity of Neural Progenitor Cells in 3D Hydrogels. *Adv. Sci.* 2019, 6 (4). <https://doi.org/10.1002/advs.201801716>.
- (53) Russell, L. N.; Lampe, K. J. Oligodendrocyte Precursor Cell Viability , Proliferation , and Morphology Is Dependent on Mesh Size and Storage Modulus in 3D Poly (Ethylene Glycol) - Based Hydrogels. *ACS Biomater. Sci. Eng.* 2017, 3, 3459–3468. <https://doi.org/10.1021/acsbiomaterials.7b00374>.
- (54) Chung, C.; Lampe, K. J.; Heilshorn, S. C. Tetrakis(Hydroxymethyl) Phosphonium Chloride as a Covalent Cross-Linking Agent for Cell Encapsulation within Protein-Based Hydrogels. *Biomacromolecules* 2012, 13 (12), 3912–3916. <https://doi.org/10.1021/bm3015279>.
- (55) Oliveira, B. L.; Guo, Z.; Bernardes, G. J. L. Inverse Electron Demand Diels-Alder Reactions in Chemical Biology. *Chem. Soc. Rev.* 2017, 46 (16), 4895–4950. <https://doi.org/10.1039/c7cs00184c>.
- (56) Rao, V. T. S.; Khan, D.; Cui, Q. L.; Fuh, S. C.; Hossain, S.; Almazan, G.; Multhaup, G.; Healy, L. M.; Kennedy, T. E.; Antel, J. P. Distinct Age and Differentiation-State Dependent Metabolic Profiles of Oligodendrocytes under Optimal and Stress Conditions. *PLoS One* 2017, 12 (8). <https://doi.org/10.1371/journal.pone.0182372>.
- (57) Barateiro, A.; Fernandes, A. Temporal Oligodendrocyte Lineage Progression: In Vitro Models of Proliferation, Differentiation and Myelination. *Biochim. Biophys. Acta - Mol. Cell Res.* 2014, 1843 (9), 1917–1929. <https://doi.org/10.1016/j.bbamcr.2014.04.018>.
- (58) Miron, V. E.; Kuhlmann, T.; Antel Jack P., J. P. Cells of the Oligodendroglial Lineage, Myelination, and Remyelination. *Biochim. Biophys. Acta* 2011, 1812 (2), 184–193. <https://doi.org/10.1016/j.bbadis.2010.09.010>.

- (59) Guardiola-diaz, H. M.; Ishii, A.; Bansal, R. Erk1 / 2 MAPK and MTOR Signaling Sequentially Regulates Progression Through Distinct Stages of Oligodendrocyte Differentiation. *Glia* 2012, 486 (December 2011), 476–486. <https://doi.org/10.1002/glia.22281>.
- (60) Fumagalli, M.; Daniele, S.; Lecca, D.; Lee, P. R.; Parravicini, C.; Douglas Fields, R.; Rosa, P.; Antonucci, F.; Verderio, C.; Letizia Trincavelli, M.; Bramanti, P.; Martini, C.; Abbracchio, M. P. Phenotypic Changes, Signaling Pathway, and Functional Correlates of GPR17-Expressing Neural Precursor Cells during Oligodendrocyte Differentiation. *J. Biol. Chem.* 2011, 286 (12), 10593–10604. <https://doi.org/10.1074/jbc.M110.162867>.
- (61) Lau, P.; Verrier, J. D.; Nielsen, J. A.; Johnson, K. R.; Notterpek, L.; Hudson, L. D. Identification of Dynamically Regulated MicroRNA and mRNA Networks in Developing Oligodendrocytes. *J. Neurosci.* 2008, 28 (45), 11720–11730. <https://doi.org/10.1523/JNEUROSCI.1932-08.2008>.
- (62) Tyler, W. A.; Gangoli, N.; Gokina, P.; Kim, H. A.; Covey, M.; Levison, S. W.; Wood, T. L. Activation of the Mammalian Target of Rapamycin (MTOR) Is Essential for Oligodendrocyte Differentiation. *J. Neurosci.* 2009, 29 (19), 6367–6378. <https://doi.org/10.1523/JNEUROSCI.0234-09.2009>.
- (63) Dai, J.; Bercury, K. K.; Macklin, W. B. Interaction of MTOR and Erk1/2 Signaling to Regulate Oligodendrocyte Differentiation. *Glia* 2014, 62 (12), 2096–2109. <https://doi.org/10.1002/glia.22729>.

5. Micro-localization of adhesive RGD peptide sequence within PEG-ELP single-network hydrogels

5.1. Formation of hydrogels with clustered cell adhesive peptides

Cross-linking poly(ethylene glycol) (PEG) and elastin-like protein (ELP) solutions at temperatures above and below the lower critical solution temperature (LCST) transition of ELP created two distinct double-network hydrogel systems (PEG-ELP) with the same input materials¹. Solutions cross-linked at temperatures below the ELP LCST formed hydrogels with a homogeneous ELP distribution, while solutions cross-linked at temperatures above the ELP LCST created hydrogels with ELP aggregated into microscale (~20 μm diameter) spheres (Figure 3-2)¹. This technique allows for the microscale localization of ELP within the bulk hydrogel network, and subsequently the localization of bioactive peptide sequences, attached to the ELP sequence. Literature suggests that clustering the cell adhesive promoting RGD peptide sequence at microscale resolutions, while not altering the total bulk hydrogel RGD concentration impacts cell proliferation^{2,3}. However, these studies were conducted on a 2-dimensional (2D) electrospun fiber mesh and cellular behavior on top of biomaterial scaffolds (in 2D) does not necessarily translate in a 3-dimensional (3D) setting²⁻⁴. The PEG-ELP hydrogel system provides an avenue for localizing RGD, with microscale resolution, in a 3D setting to assess whether or not the cell behavior observed on electrospun ELP fiber mesh translates to 3D environments.

To assess the impact of localizing the RGD peptide sequence on cells in a 3D setting, PEG-ELP double-network hydrogels with and without micro-architecture were formed by cross-linking gel precursor solutions at temperatures above and below the ELP LCST transition, respectively. The PEG-ELP double-network hydrogel system was formed by cross-linking PEG-methacrylate

(PEG-MA) using ultraviolet (UV) light in the presence of a photoinitiator (lithium phenyl-2,4,6-trimethylbenzoylphosphinate (LAP)), and simultaneously cross-linking ELP through a Mannich-type condensation reaction of lysine residue primary amines with the tetrakis(hydroxymethyl) phosphonium chloride (THPC) cross-linker. Since PEG-ELP hydrogels made at temperatures above the LCST transition created ELP-rich regions with diameters of $\sim 20 \mu\text{m}$, and the ELP sequence contained RGD (ELP-RGD), the impact of localizing RGD concentration on OPC behavior was to be assessed. In addition, PEG-ELP made at temperatures below the LCST formed hydrogels with homogenous ELP distribution, which created a control group to compare cell behavior to that of hydrogels with clustered ELP-RGD. Finally, ELP with the RDG scramble sequence (ELP-RDG) can be mixed with ELP-RGD to control the adhesive site concentration without adjusting the total PEG-ELP hydrogel protein content. However, PEG-ELP double-network hydrogels were not suitable for oligodendrocyte precursor cell (OPC) encapsulation.

5.2. THPC cytotoxicity of MADM OPCs

OPCs, isolated through the mosaic analysis with double marker technique (MADM OPC)^{5,6}, encapsulated in PEG-ELP double-network hydrogels did not survive the gelation process (Figure 5-1). Evidence of this was found through several assays. The majority of MADM OPCs encapsulated in PEG-ELP hydrogels for 4 days stained dead (Figure 5-1A). In addition, the green fluorescent protein (GFP) signal present in MADM OPCs did not grow in diameter over time, which is a typical growth pattern for these cells within hydrogels⁷. The viability of MADM OPCs encapsulated in PEG-ELP hydrogels was negligible over 7 days (Figure 5-1B). Removal of the THPC cross-linker from the gelation process improved encapsulated MADM OPC viability (Figure 5-1B). PEG-ELP hydrogels made without the THPC cross-linker formed clustered ELP aggregates, but the micro-architecture was not preserved when the hydrogels were immersed in

aqueous solution¹. Measurements of encapsulated MADM OPC ATP and DNA content confirmed that these cells were not viable in PEG-ELP double-network hydrogels because the ATP concentration was negligible and DNA remained constant over 7 days (Figure 5-1C, D). The ATP and DNA concentration of MADM OPCs encapsulated in PEG-ELP hydrogels without THPC increased over time indicating that these cells were metabolically active and proliferating (Figure 5-1C, D). Taken together, these results indicated that the THPC cross-linker was cytotoxic to MADM OPCs.

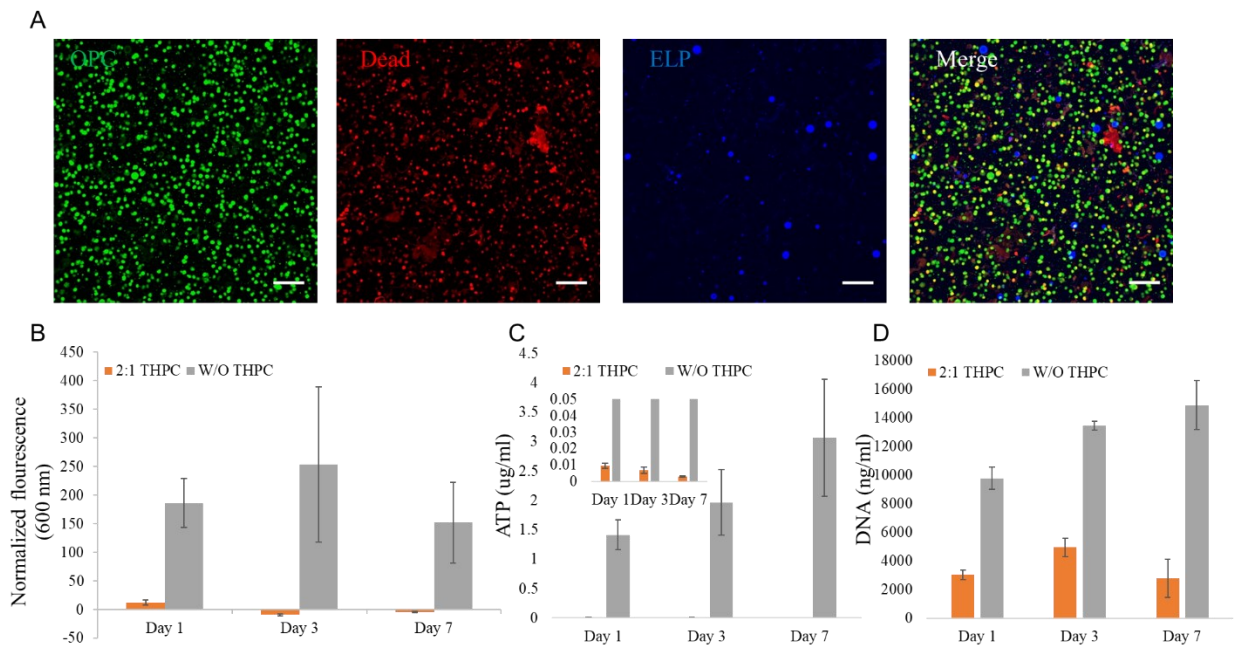


Figure 5-1: MADM OPCs encapsulated in PEG-ELP double-network hydrogels did not survive the gelation process. (A) Max z-projections of 225 μm slice of MADM OPCs encapsulated in 6/1.5 wt/v % PEG-ELP (2:1 THPC hydroxyl group to amine ratio) hydrogels for 4 days. Scale bars = 100 μm . Green represents MADM OPC GFP+ signal, red represents dead stain, and blue represents ELP tagged with AlexaFluor 405 dye. (B) OPC viability, (C) ATP concentration and (D) DNA concentration in 10/1.5 PEG-ELP hydrogels with and without THPC over 7 days as determined via alamarBlue, ATP and DNA assays, respectively. Gelation performed at temperatures above the ELP LCST. Error bars show standard deviation.

5.3. SPAAC cross-linking

Several different cross-linking schemes were analyzed as potential replacements for the double-network hydrogel system and forming PEG-ELP single-network hydrogels using strain promoted azide-alkyne cycloaddition (SPAAC) cross-linking showed promise (Figure 5-2A). The SPAAC chemical reaction has several favorable properties that made it a viable option for encapsulating MADM OPCs in PEG-ELP hydrogels: The reaction is bio-orthogonal and does not interfere with native cellular biochemical processes, reaction times are fast enough to mitigate cell settling (on the order of minutes), and it avoids the use of the cytotoxic copper catalyst used in similar copper-catalyzed azide-alkyne cycloaddition (CuAAC) reactions⁸⁻¹⁷. The PEG-ELP cross-linking scheme required the purchase of commercially available PEG-azide (20 kDa 4arm-PEG-azide), functionalization of ELP with azide groups and the creation of a strained ring cross-linker. Primary amines in the ELP sequence were converted into azide functional groups using previously described methods^{11,14}. Azide functionalization of ELP was confirmed using Fourier-transform infrared spectroscopy (FTIR) by the appearance of a peak at 2100 cm^{-1} (Figure B-1). The average number of azides added to each ELP molecule was controlled by stoichiometrically limiting the azide present during the reaction and quantified using high resolution electrospray ionization-mass spectrometry (ESI-MS, Figure B-2). The crosslinker was made by functionalizing a 4arm-PEG-amine (10 kDa) with (1R, 8S, 9s)-bicyclo[6.1.0]non-4-yn-9-ylmethyl (2, 5-dioxopyrrolidin-1-yl) carbonate (BCN) using previously described methods¹⁸. BCN functionalization was determined to be 92 – 99 % by comparing the appearance of BCN hydrogen peaks (0.8, 1.3, and 2.3 ppm) to the PEG backbone hydrogen peak (3.6 ppm) on the proton nuclear magnetic resonance (HNMR) spectrum (Figure 5-2B). Simple mixing of all components (ELP-azide, PEG-azide, and PEG-BCN) formed hydrogels.

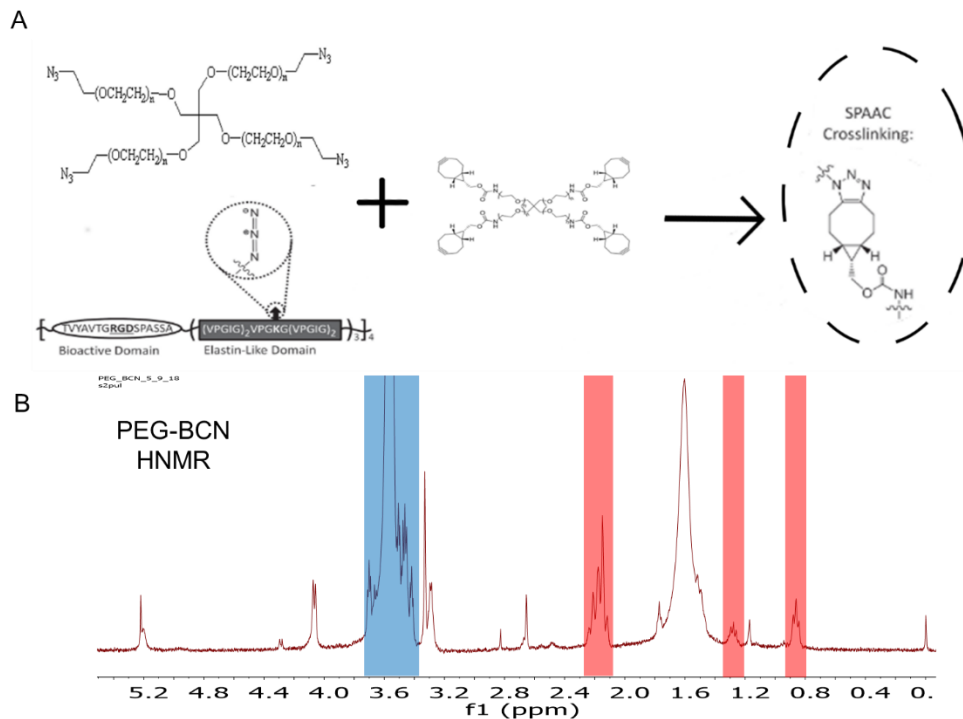


Figure 5-2: (A) SPAAC cross-linking between azides and strained alkyne bonds. (B) HNMR of BCN functionalized PEG (PEG-BCN). BCN functionalization determined by comparing BCN hydrogen peaks (highlighted with red box) to the PEG backbone hydrogen peak (highlighted with blue box).

Preliminary work using SPAAC cross-linking chemistry to encapsulate MADM OPCs in PEG- and ELP-azide (PEA) single-network hydrogels with microscale clustering of ELP was promising (Figure 5-3). 3/3 PEA (0.5:1) solutions (3 wt/v % PEG-azide, 3 wt/v % ELP-azide and 0.5:1 BCN to azide ratio) formed hydrogels when mixed at both temperatures below and above the ELP LCST (Figure 5-3A, B). 80 % of ELP amine groups were converted into azides for these experiments and this shifted the ELP LCST from $\sim 31^\circ\text{C}$ to $\sim 17^\circ\text{C}$ (data not shown) so room temperature (RT) gelation was used to create hydrogels with clustered ELP micro-architecture and 4°C gelation created hydrogels with a homogeneous ELP distribution (Figure 5-3A, B). PEA hydrogel ELP distribution was preserved in both hydrogel systems after swelling in phosphate buffered saline (PBS) for 24 hours (Figure 5-3C, D). When MADM OPCs were encapsulated in

PEA hydrogels gelled below the ELP-azide LCST transition MADM OPCs grew into larger cell clusters which is similar to their growth in other hydrogel systems (Figure 5-3E)⁷. In addition, the ELP micro-architecture was preserved in PEA hydrogels made at RT (Figure 5-3F). The PEA single-network hydrogel system cross-linked with SPAAC chemistry was promising for studying the effects of localizing the RGD adhesive peptide sequence on MADM OPC behavior.

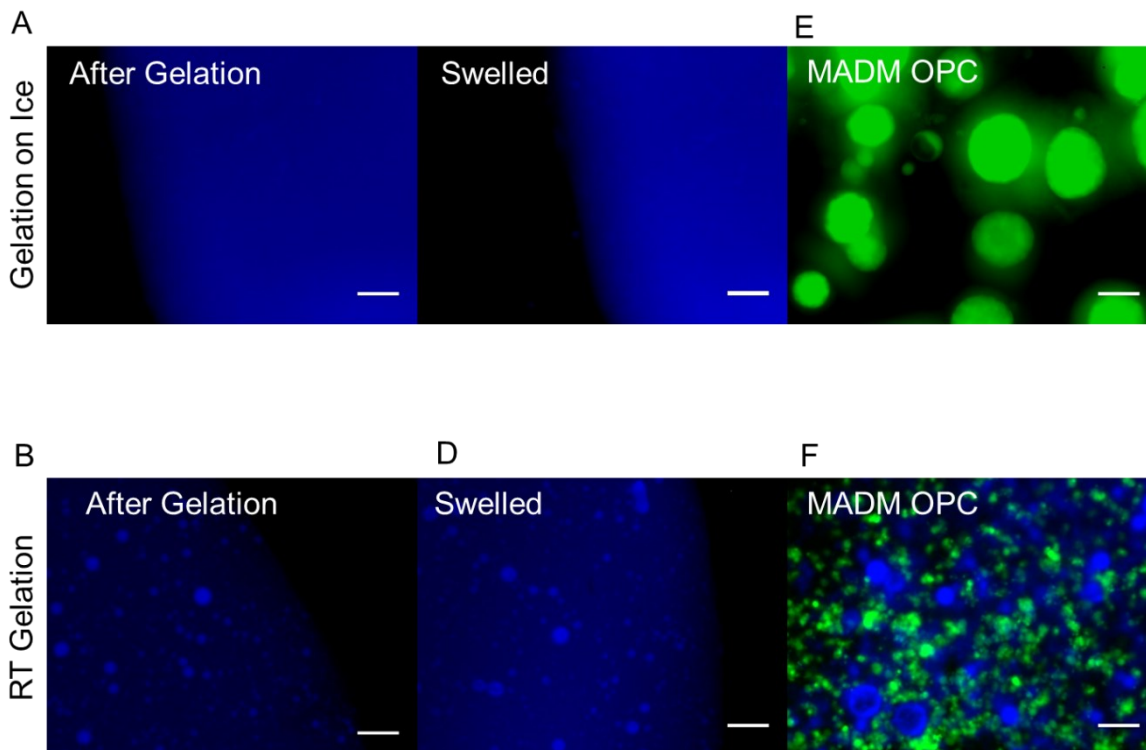


Figure 5-3: Creation of PEG- and ELP-azide (PEA) single-network hydrogels. ELP-azide (tagged with Alexa Fluor 405) distribution in 3/3 PEA (0.5:1) hydrogels cross-linked (A) on ice and (B) at RT. ELP distribution is homogeneous in hydrogels made at temperatures below the ELP LCST (A) and ELP is clustered in hydrogels made at temperatures above the ELP LCST (B). Both (C) homogeneous and (D) clustered ELP distribution is preserved after swelling PEA hydrogels in PBS for 24 hours. (E) MADM OPCs encapsulated for 9 days in 3/3 PEA (0.5:1) hydrogels cross-linked on ice (ELP not shown) grew into large clusters. (F) ELP micro-architecture was preserved when MADM OPCs were encapsulated for 2 days in 3/3 PEA (0.5:1) hydrogels cross-linked at RT. Scale bars = 100 μm .

5.4. Impact of ELP azide functionalization on protein properties

Azide functionalization of ELP affected the physical properties of the coacervate phase.

ELP with 11 of 14 primary amines converted into azides (80 % functionalization) had an LCST

shift from 31°C to ~17°C and could not be pipetted while at temperatures above the LCST (data not shown). PEA hydrogels with ELP clusters could not be formed with the same mixing procedure used for PEG-ELP double-network hydrogels (Figure 3-2)¹. PEA hydrogels with ELP aggregates were formed by mixing the ELP solution with a PEG solution while the ELP solution was undergoing a temperature change from below the LCST to above it. This process of mixing (and cross-linking) ELP as the coacervate phase was forming was not stable and uniform ELP domains could not be formed consistently (Figure 5-4A). The inconsistent ELP aggregate formation translated into inconsistent PEA hydrogel storage and loss moduli. While MADM OPCs could be encapsulated in these hydrogels, hydrogels with consistent properties could not be formed.

PEA hydrogels with consistent ELP aggregate size were formed by reducing the azide functionalization of ELP. The coacervate phase of ELP with only 4 of 14 primary amines converted into azides could be pipetted and a similar mixing procedure to that of PEG-ELP double-network hydrogels created consistent ELP aggregates within PEA hydrogels (Figure 5-4B). However, when swelled in PBS the ELP aggregates did not remain fully intact (Figure 5-4C). Many of the ELP clusters only remained as an empty ring after swelling (Figure 5-4C). This is likely caused by the partitioning coefficient of the cross-linker, which is PEG-BCN, favoring the PEG-azide phase over that of the ELP coacervate phase. In this single-network system, both the ELP-azide and PEG-azide macromers are competing for PEG-BCN cross-linking sites. It is likely that not enough PEG-BCN cross-linker is available within the ELP aggregates to immobilize the structure. When MADM OPCs were encapsulated into these PEA hydrogels the ELP micro-architecture was not preserved (Figure 5-4D). It is unclear as to why MADM OPCs affected the formation of ELP micro-architecture when the azide functionalization was limited to 4 out of 14 primary amines.

The PEA single-network hydrogel system was not suitable for localizing ELP, and subsequently RGD, into microscale clusters.

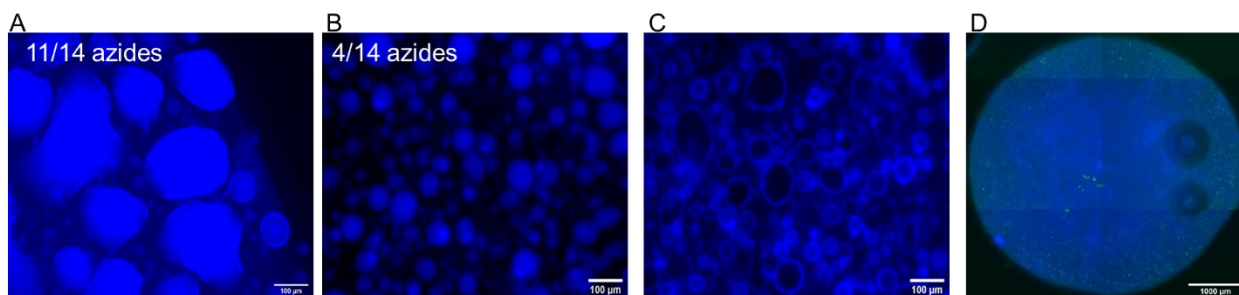


Figure 5-4: Problems with PEA hydrogel domain formation and retention. (A) 6/1.5 PEA (1:1) hydrogels cross-linked at temperatures above the ELP LCST did not form ELP aggregates with consistent size and shape. ELP is tagged with Alexa Fluor 405 (represented in blue) and 11/14 primary amines were functionalized into azides. (B) 6/1.5 PEA (1:1) hydrogels cross-linked at temperatures above the ELP LCST did form ELP aggregates with consistent size and shape when only 4/14 ELP amines were converted into azides. (C) 6/1.5 PEA (1:1) hydrogels with uniform ELP aggregates did not maintain ELP aggregate structure after swelling in PBS for 24 hours. Scale bars = 100 μm. (D) Encapsulation of MADM OPCs in 6/1.5 PEA (1:1) hydrogels interferes with ELP micro-architecture. Scale bar = 1,000 μm.

5.5. Conclusions and future perspectives

The goal of this work was to demonstrate that clustering of the RGD adhesive peptide sequence would affect the cellular proliferative behavior in a 3D hydrogel system similarly to previous work on a 2D hydrogel system^{2,3}. However, a hydrogel system capable of clustering ELP while maintaining encapsulated MADM OPC viability was not found. The THPC cross-linker was cytotoxic to MADM OPCs, making the PEG-ELP double-network hydrogel system unusable for this cell type. It's important to note that THPC is cytocompatible with other cell types and the best avenue forward for this project is to try this experiment with another cell line^{19,20}. These hydrogel systems provide a simple way to cluster ELP and any bioactive peptide sequence attached to the protein. However, there is a clear limitation to the type of micro-architecture that can be formed which limits the impact this system can have in the hydrogel micro-architecture design

field. Hydrogel materials amenable to 3D bioprinting and lithography techniques have the potential to create more sophisticated designs.

Efforts to create single-network PEA hydrogels with similar ELP micro-architecture were unsuccessful. The addition of azide groups to ELP affects the LCST transition in a disadvantageous way. Converting too many primary amines into azides decreased the LCST below RT and affected the physical properties of the coacervate phase. It is unclear whether the newly formed coacervate phase had gelled or was simply too viscous to pipet, but the ELP LCST transition is utilized as a thermo-responsive gelation mechanism in some ELP sequences²¹. Reducing the number of azides added to each ELP molecule helped alleviate these issues: the LCST still shifted but remained above RT and the coacervate phase could be pipetted. However, the newly formed hydrogels did not maintain the ELP micro-architecture after swelling and in the presence of MADM OPCs. From these experiments it's clear that double-network hydrogel systems are inherently better than single-network hydrogel systems for utilizing the ELP LCST to form protein clusters. In single-network hydrogels the cross-linker is consumed by both phases and is likely to favor one phase over the other during mixing. This skews the cross-linking density of each phase and may leave one phase inadequately cross-linked.

5.6. References

- (1) Meco, E.; Lampe, K. J. Impact of Elastin-like Protein Temperature Transition on PEG-ELP Hybrid Hydrogel Properties. *Biomacromolecules* 2019, 20, acs.biomac.9b00113. <https://doi.org/10.1021/acs.biomac.9b00113>.
- (2) Benitez, P. L.; Mascharak, S.; Proctor, A. C.; Heilshorn, S. C. Use of Protein-Engineered Fabrics to Identify Design Rules for Integrin Ligand Clustering in Biomaterials. *Integr. Biol. (Camb)*. 2016, 8 (1), 50–61. <https://doi.org/10.1039/c5ib00258c>.
- (3) Benitez, P. L.; Sweet, J. A.; Fink, H.; Chennazhi, K. P.; Nair, S. V.; Enejder, A.; Heilshorn, S. C. Sequence-Specific Crosslinking of Electrospun, Elastin-Like Protein Preserves Bioactivity and Native-Like Mechanics. *Adv. Healthc. Mater.* 2013, 2 (1), 114–118. <https://doi.org/10.1002/adhm.201200115>.
- (4) Lampe, K. J.; Mooney, R. G.; Bjugstad, K. B.; Mahoney, M. J. Effect of Macromer Weight Percent on Neural Cell Growth in 2D and 3D Nondegradable PEG Hydrogel Culture. *J. Biomed. Mater. Res. - Part A* 2010, 94 (4), 1162–1171. <https://doi.org/10.1002/jbm.a.32787>.
- (5) Liu, C.; Sage, J. C.; Miller, M. R.; Verhaak, R. G. W.; Hippenmeyer, S.; Vogel, H.; Foreman, O.; Bronson, R. T.; Nishiyama, A.; Luo, L.; Zong, H. Mosaic Analysis with Double Markers Reveals Tumor Cell of Origin in Glioma. *Cell* 2011, 146 (2), 209–221. <https://doi.org/10.1016/j.cell.2011.06.014>.
- (6) Zong, H.; Espinosa, J. S.; Su, H. H.; Muzumdar, M. D.; Luo, L. Mosaic Analysis with Double Markers in Mice. *Cell* 2005, 121 (3), 479–492. <https://doi.org/10.1016/j.cell.2005.02.012>.

- (7) Russell, L. N.; Lampe, K. J. Oligodendrocyte Precursor Cell Viability , Proliferation , and Morphology Is Dependent on Mesh Size and Storage Modulus in 3D Poly (Ethylene Glycol) -Based Hydrogels. *ACS Biomater. Sci. Eng.* 2017, 3, 3459–3468. <https://doi.org/10.1021/acsbiomaterials.7b00374>.
- (8) DeForest, C. A.; Tirrell, D. A. A Photoreversible Protein-Patterning Approach for Guiding Stem Cell Fate in Three-Dimensional Gels. *Nat. Mater.* 2015, 14 (5), 523–531. <https://doi.org/10.1038/nmat4219>.
- (9) Brase, S.; Gil, C.; Knepper, K.; Zimmermann, V. Organic Azides: An Exploding Diversity of a Unique Class of Compounds. *Angew. Chemie - Int. Ed.* 2005, 44 (33), 5188–5240. <https://doi.org/10.1002/anie.200400657>.
- (10) Madl, C. M.; Heilshorn, S. C. Tyrosine-Selective Functionalization for Bio-Orthogonal Cross-Linking of Engineered Protein Hydrogels. *Bioconjug. Chem.* 2017, 28 (3), 724–730. <https://doi.org/10.1021/acs.bioconjchem.6b00720>.
- (11) Van Dongen, S. F. M.; Teeuwen, R. L. M.; Nallani, M.; Van Berkel, S. S.; Cornelissen, J. J. L. M.; Nolte, R. J. M.; Van Hest, J. C. M. Single-Step Azide Introduction in Proteins via an Aqueous Diazo Transfer. *Bioconjug. Chem.* 2009, 20 (1), 20–23. <https://doi.org/10.1021/bc8004304>.
- (12) D’Arcy, R.; Tirelli, N. Mitsunobu Reaction: A Versatile Tool for PEG End Functionalization. *Macromol. Rapid Commun.* 2015, 36 (20), 1829–1835. <https://doi.org/10.1002/marc.201500380>.
- (13) Eldijk, M. B. Van; Smits, F. C. M.; Vermue, N.; Debets, M. F.; Scho, S.; Hest, J. C. M. Van. Synthesis and Self-Assembly of Well-Defined Elastin-Like Polypeptide – Poly(Ethylene Glycol) Conjugates. *Biomacromolecules* 2014, 15, 2751–2759.

- (14) Madl, C. M.; Katz, L. M.; Heilshorn, S. C. Bio-Orthogonally Crosslinked, Engineered Protein Hydrogels with Tunable Mechanics and Biochemistry for Cell Encapsulation. *Adv. Funct. Mater.* 2016, 26 (21), 3612–3620. <https://doi.org/10.1002/adfm.201505329>.
- (15) Baskin, J. M.; Prescher, J. A.; Laughlin, S. T.; Agard, N. J.; Chang, P. V; Miller, I. A.; Lo, A.; Codelli, J. A.; Bertozzi, C. R. Copper-Free Click Chemistry for Dynamic in Vivo Imaging. *Proc. Natl. Acad. Sci. U. S. A.* 2007, 104 (43), 16793–16797. <https://doi.org/10.1073/pnas.0707090104>.
- (16) Ruskowitz, E. R.; Deforest, C. A. Photoresponsive Biomaterials for Targeted Drug Delivery and 4D Cell Culture. *Nat. Rev. Mater.* 2018, 3. <https://doi.org/10.1038/natrevmats.2017.87>.
- (17) DeForest, C. A.; Anseth, K. S. Photoreversible Patterning of Biomolecules within Click-Based Hydrogels. *Angew. Chemie - Int. Ed.* 2012, 51 (8), 1816–1819. <https://doi.org/10.1002/anie.201106463>.
- (18) Deforest, C. A.; Tirrell, D. A. A Photoreversible Protein-Patterning Approach for Guiding Stem Cell Fate in Three-Dimensional Gels. *Nat. Mater.* 2015, 14 (5), 523–531. <https://doi.org/10.1038/nmat4219>.
- (19) Chung, C.; Lampe, K. J.; Heilshorn, S. C. Tetrakis(Hydroxymethyl) Phosphonium Chloride as a Covalent Cross-Linking Agent for Cell Encapsulation within Protein-Based Hydrogels. *Biomacromolecules* 2012, 13 (12), 3912–3916. <https://doi.org/10.1021/bm3015279>.
- (20) Lampe, K. J.; Antaris, A. L.; Heilshorn, S. C. Design of Three-Dimensional Engineered Protein Hydrogels for Tailored Control of Neurite Growth. *Acta Biomater.* 2013, 9 (3), 5590–5599. <https://doi.org/10.1016/j.actbio.2012.10.033>.

- (21) Asai, D.; Xu, D.; Liu, W.; Garcia Quiroz, F.; Callahan, D. J.; Zalutsky, M. R.; Craig, S. L.; Chilkoti, A. Protein Polymer Hydrogels by in Situ, Rapid and Reversible Self-Gelation. *Biomaterials* 2012, 33 (21), 5451–5458. <https://doi.org/10.1016/j.biomaterials.2012.03.083>.

6. 3D bioprinting of ELP

6.1. Introduction

The elastin-like protein (ELP) lower critical solution temperature (LCST) transition provides a simple way to introduce micro-architecture into biomaterial constructs. However, there are limitations to the type of micro-architecture that can be achieved through the formation of ELP aggregates. 3-dimensional (3D) extrusion bioprinting is an additive manufacturing process that has emerged as a novel technique to develop more sophisticated micro-architecture within biomaterial scaffolds¹. Biomaterial scaffolds with hierarchical architecture can be constructed from printed micron and sub-micron filaments². For example, a gelatin-based bioink was printed into a tubular structure with the walls patterned into a cross-hatch to create blood vessel-like structure with porosity². With 3D bioprinting the porosity of the walls could be controlled to act as a selective barrier for radial transport into the tubular construct. 3D bioprinting has the potential to construct biomaterials scaffolds that mimic complex native tissue functionality, but most biomaterials do not possess the physical properties required for the 3D bioprinting process^{3,4}. The ELP sequence used in this study cannot be 3D printed without further modification because the pre-gelation solutions are Newtonian liquids, and the ELP cross-linking reactions (tetrakis(hydroxymethyl) phosphonium chloride (THPC) and strain-promoted azide-alkyne cycloaddition (SPAAC) cross-linking) occur on the order of several minutes. The creation of 3D printable ELP hydrogels would allow for a greater capacity to design hydrogel micro-architecture than simple LCST transition-based mixing.

6.2. ELP bioinks: Mixing with yield stress materials

Bioinks are materials that contain the properties necessary for 3D bioprinting: they can be extruded through a needle, printed filaments maintain their shape, and help maintain the viability of mammalian cells going through the printing process. Simple mixing of cytocompatible yield stress materials with biomaterials is an effective strategy for creating bioinks^{5,6}. Yield stress materials maintain their structure at low shear stress and undergo structural deformation, entering a viscous liquid-like state, above a material-dependent shear stress value. These properties are favorable for 3D extrusion bioprinting because high stress is applied to make the bioink flow through the nozzle, and the printed filaments will maintain their structure after leaving the nozzle when the applied stress is reduced. An ELP-based bioink was successfully 3D printed by mixing ELP with xanthum gum (XG), which is a food additive with yield stress properties (Figure 6-1). 3D printed hydrogels were formed by printing ELP and XG (ELP/XG) bioink and subsequently incubating printed filaments in a solution of the THPC crosslinker for several minutes (Figure 6-1A). ELP/XG mixtures displayed the necessary yield stress properties for 3D bioprinting: storage modulus (G') was greater than the loss modulus (G'') at low strain which indicates the material does not flow, $G'' > G'$ at high strain which indicates the material flows, and $G' > G''$ after returning to low strain which indicates the material can retain its printed structure (Figure 6-1B). In addition, the ELP crosslinking reaction with THPC was not hindered by XG and finished after 20 minutes as indicated by an increase of G' until a plateau is reached when the crosslinking reaction is completed (Figure 6-1C). Smooth muscle cells (SMC) were successfully printed using the ELP/XG bioink with 74 % viability (Figure 6-1D). However, there are several drawbacks to this 3D bioprinting strategy that limit hydrogel design capabilities.

ELP/XG bioinks have inherent drawbacks that can be improved upon. Proper pre-print mixing of the ELP/XG bioink requires applying enough force to induce material flow (Figure 6-

1B). High mechanical forces, especially shear forces, increase cell membrane permeability and negatively impact viability in the printed construct⁷. In addition, every additional component added to the ELP/XG bioink changes the physical properties, which not only requires adjusting the bioprinter settings, but may affect printed filament integrity. For example, even the addition of THPC, a small molecule, to XG increased the G' (Figure 6-1C). There is also a limitation on the number of filaments can be stacked on top of each other, limiting construct build height, because this strategy relies on the printed ELP/XG filaments to maintain their structure until THPC is added to cross-link ELP. Yield stress bioinks can only retain their structure up to a specific amount of stress. Stacking filaments on top of each other will eventually cause the bottom filaments to deform and collapse once enough stress is applied by subsequent filaments. Similar work, using adamantane and β -cyclodextrin supramolecular assembly to print hyaluronic acid-based bioinks, demonstrated that a secondary covalent crosslinking reaction was required for constructs with more than 5 layers to maintain structural integrity⁸. The exact number of layers that can be printed will depend on many factors, such as ELP/XG bioink mixture concentrations, but this is an inherent limitation of this bioprinting scheme that limits the ability to design scaffolds with micro-architecture.

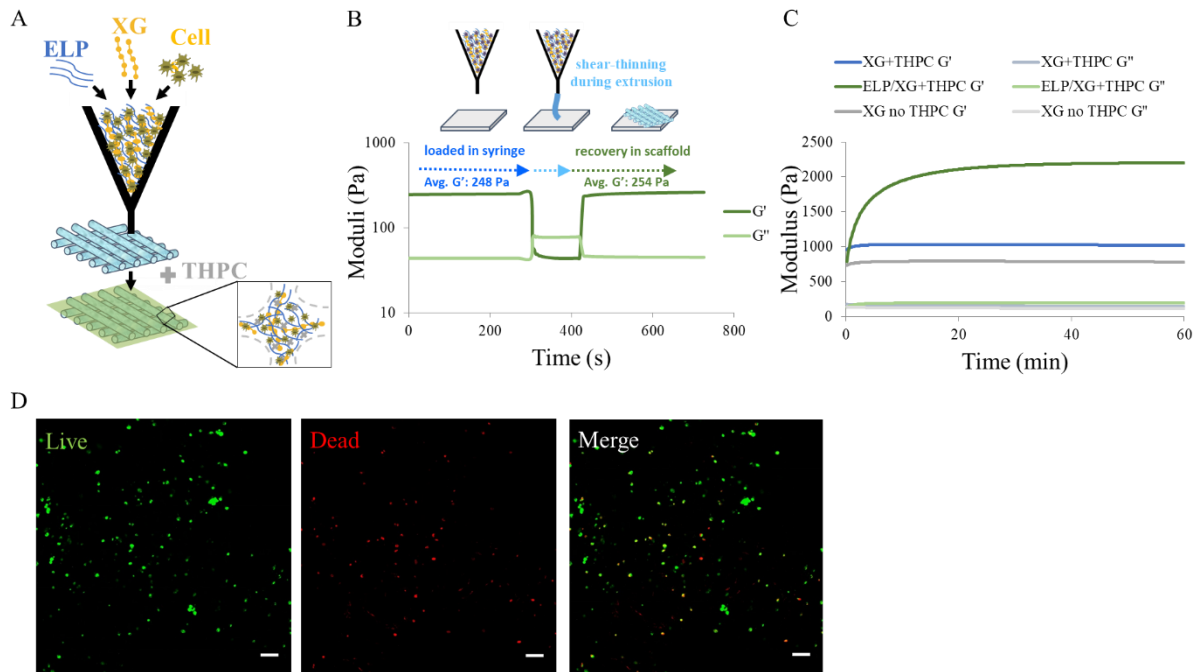


Figure 6-1: ELP/XG bioinks. (A) Schematic of the 3D bioprinting process. XG helps maintain printed filament structural integrity while ELP and THPC cross-linking reaction proceeds. (B) Thixotropic testing of ELP/XG bioink. Bioink does not flow when 0.1 % strain is applied ($G' > G''$), becomes fluid at 100 % strain ($G'' > G'$), and quickly regains non-flow behavior when returning to 1 % strain ($G' > G''$). Test performed with 25 mm cone plate at 1 Hz. (C) Time sweeps of ELP/XG bioink with THPC cross-linker, XG with THPC cross-linker and XG. Test performed with 25 mm cone plate at 1 % strain and 1 Hz. (D) Viability of smooth muscle cells (SMC) 24 hours after 3D printing with ELP/XG bioink. Scale bars = 100 μm .

6.3. ELP bioinks: UV-light induced self-healing

The design capabilities of 3D printed ELP scaffolds can be improved by developing ELP-based bioinks that allow for easy pre-print solution mixing with improved filament build height potential. The introduction of trithiolcarbonates into the ELP hydrogel cross-linking scheme was a promising way to impart ultraviolet (UV)-light induced self-healing properties into ELP bioinks. Trithiolcarbonates were developed for reversible addition-fragmentation chain transfer (RAFT) polymerization techniques, and act as reversible free radical transfer agents that carry a free radical but do not consume it⁹. Free radicals fragment trithiolcarbonate molecules into two species: A free

radical containing fragment and a second trithiolcarbonate fragment (Figure 6-2A)¹⁰. Molecular symmetry around the trithiolcarbonate functional group creates similar molecules in both fragmentation directions. Polymers, with trithiolcarbonate functional groups in the chemical structure, created hydrogels with self-healing properties¹¹⁻¹³. In the context of a hydrogel network, the trithiolcarbonate fragmentation reaction acted as a network shuffling mechanism, and restored hydrogel integrity after mechanical breaks¹¹⁻¹³.

Trithiolcarbonates are not the only type of free radical transfer agents; hydrogels that undergo similar reactions were also created using allyl sulfides^{14,15}. However, trithiolcarbonate molecules, unlike other allyl sulfide functional groups, also absorb UV light to form free radicals, and can self-photoinitiate hydrogel network shuffling reactions (Figure 6-2B)^{16,17}. In hydrogel networks where the free radical shuffling reactions need to be photoinitiated with small molecules, such as lithium phenyl-2,4,6-trimethylbenzoylphosphinate (LAP) or Irgacure 2959, the photoinitiator free radical termination reactions are likely to create breaks in the crosslinked network. This process reduces the resulting hydrogel stiffness after each photoinitiation¹⁵. Since trithiolcarbonates can self-photoinitiate, the hydrogel stiffness is expected to remain constant because the UV-light photoinitiation creates a break in the hydrogel network, and the termination reaction reforms a network cross-link (no net change in number of cross-links). Previous work incorporated trithiolcarbonate functional groups into the pre-hydrogel polymer structure¹¹⁻¹³, but similar hydrogels with self-healing properties should be achievable by incorporating a small molecule with trithiolcarbonate functionality into the ELP crosslinking scheme.

The goal was to create ELP hydrogels with UV-light induced self-healing capabilities by using the norbornene and thiol free radical crosslinking scheme¹⁸⁻²⁰. The trithiolcarbonate functional group cannot be used as the crosslinking mechanism because the reaction with free

radicals does not result in a cross-link. The UV-light induced cross-linking of norbornene with thiols is favorable for 3D bioprinting because the reaction times are fast (on the order of several seconds)^{18–20}. In addition, this reaction occurs through step-growth polymerization instead of chain-growth, which allows for better control over the location of molecules with trithiolcarbonate functionality during cross-linking. Primary amines on ELP lysine residues were functionalized with norbornene groups by adapting a reaction method used in previous work to functionalize PEG-amine polymers with norbornene groups^{20–22}. Norbornene functionalization of 66 – 85% was achieved and determined by comparing the integral of the norbornene double bond hydrogen peak to the peak representing hydrogens on tyrosine residues in the ELP sequence proton nuclear magnetic resonance (HNMR) spectrum (Figure 6-2C). Functionalizing ELP with norbornene groups (ELP-nb) reduced the LCST to ~12°C (visual observation). ELP-nb was crosslinked with dithiothreitol (DTT), a commercially available dithiol small molecule, in the presence of LAP and UV light (Figure 6-2D). Gelation was fast, occurring within 30 seconds after UV light was applied, and the storage modulus was similar to that of ELP hydrogels crosslinked with THPC (Figure 6-2D). UV-light induced self-healing properties were to be imparted into this hydrogel system by incorporating trithiolcarbonate functional groups through small molecule addition to the pre-cross-linked solution.

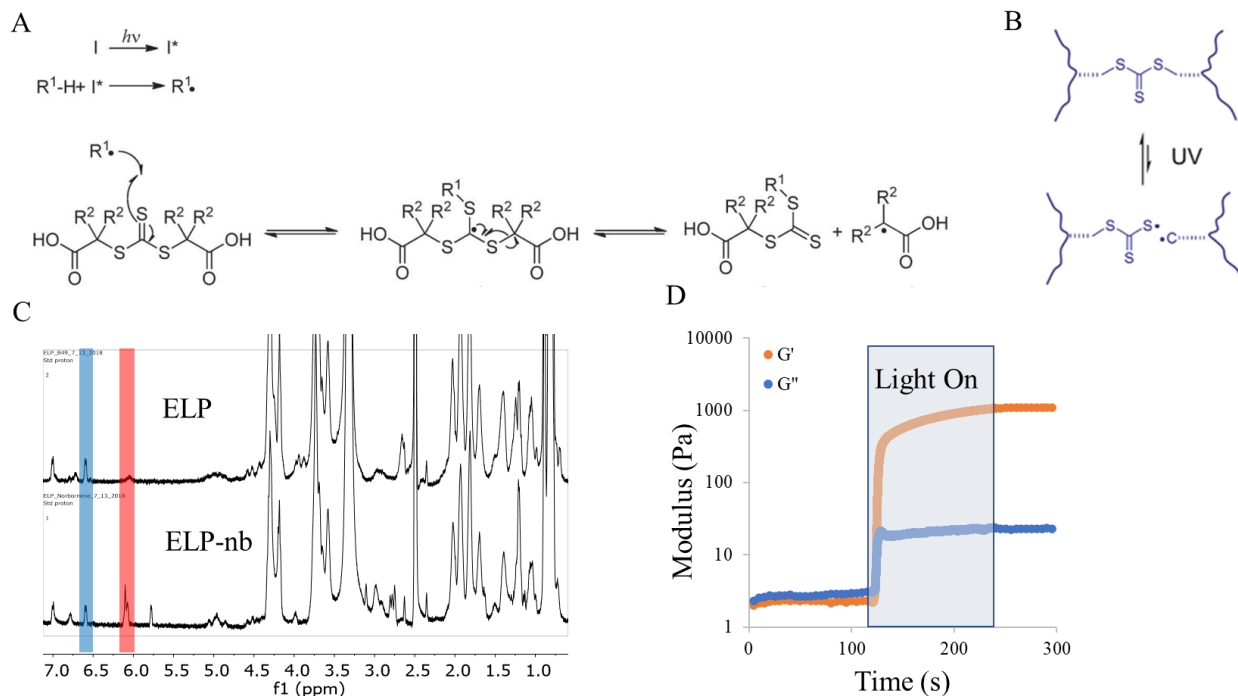


Figure 6-2: UV light sensitive ELP hydrogels (A) Free radical reaction with trithiolcarbonate molecule produces two molecular fragments [Adapted from ref. 11]. (B) Trithiolcarbonates absorb UV light to produce free radicals [Adapted from ref. 19]. (C) Nornbornene functionalization of ELP was determined by comparing nornbornene double bond hydrogen peaks (6.3 ppm, highlighted with red bar) to the tyrosine hydrogen peak (6.6 ppm, highlighted with blue bar). (D) Cross-linking of 5 wt/v % ELP solution with 1:1 ratio of nornbornene to thiol functional groups and 0.5 wt/v % LAP. Measurements taken with 25 mm cone plate at 4°C, 1 % strain, 1 Hz and 6 mW/cm² light power.

UV-light induced self-healing properties were to be incorporated into the ELP hydrogel network by adding nornbornene functionalized S,S'-bis(α,α' -dimethyl- α'' -acetic acid)-trithiocarbonate (TTCA, Figure 6-3A) to the pre-gel solution. TTCA is a well-studied molecule that displayed the properties required for this project: it absorbs UV light and fragments into free radicals, undergoes free radical shuffling reactions both as a standalone molecule and when incorporated into an n-butyl acrylate-based gels, and was functionalized with nornbornene groups using a relatively simple purification process (crystallization in methanol)^{10,11,16,23}. However, TTCA is an expensive specialty chemical (~\$5/mg) and requires a multistep synthesis¹⁶.

Bis(carboxymethyl) trithiocarbonate (BsTC) is an inexpensive commercially available (\$4.76/g, Sigma Aldrich) chemical with a similar chemical structure to TTCA that may act as a suitable replacement (Figure 6-3B). BsTC absorbance spectrum was similar to that of TTCA (Figure 6-3D)¹⁶. To determine if BsTC UV light absorbance resulted in free radical formation it was mixed with PEG-diacrylate (1,000 kDa, 10 wt %) and solutions were exposed to UV light. PEG-diacrylate and BsTC solutions did not gel under 365 nm light. Lower wavelength UV light was required for BsTC to act as a photoinitiator and PEG-diacrylate solutions gelled when exposed to light from an Omnicure system with a 320 – 390 nm light filter (Figure 6-3C). BsTC displays similar chemical behavior to TTCA.

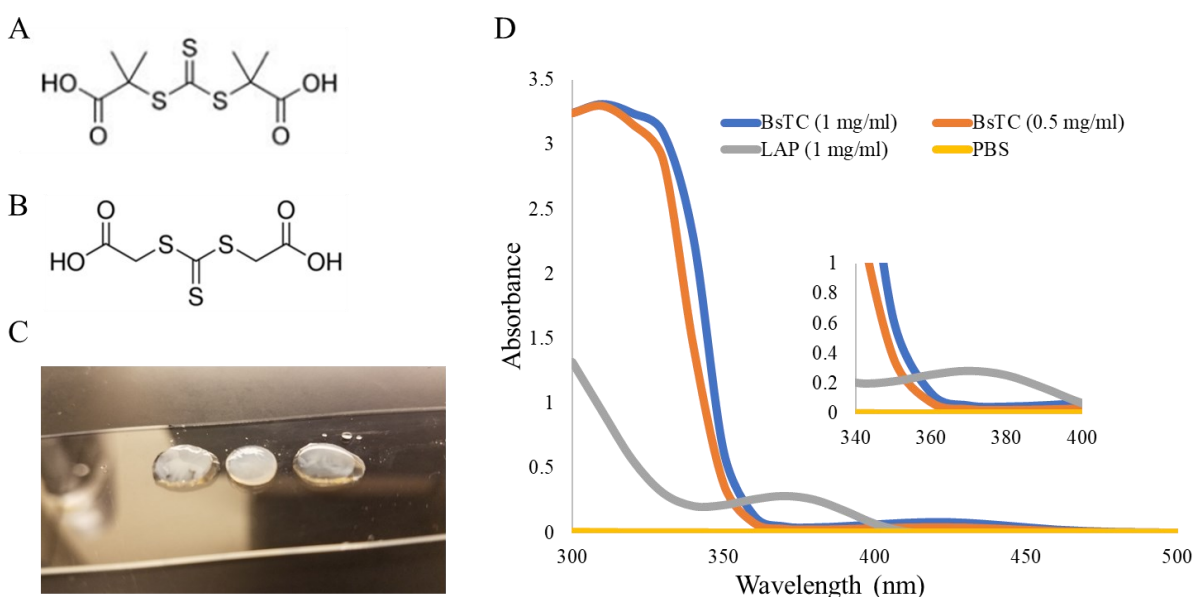


Figure 6-3: BsTC chemistry. (A) TTCA chemical structure. (B) BsTC chemical structure. (C) PEG-acrylate (1,000 kDa, 10 wt/v %) and BsTC (0.05 wt/v %) solutions gel after exposure to 320-390 nm UV light. (D) Absorbance spectrum of BsTC, LAP and PBS.

Attempts to functionalize BsTC with norbornene groups using the Benzotriazole-1-yl-oxy-tris-(dimethylamino)-phosphonium hexafluorophosphate (BOP) coupling reaction did not succeed²⁴. The reaction mixture did not form BsTC-norbornene crystals when methanol was added

dropwise. It was discovered that trithiolcarbonates undergo aminolysis under mild conditions (room temperature)²⁵. The trithiolcarbonate bond is cleaved in the presence of amines. The HNMR spectrum of the reaction products indicated that BsTC fragments existed in the reaction mixture (Figure 6-4). The predicted HNMR spectrum of BsTC-norbornene only has one multiplet peak at ~6 ppm (Figure 6-4A). Only one of the potential BsTC animolysis fragments was predicted to contain multiple multiplets at ~6 ppm (6-4B). The HNMR spectrum of the reaction products contained multiple multiplets ~6 ppm confirming the presence of BsTC animolysis fragments (Figure 6-4C). There are other reactions that can potentially functionalize BsTC with norbornene groups, but aminolysis of the trithiolcarbonate bond under mild conditions makes them unsuitable for biological applications given the prevalence of amines in peptides and proteins.

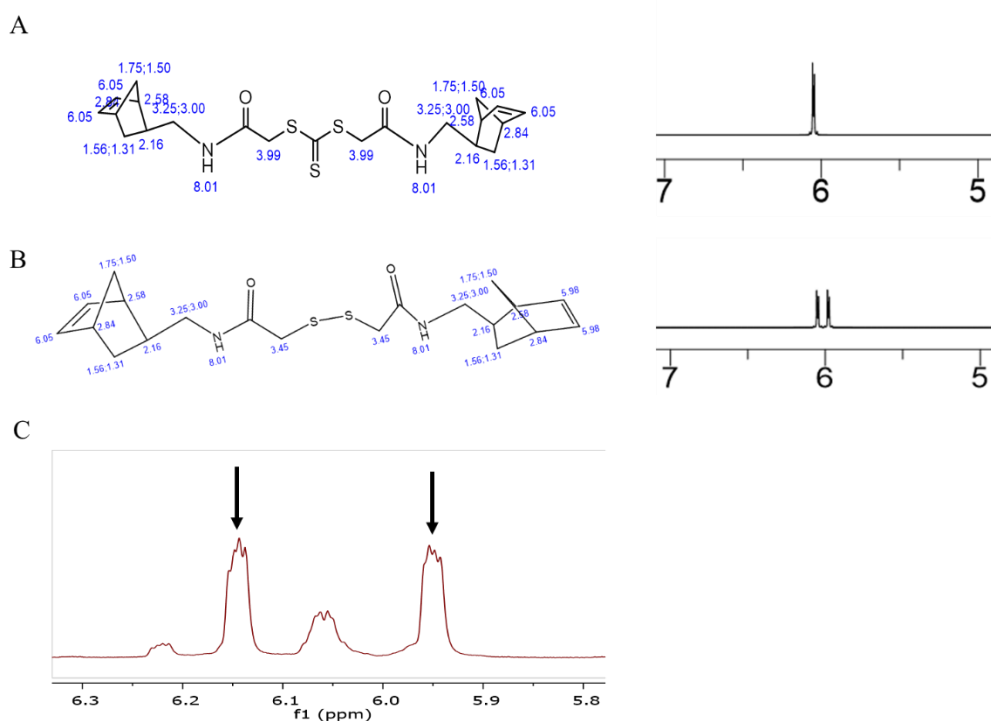


Figure 6-4: BsTC norbornene reaction mixture HNMR. (A) HNMR prediction of norbornene functionalized BsTC has one multiplet peak near 6 ppm. (B) Only one dimerized aminolysis fragment was predicted to have multiple multiplets near 6 ppm. (C) The BsTC norbornene reaction mixture contains two multiplets near 6 ppm that indicate the aminolysis fragment from B is present.

6.4. Conclusions and future perspective

The main focus of this project was to develop an ELP-based bioink that improves on previous ELP/XG bioink limitations. The mixture of ELP-nb cross-linked with BsTC-nb and DTT was designed to make a hydrogel with self-healing capabilities. However, aminolysis of the trithiolcarbonate bond prevents the use of BsTC for biological applications. Allyl sulfides maybe the optimal small molecule to use to create UV-light induced self-healing ELP bioinks because they do not undergo aminolysis^{14,15}. However, unlike TTCA and BsTC, allyl sulfides require the use of photoinitiators for the free radical shuffling reaction to proceed. The initial goal was to create a hydrogel system that would indefinitely act like silly putty in the presence of UV light. Using a photoinitiator with allyl sulfides limits the number of times the free radical shuffling reaction can occur and some hysteresis of the hydrogel stiffness would occur each time.

It was shown that ELP can be functionalized with norbornene groups, and subsequently cross-linked using UV-light and a photoinitiator. Although these hydrogels do not possess self-healing properties, the norbornene cross-linking reaction occurs much faster than other cross-linking methods (on the order of seconds versus minutes). ELP-nb can still potentially be 3D bioprinted using a system that gels the solution drops immediately after they are ejected from the printer nozzle. The ELP-nb reaction reduced the LCST to $\sim 12^{\circ}\text{C}$ so this type of printing system would also need to keep the ELP-nb bioink cool in the syringe. ELP can be 3D printed if the bioinks are developed further.

6.5. References

- (1) Truby, R. L.; Lewis, J. A. Printing Soft Matter in Three Dimensions. *Nature* 2016, 540 (7633), 371–378. <https://doi.org/10.1038/nature21003>.
- (2) Dai, X.; Ma, C.; Lan, Q.; Xu, T. 3D Bioprinted Glioma Stem Cells for Brain Tumor Model and Applications of Drug Susceptibility. *Biofabrication* 2016, 8 (4), 045005. <https://doi.org/10.1088/1758-5090/8/4/045005>.
- (3) Macaya, D.; Spector, M. Injectable Hydrogel Materials for Spinal Cord Regeneration: A Review. *Biomed. Mater.* 2012, 7 (1), 012001. <https://doi.org/10.1088/1748-6041/7/1/012001>.
- (4) Khaing, Z. Z.; Thomas, R. C.; Geissler, S. A.; Schmidt, C. E. Advanced Biomaterials for Repairing the Nervous System: What Can Hydrogels Do for the Brain? *Mater. Today* 2014, 17 (7), 332–340. <https://doi.org/10.1016/j.mattod.2014.05.011>.
- (5) Diamantides, N.; Wang, L.; Pruiksma, T.; Siemiatkoski, J.; Dugopolski, C.; Shortkroff, S.; Kennedy, S.; Bonassar, L. J. Correlating Rheological Properties and Printability of Collagen Bioinks: The Effects of Riboflavin Photocrosslinking and PH. *Biofabrication* 2017, 9 (3), 034102. <https://doi.org/10.1088/1758-5090/aa780f>.
- (6) Siqueira, G.; Kokkinis, D.; Libanori, R.; Hausmann, M. K.; Gladman, A. S.; Neels, A.; Tingaut, P.; Zimmermann, T.; Lewis, J. A.; Studart, A. R. Cellulose Nanocrystal Inks for 3D Printing of Textured Cellular Architectures. *Adv. Funct. Mater.* 2017, 27 (12). <https://doi.org/10.1002/adfm.201604619>.
- (7) LaPlaca, M. C.; Simon, C. M.; Prado, G. R.; Cullen, D. K. CNS Injury Biomechanics and Experimental Models. *Prog. Brain Res.* 2007, 161, 13–26. [https://doi.org/10.1016/S0079-6123\(06\)61002-9](https://doi.org/10.1016/S0079-6123(06)61002-9).

- (8) Ouyang, L.; Highley, C. B.; Rodell, C. B.; Sun, W.; Burdick, J. A. 3D Printing of Shear-Thinning Hyaluronic Acid Hydrogels with Secondary Cross-Linking. *ACS Biomater. Sci. Eng.* 2016, 2 (10), 1743–1751. <https://doi.org/10.1021/acsbiomaterials.6b00158>.
- (9) Moad, G.; Rizzardo, E.; Thang, S. H. Living Radical Polymerization by the RAFT Process – A Third Update. *Aust. J. Chem.* 2012, 65 (8), 985. <https://doi.org/10.1071/ch12295>.
- (10) Leung, D.; Bowman, C. N. Reducing Shrinkage Stress of Dimethacrylate Networks by Reversible Addition-Fragmentation Chain Transfer. *Macromol. Chem. Phys.* 2012, 213 (2), 198–204. <https://doi.org/10.1002/macp.201100402>.
- (11) Amamoto, Y.; Kamada, J.; Otsuka, H.; Takahara, A.; Matyjaszewski, K. Repeatable Photoinduced Self-Healing of Covalently Cross-Linked Polymers through Reshuffling of Trithiocarbonate Units. *Angew. Chemie - Int. Ed.* 2011, 50 (7), 1660–1663. <https://doi.org/10.1002/anie.201003888>.
- (12) Amamoto, Y.; Otsuka, H.; Takahara, A.; Matyjaszewski, K. Self-Healing of Covalently Cross-Linked Polymers by Reshuffling Thiuram Disulfide Moieties in Air under Visible Light. *Adv. Mater.* 2012, 24 (29), 3975–3980. <https://doi.org/10.1002/adma.201201928>.
- (13) Nicolaÿ, R.; Kamada, J.; Van Wassen, A.; Matyjaszewski, K. Responsive Gels Based on a Dynamic Covalent Trithiocarbonate Cross-Linker. *Macromolecules* 2010, 43 (9), 4355–4361. <https://doi.org/10.1021/ma100378r>.
- (14) Gandavarapu, N. R.; Azagarsamy, M. A.; Anseth, K. S. Photo-Click Living Strategy for Controlled, Reversible Exchange of Biochemical Ligands. *Adv. Mater.* 2014, 26 (16), 2521–2526. <https://doi.org/10.1002/adma.201304847>.

- (15) Brown, T. E.; Marozas, I. A.; Anseth, K. S. Amplified Photodegradation of Cell-Laden Hydrogels via an Addition–Fragmentation Chain Transfer Reaction. *Adv. Mater.* 2017, 29 (11). <https://doi.org/10.1002/adma.201605001>.
- (16) Ran, R.; Yu, Y.; Wan, T. Photoinitiated RAFT Polymerization in the Presence of Trithiocarbonate. *J. Appl. Polym. Sci.* 2007, 105, 398–404. <https://doi.org/10.1002/app>.
- (17) Amamoto, Y.; Otsuka, H.; Takahara, A.; Matyjaszewski, K. Changes in Network Structure of Chemical Gels Controlled by Solvent Quality through Photoinduced Radical Reshuffling Reactions of Trithiocarbonate Units. *ACS Macro Lett.* 2012, 1 (4), 478–481. <https://doi.org/10.1021/mz300070t>.
- (18) Fairbanks, B. D.; Schwartz, M. P.; Halevi, A. E.; Nuttelman, C. R.; Bowman, C. N.; Anseth, K. S. A Versatile Synthetic Extracellular Matrix Mimic via Thiol-Norbornene Photopolymerization. *Adv. Mater.* 2009, 21 (48), 5005–5010. <https://doi.org/10.1002/adma.200901808>.
- (19) Frank, D.; Espeel, P.; Badi, N.; Du, F. Structurally Diverse Polymers from Norbornene and Thiolactone Containing Building Blocks. *Eur. Polym. J.* 2018, 98 (September 2017), 246–253. <https://doi.org/10.1016/j.eurpolymj.2017.11.023>.
- (20) Acosta-Vélez, G.; Linsley, C.; Craig, M.; Wu, B. Photocurable Bioink for the Inkjet 3D Pharming of Hydrophilic Drugs. *Bioengineering* 2017, 4 (1), 11. <https://doi.org/10.3390/bioengineering4010011>.
- (21) Roberts, J. J.; Bryant, S. J. Comparison of Photopolymerizable Thiol-Ene PEG and Acrylate-Based PEG Hydrogels for Cartilage Development. *Biomaterials* 2013, 34 (38), 9969–9979. <https://doi.org/10.1016/j.biomaterials.2013.09.020>.

- (22) Shih, H.; Fraser, A. K.; Lin, C. Interfacial Thiol-Ene Photoclick Reactions for Forming Multilayer Hydrogels. *Appl. Mater. Interfaces* 2013, 5, 1673–1680. <https://doi.org/10.1021/am302690t>.
- (23) Zhou, H.; Johnson, J. A.; Turro, N. J. Photo-Controlled Growth of Telechelic Polymers and End-Linked Polymer Gels. *Angew. Chemie - Int. Ed.* 2013, No. 52, 2235–2238. <https://doi.org/10.1002/anie.201207966>.
- (24) Al-Warhi, T. I.; Al-Hazimi, H. M. A.; El-Faham, A. Recent Development in Peptide Coupling Reagents. *J. Saudi Chem. Soc.* 2012, 16 (2), 97–116. <https://doi.org/10.1016/j.jscs.2010.12.006>.
- (25) Desmet, G. B.; D’Hooge, D. R.; Sabbe, M. K.; Reyniers, M. F.; Marin, G. B. Computational Investigation of the Aminolysis of RAFT Macromolecules. *J. Org. Chem.* 2016, 81 (23), 11626–11634. <https://doi.org/10.1021/acs.joc.6b01844>.

7. MADM OPCs in media with FBS

7.1. Introduction

Oligodendrocyte precursor cells isolated through the mosaic analysis with double markers (MADM OPCs) have delayed differentiation *in vivo* and do not differentiate *in vitro*^{1,2}. This phenomenon likely occurs because these cells are Nf1 and p53 gene knockouts^{1,2}. Primary OPC *in vitro* differentiation is performed by first removing proliferation media, which contains growth factors, and replacing it with media that contains serum. OPCs differentiate into oligodendrocytes (OLs) in low serum media (~1 % by volume) and into type II astrocytes (O2A) in high serum media (~20 % by volume)^{3,4}. MADM OPCs are cultured in base media that contains Dulbecco's Modified Eagle Medium (DMEM) with 4.5 g/L glucose, 4 mM L-glutamine, 1mM sodium pyruvate, 1x penicillin/streptomycin, 1x B27 supplement, and 1x N2 supplement. This media used to contain growth factors neurotrophin-3 (NT-3, 50 ng/ml) and platelet derived growth factor-AA (PDGF-AA, 10 ng/ml), but it was discovered that MADM OPC growth was not affected by them (data not shown). Previous work attempted to differentiate MADM OPCs by controlling the delivery of PDGF-AA with nanoparticles⁵. In this study the effect(s) of fetal bovine serum (FBS) on MADM OPC proliferation and morphology were investigated.

7.2. MADM OPCs in media with serum

MADM OPCs were seeded on 24-well plates coated with polyornithine at a surface density of 1×10^4 cells/cm². They were cultured in base media (control group) and in media containing 1 % and 20 % FBS by volume. On day 1 all MADM OPCs were cultured in base media (another control) and on day 2 the media was changed to include FBS (Figure 7-1). Media was then changed every two days until day 7, when it was changed every day (Figure 7-1). By day 5 MADM OPCs in base media reached confluency (Figure 7-1). MADM OPCs cultured in base media

supplemented with 1 % FBS did not exhibit any differences in morphology (Figure 7-1). However, the proliferation rate of these cells was slowed down. MADM OPCs cultured in base media supplemented with 20 % FBS had reduced process extensions and were not proliferating (Figure 7-1). Based on day 1 images, 20 % FBS not only inhibited the extension of processes, it caused MADM OPCs to retract extended processes. During differentiation primary OPCs lose their ability to proliferate, but also extend more processes with higher degrees of branching (for both lineages)⁴. FBS was not sufficient to differentiate MADM OPCs in either OLs or O2As.

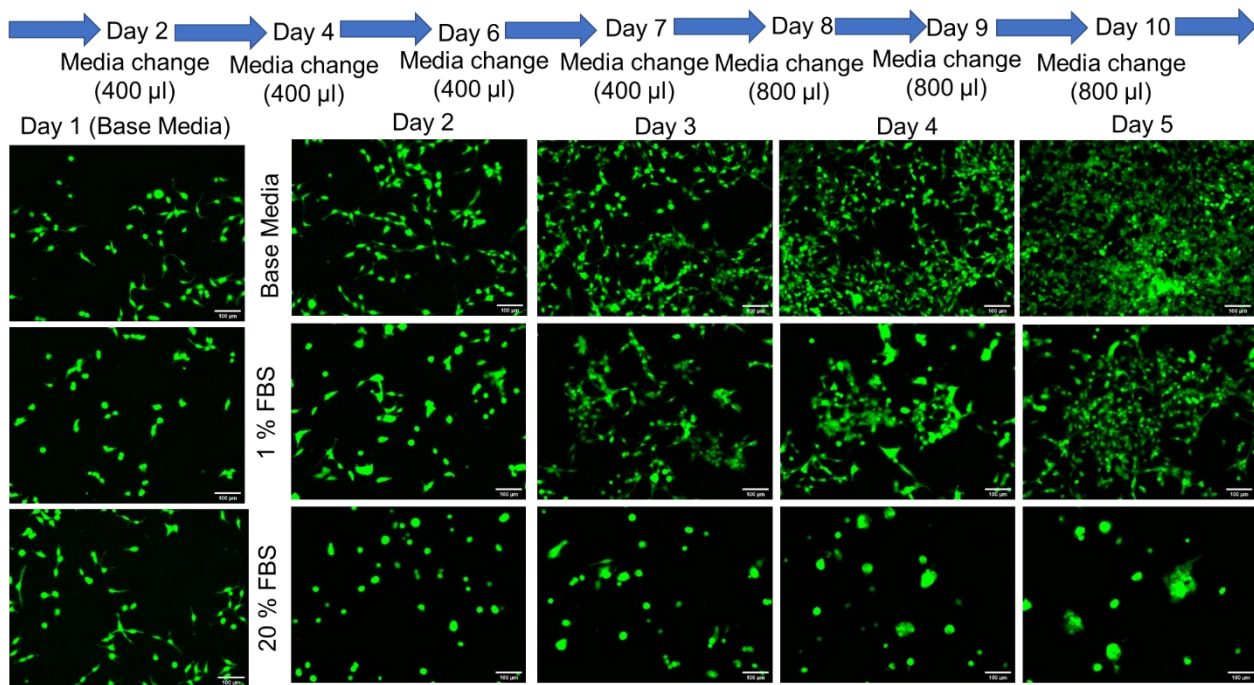


Figure 7-1: MADM OPCs cultured in media supplemented with FBS. Cells were seeded on polyornithine coated 24-well plates at a density of $1e4$ cells/cm². All cells were cultured in base media on day 1. Media was changed on day 2, 4, 6, 7, 8, 9, and 10 for all conditions. MADM OPCs are green fluorescent protein positive (GFP+) and the signal was used to image morphology over time. FBS inhibits MADM OPC proliferation and process extensions. Scale bars = 100 μ m.

MADM OPCs cultured in base media started to cluster together on day 6 (Figure 7-2A white arrow). Empty web-like gaps between cells indicated that MADM OPCs were actively migrating towards the cell clusters (Figure 7-2A gray arrow). On day 7 the cell clusters grew larger

and the media had turned acidic (Figure 7-2B). On day 8, all MADM OPCs were in clusters and the media was acidic again. Typically, these cells are considered dead when this happens. Many cells were floating in the media, so to an extent it is true. On day 8 the quantity of media added was doubled to help prevent acidification of the media (Figure 7-1). This did keep the media from turning acidic and caused a reversal of cell clustering on day 9 (Figure 7-2D). MADM OPCs were observed leaving the cell clusters and spreading across the well plate surface (Figure 7-2D, E). By day 11, MADM OPCs were no longer clustered together (Figure 7-2F). This suggests that the clustering of MADM OPCs is a protective reaction to acidic media and that these cells will recover if base media is replenished.

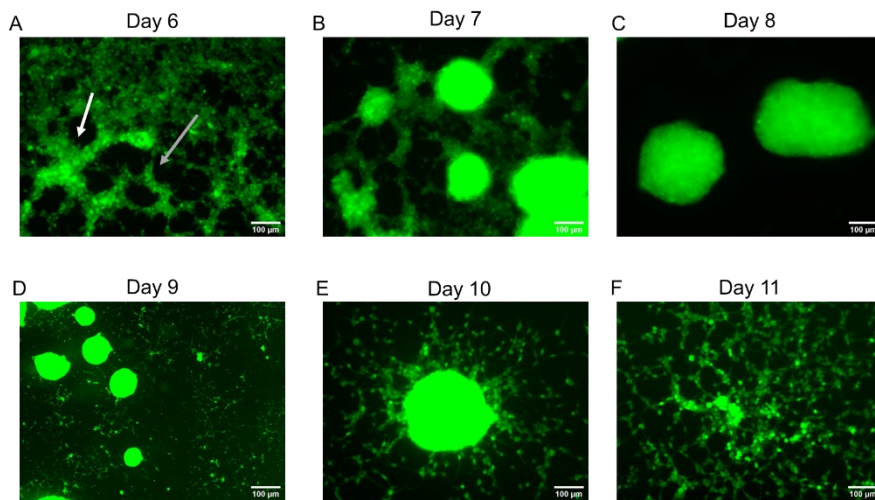


Figure 7-2: MADM OPCs in base media on days 6-11. (A, B, C) In acidic media MADM OPCs cluster together. (D, E, F) When base media is replenished MADM OPCs spread across the surface and cell clusters dissipate. Scale bars = 100 µm.

MADM OPCs cultured in base media supplemented with 1 % FBS reacted in a similar manner to cells in media without FBS (Figure 7-3). Proliferation was slowed down because cell clusters did not appear until day 9 (Figure 7-3D). The media for these cells never turned acidic.

MADM OPCs cultured in base media supplemented with 20 % FBS remained senescent over 7 days (Figure 7-4B, C). On day 7 the media for these cells was changed to base media to

investigate if these cells could still proliferate (Figure 7-4A). While in base media on days 8 and 9 MADM OPCs did proliferate and their morphology was similar to the control group (Figure 7-4D, E). This indicated that the effects of FBS on MADM OPC morphology and proliferation were reversible. It also indicated that these cells did not terminally differentiate because they did not lose the capability to proliferate. Re-adding media supplemented with 20 % FBS caused similar effects that occurred on day 2. MADM OPCs stopped proliferating and process extensions were retracted (Figure 7-4F, G). The effects of FBS on MADM OPCs are reversible.

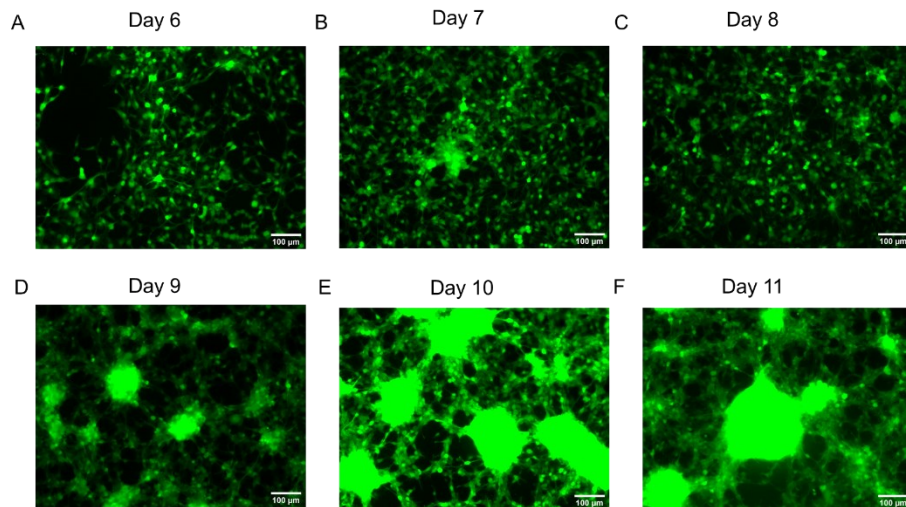


Figure 7-3: MADM OPCs in base media supplemented with 1 % FBS on days 6-11. MADM OPC proliferation is slowed down, but cells act in a similar manner to MADM OPCs in base media. Scale bars = 100 μm.

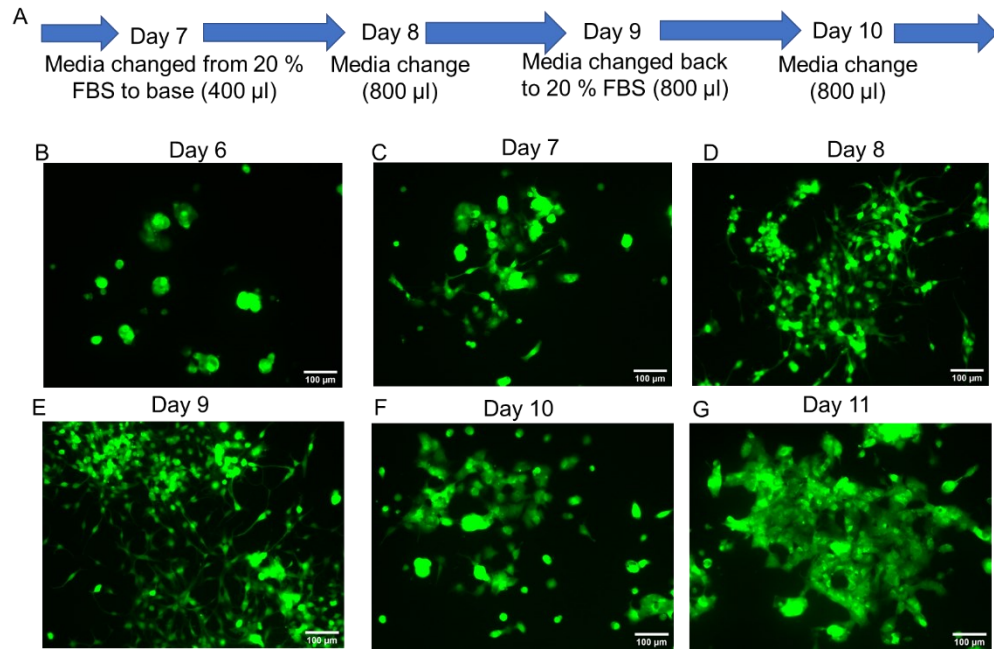


Figure 7-4: MADM OPCs in base media supplemented with 20 % FBS on days 6-11. (A) Timeline of media changes during days 6-11. Media was changed to proliferation media after imaging cells on days 7 and returned to 20 % FBS media after imaging on day 9. (B, C) MADM OPCs remain senescent in 20 % FBS media. (D, E) MADM OPCs proliferate normally in base media. (F, G) The re-addition of FBS causes MADM OPCs to retract process extensions and return to a senescent state. The effects of FBS on MADM OPCs are reversible. Scale bars = 100 µm.

7.3. Conclusions and future perspectives

FBS inhibits MADM OPC proliferation and process extension. These effects are reversible by removing FBS from the media. FBS did not induce MADM OPC differentiation. It is important to elucidate the trophic support that helps MADM OPCs differentiate *in vivo*². Currently there are limitations to what can be investigated *in vitro* with MADM OPCs because mature OLs may react differently to external factors than OPCs. In particular, for demyelinating diseases it is important to investigate myelin production and structure. Studies to that effect cannot be currently done with MADM OPCs. Primary OPCs are not immortalized making them a more expensive and difficult cell to work with³. Ideally, a simple change to the media of MADM OPCs would induce their

differentiation. The Nf1 and p53 gene knockouts impact the Erk 1/2 and mTORC1 pathways which affect OPC differentiation^{6,7}. Further investigation of these pathways may inform the next round of efforts to differentiate MADM OPCs.

7.4. References

- (1) Zong, H.; Espinosa, J. S.; Su, H. H.; Muzumdar, M. D.; Luo, L. Mosaic Analysis with Double Markers in Mice. *Cell* 2005, 121 (3), 479–492. <https://doi.org/10.1016/j.cell.2005.02.012>.
- (2) Liu, C.; Sage, J. C.; Miller, M. R.; Verhaak, R. G. W.; Hippenmeyer, S.; Vogel, H.; Foreman, O.; Bronson, R. T.; Nishiyama, A.; Luo, L.; Zong, H. Mosaic Analysis with Double Markers Reveals Tumor Cell of Origin in Glioma. *Cell* 2011, 146 (2), 209–221. <https://doi.org/10.1016/j.cell.2011.06.014>.
- (3) Suzuki, N.; Sekimoto, K.; Hayashi, C.; Mabuchi, Y.; Nakamura, T.; Akazawa, C. Differentiation of Oligodendrocyte Precursor Cells from Sox10-Venus Mice to Oligodendrocytes and Astrocytes. *Sci. Rep.* 2017, 7 (1), 1–11. <https://doi.org/10.1038/s41598-017-14207-0>.
- (4) Behar, T. N. Analysis of Fractal Dimension of O2A Glial Cells Differentiating in Vitro. *Methods* 2001, 24, 331–339. <https://doi.org/10.1016/j.expneurol.2016.03.019>.
- (5) Pinezich, M. R.; Russell, L. N.; Murphy, N. P.; Lampe, K. J. Encapsulated Oligodendrocyte Precursor Cell Fate Is Dependent on PDGF-AA Release Kinetics in a 3D Microparticle-Hydrogel Drug Delivery System. *J. Biomed. Mater. Res. - Part A* 2018, 106 (9), 2402–2411. <https://doi.org/10.1002/jbm.a.36432>.
- (6) Tyler, W. A.; Gangoli, N.; Gokina, P.; Kim, H. A.; Covey, M.; Levison, S. W.; Wood, T. L. Activation of the Mammalian Target of Rapamycin (MTOR) Is Essential for Oligodendrocyte Differentiation. *J. Neurosci.* 2009, 29 (19), 6367–6378. <https://doi.org/10.1523/JNEUROSCI.0234-09.2009>.

- (7) Guardiola-diaz, H. M.; Ishii, A.; Bansal, R. Erk1 / 2 MAPK and MTOR Signaling Sequentially Regulates Progression Through Distinct Stages of Oligodendrocyte Differentiation. *Glia* 2012, 486 (December 2011), 476–486. <https://doi.org/10.1002/glia.22281>.

8. Appendix A: Chapter 3 Supplementary Information

Supplemental information for: E. Meco, KJ Lampe, "Impact of Elastin-like Protein Temperature Transition on PEG-ELP Hybrid Hydrogel Properties." *Biomacromolecules*, 50, 5:1914-1925 (2019)

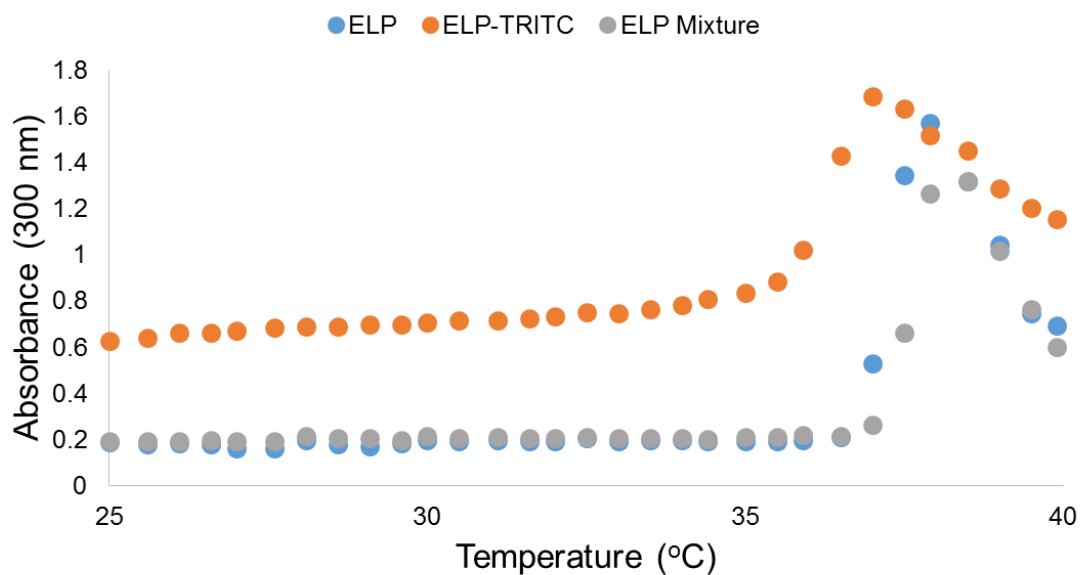


Figure A-1: Optical density of ELP, TRITC modified ELP, and the mixture used for fluorescent microscopy (1:19 ELP:ELP-TRITC) as a function of temperature.

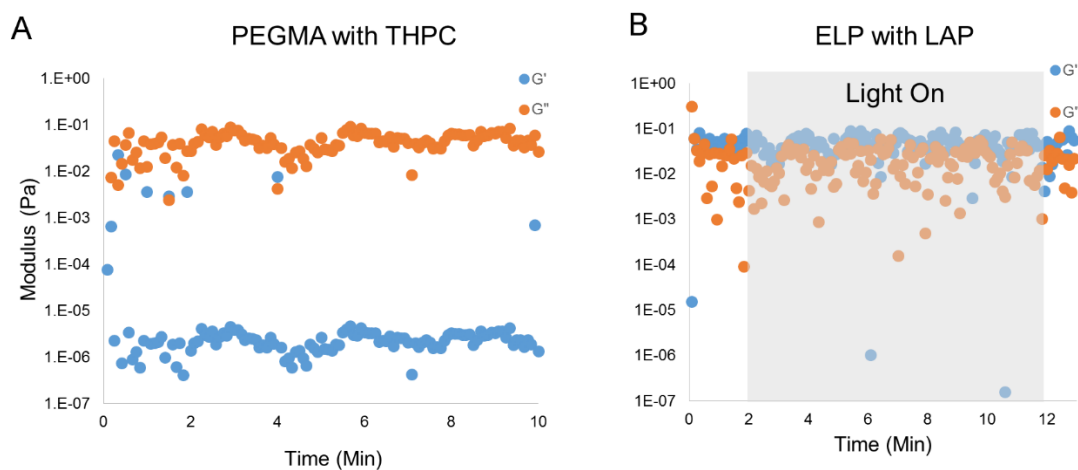


Figure A-2: PEGMA and ELP cross-reactions. (A) No rheological changes to 6 wt % PEGMA solution occur over 10 minutes when mixed with THPC (1 mg/ml). (B) No rheological changes to 3wt % ELP solution occur when mixed with LAP (0.05 wt/v %) and exposed to UV light for 10 minutes.

Figure 3-7 data points where at least one sample reached the instrument detection limit.

1. Figure 7A: filled red squares from 2-6 wt/v% ELP concentration.
2. Figure 7B: filled red squares from 2-6 wt/v% ELP concentration.
3. Figure 7C: filled black square 6 wt/v% ELP concentration.
4. Figure 7D: filled black squares from 2-6 wt/v% ELP concentration.

9. Appendix B: Chapter 4 Supplementary Information

Supplemental information for: E. Meco, WS Sharon, AH Sharma and KJ Lampe, "Guiding oligodendrocyte precursor cell maturation with urokinase plasminogen activator-degradable elastin-like protein hydrogels," in review at Biomacromolecules

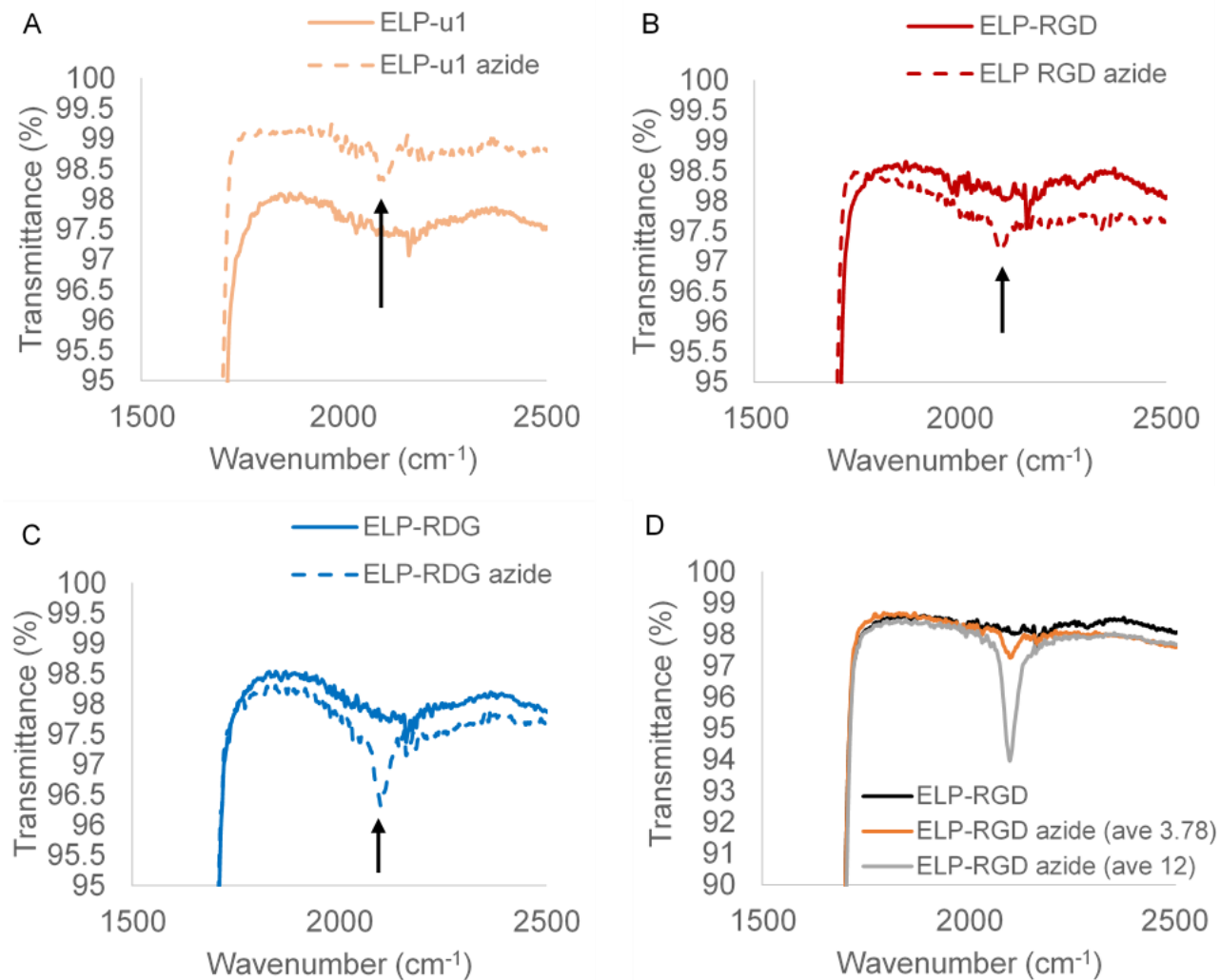


Figure B-1: FTIR of ELP pre- and post-azide functionalization. The appearance of a peak at 2100 cm^{-1} for (A) uPA degradable sequence ELP-u1, (B) integrin binding sequence ELP-RGD, and (C) non-bioactive sequence ELP-RDG indicated the presence of azide bonds within the protein structure. (D) The azide peak intensity increased with higher azide functionalization as indicated by FTIR of ELP-RGD sequence pre-modification and protein batches modified with an average of 3.78 and 12 azides. The average azide group addition was controlled by stoichiometrically limiting the number of azides present during the diazotransfer reaction.

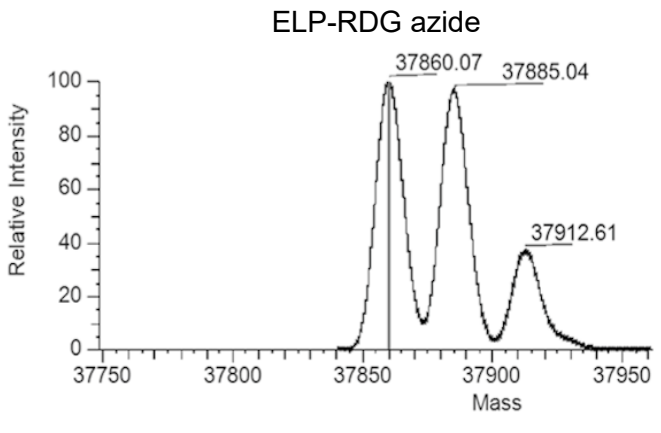
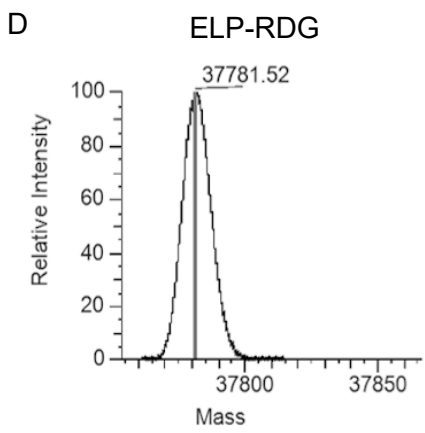
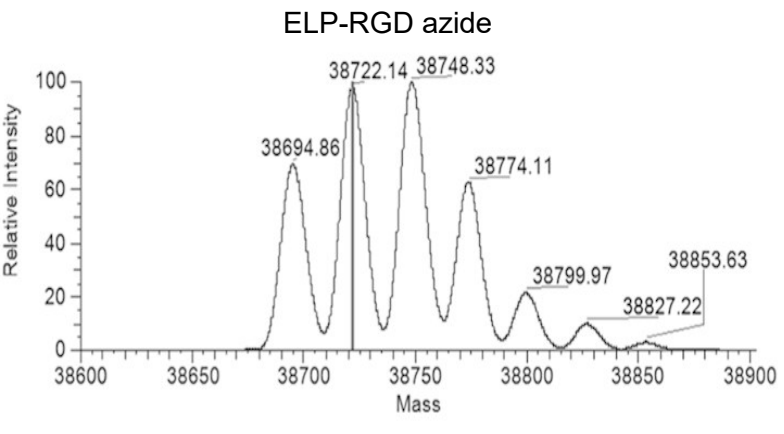
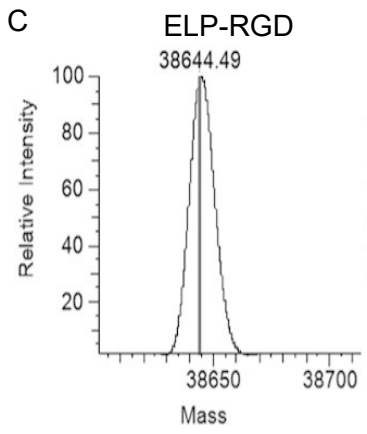
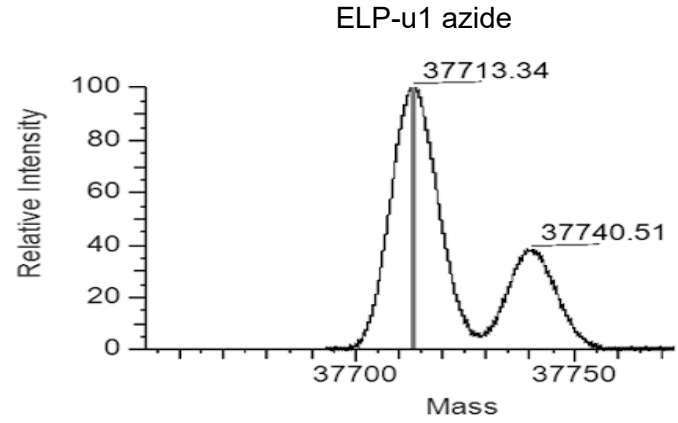
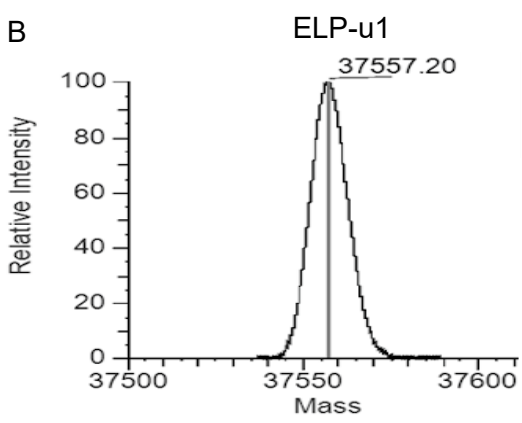
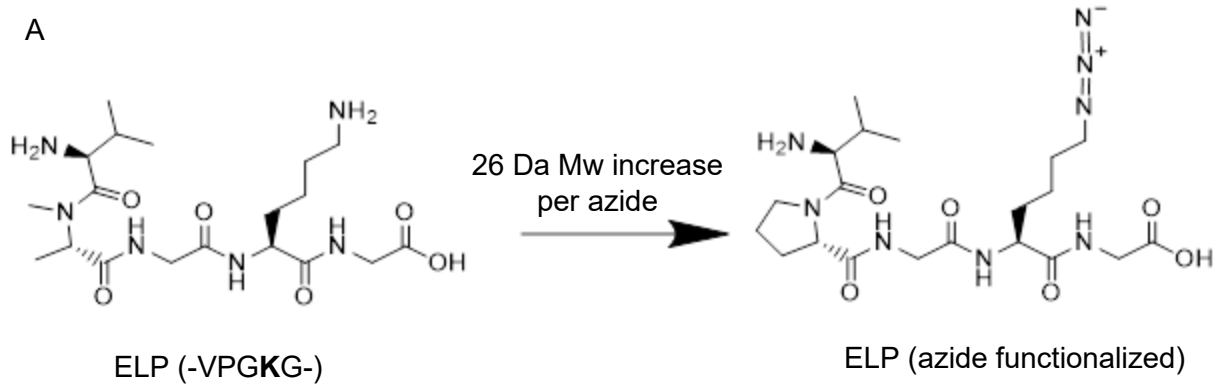


Figure B-2: High resolution electrospray ionization-mass spectrometry (ESI-MS) of ELP pre- and post-azide functionalization. (A) Each lysine residue modification with azides increases protein mass by 26 Da. Pre-azide modification ELP sequence appears as one peak, indicating monodisperse protein molecular weight. Post-azide modification ELP appears as multiple peaks with 26 Da differences, indicating that the diazo transfer reaction created ELPs with a distribution of attached azides: (B) uPA degradable sequence ELP-u1 pre- and post-azide functionalization, (C) cell-adhesive sequence ELP-RGD pre- and post-azide functionalization, and (D) non-bioactive sequence ELP-RDG pre- and post-azide functionalization. The relative peak intensities were quantified to determine the molecular average of azides added to ELP-u1, -RGD and -RDG, which were 6.28, 3.78, and 3.74, respectively.

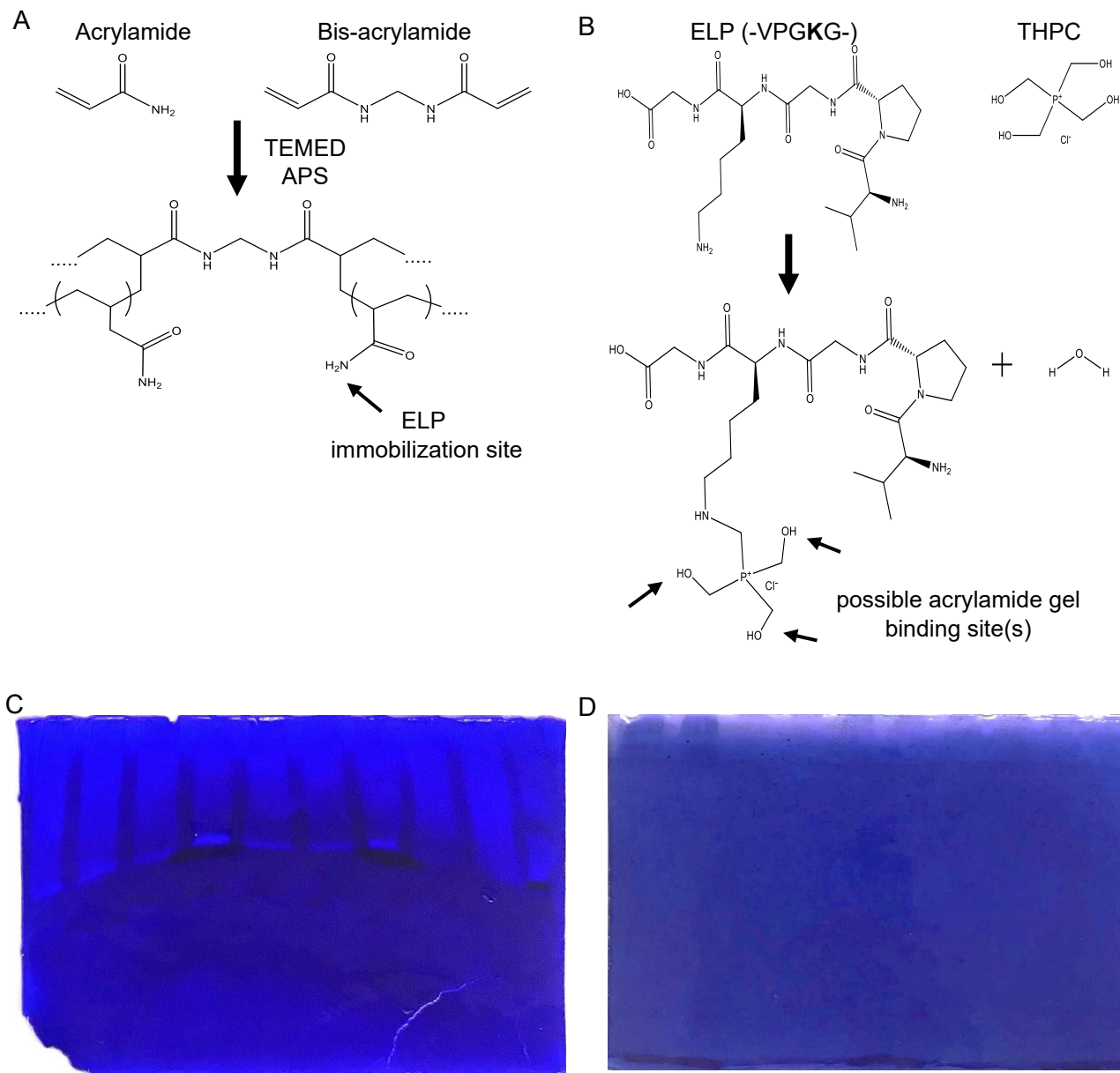


Figure B-3: THPC used to immobilize ELP to poly(acrylamide) gel for zymography. (A) Poly(acrylamide) crosslinking chemistry creates a gel with primary amines in the structure. (B) THPC has four primary amine reactive sites that allow for ELP to be immobilized onto poly(acrylamide) gel network. (C) Poly(acrylamide) gel dosed with ELP without THPC causes ELP to migrate down the wells during electrophoresis. (D) Poly(acrylamide) gel dosed with immobilized ELP maintains uniform protein distribution after electrophoresis.

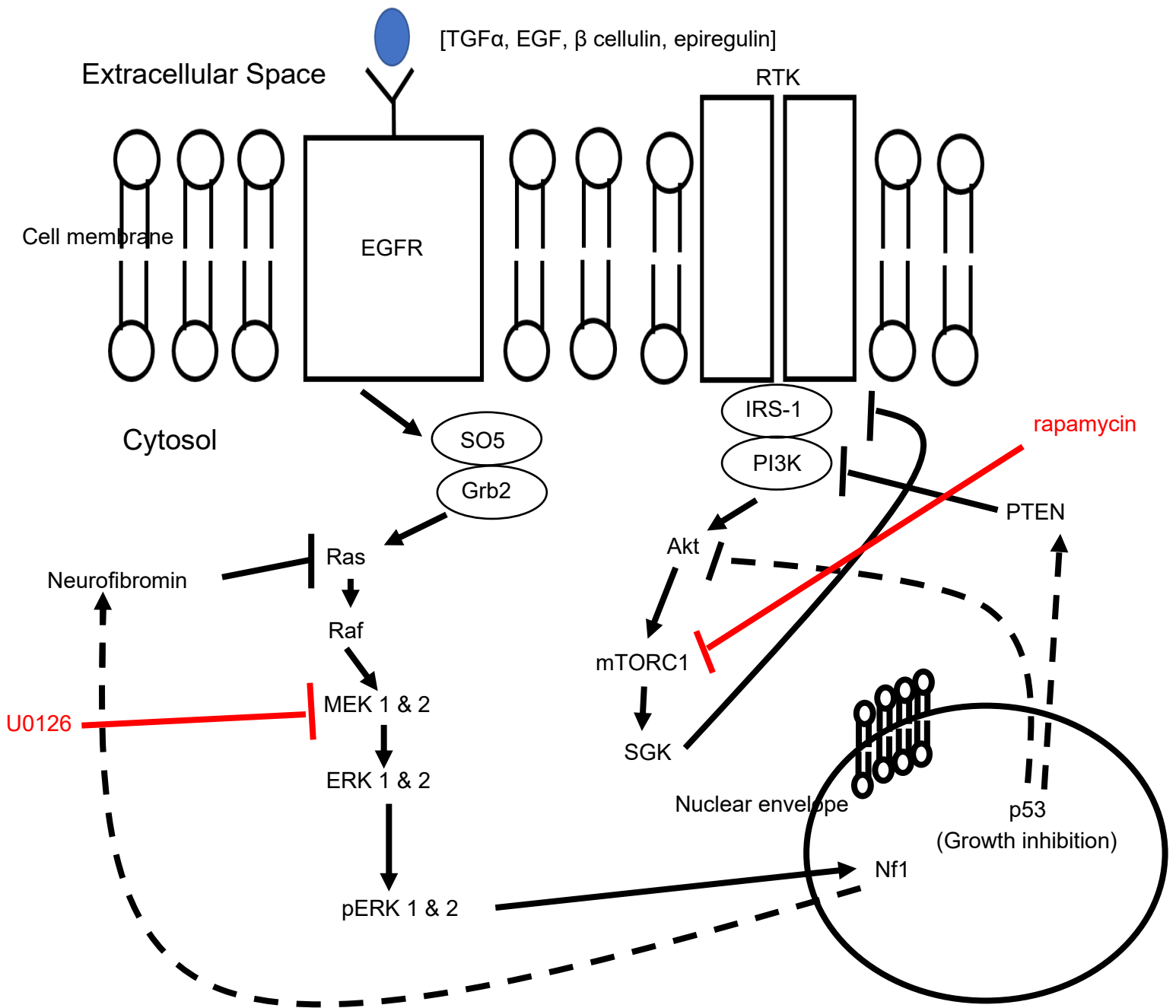


Figure B-4: OPC differentiation relevant pathways are impacted by the absence of Nf1 and p53. Disruption of ERK 1 & 2 pathway results in delayed OPC differentiation *in vivo*. Solid arrows indicate pathway promotion, solid bars indicate pathway inhibition, dashed lines indicate pathways not occurring in MADM OPCs. Red bars indicate drugs used to assess changes to OPC differentiation *in vivo* from the disruption of the Erk 1 & 2 and mTORC1 pathways.

10. Appendix C: Procedures and Protocols

List of procedures and protocols written for in-lab use. This list includes protocols for both published and unpublished experiments, and may provide more detail than published experimental methods sections because of the inclusion of notes and references. Both manufacturer protocols and protocols written by other students are not included.

10.1. Zymography for uPA degradable ELP

1. Preparation of conditioned media

1. Plate cells in a 75 cm² flask (8 mL).
2. At confluency (day of passage). Collect media.
3. Centrifuge for 5 min at 1,000 rpm and decant to eliminate dead cells.
4. Store samples at -80°C.

2. Concentrate conditioned media 10x (might not be necessary)

1. Place sample into the concentrator sample chamber. Sample volume range is 20-100 mL.
2. Centrifuge at 1,200 x g for 10 minutes (10x) or for 15 minutes (30x).
3. Collect retentate.

3. ELP zymography Gel

1. Prepare a 7.5% acrylamide gel containing ELP. Use a 1 mm thickness plate.

Separating gel (7.5 % acrylamide)

2 mL	1.5 M Tris pH 8.8
2 mL	30% acrylamide
2 mL	H ₂ O
2 mL	ELP/THPC solution
80 µL	10% APS
10 µL	TEMED

ELP/THPC solution – 2 mg/ml ELP mixed with 1:10 THPC hydroxyl group to ELP amine group ratio (2ml DI water, 16mg ELP, 1.66 ul of 50 fold diluted THPC stock).

Stacking gel (3.9 % acrylamide)

1.25 mL	0.5 M TrisCl/SDS pH 6.8
0.67 mL	30% acrylamide
3.075 mL	H ₂ O
50 µL	10 % APS

10 μ L TEMED

2. Add 3 μ l of 5x non-reducing sample buffer to 12 μ l cell media samples.

5X non-reducing sample buffer

<u>Final concentration</u>	<u>For 250 mL</u>
4% SDS	10 g
20% glycerol	50 mL
0.01% bromophenol blue	0.025 g
125 mM TrisCl, pH 6.8	4.91 g

3. Load 15 μ L cell media sample.

4. Run the gel at 140 V for 40 min to achieve good band separation is achieved.

4. Gel washing and staining

1. Perform 2 - 30 min washes with washing buffer. Soaking the gel in washing buffer removes SDS from the gel. (60 min total)

Washing buffer

<u>Final concentration</u>	<u>For 250 mL</u>
2.5% Triton X-100	6.25 ml
Distilled water	243.75 ml

2. Rinse for 5-10 min in incubation buffer at 37°C with agitation.

Incubation buffer

<u>Final concentration</u>	<u>For 250 mL</u>
0.1 M Glycine pH 8.3	1.876 g
DI water	250 ml

3. Replace with fresh incubation buffer and incubate for 24 h at 37°C.

4. Stain the gel with staining solution for 1 h. Rinse with water.

Staining solution

For 100 mL

Methanol	30ml
Acetic acid	10 mL
H ₂ O	60ml
Coomassie Blue	0.5 g

5. Incubate with destain solution until bands can clearly be seen. Areas of enzyme activity appear as white bands against a dark blue background.

Destaining solution

For 1 L

Methanol	300 mL
Acetic acid	100 mL
H ₂ O	600 mL

10.2. ELP hydrogel RT-qPCR

Note: Always maintain samples on ice while performing RNA isolation unless otherwise mentioned to help prevent RNA degradation.

- 1) Collect hydrogels in 700 ul of TRIzol reagent and freeze at -80°C.
- 2) Thaw samples and homogenize hydrogels with mortar and pestle.

Note: TRIzol is corrosive. Homogenize samples in the fume hood. Do not get TRIzol on skin.

- 3) Sonicate samples for 10 seconds to lyse cells.

Note: This is a stopping point. Samples can be stored in -80 freezer.

RNA isolation using TRIzol Reagent Protocol (Invitrogen Catalog #'s 15596026 and 15596018)

- 4) Add 140 ul chloroform to each tube. Gently mix by inverting tube back and forth.
- 5) Incubate tubes for 10 minutes at room temperature (RT).
- 6) Centrifuge samples for 15 minutes at 12,000 RCF and 4°C.
- 7) Collect upper aqueous phase (which contains RNA) and transfer to new tube.

Note: It's important to not collect any of the interphase. Normally this means a portion of the aqueous layer will not be collected.

- 8) Repeat steps 4-7 two additional times.
- 9) Add 2 ul GlycoBlue to each sample. Gently mix by inverting tube back and forth.
- 10) Add 350 ul isopropanol to the aqueous phase.
- 11) Incubate for 15 minutes at -20°C.
- 12) Centrifuge samples for 10 minutes at 12,000 RCF and 4°C.
- 13) Remove supernatant.
- 14) Wash RNA pellet in 700 ul of RT 75% ethanol solution.

Note: This is a stopping point. Samples can be stored in 4°C for 1 week or at -20°C for 1 year.

- 15) Vortex and centrifuge samples for 5 minutes at 7,500 RCF and 4°C.
- 16) Remove supernatant. Make sure to pipet off the remaining liquid without disturbing the RNA pellet.
- 17) Repeat wash steps (13-15) two more times (3 total washes).
- 18) Air dry samples (leave in fume hood) for 40 minutes.
- 19) Resuspend samples in 20 ul RNase-free water.
- 20) Incubate at 55-60°C for 15 minutes.
- 21) Measure absorbance at 260, 280, 230 and 340 nm.

22) Calculate RNA concentration and purity between samples.

$$RNA_{conc}(ug/ml) = Abs_{260nm} * 40 * dilution\ factor$$

Samples are pure if

$$\frac{Abs_{260nm}}{Abs_{280nm}} > 1.7$$

$$\frac{Abs_{260nm}}{Abs_{230nm}} > 1$$

Note: Ideal Abs 260/230 > 1.8. However, using GlycoBlue will lower this value. It does not affect downstream analysis.

23) Normalize RNA concentration in all samples to 30 ug/ml by diluting further with RNase-free water.

Note: This is a stopping point. Samples can be stored at -20°C. However, it is better to make and store cDNA because it is more stable than RNA.

Note 2: For next mixing steps use plates, tubes and pipettes designed for PCR machine. iScript cDNA Synthesis Kit (BIO-RAD catalog # 170-8891)

24) Mix the following in qPCR tubes.

1. 4 ul of 5x iScript Reaction Mix
2. 1 ul of iScript Reverse Transcriptase
3. 15 ul of RNA sample.

25) Centrifuge plate at 1,000 rpm for 2 minutes to ensure liquid is at the bottom.

26) Perform the following thermal cycling protocol:

1. 5 minutes at 25°C (Priming)
2. 20 minutes at 46°C (Reverse transcription)
3. 1 minute at 95°C (Reverse transcription inactivation)
4. Hold samples at 4°C

Note: This is a stopping point. Samples can be stored at -20°C.

SsoAdvanced Universal SYBR Green Supermix (BIO-RAD catalog # 172-5271)

27) Thaw SYBR green supermix and allow it to reach RT. Leave other solutions on ice.

28) Mix the following in a qPCR plate:

1. 10 ul SYBR green mix.
2. 1 ul of each forward and reverse primer.
3. 8 ul RNase-free water.
4. 1 ul of sample cDNA mixture (add last).

29) Centrifuge plate at 1,000 rpm for 2 minutes to ensure liquid is at the bottom.

30) Set the following thermal cycling protocol:

1. Polymerase activation: 30 seconds at 95°C
2. Denaturation: 15 seconds at 95°C

3. Annealing/Extension: 30 seconds at 60°C
4. Cycles: 40
5. 10 seconds at 95°C.
6. Melt curve analysis: 65 - 95°C range with 0.5°C increments at 5 seconds per step.

Primers for OPCs

Gene	Forward Sequence	Reverse sequence
GAPDH	5'-TGTGTCCGTCGTGGATCTGA-3'	5'-TTGCTGTTGAAGTCGCAGGAG-3'
NG2	5'-AGCAAGGAAGTGCAGAGGAG-3'	5'-CATCGAAAGACACCATCACG-3'
PDGFRa	5'-GACGAGACCATCGAGGACAT-3'	5'-GCCTCGGGAACCTTCTCTCT-3'
GalC (O1)	5'-CACAGCTGACCTGGGTGGAT-3'	5'-AGGATCGTGCCGTTCAACAT-3'
MBP	5'-CTCAGAGTCCGACGAGCCTC-3'	5'-GACACGGGCATCCTTGAC-3'
uPA	5'-CCATCCAGTCCTTGCGTGTC-3'	5'-AGTACACTGCCACCTTCAGAGT-3'

OPC protein expression by stage.

	Early OPC	Late OPC	Immature OL	Mature OL
PDGFRa	+	+	-	-
NG2	+	+	-	-
O4	-	+	+	+
GalC (O1)	-	-	+	+
MBP	-	-	-	+
MOG	-	-	-	+
MAG	-	-	-	+
PLP	-	-	-	+

10.3. OPC cryopreservation

1. Passage cells (follow Cell Expansion Protocol).
2. Mix DMSO with cold OPC media in a 1:9 volumetric ratio, respectively.

Note1: Make enough solution for 1 ml per 75×10^4 cells.

Note2: Make sure to account for sterile filter losses.

3. Sterile filter OPC media and DMSO mixture.
4. Add mixture to cells and pipette into cryopreservation vials in 1 ml aliquots.
5. Fill cell freezing container with isopropanol.

Note: May not be necessary if container is recently used and isopropanol is still present.

6. Put vials in cell freezing container and store in -80°C freezer for 2 – 4 hours.
7. Move vials from -80°C freezer to liquid nitrogen storage container.

10.4. ELP azide functionalization

1. Prepare the following the following 1 day before reaction.
 1. Dissolve ELP (25mg/ml) in potassium carbonate buffer (10mg/mL in DI water).
 2. Put round bottom flask (RBF) in vacuum oven to dry overnight.
2. Add ELP to RBF and purge with Argon.
3. Add 100 uL of copper(II) chloride solution (1 mg/mL) per mL of ELP solution.
4. Dissolve 1H-imidazole-1-sulfonyl azide HCl in potassium carbonate buffer (10mg/mL in DI water).
5. Add 1H-imidazole-1-sulfonyl azide HCl solution to the ELP solution to achieve a theoretical lysine residue amine to azide ratio of 14:4.
6. Agitate mixture for 24 hours at 25°C.
7. Dialyze mixture using DI water (3 times).
8. Freeze and lyophilize.
9. Determine ELP-azide modification through FTIR and high resolution mass spec.

10.5. ELP norbornene functionalization

Reaction:

- 1) Prepare an inert Argon atmosphere in a round bottom flask (leave overnight in vacuum oven and run at least 10 min of argon).
- 2) Dissolve ELP in DMF (50 mg/ml).
- 3) Mix 2 M excess N,N-diisopropylethylamine (DIEA) to amine groups on ELP with 1 ml DMF.
- 4) Dissolve 2 M excess of 2-(1H-7-Azabenzotriazol-1-yl)-1,1,3,3-tetramethyl uronium hexafluorophosphate methanaminium (HATU) to amine groups on ELP in 1 ml DMF.
- 5) Mix 4 M excess of 5-norbornene-2-carboxylic acid to amine groups on ELP with 1 ml DMF.
- 6) Mix norbornene acid and HATU solutions for 3 minutes in the flask.
- 7) Add DIEA solution to flask and mix for 5 minutes.
- 8) Add ELP solution dropwise while stirring.
- 9) React with stirring for 48 hrs.

Purification:

- 1) Precipitate ELP in ice cold ethyl ether.
- 2) Vacuum filter using a Buchner funnel.
- 3) Rotovap off ether.
- 4) Dissolve in DI water and adjust pH to 9.
- 5) Dialyze (3.5-5 kDa MWCO CE tubing, 3 buckets).
- 6) Lyophilize.

References:

- 1) Roberts, J. J., & Bryant, S. J. (2013). Comparison of photopolymerizable thiol-ene PEG and acrylate-based PEG hydrogels for cartilage development. *Biomaterials*, *34*(38), 9969–9979. <http://doi.org/10.1016/j.biomaterials.2013.09.020>
- 2) Acosta-Vélez, G., Linsley, C., Craig, M., & Wu, B. (2017). Photocurable Bioink for the Inkjet 3D Pharming of Hydrophilic Drugs. *Bioengineering*, *4*(1), 11. <http://doi.org/10.3390/bioengineering4010011>
- 3) Shih, H., Fraser, A. K., & Lin, C. (2013). Interfacial Thiol-ene Photoclick Reactions for Forming Multilayer Hydrogels. *Applied Materials & Interfaces*, *5*, 1673–1680. <http://doi.org/10.1021/am302690t>

10.6. PEG-BCN synthesis

Prep work: Put round-bottom flask in vac-oven overnight.

1. Argon purge round-bottom flask (5 min)
2. Dissolve PEG-amine (1g/5mL) in Dimethylformamide (DMF).
3. Separately dissolve BCN-NHS (1.5:1 molar ratio to amines) in DMF (5mL total).
4. Using a needle, add PEG-amine solution then BCN-NHS solution to flask.
5. Add N,N-Diisopropylethylamine (DIEA, 4:1 molar ratio to amines).
6. Stir for 24 hours at 25°C.
7. Dissolve in DI water (20% v/v DMF in DI water).
8. Purify by dialysis (3 buckets of deionized water, switch every 12 hrs).
9. Lyophilize.
10. Setting aside a small dry sample for H-NMR, dissolve the dried PEG-BCN in PBS immediately after lyophilizing.
11. Store aliquots of PEG-BCN solution in -80°C freezer.
12. Analyze with H-NMR (compare BCN peaks δ 2.24, 1.57, 1.34, 0.92) with those from the PEG backbone (δ 3.63)).

Reference:

Deforest, C. A., & Tirrell, D. A. (2015). A photoreversible protein-patterning approach for guiding stem cell fate in three-dimensional gels. *Nature Materials*, 14(5):523–531.

10.7. HNMR quick guide (Flipper)

- 1) Make HNMR reservation
 - a. Go to <https://uva.corefacilities.org/account/login>
 - b. Log in using UVA email username and password.
 - c. Click on “core facilities” – “BioNMR facility” – “Schedule Equipment” – “Flipper”
 - d. Double click on day you want to reserve time for.
 - e. Fill out reservation form

Note 1: Lab phone is 31151

Note 2: You must be approved by professor Lampe to use a PTAE0 on this system.

- 2) Login
- 3) Press “e” to run eject air.
- 4) Use the measuring device and put tube in machine.
- 5) Press “i” to insert sample in the machine.
- 6) Run spin at 20Hz.

Note: It is not necessary to spin the NMR tube if you are characterizing a known sample. Spinning improves the signal, but sometimes doesn't work.

- 7) Use “solvent = ‘cdcl3’” to set solvent

Note: May not need to do this after first time. Use “solvent?” To see if solvent is already correctly set. Other solvent codes ‘dmsd’, and ‘d2o’.

- 8) Find lock (this aligns the electric field).
 - a. You may have to find lock manually. Picture below is what kind of signal you are looking for.



- 9) Autoshim on lock.

Note: Can also type in code “gmap sys” and perform a gradient shim when not spinning. Make sure to hit the “quit gradient shim” button when done.

- 10) Acquisition = 16 scans.
 - a. Most manuals say to run 64 scans but 16 is adequate for a known sample.
- 11) Type in “go” to run the experiment.

- 12) When scans are done, press “wft aph” to bring up the spectra.
- 13) Save the file.
- 14) Stop spinning.
- 15) Press “e” to remove sample.
- 16) Email files to yourself for inspection with Mestrenova.
 - a. Archive entire saved folder into one file before emailing.

Other useful codes

“aa” -> aborts acquisition

“ga” -> similar to “go”, but performs “go” and “wft” codes together. Still need to run “aph” afterwards.

“bs = #” -> changes the number of scans after which the spectrum will display on screen.

10.8. Addition of Alexa Fluor 405 NHS Ester onto PEG-amine

Alexa Fluor 405 NHS Ester (Succinimidyl Ester) has excitation and emission peaks of 401 and 421nm, respectively. The reaction forms an amide bond and releases N-hydroxysuccinimide (NHS).

- a. Make 100mM sodium bicarbonate buffer (pH 8.3).
 - i. Dissolve 8.4 mg/mL of Sodium bicarbonate in DI water.
 - ii. Adjust pH to 8.3.
- b. Dissolve PEG in sodium bicarbonate buffer within the concentration range 2 - 5 wt%.
- c. Add Alexa Fluor 405 NHS ester to PEG solution at a 1:250 NHS ester to primary amine ratio.
- d. Shake overnight at 4°C.
- e. Remove unreacted fluorophore using a Zebra™ desalting column (7,000 MWCO).
- f. Freeze and lyophilize solution.
- g. Mix tagged PEG with unlabeled PEG in a 1:9 weight ratio, respectively.

Reagents Required

- a. Sodium bicarbonate (sigma – 500g) - \$40.30
- b. Alexa Fluor 405 NHS Ester - \$295.00 for 1 mg
- c. Zebra desalt column (Thermo fisher Cat. # 89893 – 5 columns) - \$78.25

10.9. Addition of Rhodamine onto ELP

ELP staining with Rhodamine – Rhodamine is Tetramethylrhodamine-5-(and 6)-isothiocyanate (TRITC) that has excitation wavelength of 555 nm and emission wavelength of 580 nm. TRITC will form stable derivatives with primary and secondary amines.

- a. Make 100mM conjugate buffer (pH 9).
 - i. Dissolve 8.4 mg/mL of Sodium bicarbonate in DI water.
 - ii. Dissolve 28.62 mg/mL of Sodium carbonate decahydrate in DI water.
 - iii. Mix sodium bicarbonate and sodium carbonate solutions in a 9:1 volumetric ratio, respectively.
- b. Dissolve ELP in conjugate buffer at 5 wt%.
- c. Add TRITC to ELP solution at a 1:250 isothiocyanate to primary amine ratio.
- d. Shake overnight at 4°C.
- e. Remove unreacted fluorophore using a Zebra™ desalting column (7,000 MWCO).
- f. Freeze and lyophilize solution.
- g. Mix rhodamine tagged ELP with unlabeled ELP in a 1:100 weight ratio, respectively.

Reagents Required

- a. Sodium bicarbonate (sigma – 500g) - \$40.30
- b. Sodium carbonate decahydrate (sigma – 250g) – \$39.80
- c. TRITC (Thermo fisher Cat. # T1480 – 5mg) - \$173.00
- d. Zebra desalt column (Thermo fisher Cat. # 89893 – 5 columns) - \$78.25

10.10. PEG microwave-assisted methacrylation

- 1) Measure out a quantity of PEG or PEG-LA you want to methacrylate (5-20g).
- 2) Add to scintillation vial.
- 3) Add methacrylic anhydride in 10 molar excess per PEG hydroxyl end group.
 - a. Add in fume hood using a syringe.
 - b. Mw of methacrylic anhydride is 154g/mol.
 - c. Density of methacrylic anhydride is 1.035g/mL.
- 4) Put vial in the microwave with cap loosened.
- 5) Run microwave for 5 minutes. Every 30 seconds stop the microwave and vortex the sample.
 - a. The vial will be very hot when microwaving so use the insulating gloves.
 - b. Tighten the cap every time you vortex. Also, vortex inside fume hood.
 - c. Loosen the cap every time you put it into the microwave.
 - d. Make sure the microwave power is set to the max setting.
- 6) Purification process is the same as PEG-LA.

10.11. Cell expansion (passage)

1. Aspirate media off.
2. Add trypsin in DPBS to cell culture (Final concentration of trypsin should be 0.125%).
Trypsin is an esterase that will remove cells adhered to the surface and put them solution.
 - A. For PC12 cells use 250 μ L of 2.5% trypsin in 5mL DPBS.
3. Incubate cells for 5 minutes.
4. Tap sided of petri dish to shake cells off of surface.
5. Gently rinse and agitate cell solution to break up cell clusters.
6. Put cell solution(s) into a falcon tube.
7. Rinse cell culture petri dish with an additional 10mL of DPBS.
8. Centrifuge falcon tube with at 1000rpm for 5 minutes.

Note 1: Do not forget to balance centrifuge.

Note 2: Bleach petri dish for 10 minutes and throw out.

9. Aspirate off liquid and leave cell pellet.
10. Resuspend cell pellet with the appropriate media (~100-500 μ L of media) for the cell culture.
 - A. PC12 Cells
 - i. 81.5% F12K Media
 - ii. 2.5% Fetal Bovine Serum (FBS)
 - iii. 1% Penicillin Streptomycin (Pen/Strep)
 - iv. 15% Donor Horse Serum (HS)

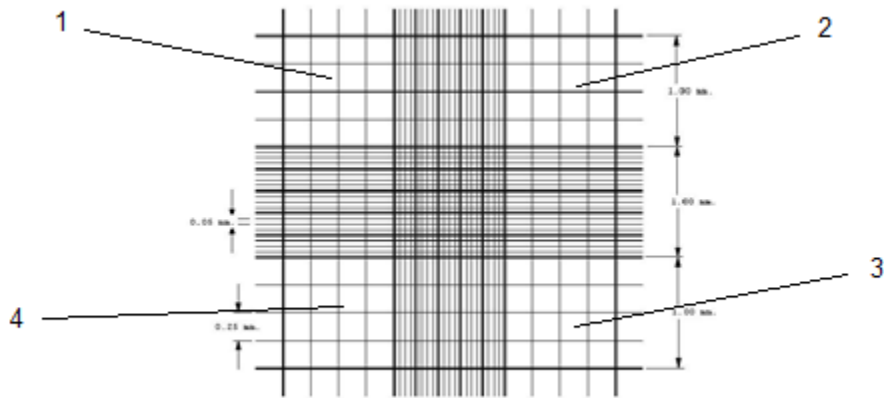
Note: Media formulation listed above tissue culture hood.

11. Extract a 20 μ L sample for cell counting and place in microtube.
12. Dilute microtube solution with Trypan Blue, and record dilution amount.

Note 1: Optimal dilution leaves ~50 cells per 4x4 grid when performing cell count on hemocytometer.

Note 2: Perform cell count within 5 minutes of adding Trypan Blue. Over long periods of time the dye starts leaking into live cells.

13. Inject 10 μ L of sample into cytometer.
14. Count cells in each of the four 4x4 grids. Cytometer picture shown below.



15. Determine cell density from cytometer cell count and dilution amount. Each 4x4 grid is 10^{-4} mL.

Example Calculation:

- Cytometer cell counts: 171, 283, 140, 264
- Dilution: 20 μ L cell sample with 80 μ L TrypanBlue (five-fold dilution)
Average cell count = $(171+283+140+264)/4 = 214.5$
Cell density = $214.5 \times 5 = 1.36 \times 10^7$ cells/mL

16. Calculate volume of cell solution needed for each new petri dish. The desired cell culture surface area in the new solution is $\sim 1 \times 10^4$ cells/cm².

Example Calculation:

- Petri dish surface area is 55 cm²
Volume needed = $(55 \text{ cm}^2) \times (1 \times 10^4 \text{ cells/cm}^2) / (1.36 \times 10^7 \text{ cells/mL}) = 0.04 \text{ mL}$

17. Get new petri dishes and plate them with 10 mL of appropriate media.

Note: Depending on cell culture you may need to rinse the surface of the new petri dishes three times with DPBS. This is NOT required for PC12 cells.

18. Add the calculated volume of cell culture solution to each petri dish.
19. Gently swirl mixture around to get ideal cell monolayer.
20. Inspect cells under microscope to ensure ideal cell surface area.
21. Incubate cell petri dishes.

Note 1: Media should be changed every two days.

Note 2: Tissue culture hood and incubator are sterile environments. Take appropriate actions when moving items in and out of them.

Note 3: Clean hemocytometer with water, followed by 70% ethanol and use kimwipes.

10.12. Cell expansion (OPC)

1. Aspirate media off.
2. Add trypsin in DPBS to cell culture (Final concentration of trypsin should be 0.5x).
 - A. Trypsin is an esterase that will remove cells adhered to the surface and put them in solution.
 - B. For OPCs in T-75 plates use 250 μ L of 2.5% trypsin in 5mL DPBS.
3. Incubate cells for 5 minutes at 37°C.
4. Tap sided of petri dish to shake cells off of surface.
5. Gently rinse and agitate cell solution to break up cell clusters.
6. Put cell solution(s) into a falcon tube.
7. Rinse cell culture T-75 plate with an additional 10mL of DPBS.
8. Centrifuge falcon tube with at 1,000 rpm for 5 minutes.

Note 1: Do not forget to balance centrifuge.

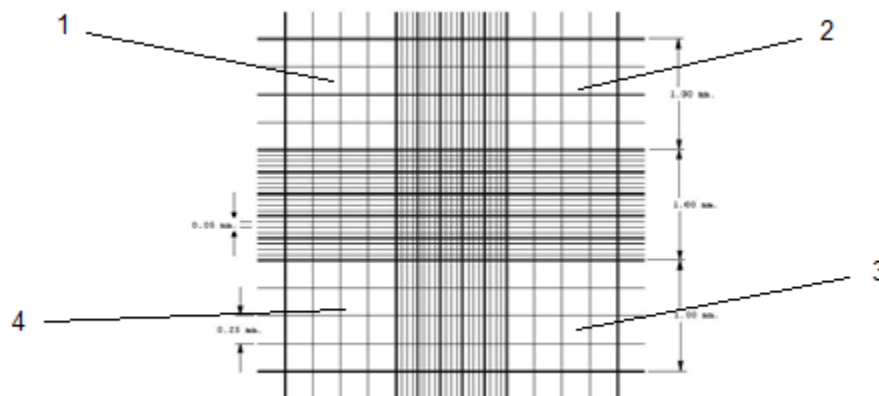
Note 2: Bleach used t-75 plate for 10 minutes and throw out.

9. Aspirate off liquid and leave cell pellet.
10. Resuspend cell pellet with 1x PBSG (~300 μ L per T-75 plate).
11. Extract a 20 μ L sample for cell counting and place in microtube.
12. Dilute microtube solution with Trypan Blue, and record dilution amount.

Note 1: Optimal dilution leaves ~50 cells per 4x4 grid when performing cell count on hemocytometer.

Note 2: Perform cell count within 5 minutes of adding Trypan Blue. Over long periods of time the dye starts leaking into live cells.

13. Inject 15 μ L of sample into cytometer.
14. Count cells in each of the four 4x4 grids. Cytometer picture shown below.



15. Determine cell density from cytometer cell count and dilution amount. Each 4x4 grid is 10⁻⁴mL.

Example Calculation:

- Cytometer cell counts: 171, 283, 140, 264
- Dilution: 20 μ L cell sample with 80 μ L Trypan Blue (five-fold dilution)
Average cell count = $(171+283+140+264)/4 = 214.5$
Cell density = $214.5 \times 5 = 1.36 \times 10^7$ cells/mL

16. Calculate volume of cell solution needed for each new T-75 plate. The desired cell culture surface area in the new solution is $\sim 1 \times 10^4$ cells/cm².

Example Calculation:

- T-75 plate surface area is 75 cm²
Volume needed = $(75 \text{ cm}^2) \times (1 \times 10^4 \text{ cells/cm}^2) \times (1,000 \text{ ul/ml}) / (1.36 \times 10^7 \text{ cells/mL}) = 55$ uL per T-75 plate

17. Immerse cell volume in 8 ml OPC media per T-75 plate.

A. OPC media mixture:

- 40 ml DMEM +G
- 400 ul Pen/Strep (1x)
- 400 ul N2 supplement (1x)
- 800 ul B27 supplement (1x)

18. Add mixture to new T-75 plate.

19. Gently swirl mixture around to get ideal cell monolayer.

20. Inspect cells under microscope to ensure ideal cell surface area.

21. Incubate cell petri dishes.

Note 1: Media should be changed every two days.

Note 2: Tissue culture hood and incubator are sterile environments. Take appropriate actions when moving items in and out of them.

Note 3: Clean hemocytometer with water, followed by 70% ethanol and use kim wipes.